UQAC
Université du Québec
à Chicoutimi

DEVELOPMENT AND CHARACTERIZATION OF SUPERPLASTIC Al–Mg–Mn 5XXX ALLOYS FOR AUTOMOBILE APPLICATION

By

Eric Kojo Kweitsu

Under the supervision of Prof Dilip Sarkar Kumar and co-supervision of Prof. X.-Grant Chen

Manuscript-Based Thesis presented to the University of Quebec at Chicoutimi with a view to obtaining the degree of Philosophiae doctor (Ph.D.) in engineering.

BOARD OF EXAMINERS:

Professor Yasar Kocaefe, Department of Applied Sciences at UQAC, President of the board of examiners

Professor Lei Ray Pan, Rio Tinto Aluminum**,** Saguenay, Quebec, External member of examiners

Professor Dilip Kumar Sarkar, Department of Applied Sciences at UQAC, Internal member of examiners

Professor X.-Grant Chen, Department of Applied Sciences at UQAC, Internal member of examiners

Professor Mousa Javidani, Department of Applied Sciences at UQAC, Internal member of examiners

Québec, Canada

© Eric Kojo Kweitsu (2026)

Résumé

La demande croissante pour des systèmes de transport légers et écoénergétiques a intensifié le développement d'alliages Al–Mg–Mn 5xxx à faible coût. En particulier, des alliages capables de soutenir une déformation à haute température sur une large gamme de vitesses de déformation sont nécessaires pour le formage par soufflage à grande vitesse (*High-Speed Blow Forming*, HSBF). Le HSBF constitue une alternative prometteuse au formage superplastique conventionnel (*Superplastic Forming*, SPF), en combinant une première étape de déformation à vitesse de déformation élevée avec une étape subséquente de formage au gaz à faible vitesse de déformation. Cette approche réduit considérablement le temps de formage tout en permettant la fabrication de composants automobiles complexes. Cependant, la réussite du procédé HSBF nécessite des alliages capables de développer des structures de grains stables pendant un recuit de courte durée et de soutenir la déformation sur une large gamme de vitesses de déformation sans localisation prématurée de la déformation ni cavitation. Les études existantes se sont principalement concentrées sur les recuits de longue durée et la déformation à faible vitesse de déformation, laissant les effets du recuit rapide, de la déformation à haute vitesse de déformation et de l'évolution de la cavitation dans des conditions pertinentes pour le HSBF insuffisamment compris. Ainsi, cette thèse développe un cadre mécanistique décrivant les relations procédé–microstructure–déformation dans les alliages Al–Mg–Mn 5xxx sous conditions HSBF, puis applique cette compréhension à la conception d'alliages microalliés au Sc, au Zr et à l'Er, à faible coût, adaptés aux applications HSBF.

Dans un premier temps, ce travail examine le recuit de courte durée comme voie rapide pour produire des structures de grains fines et stables. Deux alliages Al–Mg–Mn 5xxx, l'alliage 1 (Al–4,5Mg–0,74Mn) et l'alliage 2 (Al–4,0Mg–1,18Mn), subissent une recristallisation statique rapide après seulement 2 min de recuit à 520 °C. Après 4 min, l'alliage 2 présente une fraction plus élevée de grains inférieurs à 10 µm ainsi qu'une meilleure résistance à la croissance des grains. Cette stabilité améliorée est attribuée à sa plus grande densité numérique de dispersoïdes riches en Mn. Ces résultats démontrent que le recuit de courte durée peut générer des microstructures capables de soutenir une déformation superplastique et fournissent une meilleure compréhension de l'évolution de la structure des grains dans les conditions thermiques rapides pertinentes pour le HSBF.

S'appuyant sur ces résultats, la deuxième étude examine le comportement en déformation et l'évolution microstructurale de l'alliage 2 dans des conditions pertinentes pour le HSBF. L'alliage a été testé entre 450 et 520 °C à des vitesses de déformation comprises entre 0,001 et 1 s^{-1} après un recuit de courte durée, lequel a produit une structure de grains fine, entièrement recristallisée, de 4,5 à 5,6 µm. L'allongement et la contrainte d'écoulement montrent une forte dépendance à la température et à la vitesse de déformation, avec une ductilité maximale atteinte à 500 °C. À faibles vitesses de déformation, la déformation est dominée par le glissement aux joints de grains. La réduction de la ductilité à 450 °C est associée au fluage contrôlé par traînage de soluté, tandis que la diminution de la formabilité à 520 °C est liée à une croissance des grains contrôlée par diffusion. À 1 s^{-1}, un raffinement significatif des grains se produit par recristallisation dynamique continue. Les

dispersoïdes contenant du Mn améliorent la stabilité microstructurale en limitant la migration des joints de grains. Ces résultats clarifient les mécanismes de déformation dominants dans des conditions pertinentes pour le HSBF et fournissent des orientations pour la conception microstructurale des alliages Al–Mg–Mn 5xxx.

La troisième étude examine l'évolution de la cavitation dans les alliages 1 et 2 afin de clarifier l'influence de la vitesse de déformation, des particules intermétalliques, de la structure des grains et des mécanismes de déformation sur le développement de l'endommagement et les limites de formabilité dans des conditions pertinentes pour le HSBF. Les alliages ont été testés à 500 °C à des vitesses de déformation allant de 0,001 à 1 s^{-1}. Le comportement de cavitation montre une transition nette avec l'augmentation de la vitesse de déformation. À 0,001 s^{-1}, la déformation assistée par le glissement aux joints de grains favorise la croissance et la coalescence des cavités assistées par diffusion, conduisant aux fractions surfaciques de cavités les plus élevées. À 0,01 s^{-1}, l'interaction entre le glissement aux joints de grains et l'activité dislocationnelle intragranulaire limite la croissance des cavités et retarde leur coalescence. À 1 s^{-1}, la croissance des cavités assistée par diffusion est fortement supprimée, et l'endommagement se développe principalement sous forme de fins microvides allongés directionnellement. Bien que l'alliage riche en Mn, l'alliage 2, présente une densité de nucléation des cavités plus élevée en raison de sa plus grande population de particules intermétalliques, il conserve une ductilité supérieure sur toute la gamme de vitesses de déformation étudiée. Ce comportement est attribué à sa structure de grains plus fine et thermiquement stable, qui permet d'accommoder une accumulation plus importante de cavités tout en retardant leur liaison et la localisation de l'endommagement. Ces résultats établissent un cadre de cavitation dépendant de la vitesse de déformation, reliant les mécanismes de déformation, la stabilité microstructurale et l'évolution de l'endommagement dans des conditions pertinentes pour le HSBF. Ils soulignent également la nécessité de contrôler les IMC grossiers excessifs tout en favorisant des microstructures à grains fins et stables pour la conception d'alliages Al–Mg–Mn 5xxx tolérants à l'endommagement et adaptés au HSBF.

La phase finale de la thèse porte sur le développement d'alliages Al–Mg–Mn issus de rebuts, à faible coût et économes en ressources, pour les applications HSBF, en s'appuyant sur la compréhension de la recristallisation, de la cavitation et du comportement en déformation établie à partir des alliages commerciaux étudiés dans les phases précédentes. Trois alliages Al–Mg–Mn 5xxx issus de rebuts ont été développés : un alliage de base sans Sc, Zr ni Er ; un alliage Al–Mg–Mn microallié au Sc–Zr, BSc10Zr ; et un alliage Al–Mg–Mn microallié à l'Er–Sc–Zr, BSc05ZrEr. Le recuit de courte durée à 500 °C produit une structure entièrement recristallisée dans l'alliage de base, tandis que les alliages contenant du Sc conservent des microstructures majoritairement bandées ou partiellement recristallisées en raison du fort effet d'ancrage des précipités cohérents de structure $L1_2$, $Al_3(Sc,Zr)$ et $Al_3(Sc,Zr,Er)$. À 0,01 s^{-1}, BSc05ZrEr présente l'allongement le plus élevé, soit environ 256 %, en raison de sa fraction plus élevée de grains fins recristallisés, tandis que BSc10Zr montre une ductilité plus faible, d'environ 200 %, en raison de sa structure majoritairement non recristallisée/bandée. À 0,1 s^{-1}, BSc10Zr atteint la ductilité maximale, d'environ 259 %, tandis que BSc05ZrEr maintient une ductilité stable d'environ 254 %, indiquant une formabilité améliorée sur une gamme plus large de vitesses de déformation. L'analyse EBSD montre que cette ductilité améliorée est associée à une augmentation de la fraction de joints

de grains à grand angle, à la subdivision des joints et à un raffinement dynamique des grains compatible avec une évolution de type CDRX. À 1 s^{-1}, la déformation contrôlée par les dislocations réduit la ductilité de tous les alliages ; toutefois, les alliages contenant du Sc conservent un allongement appréciable grâce à leur meilleure résistance à la localisation de l'écoulement. Dans BSc05ZrEr, les zones dépourvues de dispersoïdes liés au Mn favorisent la partition de la déformation, limitant ainsi une amélioration supplémentaire de la ductilité. Sous déformation en deux étapes pertinente pour le HSBF, de 1 s^{-1} à 0,01 s^{-1}, l'alliage BSc05ZrEr, à faible teneur en Sc et contenant de l'Er, atteint un allongement d'environ 286 %, démontrant une formabilité améliorée et une tolérance supérieure aux transitions de vitesse de déformation. Ces résultats montrent qu'un microalliage ciblé des alliages Al–Mg–Mn issus de rebuts peut équilibrer le contrôle de la recristallisation, la stabilité en déformation, le coût de l'alliage et l'efficacité des ressources, fournissant ainsi des orientations pour la conception d'alliages d'aluminium en tôle durables destinés aux applications HSBF.

Dans l'ensemble, cette thèse établit un cadre intégré procédé–microstructure–déformation–endommagement pour les alliages Al–Mg–Mn 5xxx dans des conditions pertinentes pour le HSBF. Les résultats démontrent que le recuit de courte durée, les structures de grains stabilisées par les dispersoïdes de Mn, les mécanismes de déformation dépendants de la vitesse de déformation, la résistance à la cavitation et le microalliage Sc–Zr–Er à faible coût sont des facteurs essentiels pour obtenir un formage stable à grande vitesse. Ce travail fournit à la fois une compréhension fondamentale et des orientations pratiques pour la conception d'alliages Al–Mg–Mn 5xxx durables et à faible coût, soutenant ainsi le développement industriellement viable du HSBF pour la fabrication de composants automobiles légers et complexes.

Abstract

The growing demand for lightweight and energy-efficient transportation systems has intensified the development of cost-effective Al–Mg–Mn 5xxx alloys. In particular, alloys capable of sustaining high-temperature deformation across a wide strain-rate range are required for high-speed blow forming (HSBF). HSBF offers a promising alternative to conventional superplastic forming (SPF) by combining an initial high strain-rate deformation stage with a subsequent low strain-rate gas-forming stage. This approach significantly reduces forming time while enabling the fabrication of complex automotive components. However, successful HSBF processing requires alloys that can develop stable grain structures during short-duration annealing and sustain deformation over a wide strain-rate range without premature strain localization or cavitation. Existing studies have mainly focused on long-duration annealing and low strain-rate deformation, leaving the effects of rapid annealing, high strain-rate deformation, and cavitation evolution under HSBF-relevant conditions insufficiently understood. Accordingly, this thesis develops a mechanistic framework to describe the processing–microstructure–deformation relationships in Al–Mg–Mn 5xxx alloys under laboratory conditions representative of the key thermal and deformation stages of HSBF, hereafter referred to as HSBF-relevant conditions. This understanding is then applied to the design of cost-effective Sc-, Zr-, and Er-microalloyed Al–Mg–Mn alloys tailored for HSBF applications.

The work first examines short-duration annealing as a rapid route to produce fine and stable grain structures. Two Al–Mg–Mn 5xxx alloys, Alloy 1 (Al–4.5Mg–0.74Mn) and Alloy 2 (Al–4.0Mg–1.18Mn), undergo rapid static recrystallization after only 2 min of annealing at 520 °C. After 4 min, Alloy 2 exhibits a higher fraction of grains below 10 μm and greater resistance to grain coarsening. This improved stability is attributed to its higher number density of Mn-rich dispersoids. These results demonstrate that short-time annealing can generate microstructures capable of sustaining superplastic deformation and provide insight into grain structure evolution under the rapid thermal conditions relevant to HSBF.

Building on this, the second study investigates the deformation behavior and microstructural evolution of Alloy 2 under HSBF-relevant conditions. The alloy was tested between 450 and 520 °C at strain rates from 0.001 to 1 s^{-1} after short-time annealing, which produced a fine, fully recrystallized grain structure of 4.5–5.6 μm. Elongation and flow stress show strong dependence on temperature and strain rate, with maximum ductility achieved at 500 °C. At low strain rates, deformation is dominated by grain-boundary sliding. Reduced ductility at 450 °C is associated with solute-drag creep, while decreased formability at 520 °C is linked to diffusion-controlled grain growth. At 1 s^{-1}, significant grain refinement occurs through continuous dynamic recrystallization. Mn-containing dispersoids enhance microstructural stability by restricting grain-boundary migration. These findings clarify the governing deformation mechanisms across HSBF-relevant conditions and provide guidance for microstructure design in Al–Mg–Mn 5xxx alloys.

The third study examines cavitation evolution in Alloy 1 and Alloy 2 to clarify how strain rate, intermetallic particles, grain structure, and deformation mechanisms influence damage development and formability limits under HSBF-relevant conditions. The alloys

were tested at 500 °C over strain rates from 0.001 to 1 s^{-1}. Cavitation behavior shows a clear transition with increasing strain rate. At 0.001 s^{-1}, grain-boundary-sliding-assisted deformation promotes diffusion-assisted cavity growth and coalescence, resulting in the highest cavity area fractions. At 0.01 s^{-1}, the interaction between grain-boundary sliding and intragranular dislocation activity limits cavity growth and delays coalescence. At 1 s^{-1}, diffusion-assisted cavity growth is strongly suppressed, and damage develops mainly through fine, directionally extended microvoids. Although the Mn-rich alloy, Alloy 2, exhibits a higher cavity nucleation density due to its larger intermetallic particle population, it maintains superior ductility across the investigated strain-rate range. This behavior is attributed to its finer and thermally stable grain structure, which accommodates greater cavity accumulation while delaying cavity linkage and damage localization. These findings establish a strain-rate-dependent cavitation framework linking deformation mechanisms, microstructural stability, and damage evolution under HSBF-relevant conditions. They also highlight the need to control excessive coarse IMCs while promoting stable fine-grained microstructures for the design of damage-tolerant Al–Mg–Mn 5xxx alloys tailored for HSBF.

The final phase of the thesis focuses on the development of cost-effective and resource-efficient scrap-derived Al–Mg–Mn alloys for HSBF applications, based on the understanding of recrystallization, cavitation, and deformation behavior established from the commercial alloys investigated in the earlier phases. Three scrap-derived Al–Mg–Mn 5xxx alloys were developed: a base alloy without Sc, Zr, or Er; a Sc–Zr-microalloyed Al–Mg–Mn alloy, BSc10Zr; and an Er–Sc–Zr-microalloyed Al–Mg–Mn alloy, BSc05ZrEr. Short-time annealing at 500 °C produces a fully recrystallized structure in the base alloy, whereas the Sc-containing alloys retain predominantly banded or partially recrystallized microstructures owing to the strong pinning effect of coherent $L1_2$-structured $Al_3(Sc,Zr)$ and $Al_3(Sc,Zr,Er)$ precipitates. At 0.01 s^{-1}, BSc05ZrEr exhibits the highest elongation of approximately 256 %, owing to its higher fraction of fine recrystallized grains, while BSc10Zr shows lower ductility of approximately 200 % due to its predominantly unrecrystallized/banded structure. At 0.1 s^{-1}, BSc10Zr achieves the maximum ductility of approximately 259 %, while BSc05ZrEr maintains stable ductility of approximately 254 %, indicating enhanced formability over a broader strain-rate range. EBSD analysis shows that the improved ductility is associated with increased high-angle grain-boundary fractions, boundary subdivision, and dynamic grain refinement consistent with CDRX-type evolution. At 1 s^{-1}, dislocation-mediated deformation reduces ductility in all alloys; however, the Sc-containing alloys retain appreciable elongation due to their greater resistance to flow localization. In BSc05ZrEr, Mn-related dispersoid-free zones promote strain partitioning, limiting further ductility improvement. Under HSBF-relevant dual-stage deformation from 1 s^{-1} to 0.01 s^{-1}, the low-Sc, Er-containing BSc05ZrEr alloy achieves approximately 286 % elongation, demonstrating improved formability and superior tolerance to strain-rate transitions. These findings show that targeted microalloying of scrap-derived Al–Mg–Mn alloys can balance recrystallization control, deformation stability, alloy cost, and resource efficiency, providing guidance for the design of sustainable aluminum sheet alloys for HSBF applications.

Overall, this thesis establishes an integrated processing–microstructure–deformation–damage framework for Al–Mg–Mn 5xxx alloys under HSBF-relevant conditions. The results demonstrate that short-duration annealing, Mn-dispersoid-stabilized grain structures, strain-rate-dependent deformation mechanisms, cavitation resistance, and

cost-effective Sc–Zr–Er microalloying are critical factors for achieving stable high-speed forming. This work provides both fundamental understanding and practical guidance for the design of cost-effective and sustainable Al–Mg–Mn 5xxx alloys, thereby supporting the advancement of industrially viable HSBF for manufacturing complex lightweight automotive components.

Table of Contents

Résumé ii
Abstract v
Table of Contents viii
List of Tables xiii
List of Figures xiv
List of Abbreviations xxiii
Dedication xxiv
Acknowledgment xxv
Chapter 1 1
Introduction 1
1.1 Background 1
1.2 Problem statement 2
1.3 Research objectives 4
1.4 Originality statement 6
1.5 Thesis outline 9
Chapter 2 17
Literature Review 17
2.1 Introduction 17
2.2 Superplastic aluminum alloys 19
2.3 Deformation mechanisms in superplastic aluminum alloys 22
2.4 Factors affecting superplasticity of aluminum alloys 26
2.4.1 Effect of grain size and texture 26
2.4.2 Effect of precipitation (Precipitates and Dispersoids) 27
2.4.3 Effect of temperature 29
2.5 Cavitation behavior under superplastic forming conditions 30
2.6 High-strain-rate superplastic forming processes 32
2.7 Recycled aluminum and scrap-based alloy design 33
2.8 Superplastic Al–Mg alloy design strategy 35
2.9 Summary and research gaps 37

References 39
Chapter 3 47
Effect of Annealing Time on Grain Structure Evolution and Superplastic Response of Al-Mg 5xxx Alloys 47
Abstract 47
3.1 Introduction 48
3.2 Material and methods 50
3.3 Results 53
3.3.1 Chemical composition and as-received microstructure 53
3.3.2 Grain structure evolution during annealing 57
3.3.3 Tensile properties 62
3.4 Discussion 64
3.4.1 Effect annealing time on grain structure evolution 64
3.4.2 Superplastic behavior 67
3.5 Conclusions 68
References 69
Chapter 4 75
Superplastic Deformation and Microstructural Evolution of an Al–Mg–Mn 5xxx Alloy for High-Speed Blow Forming Applications 75
Abstract 75
4.1 Introduction 76
4.2 Material and methods 80
4.2.1 Material 80
4.2.2 Tensile test 80
4.2.3 Microstructure analysis 81
4.3 Results 83
4.3.1 As-received and annealed microstructures 83
4.3.2 Hot tensile deformation and superplastic behavior 86
4.3.3 Grain structure after deformation 90
4.4. Discussion 95
4.4.1 Effect of temperature on grain structure and superplastic deformation behavior 95

4.4.2 Effect of strain rate on grain structure and superplastic deformation behavior ... 98
4.4.3 Implications of deformation behavior on HSBF ... 103
4.5 Conclusion ... 105
Reference ... 106
Chapter 5 ... 114
Strain-Rate-Dependent Cavitation in Al–Mg–Mn 5xxx Alloys: Mechanistic Insights for High-Speed Blow Forming ... 114
Abstract ... 114
5.1 Introduction ... 115
5.2 Materials and methods ... 117
5.2.1 Materials and hot tensile testing ... 117
5.2.2 Microstructure characterization ... 119
5.3 Results ... 120
5.3.1 As-received microstructure ... 120
5.3.2 High-temperature deformation behavior ... 123
5.3.3 Grain structure evolution ... 126
5.3.4 Strain-rate-dependent cavitation behavior ... 129
5.3.5 Cavity evolution with strain during deformation at low strain rate ... 135
5.3.6 Fracture surface morphology ... 137
5.4. Discussion ... 143
5.4.1 Strain-rate-dependent transition in cavitation and fracture behavior ... 143
5.4.2 Role of IMCs and grain-structure stability in controlling cavitation damage and ductility ... 146
5.4.3 Implications for HSBF processing and cavitation modeling ... 151
5.5 Conclusions ... 153
References ... 156
Chapter 6 ... 161
Microstructural Evolution and Strain-Rate-Dependent Deformation of Sc–Zr–Er Microalloyed Al–Mg–Mn 5xxx Alloys Produced from Recycled Automotive Sheet Scrap for High-Speed Blow Forming ... 161
Abstract ... 161
6.1 Introduction ... 162

6.2 Materials and methods 165
6.2.1 Alloy preparation 165
6.2.2 Hot tensile testing 167
6.2.3 Microstructure characterization 169
6.3 Results 171
6.3.1 As-cast microstructures 171
6.3.2 As-homogenized microstructure 173
6.3.3 As-rolled microstructure 174
6.3.4 Static recrystallization behavior during annealing 175
6.3.5 TEM characterization of dispersoids and precipitates after annealing 180
6.3.6 Hot tensile properties. 182
6.3.7 Dual-stage deformation 186
6.3.8 Grain structure evolution during tensile deformation 188
6.4 Discussion 194
6.4.1 Effect of microalloying on microstructure evolution and recrystallization behavior 194
6.4.2 Effect of microalloying on strain-rate-dependent deformation behavior 198
6.4.3 Implications for high-speed blow forming 207
6.5 Conclusions 210
References 212
Chapter 7 219
Conclusions, limitations, and recommendations 219
7.1 General conclusions 219
7.2 Limitations and clarifications of the present study 222
List of Publications 227
Conference presentations 227
Scientific posters 227
Appendix A 228
Supplementary Experimental Methodology and Clarifications 228
A.1 Comparison and Rationale of Experimental Protocols across Chapters 228
A.2 Mechanical Data Analysis and Apparent Activation-Energy Determination 235

A.3 Interrupted Deformation and Cavitation Assessment 236
A.4 Microstructural Evidence for Identification of Continuous Dynamic Recrystallization 238
A.5 Dual-Stage Strain-Rate Deformation Methodology 240
Appendix B – Research Ethics Declaration.....244

List of Tables

Table 2.1 Superplastic aluminum alloys and their deformation characteristics.....20

Table 3.1. Chemical composition of Al-Mg 5xxx alloys studied (wt.%). 54

Table 3.2 Quantitative TEM analysis of Mn dispersoids in two Alloys. 57

Table 4.1 Chemical composition of Al–Mg–Mn 5xxx alloy (wt.%) 80

Table 5.1. Mean cavity ECD and D_{90} values obtained from the cavity-size distributions. 134

Table 6.1 Characteristics of Mn-dispersoids and precipitates after annealing at 500 °C for 10 min 182

Table 6.2. Proposed principal deformation mechanisms across the investigated strain-rate range, interpreted from the combined mechanical and microstructural evidence. 206

List of Figures

Figure 2.1. Schematic diagram showing microstructures of Al alloys (a) produced.....21
via discontinuous recrystallization and (b) produced via continuous recrystallization. 21
Figure 2.2 Schematic representation of GBS occurring in fine-grained Al alloys: (a) initial grain structure and (b) GBS mechanism, the blue arrows show the grain sliding direction 23
Figure 2.3 Schematic representation of DC occurring in coarse-grained Al alloys: (a) initial grain structure and (b) diffusion creep mechanism, the blue arrows show atomic transport along grain boundaries.....24
Figure 3.1 Experimental procedure and condition for high-temperature tensile testing. (a) Gleeble tensile test procedure showing the annealing stage and deformation at three different strain rates (ε). (b) Dimensions of tensile samples with red dots indicating the surface attached thermocouples during the temperature distribution study. (c) Temperature distribution profile along the gauge length. The green lines show the 6 mm uniform temperature zone in the center region of the sample. 52
Figure 3.2 Polarized light optical micrographs showing the deformed grain structure; (a) Alloy 1 and (b) Alloy 2 in the as-received state; the black dots indicated by the white arrows show intermetallic phases (IMCs) in the microstructure. 54
Figure 3.3 SEM images depicting intermetallic phases (IMCs) in (a) Alloy 1 and (c) Alloy 2. SEM-EDS spectra and inserted EDS results showing (b) $Al_6(Mn,Fe)$ and (d) Mg_2Si IMCs in Alloy 1 and Alloy 2. (e) Area fraction diagram of two IMCs.....55
Figure 3.4 Bright-field TEM images showing the distribution of Mn dispersoids in (a) Alloy 1 and (b) Alloy 2. TEM images were taken along the $[001]_{Al}$ zone axis. 57
Table 3.2 Quantitative TEM analysis of Mn dispersoids in two Alloys. 57

Figure 3.5 Polarized light optical micrographs illustrating the evolution of grain structure in Alloy 1 (a,c,e,g,i) and Alloy 2 (b,d,f,h,j) after annealing at 520 °C for 2, 4, 10, 15, and 30 min, respectively. 58

Figure 3.6 Grain size variation with annealing time at 520 °C for Alloy 1 and Alloy 2. 59

Figure 3.7 Inverse pole figures of ESBD showing grain structure in Alloy 1 (a–c) and Alloy 2 (d–f) after annealing for 4, 10 and 15 min at 520 °C. 60

Figure 3.8 Grain size distribution in Alloy 1 (a–c) and Alloy 2 (d–f) after annealing for 4,10, and 15 min at 520 °C obtained by EBSD analysis. The blue dash line indicates the fractions of grains with a size less than 10 μm f_{SG} in the annealed samples. 61

Figure 3.9 Engineering stress–strain curves of the alloys at different strain rates: (a) 0.001 s^{-1}, (b) 0.01 s^{-1}, and (c) 1 s^{-1}. 63

Figure 3.10 (a) Tensile elongation of the alloys at different strain rates and (b) flow stress as a function of the strain rate in the logarithmic scale, from which the strain rate sensitivity (m-value) is evaluated. 63

Figure 4.1 Optical and SEM microstructures of the as-received (cold-rolled) alloy: (a) polarized optical image showing elongated grains along the rolling direction (RD); (b) SEM image revealing $Al_6(Mn,Fe)$ and Mg_2Si intermetallic particles within the Al matrix; (c) EDS spectrum of $Al_6(Mn,Fe)$; (d) EDS spectrum of Mg_2Si.....84

Figure 4.2 EBSD IPF maps showing grain structures after 4 min annealing at (a) 450 °C, (b) 480 °C, (c) 500 °C, and (d) 520 °C; (e) average grain size and the fraction of recrystallized grains smaller than 5 μm at various annealing temperatures. The grains remain fine and equiaxed at all annealing temperatures, with slight coarsening observed as temperature increased. 85

Figure 4.3 Stress-strain curves of the Al–Mg–Mn alloy deformed at strain rates of (a) 0.001 s^{-1}, (b) 0.01 s^{-1}, and (c) 1 s^{-1}over 450-520 ºC. Flow stress decreased with increasing temperature at all strain rates, indicating thermal softening. 87

Figure 4.4 Tensile elongation of the Al–Mg–Mn alloy as a function of deformation temperature and strain rate. Elongation increased with temperature up to 500 °C due to enhanced strain-rate sensitivity (m) and activation of GBS, then decreased at 520 °C due to grain coarsening. 88

Figure 4.5 (a) Log–log plot of flow stress (σ) versus strain rate ($\dot{\varepsilon}$) used to determine the strain-rate sensitivity (m), and (b) Arrhenius plot of ln(σ) versus 1/T (K-1) used to calculate Q for deformation. The m increases with temperature (0.30–0.43), indicating favorable conditions for superplasticity at high temperatures. The Q decreases with increasing strain rate, suggesting a transition from lattice diffusion to grain boundary or dislocation-based mechanisms. 89

Figure 4.6 EBSD IPF maps showing the grain structure after deformation at (a) and (d) 450 °C, (b) and (e) 500 °C, and (c) and (f) 520 °C; (a)–(c) correspond to strain rates of 0.001 s^{-1} and (d) – (f) 1 s^{-1}. All EBSD maps were obtained from central region of the fractured half of the gauge section, where deformation was most representative of the specimen. Black regions in (b) and (c) are cavities after deformation. 91

Figure 4.7 Influence of deformation temperature on (a) average grain size and aspect ratio, and (b) fraction of fine grains (< 5 μm) after deformation at strain rates of 0.001 and 1 s^{-1}. At 0.001 s^{-1}, grain size increases with temperature, while at 1 s^{-1}, grains remain fine and equiaxed. 91

Figure 4.8**.** EBSD Euler maps of the alloy in (a) the annealed condition and after deformation at 500 ºC at strain rates of (b) 0.001 s^{-1}, (c) 0.01 s^{-1}, and (d) 1 s^{-1}. (e) Fragmentation of large

grains into finer ones in (d), where LABs (white) evolved into MABs (blue) and subsequently into HABs. The yellow circles in (c) show small grains, indicating the onset of continuous dynamic recrystallization at 0.01 s^{-1}. 93
Figure 4.9 Comparison of (a) average grain size and aspect ratio of the alloy in the annealed and deformed conditions at 500 °C, and (b) relative volume fractions of LABs, MABs, and HABs under the same conditions.....94
Figure 4.10 Misorientation angle distributions after deformation at 500 °C and strain rates of (a) 0.001 s^{-1}, (b) 0.01 s^{-1}, and (c) 1 s^{-1}. The distributions at lower strain rates remain similar to that of the annealed condition, whereas at 1 s^{-1} the profile changes markedly, showing increased relative fractions of LABs and MABs. 94
Figure 4.11 EBSD–IPF maps showing the grain structure evolution of the alloy deformed at 500 °C and a strain rate of 0.001 s^{-1}, corresponding to strain levels of (a) $\varepsilon = 0$, (b) $\varepsilon = 0.2$, (c) $\varepsilon = 1.0$, and (d) post–fracture. Black regions in (d) indicate cavities formed in the microstructure during fracture. The grains remained nearly equiaxed with a modest aspect ratio increase from 1.4 to 2.1, indicating limited grain elongation.....97
Figure 5.1. Schematic illustration of the fractured tensile specimen showing the longitudinal thickness section (RD–ND plane) used for cavitation and EBSD analyses, and the fracture surface normal to the tensile direction used for SEM fractography 120
Figure 5.2. As-received microstructures of the AlMg–0.74Mn and AlMg–1.18Mn alloys: (a, c) polarized-light optical micrographs showing elongated grains along the rolling direction, and (b, d) backscattered electron (BSE) micrographs showing fragmented intermetallic particles, mainly $Al_6(Mn,Fe)$ and few Mg_2Si, distributed along the rolling direction.....121
Figure 5.3. Quantitative analysis of intermetallic compounds (IMCs) in AlMg–0.74Mn and Al–1.18Mn alloys. (a) IMC area fraction and (b) equivalent diameter distribution of IMCs.

The blue vertical dashed line indicates the 20 μm threshold used to quantify the relative fraction of coarse IMCs. 122

Figure 5.4. Bright-field TEM micrographs revealing Mn-rich dispersoids in (a) AlMg–0.74Mn and (b) AlMg–1.18Mn. 123

Figure 5.5. Engineering stress–strain curves of the alloys deformed at 500 °C at different strain rates: (a) 0.001 s^{-1}, (b) 0.01 s^{-1}, and (c) 1 s^{-1}. 124

Figure 5.6 Flow stress as a function of strain rate on a logarithmic scale. Local strain-rate sensitivity values (m) calculated between adjacent strain-rate intervals are indicated for both alloys. 126

Figure 5.7 EBSD inverse pole figure (IPF) maps comparing the grain structures of the alloys before and after deformation at 500 °C: (a, b) annealed condition, (c, d) after deformation at 0.001 s^{-1}, and (e, f) after deformation at 1 s^{-1}. Black regions in the IPF maps (c, d) correspond mainly to non-indexed areas associated with cavities. 128

Figure 5.8. Comparison of (a) the average grain size and (b) the grain aspect ratio of AlMg-074Mn and AlMg-1.18Mn alloys in the annealed state and after deformation at 500 °C. Grain coarsening and elongation occurred at 0.001 s^{-1}, while fine, equiaxed grains were retained at 1 s^{-1}. 129

Figure 5.9 Optical micrographs showing cavity formation near the fracture surface of (a,c,e) AlMg–0.74Mn and (b,d,f) AlMg–1.18Mn alloys after tensile deformation at 500 °C under different strain rates (0.001–1 s^{-1}). Red circles indicate cavities linked in the transverse direction, while blue rectangles indicate those cavities linked along the tensile direction 131

Figure 5.10 (a) Effect of strain rate on (a) cavity area fraction and (b) cavity number density in AlMg–0.74Mn and AlMg–1.18Mn alloys deformed at 500 °C. 132

Figure 5.11 Cavity-size distributions and cumulative relative frequency curves for AlMg–0.74Mn and AlMg–1.18Mn alloys deformed at 500 °C at strain rates of (a) 0.001 s^{-1}, (b) 0.01 s^{-1}, and (c) 1 s^{-1}. The cumulative curves were used to determine D_{90}, defined as the cavity diameter below which 90% of the measured cavities fall. 134
Figure 5.12. Optical micrographs showing cavitation evolution at different strain levels during deformation at 500 °C and 0.001 s^{-1}**:** (a,d) ε ≈ 20%, (b,e) ε ≈ 100%**,** and (c,f) after fracture for the two alloys. The corresponding quantitative measurements show (h) the cavity area fraction and (i) the cavity number density, both evolving with strain 136
Figure 5.13. SEM fracture surface morphologies of (a, d, g) AlMg–0.74Mn and (b, e, h) AlMg–1.18Mn alloys deformed at 500 °C at strain rates of (a, b) 0.001 s^{-1}, (d, e) 0.01 s^{-1}, and (g, h) 1 s^{-1}; corresponding equivalent dimple diameter distributions at different strain rates of (c) 0.001 s^{-1}, (f) 0.01 s^{-1}, and (i) 1 s^{-1}, illustrating the strain-rate-dependent evolution of cavitation from large, coalesced dimples at the low strain rate to fine microvoid-dominated fracture at the high strain rate 140
Figure 5.14. SEM images showing crack path features on fracture surfaces of AlMg–0.74Mn and AlMg–1.18Mn alloys deformed at 500 °C under different strain rates: (a,b) 0.001 s^{-1}, (c,d) 0.01 s^{-1}, and (e,f) 1 s^{-1}. Red dashed boxes indicate intragranular cracks, yellow dashed boxes indicate intergranular cracks, and blue dashed boxes highlight tear ridges formed during shear-localized ductile tearing. 142
Figure 5.15. SEM–EBSD inverse pole figure (IPF) maps showing the grain structure evolution of the two alloys during progressive deformation at 500 °C and a strain rate of 0.001 s^{-1}. (a and d) correspond to true strains of ε = 20%, (b and e) ε = 100%, and (c and f) post-fracture. The black shaded regions in (c and f) indicate cavities formed in the samples after fracture. (g) shows the variation of grain aspect ratio with strain for both alloys.....149

Figure 6.1. Schematic of the alloy processing route, including casting at 750 °C, two-step homogenization (300 °C/12 h + 425 °C/6 h), sheet formation by hot rolling (425–450 °C, 70% reduction) followed by cold rolling (75% reduction), and annealing at various temperatures. 167

Figure 6.2. Schematic of the heating and tensile-testing procedure: (a) insertion of the tensile-sample holder into the furnace at 25 °C; (b) preheating of the holder at 500 °C for 2 h; (c) installation and thermal equilibration of the specimen for three minutes; (d) annealing at 500 °C for 10 min; and (e) hot tensile testing. 169

Figure 6.3. Optical polarized light images showing the as-cast grain structures of (a) B, (b) BSc10Zr, and (c) BSc05ZrEr. SEM images showing the intermetallic compounds (IMCs) in (d) B, (e) BSc10Zr, and (f) BSc05ZrEr. SEM–EDS spectra of particles with compositions consistent with (g) Al_6(Mn,Fe)-type, (h) Mg_2Si, and (i) Al_6(Mn,Fe,Er)-type particles. 172

Figure 6.4. SEM–EDS elemental maps showing localized Er enrichment within Al_6(Mn,Fe,Er)-type particles in the BSc05ZrEr alloy. 173

Figure 6.5. Optical images showing as-homogenized microstructures after 0.5% HF etching for 30 s: (a) B, (b) BSc10Zr, and (c) BSc05ZrEr alloys, highlighting Mn dispersoid zones (DZ) and Mn dispersoid-free zones (DFZ). (d) Corresponding DFZ fraction for each alloy. 174

Figure 6.6. Optical micrographs of the as-rolled microstructures. Polarized light OM images showing elongated grain structures in (a) B, (b) BSc10Zr, and (c) BSc05ZrEr alloys. HF-etched OM images (0.5% HF, 30 s) highlighting alternating dispersoid zones (DZ) and dispersoid-free zones (DFZ) in (d) B, (e) BSc10Zr, and (f) BSc05ZrEr. 175

Figure 6.7. Effect of annealing temperature on hardness evolution in the three alloys. 177

Figure 6.8. Effect of annealing temperature on static recrystallization behaviour of alloys B, BSc10Zr and BSc05ZrEr at (a-c) 400 °C, (d-f) 450 °C, (g-i) 500 °C and (j-l) 520 °C. 178
Figure 6.9. Polarized optical OM micrographs showing the grain structure evolution of the three alloys after annealing at 500 °C for two different times: (a–c) 5 min and (d–f) 10 min. 179
Figure 6.10. TEM bright-field images showing Mn-dispersoids in (a) B, (d) BSc10Zr, and (g) BSc05ZrEr alloys. Dark-field images highlighting nanoscale Sc-containing precipitates in (e–f) BSc10Zr alloy and (h–i) BSc05ZrEr alloy. The corresponding EDS spectra of (b) Mn-dispersoids and (c) Al_3(Sc,Zr,Er) precipitates in the BSc05ZrEr alloy. The inset in (i) shows the corresponding SAED pattern indexed along the [001] zone axis of the Al matrix. 181
Figure 6.11. Engineering stress–strain curves from tensile tests conducted at 500 °C under different strain rates of (a) 0.01 s^{-1}, (b) 0.1 s^{-1}, and (c) 1 s^{-1}. 183
Figure 6.12**.** (a) Engineering elongation as a function of strain rate for alloys B, BSc10Zr, and BSc05ZrEr tested at 500 °C. (b) Evolution of the global strain-rate sensitivity index (m) with true strain, evaluated at 0.1, 0.3, and 0.5 over the investigated strain-rate range of 0.01–1 s^{-1}. (c) Representative tensile specimens after deformation to approximately 70% engineering strain under the high-strain-rate condition (1 s^{-1}), showing pronounced strain localization in the base alloy (B) and more uniform deformation in BSc10Zr and BSc05ZrEr. 185
Figure 6.13. (a) Tensile elongation at 500 °C under monotonic deformation at 0.01 s^{-1} and under a dual-stage high-to-low strain-rate deformation path for alloys B and BSc05ZrEr. (b) Representative tensile specimens after dual-stage deformation, showing the retained ductility following the strain-rate transition. 187

Figure 6.14. Polarized optical OM micrographs showing the microstructural evolution during tensile deformation at 500 °C with increasing strain rates**.** White arrows indicate grain refinement and localized fragmentation. 190

Figure 6.15. EBSD inverse pole figure (IPF) maps at the annealed (500ºC/10 min) and deformed ($0.1s^{-1}$) conditions for the (a–b) B, (d-e) BSc10Zr and (g-h) BSc05ZrEr alloys together with the corresponding misorientation angle distributions (c, f and i). The white circles in (b, e, and h) highlight localized fine grains, consistent with deformation-induced grain subdivision and possible continuous dynamic recrystallization (CDRX). 191

Figure 6.16. Relative fractions of low-angle grain boundaries (LABs), medium-angle grain boundaries (MABs), and high-angle grain boundaries (HABs) in the annealed and deformed ($0.1\ s^{-1}$) conditions for the B, BSc10Zr, and BSc05ZrEr alloys. 192

Figure 6.17. EBSD inverse pole figure (IPF) maps of the alloys after tensile deformation at 500 °C and $1\ s^{-1}$: (a) B, (b) BSc10Zr, (c) BSc05ZrEr, and (d) relative fractions of low-angle grain boundaries (LABs), medium-angle grain boundaries (MABs), and high-angle grain boundaries (HABs) in the annealed and deformed conditions. White circles highlight representative regions of localized grain refinement and boundary evolution. 194

List of Abbreviations

HSBF	High Speed Blow Forming
SPF	Superplastic Forming
SP	Superplasticity
GBS	Grain Boundary Sliding
SDC	Solute Drag Creep
DC	Diffusion Creep
DS	Dislocation Slip
CDRX	Continuous Dynamic Recrystallization
DFZ	Dispersoid-Free Zones
EBSD	Electron Backscattered Diffraction
IPF	Inverse Pole Figure
TEM	Transmission Electron Microscopy
SEM	Scanning Electron Microscopy
EDS	Energy-Dispersive X-ray Spectroscopy
N_a	Number Density
ECD	Equivalent Cavity Diameter
IMCs	Intermetallic Phases
BF	Bright-Field
LABs	Low Angle Boundaries
MABs	Medium Angle Boundaries
HABs	High Angle Boundaries

Dedication

This thesis is dedicated to Jesus Christ, my Lord and Saviour, whose grace and strength sustained me throughout this journey.

To my beloved wife, Moud Eunice Boamah, and my children, Caleb, Gabriella, Jude, and Zoe Kweitsu, thank you for your love, prayers, sacrifices, and unwavering support.

To my parents, siblings, and all who believed in me, this achievement is also yours.

All glory to Jesus.

Acknowledgment

I first and foremost give all glory to the Lord Jesus Christ, the intelligent Designer, who created this world with wisdom and gave us the privilege to uncover the logic behind His creation, so that we may apply this knowledge for technological advancement, the good of humankind, and the glory of His holy name.

I am sincerely grateful to my supervisors, Prof. Dilip Kumar Sarkar and Prof. X.-Grant Chen, for their exceptional mentorship, insightful guidance, and steadfast support throughout my doctoral studies. Their expertise, constructive feedback, and continuous encouragement were instrumental in shaping this research and bringing it to successful completion.

I would also like to express my sincere appreciation to Dr. Ahmed Y. Algendy of UQAC and Prof. Jocelyn Veilleux of Université de Sherbrooke for their valuable support and contributions to this work. My appreciation also goes to Mr. Nicolas Bombardier of VERBOM and Dr. Julie Levesque of CMQ for their technical assistance, collaboration, and support during this project.

My heartfelt appreciation is extended to our industrial partners, VERBOM and CMQ, for their collaboration, technical assistance, and valuable contributions to this research. I also thank my colleagues and fellow researchers at CIMTAL and CURAL, whose discussions, cooperation, and camaraderie enriched my research experience and created a supportive working environment.

Finally, I owe profound gratitude to my beloved wife, Moud Eunice Boamah, and my children, Caleb, Gabriella, Jude, and Zoe Kweitsu, for supporting me spiritually and emotionally throughout this journey. I am also deeply grateful to my parents and siblings for their love, prayers, encouragement, and unwavering belief in me. Your support sustained and inspired me through both the demanding and rewarding stages of this journey. This achievement would not have been possible without you.

All glory to Jesus

Chapter 1

Introduction

1.1 Background

The increasing demand for lightweight and energy-efficient transportation systems has driven the development of metallic alloys with high specific strength and enhanced formability. Superplasticity (SP), defined by tensile elongations exceeding 200 % at elevated temperatures, enables the fabrication of complex geometries in a single forming step, thereby reducing part count and manufacturing cost [1,2]. Among structural materials, Al–Mg–Mn 5xxx alloys are widely used in the automotive industry due to their favorable combination of strength, corrosion resistance, and cost [3–7], and can exhibit superplastic behavior under appropriate conditions [8,9].

This exceptional ductility has been successfully exploited in superplastic forming (SPF) to manufacture complex autobody components that are difficult or impossible to produce using conventional forming techniques [8,9]. However, conventional SPF is limited by slow forming rates, as superplasticity in these alloys typically occurs at low strain rates (10^{-4}–10^{-3} s^{-1}) [2,8,10–12]. To address this limitation, High-Speed Blow Forming (HSBF) has emerged as a promising technique that combines an initial high strain-rate deformation stage (≥1 s^{-1}) with a subsequent low strain-rate superplastic forming stage, enabling significantly reduced cycle times [10].

Despite its advantages, HSBF imposes complex deformation conditions, requiring materials to accommodate a wide strain-rate range under transient thermal cycles. This often leads to challenges such as strain localization and cavitation, which limit formability [10,13].

To enable effective HSBF processing, there is a need to develop Al–Mg–Mn 5xxx alloys with thermally stable microstructures capable of sustaining deformation across wide strain-rate regimes. While microalloying with Sc and Zr improves grain stability, their high cost limits industrial application. The use of alternative alloying elements such as Er, combined with scrap-based alloy design, offers a promising and sustainable pathway for developing cost-effective, high-performance alloys tailored for HSBF applications. This highlights the need for integrated studies linking microstructural design and deformation behavior under HSBF-relevant conditions. In this thesis, HSBF-relevant conditions refer to laboratory testing conditions selected to reproduce the key thermal and deformation stages of HSBF, including short-duration heating or annealing, elevated-temperature deformation, high strain-rate loading, low strain-rate deformation, and strain-rate transitions.

1.2 Problem statement

HSBF offers significant advantages over conventional SPF by enabling substantially reduced forming times through a hybrid deformation strategy that combines high and low strain-rate regimes. A key feature of HSBF is the use of rapid, short-duration annealing (typically < 5 min) to establish a suitable grain structure prior to deformation. However, most existing studies on Al–Mg–Mn 5xxx alloys [14–16] have focused on long-duration annealing conditions (≥ 20–30 min), which do not reflect HSBF processing. Consequently, the evolution of grain structure under rapid annealing, and its influence on high-temperature deformation behavior, remains poorly understood, limiting the design of optimized thermal processing routes for HSBF applications.

In addition to thermal effects, HSBF imposes complex deformation conditions, requiring materials to accommodate a wide strain-rate range under transient thermal cycles. This leads to formability challenges such as non-uniform thinning, dimensional inaccuracies, and cavitation, which can result in premature failure [10,13]. These defects compromise surface quality and structural integrity, thereby limiting the production of Class A automotive components. Therefore, the ability of Al–Mg–Mn alloys to sustain stable deformation across a wide strain-rate range without failure is critical for the successful implementation of HSBF.

Achieving an optimal balance between high strain-rate capability and cavitation resistance requires a deeper mechanistic understanding of deformation and microstructural evolution under hybrid forming conditions. However, most studies on Al–Mg–Mn 5xxx alloys [14–16], including advanced Sc- and Zr-modified systems [17–22], have focused on deformation at strain rates $\leq 0.1\ s^{-1}$. In contrast, tensile behavior at high strain rates ($\geq 1\ s^{-1}$), relevant to the crash-forming stage of HSBF, remains largely unexplored. Furthermore, existing high strain-rate studies are predominantly conducted under compressive loading [23–25], which does not adequately represent the tensile conditions encountered in sheet forming or capture critical damage mechanisms such as cavitation and strain localization.

Moreover, there has been limited systematic effort to develop Al–Mg–Mn 5xxx alloys specifically tailored for HSBF applications. Existing commercial superplastic alloys are primarily designed for conventional SPF and may not exhibit sufficient microstructural stability or deformation compatibility under HSBF-relevant conditions. While microalloying with Sc and Zr enhances microstructure stability through coherent dispersoid formation [17–21], most studies rely on relatively high Sc additions (≥ 0.1 wt.%) [20,21,26,27], which significantly increases alloy cost and limits industrial applicability. Although erbium (Er) has

emerged as a cost-effective alternative [28–30], its integration into alloy design strategies for HSBF remains limited.

In addition, the use of industrial scrap presents a promising pathway for reducing cost and improving sustainability. However, most studies on recycled aluminum have focused on casting processes, with limited attention given to high-performance sheet alloys for forming applications. Therefore, integrating microalloying strategies with scrap-based alloy design remains largely unexplored. Accordingly, there is a need to establish the relationships among microstructural evolution, deformation mechanisms, and cavitation behavior across the wide strain-rate range relevant to HSBF. Such understanding is essential for the development of cost-effective Al–Mg–Mn 5xxx alloys capable of sustaining stable deformation under HSBF-relevant conditions and for enabling robust, industrially viable manufacturing of complex automotive components.

1.3 Research objectives

The overall objective of this doctoral research is to develop a mechanistic understanding of microstructural evolution, deformation behavior, and cavitation in Al–Mg–Mn 5xxx alloys under HSBF-relevant conditions, and to apply this understanding to the design of alloys optimized for high-strain-rate forming. This objective is addressed through three complementary research phases.

Phase One: Static Recrystallization Behavior and Superplastic Response.

1. Effect of Annealing Time on Grain Structure and Superplastic Response of Al–Mg–Mn 5xxx Alloys.

(a) Investigate the effect of annealing time on static recrystallization and grain structure evolution.

(b) Examine how short-duration annealing influences superplastic behavior across a range of strain rates, including flow stress, strain-rate sensitivity, and elongation.

Phase Two: Deformation Mechanisms and Cavitation under HSBF-relevant conditions

1. Superplastic Deformation and Microstructural Evolution of an Al–Mg–Mn 5xxx Alloy.
   (a) Identify strain-rate- and temperature-dependent deformation mechanisms using flow behavior, strain-rate sensitivity, activation energy, and post-deformation microstructures.

2. Effect of Strain Rate on Deformation and Cavitation Behavior of Al–Mg–Mn 5xxx Alloys.
   (a) Investigate cavitation initiation, growth, and evolution, and relate it to microstructure and formability limits at HSBF-relevant strain rates (0.001–1 s^{-1}).

Phase Three: Alloy Development via Microalloying and Thermomechanical Processing

1. Microstructural Evolution and Strain-Rate-Dependent Deformation of Sc–Zr–Er Microalloyed Al–Mg–Mn 5xxx Alloys Produced from Recycled Automotive Sheet Scrap for High-Speed Blow Forming.

(a) Evaluate the effects of minor Sc, Zr, and Er additions on recrystallization behavior and grain structure evolution of Al–Mg–Mn 5xxx alloys.

(b) Assess the impact of Sc, Zr and Er precipitates on high strain-rate deformation behavior of Al–Mg–Mn 5xxx alloys.

1.4 Originality statement

The originality of this research lies in addressing critical gaps in the mechanistic understanding of microstructural evolution, deformation behavior, and cavitation in Al–Mg–Mn 5xxx alloys under HSBF-relevant conditions, while also enabling the development of high-performance alloys tailored for HSBF applications.

First, this work demonstrates that short-duration annealing (< 5 min), representative of the rapid thermal exposure associated with HSBF processing, is sufficient to produce fine and thermally stable grain structures in Al–Mg–Mn 5xxx alloys. This finding establishes a direct relationship between annealing time, recrystallization behavior, and grain stability under short thermal exposures, in contrast to the longer annealing treatments commonly employed in conventional superplastic-forming studies. The resulting microstructures, stabilized by Mn-containing dispersoids, are shown to support substantial deformation over a wide strain-rate range, demonstrating the potential for reduced pre-forming thermal exposure under HSBF-relevant conditions.

Second, this study provides a systematic experimental investigation of tensile deformation behavior over a broad strain-rate range extending to 1 s^{-1} in conventionally processed Al–Mg–Mn 5xxx alloys, with particular emphasis on the high-strain-rate regime relevant to HSBF. The study establishes a mechanistic framework describing the evolution

of deformation behavior with increasing strain rate, from predominantly grain-boundary-sliding-assisted deformation at low strain rates, through mixed grain-boundary sliding and intragranular dislocation activity at intermediate strain rates, to dislocation-mediated deformation associated with boundary subdivision and continuous dynamic recrystallization-type grain refinement at high strain rates. By integrating flow-stress behavior, strain-rate sensitivity, apparent activation-energy analysis, EBSD, and TEM characterization, the work links the observed mechanical response with corresponding microstructural evolution across the investigated strain-rate range, thereby providing critical insight into the possible deformation mechanisms governing material response under HSBF-relevant conditions.

Third, this research establishes a strain-rate-dependent framework for understanding cavitation in Al–Mg–Mn 5xxx alloys under HSBF-relevant conditions. The results reveal a transition from diffusion-assisted cavity growth and coalescence at low strain rates toward increasing control by particle-assisted cavity nucleation, cavity elongation, and microvoid coalescence at high strain rates, demonstrating that the mechanisms governing cavitation evolve together with the dominant deformation mechanisms. By correlating cavity characteristics with grain structure evolution and deformation behavior, the study provides new insight into the coupled relationships among strain rate, deformation mechanism, microstructural stability, and damage development. This framework further demonstrates that formability cannot be assessed from tensile elongation alone but must also consider the evolution and accumulation of cavitation during deformation.

Finally, from an alloy-design perspective, this work integrates recycled automotive Al–Mg–Mn sheet scrap with targeted Sc–Zr–Er microalloying to develop alloys specifically for HSBF-relevant conditions. The study demonstrates that differences in particle type and

distribution introduced through microalloying strongly influence recrystallization resistance, the resulting microstructural state, and deformation stability across a wide strain-rate range. Partial substitution of Sc with Er is further explored as a strategy for reducing reliance on Sc while retaining favorable microstructural stability and deformation performance. Importantly, this work highlights that alloy development for HSBF should consider not only the maximum ductility achievable at a given strain rate, but also the ability of the microstructure to sustain stable deformation at high strain rates and accommodate transitions between different strain-rate regimes during forming. Proof-of-concept dual-stage experiments, involving high-strain-rate pre-deformation followed by lower-strain-rate deformation, demonstrate the potential of strain-rate-path control to extend deformation capacity. These findings identify high-strain-rate deformation stability and tolerance to strain-rate transitions as important considerations in the design and evaluation of alloys tailored for HSBF applications.

Collectively, this research establishes an integrated framework linking processing, particle characteristics, microstructural evolution, deformation mechanisms, cavitation, and alloy design in Al–Mg–Mn 5xxx alloys under HSBF-relevant conditions. By connecting fundamental deformation and damage mechanisms with processing and alloy-design considerations, the work advances the mechanistic understanding required for the development of Al–Mg–Mn alloys and forming strategies suitable for high-speed blow forming.

1.5 Thesis outline

This PhD thesis is organized into seven chapters, followed by a supplementary appendix providing additional methodological clarifications relevant to the interpretation of the experimental studies.

Chapter 1: Introduction

The first chapter provides the overall background of the study, beginning with an overview of superplasticity and its application in superplastic forming for automotive body manufacturing, together with the limitations of conventional SPF. It then introduces high-speed blow forming as an advanced forming approach aimed at overcoming these limitations. The key scientific and technological challenges associated with HSBF are identified and used to define the research problem addressed in this thesis. Finally, the chapter presents the research objectives and outlines the originality and significance of the study.

Chapter 2: Literature Review

Chapter 2 presents a literature review based on the article *"A Short Review on Superplasticity of Aluminum Alloy,"* published in *Engineering Proceedings (MDPI)*. The chapter has been expanded and adapted to incorporate additional analysis of high-strain-rate deformation, cavitation behavior, and alloy-design strategies relevant to HSBF applications. It reviews the superplastic behavior of aluminum alloys, with particular emphasis on Al–Mg 5xxx alloys and discusses the governing deformation mechanisms across low- and high-strain-rate regimes. Cavitation behavior and advanced forming processes, including Quick Plastic Forming and HSBF, are also examined. The chapter concludes by identifying the principal knowledge gaps addressed by the experimental studies.

Chapter 3: Static Recrystallization Behavior and Superplastic Response

Chapter 3 presents the study *"Effect of Annealing Time on Grain Structure Evolution and Superplastic Response of Al–Mg 5xxx Alloys,"* published in *Materials (MDPI)*. This chapter investigates the effect of annealing time on the recrystallized grain structure and superplastic response of two Al–Mg 5xxx alloys employed for HSBF. Grain-structure evolution during short-duration annealing (2–30 min) at 520 °C is analyzed to assess static recrystallization and subsequent grain growth. The role of Mn-containing dispersoids in stabilizing the grain structure is examined, and the deformation response is evaluated over a strain-rate range of 0.001–1 s^{-1} following short-duration annealing. The results establish the importance of controlling the pre-deformation thermal treatment for developing fine and thermally stable grain structures capable of sustaining deformation under HSBF-relevant conditions.

Chapter 4: Superplastic Deformation and Microstructural Evolution

Chapter 4 is based on the study *"Superplastic Deformation and Microstructural Evolution of an Al–Mg–Mn 5xxx Alloy for High-Speed Blow Forming Applications,"* published in *Journal of Materials Science (Springer Nature)*. The chapter systematically examines deformation behavior and microstructural evolution over a temperature range of 450–520 °C and strain rates from 0.001 to 1 s^{-1}. Particular attention is given to the evolution of deformation mechanisms across this broad strain-rate regime, including grain-boundary-sliding-assisted deformation, solute-drag-controlled deformation, and increasingly dislocation-mediated deformation associated with CDRX at high strain rates. By integrating mechanical response with EBSD and TEM characterization, the study develops a mechanistic

framework for interpreting deformation under HSBF-relevant conditions and provides insight for optimizing HSBF processes.

Chapter 5: Cavitation Behavior under HSBF-Relevant Conditions

Chapter 5 is based on the manuscript *"Strain-Rate-Dependent Cavitation in Al–Mg–Mn 5xxx Alloys: Mechanistic Insights for High-Speed Blow Forming."* This chapter investigates the strain-rate-dependent cavitation behavior of two Al–Mg–Mn 5xxx alloys at 500 °C over a strain-rate range of 0.001–1 s^{-1}. Cavitation characteristics are correlated with deformation behavior and microstructural evolution to examine how damage development changes across different strain-rate regimes. The study establishes relationships among strain rate, deformation mechanism, microstructural stability, and cavity evolution, providing insight into the factors controlling damage and formability under HSBF-relevant conditions.

Chapter 6: Alloy Development Tailored for HSBF Applications

Chapter 6 is based on the manuscript *"Microstructural Evolution and Strain-Rate-Dependent Deformation of Sc–Zr–Er Microalloyed Al–Mg–Mn 5xxx Alloys Produced from Recycled Automotive Sheet Scrap for High-Speed Blow Forming."* This chapter investigates the effects of Sc–Zr–Er microalloying on microstructural evolution, static recrystallization behavior, and strain-rate-dependent deformation of recycled Al–Mg–Mn alloys. Particular emphasis is placed on understanding how differences in particle type and distribution and the resulting resistance to recrystallization influence the initial microstructural state and subsequent deformation response over a strain-rate range of 0.01–1 s^{-1}. Under a common pre-deformation treatment, the developed alloys exhibit distinctly different recrystallization states, providing an opportunity to examine the deformation response of fully, partially, and largely unrecrystallized microstructures under identical thermal and loading conditions. The

resulting behavior is therefore interpreted in terms of the combined effects of particle characteristics, recrystallization state, grain structure, boundary evolution, and microalloying rather than alloy chemistry alone.

The chapter further introduces a dual-stage deformation approach as a proof-of-concept assessment of strain-rate-transition effects relevant to HSBF. Together, the results establish relationships among alloy design, particle distribution, recrystallization behavior, microstructural stability, and strain-rate-dependent deformation, providing a potential pathway toward the development of sustainable and cost-effective Al–Mg–Mn alloys tailored for HSBF applications.

Chapter 7: Conclusions, Limitations, and Recommendations

The final chapter synthesizes the principal findings from the experimental studies and establishes their broader implications for HSBF. It integrates the relationships among processing conditions, microstructural evolution, deformation mechanisms, mechanical response, and cavitation behavior across the investigated strain-rate regime. The chapter also highlights the emerging HSBF alloy-design strategy based on microstructural stability, deformation response across multiple strain-rate regimes, and the integration of recycled automotive sheet scrap with targeted Sc–Zr–Er microalloying.

The scope and principal limitations of the experimental findings are identified, followed by recommendations for future work. These include further optimization of alloy composition and thermomechanical processing, systematic investigation of strain-rate-transition paths, intermediate microstructural characterization, validation under industrial HSBF-relevant conditions, and the development of experimental and simulation-based processing frameworks for HSBF.

Appendix A: Supplementary Experimental Methodology and Clarifications

Appendix A supplements the methodologies presented in the article-based chapters by providing additional information required for interpretation of selected experimental procedures and analyses. It clarifies the rationale for the different experimental configurations employed across the thesis, the mechanical-data analysis used for deformation-mechanism assessment, the interrupted deformation approach used to examine cavitation evolution, the microstructural basis for identifying CDRX, and the methodology and scope of the dual-stage strain-rate experiments.

References

1. Bhatta L, Pesin A, Zhilyaev AP, Tandon P, Kong C, Yu H. Recent development of superplasticity in aluminum alloys: A review. *Metals*. 2020;10(1):77. https://doi.org/10.3390/met10010077.

2. Giuliano G, editor. Superplastic Forming of Advanced Metallic Materials: Methods and Applications. Cambridge: Woodhead Publishing; 2011. https://doi.org/10.1533/9780857092779.

3. Miller WS, Zhuang L, Bottema J, Wittebrood AJ, De Smet P, Haszler A, et al. Recent development in aluminium alloys for the automotive industry. *Mater Sci Eng A*. 2000;280(1):37–49. https://doi.org/10.1016/S0921-5093(99)00653-X.

4. Jeon J, Lee S, Kyeong J, Shin S, Kang H. Effect of geometrical parameters of microscale particles on particle-stimulated nucleation and recrystallization texture of Al-Si-Mg-Cu-based alloy sheets. *Materials*. 2022;15(22):7924. https://doi.org/10.3390/ma15227924.

5. Grimes R. Superplastic forming of aluminium alloys. In: Giuliano G, editor. Superplastic Forming of Advanced Metallic Materials: Methods and Applications. Cambridge: Woodhead Publishing; 2011. p. 247–271. https://doi.org/10.1533/9780857092779.3.247.

6. Kishchik AA, Mikhaylovskaya AV, Levchenko VS, Portnoy VK. Formation of microstructure and the superplasticity of Al-Mg-based alloys. *Phys Met Metallogr*. 2017;118(1):96–103. https://doi.org/10.1134/S0031918X16120085.

7. Ebenberger P, Uggowitzer PJ, Gerold B, Pogatscher S. Effect of compositional and processing variations in new 5182-type AlMgMn alloys on mechanical properties and deformation surface quality. *Materials*. 2019;12(10):1645. https://doi.org/10.3390/ma12101645.

8. Luo Y, Luckey SG, Friedman PA, Peng Y. Development of an advanced superplastic forming process utilizing a mechanical pre-forming operation. *Int J Mach Tools Manuf*. 2008;48(12–13):1509–1518. https://doi.org/10.1016/j.ijmachtools.2007.12.010.

9. Liu J, Tan MJ, Aue-U-Lan Y, Jarfors AEW, Fong KS, Castagne S. Superplastic-like forming of non-superplastic AA5083 combined with mechanical pre-forming. *Int J Adv Manuf Technol*. 2011;52:123–129. https://doi.org/10.1007/s00170-010-2729-9.

10. Majidi O, Jahazi M, Bombardier N. Finite element simulation of high-speed blow forming of an automotive component. *Metals*. 2018;8(11):901. https://doi.org/10.3390/met8110901.

11. Liu FC, Ma ZY. Achieving high strain rate superplasticity in cast 7075Al alloy via friction stir processing. *J Mater Sci*. 2009;44(10):2647–2655. https://doi.org/10.1007/s10853-009-3346-6.

12. Duan Y, Xu G, Zhou L, Xiao D, Deng Y, Yin Z, et al. Achieving high superplasticity of a traditional thermal-mechanical processed non-superplastic Al-Zn-Mg alloy sheet by low Sc additions. *J Alloys Compd*. 2015;638:364–373. https://doi.org/10.1016/j.jallcom.2015.03.090.

13. Aleyari A, Majidi O, Bombardier N, Pham XT, Jahazi M. Finite element and experimental analysis of the preheating stage of high speed blow forming (HSBF) process. *J Manuf Process*. 2020;49:10–17. https://doi.org/10.1016/j.jmapro.2019.10.009.

14. Portnoy VK, Rylov DS, Levchenko VS, Mikhaylovskaya AV. The influence of chromium on the structure and superplasticity of Al-Mg-Mn alloys. *J Alloys Compd*. 2013;581:313–317. https://doi.org/10.1016/j.jallcom.2013.07.075.

15. Mikhaylovskaya AV, Yakovtseva OA, Golovin IS, Pozdniakov AV, Portnoy VK. Superplastic deformation mechanisms in fine-grained Al-Mg based alloys. *Mater Sci Eng A*. 2015;627:31–41. https://doi.org/10.1016/j.msea.2014.12.099.

16. Pérez-Prado MT, González-Doncel G, Ruano OA, McNelley TR. Texture analysis of the transition from slip to grain boundary sliding in a discontinuously recrystallized superplastic aluminum alloy. *Acta Mater*. 2001;49(12):2259–2268. https://doi.org/10.1016/S1359-6454(01)00128-8.

17. Mikhaylovskaya AV, Kishchik AA, Kotov AD, Rofman OV, Tabachkova NY. Precipitation behavior and high strain rate superplasticity in a novel fine-grained aluminum based alloy. *Mater Sci Eng A*. 2019;760:37–46. https://doi.org/10.1016/j.msea.2019.05.099.

18. Algendy AY, Liu K, Rometsch P, Parson N, Chen XG. Effects of AlMn dispersoids and Al_3(Sc,Zr) precipitates on the microstructure and ambient/elevated-temperature mechanical properties of hot-rolled AA5083 alloys. *Mater Sci Eng A*. 2022;855:143950. https://doi.org/10.1016/j.msea.2022.143950.

19. Yakovtseva O, Sitkina M, Mosleh AO, Mikhaylovskaya A. High strain rate superplasticity in Al-Zn-Mg-based alloy: Microstructural design, deformation behavior, and modeling. *Materials*. 2020;13(9):2098. https://doi.org/10.3390/ma13092098.

20. Li M, Pan Q, Shi Y, Sun X, Xiang H. High strain rate superplasticity in an Al-Mg-Sc-Zr alloy processed via simple rolling. *Mater Sci Eng A*. 2017;687:298–305. https://doi.org/10.1016/j.msea.2017.01.091.

21. Mikhaylovskaya AV, Esmaeili Ghayoumabadi M, Mochugovskiy AG. Superplasticity and mechanical properties of Al-Mg-Si alloy doped with eutectic-forming Ni and Fe, and dispersoid-forming Sc and Zr elements. *Mater Sci Eng A*. 2021;817:141319. https://doi.org/10.1016/j.msea.2021.141319.

22. Kishchik AA, Mikhaylovskaya AV, Kotov AD, Rofman OV, Portnoy VK. Al-Mg-Fe-Ni based alloy for high strain rate superplastic forming. *Mater Sci Eng A*. 2018;718:190–197. https://doi.org/10.1016/j.msea.2018.01.099.

23. Shi C, Chen XG. Hot workability and processing maps of 7150 aluminum alloys with Zr and V additions. *J Mater Eng Perform*. 2015;24(5):2126–2139. https://doi.org/10.1007/s11665-015-1478-1.

24. Shakiba M, Parson N, Chen XG. Hot deformation behavior and rate-controlling mechanism in dilute Al-Fe-Si alloys with minor additions of Mn and Cu. *Mater Sci Eng A*. 2015;636:572–581. https://doi.org/10.1016/j.msea.2015.04.029.

25. McQueen HJ, Ryan ND. Constitutive analysis in hot working. *Mater Sci Eng A*. 2002;322(1–2):43–63. https://doi.org/10.1016/S0921-5093(01)01117-0.

26. Sun YB, Chen XP, Xie J, Wang C, An YF, Liu Q. High strain rate superplasticity and secondary strain hardening of Al-Mg-Sc-Zr alloy produced by friction stir processing. *Mater Today Commun*. 2022;33:104217. https://doi.org/10.1016/j.mtcomm.2022.104217.

27. Yakovtseva OA, Kishchik AA, Cheverikin VV, Kotov AD, Mikhaylovskaya AV. The mechanisms of the high-strain-rate superplastic deformation of Al-Mg-based alloy. *Mater Lett*. 2022;325:132883. https://doi.org/10.1016/j.matlet.2022.132883.

28. Chen B, Wang F, Ren S, Xia P, Wang Z, Hao J, et al. Influence of erbium addition on microstructure and performances of AlSi10Mg alloy prepared by selective laser melting. *J Rare Earths*. 2024;42(10):1988–1994. https://doi.org/10.1016/j.jre.2023.09.017.

29. Wu M, Wei W, Zuo R, Wen S, Shi W, Zhou X, Wu X, Gao K, Huang H, Nie Z. Effect of Zr and Er addition on the microstructural evolution of a novel Al-Mg-Zn-Er-Zr alloy during hot compression. *Materials*. 2023;16(2):858. https://doi.org/10.3390/ma16020858.

30. Kang W, Li HY, Zhao SX, Han Y, Yang CL, Ma G. Effects of homogenization treatments on the microstructure evolution, microhardness and electrical conductivity of dilute Al-Sc-Zr-Er alloys. *J Alloys Compd*. 2017;704:683–692. https://doi.org/10.1016/j.jallcom.2017.02.043.

Chapter 2

Literature Review

(Note: Parts of this literature review are adapted from the author's previously published work in Engineering Proceedings, 43(1) (2023), 1-9, titled "A Short Review on Superplasticity of Aluminum Alloy," and have been integrated and expanded to align with the scope of this thesis.)

2.1 Introduction

Conventional metallic alloys typically exhibit limited tensile ductility, with elongations generally below 100 % [1]. In contrast, superplasticity refers to the ability of certain materials to undergo exceptionally large tensile deformation, typically exceeding 200 % elongation, under appropriate deformation conditions [2]. This behavior has been widely exploited in the fabrication of complex-shaped components that are difficult or impossible to produce using conventional forming processes [3,4]. The forming process that utilizes this capability is known as superplastic forming (SPF) [3,5]. SPF is an attractive manufacturing technique due to its relatively low forming loads, simple tooling, and reduced processing energy, which contribute to lower production costs [5–9]. However, SPF is inherently limited by slow cycle times, which restrict its widespread application in high-volume industries such as automotive manufacturing [3,10].

Superplasticity has been observed in several metallic systems, including titanium, magnesium, duplex stainless steels, and aluminum alloys [4] . Among these, aluminum alloys have gained significant industrial importance, particularly in the automotive sector, due to their low density, corrosion resistance, and potential for reducing fuel consumption and greenhouse gas emissions [11]. Superplastic aluminum alloys are commonly used in the

fabrication of automobile body panels. Although many aluminum alloys exhibit superplastic behavior, those of commercial interest include AA2004, AA7475, and AA5083 [12] . In particular, Al–Mg 5xxx series alloys are of considerable interest due to their favorable combination of mechanical strength, weldability, corrosion resistance [5,7], and relatively low production cost [13]. However, Al–Mg 5xxx alloys generally exhibit lower superplastic elongation compared to other superplastic aluminum alloys, which limits their broader application in advanced forming processes [7]. Consequently, there is a need to develop improved Al–Mg 5xxx alloys with enhanced superplastic performance.

The superplastic behavior of aluminum alloys is governed by several deformation mechanisms, primarily grain boundary sliding (GBS), solute drag creep (SDC), and diffusion creep (DC). GBS is widely recognized as the dominant mechanism responsible for large superplastic elongations and is strongly dependent on a fine grain size (typically <10 μm), high strain-rate sensitivity ($m > 0.3$), and low strain rates [14–16] . In contrast, SDC and DC are less sensitive to grain size [16–18] and typically result in lower elongations [1]. SDC involves the interaction between diffusing solute atoms and dislocations and is known to dominate deformation at intermediate strain rates and elevated temperatures. DC, on the other hand, involves atomic diffusion along grain boundaries or through the lattice under low strain-rate conditions [1,19]. In this thesis, the term *superplastic response* is used in a broader sense to describe the elevated-temperature deformation behavior of the alloys, including their ductility, strain-rate sensitivity, flow behavior, and associated deformation mechanisms, even under conditions where the conventional elongation criterion for classical superplasticity is not fully satisfied. The superplastic response of aluminum alloys is therefore strongly influenced by grain size, strain-rate sensitivity, strain rate, temperature, alloy composition,

and the dominant deformation mechanism. A comprehensive understanding of these factors is essential for the development of advanced superplastic aluminum alloys.

This chapter builds upon the author's previously published review on the superplasticity of aluminum alloys and focuses on Al–Mg 5xxx alloys. It examines the deformation mechanisms governing superplasticity across different strain-rate regimes, analyzes the factors influencing superplastic behavior, and discusses advanced forming processes such as Quick Plastic Forming (QPF) and High-Speed Blow Forming (HSBF). Particular emphasis is placed on aspects relevant to high-efficiency forming applications, which form the basis for the subsequent research presented in this thesis.

2.2 Superplastic aluminum alloys

A wide range of aluminum alloys exhibit superplastic behavior under appropriate thermomechanical conditions. AA2004, commercially known as Supral, was among the first superplastic aluminum alloys developed in the 1980s [7]. This alloy exhibits exceptionally high elongation (~1200 %) at a strain rate of 1 x 10^{-3} s^{-1} and a temperature of 450 °C. However, its relatively moderate strength (~315 MPa) limits its application in high-strength structural components [7].

To address this limitation, high-strength superplastic alloys such as AA7475 were subsequently developed. AA7475 exhibits both high superplastic elongation (~1000 %) and improved strength (~462 MPa), making it suitable for aerospace structural applications [7]. Since then, several aluminum alloy systems have been developed and extensively studied for their superplastic performance, as summarized in Table 2.1.

Among these, Al–Mg 5xxx alloys have attracted significant attention due to their favorable combination of mechanical properties, corrosion resistance, and relatively low production cost [5,7,13]. These alloys are of particular interest to the automotive industry for lightweight structural applications. However, as shown in Table 2.1, Al–Mg 5xxx alloys generally exhibit lower superplastic elongation compared to other aluminum alloy systems. This limitation has motivated ongoing research efforts aimed at enhancing their superplastic response, particularly at elevated strain rates relevant to industrial forming processes.

Table 2.1 Superplastic aluminum alloys and their deformation characteristics.

Alloys	Temperature (°C)	Strain Rate	Elongation (%)	m-Value	Ref.
AA2004 (Al-6Cu-0.4Zr)	450	1×10^{-3}	1200	0.60	[7]
AA7475 (Al-5.5Zn-0.5Mg-1.5Cu-0.2Cr)	516	2×10^{-4}	1000	0.85	[7]
Al-3.9Zn-4.1Mg-2.8Ni-0.25Zr	440	1×10^{-2}	1200	0.47	[20]
Al-3.7Zn-4.2Mg-0.15Sc-0.20Zr	420	2×10^{-3}	800	0.47	[20]
Al-Zn-Mg-0.1Sc-0.1Zr	500	5×10^{-3}	1080	0.5	[21]
Al-4.8Mg-0.6Mn-0.2Cr	545	4×10^{-3}	300	0.65	[22]
Al-(6.5–7.8)Mg-0.7Mn-0.2Cr	519–527	4×10^{-3}	430	0.65	[22]
Al-Mg-Fe-Ni-Sc-Zr	460	1×10^{-2}	750	0.49	[5]
Al-Mg-Fe-Ni-Sc-Zr	460	1×10^{-1}	535	0.46	[5]

Recent studies have demonstrated that compositional modification and microalloying can significantly improve the superplastic behavior of Al–Mg 5xxx alloys. For example, Mikhaylovskaya et al. [22] reported superplastic elongation of ~430 % in Al–Mg alloys with high Mg content (6.5–7.8 wt.%). Similarly, Kishchik et al. [5] observed enhanced superplasticity through minor additions of Ni, Sc, and Zr, achieving high-strain-rate superplasticity (HSRS) with elongation of ~535 % at a strain rate of 1 x 10^{-1} s^{-1} and 460 °C. These findings highlight the potential of microalloying strategies to improve both ductility and strain-rate capability.

The superplastic response of aluminum alloys is strongly dependent on the thermomechanical processing (TMP) route used to develop a suitable microstructure. Commercial superplastic aluminum alloys are typically produced through two primary TMP approaches: discontinuous recrystallization and continuous recrystallization [23,24]. In the discontinuous recrystallization route, alloys are first subjected to overaging to generate coarse precipitates (~1 μm), followed by cold rolling. The presence of these coarse particles leads to the formation of heavily deformed zones, which act as nucleation sites for recrystallization during subsequent annealing. This process, known as particle-stimulated nucleation (PSN), results in the formation of a fine, equiaxed grain structure (Figure 2.1a) [23–25]. Alloys such as AA5083 [23] and AA7475 [12,26] are typically processed using this approach.

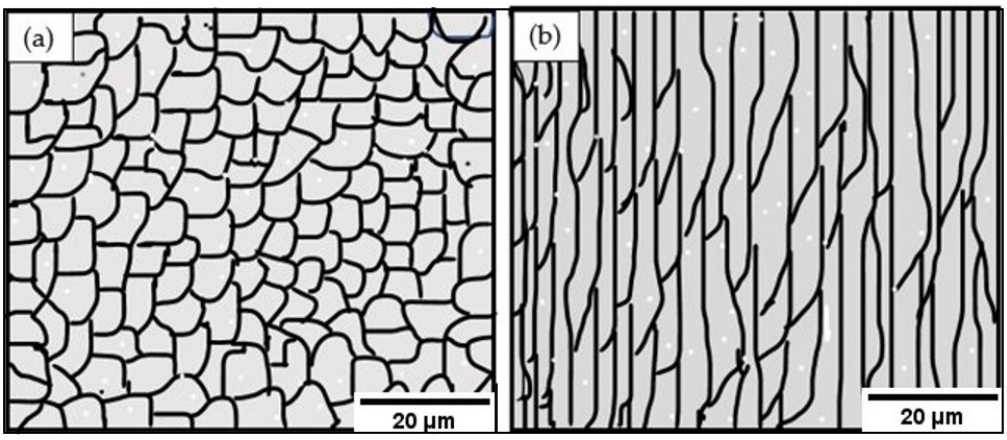


Figure 2.1. Schematic diagram showing microstructures of Al alloys (a) produced via discontinuous recrystallization and (b) produced via continuous recrystallization.

In contrast, the continuous recrystallization route involves the formation of nanoscale dispersoids (~10–50 nm) through controlled heat treatment following hot rolling [12,23,24]. These dispersoids inhibit discontinuous recrystallization during subsequent deformation and promote the gradual evolution of subgrain structures into high-angle grain boundaries during

deformation [25]. This process leads to the formation of a fine-grained microstructure via continuous dynamic recrystallization (CDRX), as illustrated in Figure 2.1b. Alloys such as Supral (Al–Cu–Zr) and AA8090 are produced using this method [12,23].

A fine and thermally stable grain structure is essential for achieving high superplastic performance, particularly under conditions where GBS is the dominant deformation mechanism [12]. However, maintaining such microstructural stability during deformation—especially at elevated strain rates—remains a key challenge for Al–Mg 5xxx alloys, which is critical for their application in advanced forming processes. This challenge becomes particularly significant under HSBF-relevant conditions, where alloys must sustain deformation across a wide strain-rate regime

2.3 Deformation mechanisms in superplastic aluminum alloys

Superplastic deformation in aluminum alloys occurs primarily through three mechanisms: GBS, SDC, and DC [27]. Among these, GBS was first identified by F. R. N. Nabarro (often credited alongside early work by A. A. Pearson [28]) as a dominant mechanism in superplastic flow. GBS governs Region II deformation, characterized by a stress exponent ($n \approx 2$) and high strain-rate sensitivity [1]. It typically results in extensive superplastic elongation (> 400 %) and is strongly dependent on a fine grain size (<10 μm) and high strain-rate sensitivity ($m > 0.3$) [14–16]. As grain size decreases, the strain-rate sensitivity (m-value) increases, which suppresses strain localization and enhances uniform deformation [29]. GBS occurs through the relative sliding of adjacent grains along grain boundaries (Figure 2.2) and is accommodated by dislocation activity within narrow mantle regions adjacent to the grain boundaries [17,24].

SDC, in contrast, is a dislocation-based mechanism involving the interaction between mobile dislocations and diffusing solute atoms at elevated temperatures. SDC dominates Region III deformation ($n > 3$), typically at intermediate strain rates and lower strain-rate sensitivity ($m < 0.3$) [1] . Unlike GBS, SDC is relatively insensitive to grain size and can therefore occur in both fine- and coarse-grained alloys [16–18]. Deformation under SDC is often associated with the formation of subgrain structures due to dislocation rearrangement into low-energy configurations [1,16].

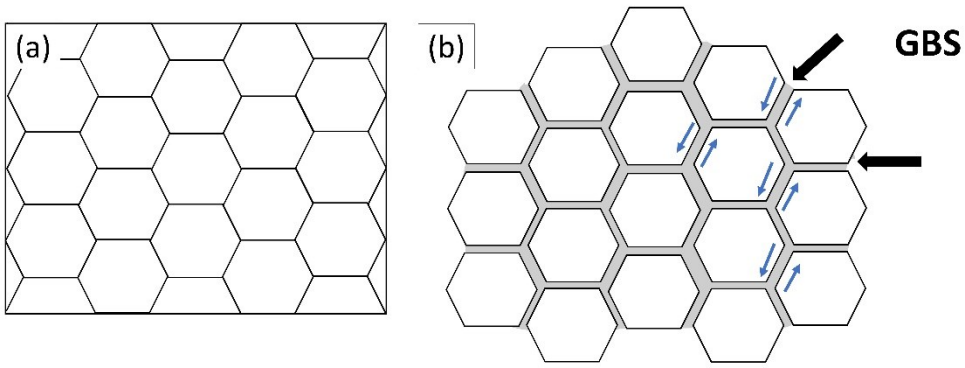


Figure 2.2 Schematic representation of GBS occurring in fine-grained Al alloys: (a) initial grain structure and (b) GBS mechanism, the blue arrows show the grain sliding direction

DC occurs at low strain rates and elevated temperatures (Region I, $n \approx 1$), where deformation is controlled by atomic diffusion either along grain boundaries or through the lattice (Figure 2.3) [1,19] . This mechanism does not involve dislocation motion and is typically accompanied by grain growth, which limits superplastic elongation and reduces formability.

Although GBS is widely accepted as the dominant mechanism for achieving high superplastic elongation in aluminum alloys, its role in Al–Mg 5xxx alloys remains limited [18–20,23,30]. Several studies have shown that SDC and DC are the primary deformation mechanisms in these alloys [23,31]. The relative contribution of these mechanisms depends

on deformation conditions, particularly temperature and strain rate [24]. In general, GBS dominates at low strain rates, while SDC becomes increasingly significant at intermediate strain rates.

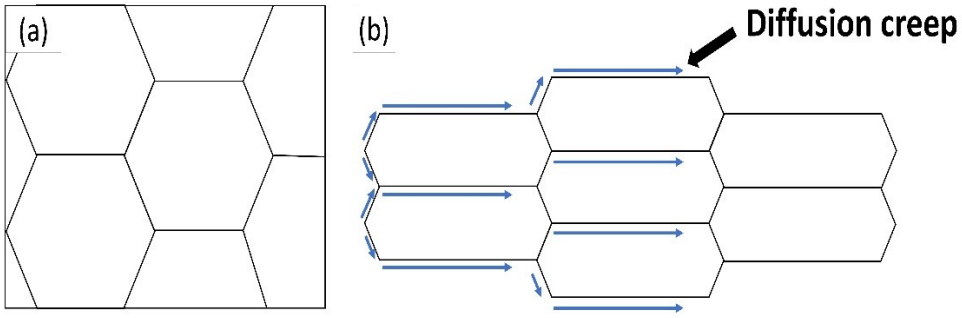


Figure 2.3 Schematic representation of DC occurring in coarse-grained Al alloys: (a) initial grain structure and (b) diffusion creep mechanism, the blue arrows show atomic transport along grain boundaries

Furthermore, deformation mechanisms are not static and may evolve during deformation [17,18,24]. For example, Hsiao Huang observed a transition from SDC to GBS in AA5083 at large strains ($\varepsilon > 0.5$), with GBS becoming dominant at elevated temperatures (>400 °C) [18]. Similarly, McNelly reported strain-rate-dependent transitions, with GBS dominating at low strain rates and SDC controlling deformation at intermediate strain rates [17]. These observations highlight the complex and dynamic nature of deformation behavior in Al–Mg alloys.

Recent studies have also demonstrated that high-strain-rate superplasticity (HSRS) in Al–Mg alloys is primarily governed by SDC and dislocation-mediated deformation mechanisms. For instance, Kishchik et al. [5] reported superplastic elongation of ~535 % at a strain rate of 1×10^{-1} s^{-1} in an Al–Mg–Fe–Ni alloy microalloyed with Sc and Zr, where

deformation was controlled by dislocation slip. This suggests that achieving superplasticity at elevated strain rates requires mechanisms beyond classical GBS.

The relatively low superplastic response of Al–Mg 5xxx alloys is attributed to their limited ability to sustain GBS. This limitation arises from the formation of Al–Mg clusters at grain boundaries, which impede grain boundary sliding [22]. Although high-angle grain boundaries (HAGBs) generally promote GBS, they also provide favorable sites for Mg segregation, leading to cluster formation that suppresses sliding [32]. Therefore, modifying grain boundary structure and chemistry has been proposed as an effective strategy to enhance superplasticity in these alloys.

Grain boundary engineering approaches, such as those explored in ultrafine-grained Al–Zn–Mg alloys, have shown that controlled solute segregation can promote GBS by stabilizing favorable grain boundary structures [33,34] . However, such ultrafine-grained microstructures are typically achieved through severe plastic deformation techniques, including high-pressure torsion (HPT), friction stir processing (FSP), accumulative roll bonding (ARB), and equal-channel angular pressing (ECAP) [35]. These methods are often costly and difficult to scale for industrial sheet production [21].

In addition to deformation mechanisms, cavitation behavior plays a critical role in determining superplastic formability. While GBS enables large elongations, it is often associated with increased cavity nucleation and growth, particularly at particle–matrix interfaces, grain boundary triple junctions, and boundary ledges [17,21]. This can lead to premature failure and loss of formability. In contrast, SDC-dominated deformation generally exhibits reduced cavitation growth rates, suggesting a trade-off between elongation and damage resistance under different deformation conditions.

Despite extensive studies on individual deformation mechanisms, a comprehensive understanding of their interaction and transition across a wide strain-rate regime remains limited. This is particularly relevant for advanced forming processes such as HSBF, where materials are subjected to both low and high strain-rate deformation. Understanding these mechanism transitions is therefore critical for the development of alloys capable of sustaining stable deformation under such hybrid conditions.

2.4 Factors affecting superplasticity of aluminum alloys

2.4.1 Effect of grain size and texture

As discussed previously, extensive superplastic elongation in aluminum alloys is typically achieved when deformation is governed by grain boundary sliding. GBS is highly sensitive to grain size, and its contribution to deformation increases with decreasing grain size [5,23,24,31]. Ultrafine-grained microstructures significantly enhance the superplastic response by increasing the fraction of grain boundaries available for sliding. For example, Liu et al. [35] reported a high GBS contribution (~72 %) in an Al–Mg–Sc alloy with an ultrafine grain size of ~0.6 μm produced via friction stir processing (FSP). This behavior was attributed to the high fraction of HAGBs, which facilitate GBS. In general, a high HAGB fraction is essential for sustaining GBS, as these boundaries are more mobile and accommodate sliding more effectively than low-angle grain boundaries (LAGBs).

Texture evolution during deformation also plays a critical role in superplasticity. Duan et al. [21] reported superplastic elongation of ~1050 % in a highly textured Al–Zn–Mn–Sc alloy, where the transformation of LAGBs into HAGBs during deformation enabled sustained GBS. Similarly, Kishchik et al. [5] observed that dynamic recrystallization in an Al–Mg–Fe–Ni alloy transformed an initially banded microstructure into a fine equiaxed grain

structure (2–4 μm) with a high fraction of HAGBs, resulting in enhanced superplasticity (~750 %). These observations demonstrate that grain refinement and grain boundary character evolution are critical factors controlling superplastic deformation. In particular, fine-grained microstructures not only promote GBS but also enable high-strain-rate and low-temperature superplasticity [33–35], which are essential for advanced forming processes.

2.4.2 Effect of precipitation (Precipitates and dispersoids)

Dispersoids and intermetallic particles have a profound influence on the superplastic performance of aluminum alloys by controlling microstructural stability during deformation [5,19]. Fine dispersoids (typically <100 nm) enhance thermal stability by suppressing grain growth through the Zener pinning mechanism [5,23,36]. In addition, ultrafine dispersoids (5–10 nm) can retard recrystallization during heating, thereby preserving deformation-induced microstructures prior to superplastic forming [5].

Dispersoids are typically formed through the addition of transition elements such as Cr, Zr, Sc, and Mn [37]. Among these, Sc and Zr are particularly effective due to the formation of coherent $Al_3(Sc,Zr)$ dispersoids, which strongly inhibit grain boundary migration and enhance superplasticity [21,26,36]. Several studies have demonstrated that minor additions of Sc and Zr promote dynamic recrystallization during deformation, leading to refined grain structures and improved ductility [14,36,38].

However, the high cost of scandium has motivated the development of alternative alloy design strategies. For example, Kotov et al. [26] demonstrated that a Sc-free Al–Zn–Mg–Cu alloy containing Zr and Ni exhibited superior superplasticity (~1200 %) compared to its Sc-containing counterpart (~430 %). This improvement was attributed to the presence of a bimodal particle distribution consisting of fine coherent Al_3Zr dispersoids and coarse eutectic

Al_3Ni particles. The dispersoids suppressed grain growth, while the coarse particles promoted dynamic recrystallization through particle-stimulated nucleation (PSN).

Similarly, Mikhaylovskaya et al. [36] reported enhanced superplasticity in Al–Zn–Mg alloys through the formation of bimodal particles, consisting of Al_3(Zr,Sc) dispersoids and Al_9FeNi eutectic particles. These studies highlight that a combination of nanoscale dispersoids and coarse particles can simultaneously enhance grain stability and promote recrystallization. This provides an effective pathway for improving superplastic performance without excessive reliance on expensive alloying elements; however, the presence of coarse particles may promote excessive cavitation.

Sc additions commonly approaching or exceeding 0.10 wt.% substantially increase alloy cost and may limit large-scale industrial application [14,39–41]. Er has therefore been investigated as a partial substitute for Sc because it can form $L1_2$-ordered Al_3Er and participate in Al_3(Sc,Zr,Er) precipitates, providing precipitate pinning and thermal stability while reducing the required Sc content [42–45]. The diffusion behavior of Er also differs from that of Sc and Zr. At 300 °C, the diffusivity of Er in α-Al is approximately 4×10^{-19} m^2 s^{-1}, compared with approximately 9×10^{-20} m^2 s^{-1} for Sc [46] , while Zr diffuses considerably more slowly, giving the sequence $D_{Er} > D_{Sc} > D_{Zr}$ [44,47] . These differences in diffusivity promote the development of coherent Al_3(Sc,Zr,Er) precipitates with an Er-enriched core, Sc-enriched intermediate shell, and Zr-enriched outer shell [44,47]. The slowly diffusing Zr-rich outer shell suppresses coarsening, and such precipitates have been reported to retain coarsening resistance for at least 64 days at 400 °C [44]. Er also has limited solid solubility in α-Al, with a reported maximum of approximately 0.046 at.% at 640 °C [46] . Consequently, excess Er can promote the formation of primary Al_3Er during solidification [46,48] . Depending on their size and distribution, these particles may modify the as-cast

grain structure and provide heterogeneous nucleation sites during subsequent recrystallization [49–51]. Thus, combining Er with Sc and Zr offers a potential approach for reducing Sc content while maintaining precipitate stability and controlling microstructural evolution in Al alloys.

In addition to microalloying, alloy composition also plays a significant role. Increasing Mg content has been shown to enhance superplasticity by stabilizing grain structure and promoting GBS. For instance, Mikhaylovskaya et al. [22] reported that increasing Mg content from 4.8 to 6.5–7.6 wt.% reduced grain growth and increased elongation from ~300 % to ~430 %. Similarly, Kishchik et al. [25] observed enhanced superplasticity (~475 %) due to the formation of a refined grain structure (~4 μm) associated with a high volume fraction of uniformly distributed coarse (~1 μm) β-Al_3Mg_2 particles. These findings demonstrate that precipitation behavior and particle distribution are critical for tailoring microstructural stability and deformation mechanisms in superplastic aluminum alloys.

2.4.3 Effect of temperature

Superplastic deformation is a thermally activated process that typically occurs at high homologous temperatures [1,2,27]. Temperature strongly influences flow stress, strain-rate sensitivity, and microstructural stability during deformation. In general, flow stress decreases with increasing temperature, facilitating plastic deformation [12,52]. Strain-rate sensitivity also increases with temperature, enhancing resistance to strain localization and promoting uniform deformation. For example, Kotov et al. [26] reported m-values of ~0.45–0.47 for Al–Zn–Mg–Cu alloys at 420–480 °C, which are favorable for GBS. Similarly, Hsiao et al.

[18] observed a significant increase in m-value from ~0.25 at 250 °C to ~0.55 at 550 °C in AA5083, corresponding to improved superplastic response.

However, elevated temperatures can also lead to dynamic grain growth, which reduces grain boundary area and weakens GBS, thereby limiting superplasticity [19,23]. Consequently, maintaining a balance between thermal activation of deformation mechanisms and microstructural stability is critical. Recent research has focused on developing alloys capable of exhibiting superplasticity at lower temperatures to reduce energy consumption and enable more sustainable manufacturing processes [33]. Such developments are particularly relevant for industrial applications where both performance and efficiency are required. Despite these advances, the combined effects of these factors under HSBF-relevant conditions, particularly under rapid thermal cycles and hybrid strain-rate deformation, remain insufficiently understood.

2.5 Cavitation behavior under superplastic forming conditions

In Al–Mg 5xxx superplastic alloys, hot formability is often limited by cavitation, as excessive cavity nucleation, growth, and coalescence can severely degrade post-forming mechanical properties and lead to premature fracture [53–56]. While a small fraction of cavities may originate from pre-existing defects introduced during casting or processing, the majority of cavitation is continuously nucleated during superplastic deformation [53].

Cavitation preferentially occurs at microstructural heterogeneities such as grain boundaries, triple junctions, and grain boundary-associated intermetallic compounds (IMCs) [17,57]. The characteristics of these IMCs—including their size, morphology, and distribution—are strongly influenced by alloy composition and thermomechanical processing history. In particular, coarse and irregular particles act as potent nucleation sites

due to localized stress concentrations and strain incompatibilities at the particle–matrix interface [53,55,58].

Following nucleation, cavity growth initially proceeds via diffusion-controlled mechanisms at low strains. As deformation progresses, the growth mechanism transitions to plasticity-controlled or coupled diffusion–plasticity-controlled processes, particularly at higher strains. Ultimately, cavities coalesce to form crack-like defects, which significantly reduce ductility and limit formability [41,53,59].

Cavitation behavior is strongly influenced by the dominant deformation mechanism. Under SDC-dominated deformation, cavity growth rates are generally lower due to enhanced accommodation of strain. In contrast, when GBS becomes dominant, incomplete accommodation of grain boundary offsets can promote cavity growth and coalescence [60]. As a result, cavitation associated with GBS tends to be more isotropic, whereas SDC-controlled cavitation often exhibits alignment along the tensile axis [56].

In addition, cavitation severity increases with increasing strain and is further exacerbated by grain growth during deformation, which reduces the effectiveness of grain boundary-mediated accommodation processes [21,58]. However, despite extensive studies under conventional superplastic conditions, the strain-rate dependence of cavitation behavior—particularly under transient thermal conditions and hybrid deformation paths involving both high and low strain rates, as encountered in processes such as HSBF—remains insufficiently understood. A comprehensive mechanistic understanding of cavitation evolution, in relation to deformation mechanisms and microstructural stability, is therefore essential for improving formability, damage tolerance, and process reliability in HSBF-formed Al–Mg 5xxx components.

2.6 High-strain-rate superplastic forming processes

As discussed earlier, superplastic forming (SPF) is an attractive manufacturing process due to its ability to produce large and complex components with reduced forming loads and simplified tooling [5–9]. However, a major limitation of SPF is its inherently slow cycle time, which results in low production rates and restricts its application in high-volume industries such as automotive manufacturing [3,10]. This limitation arises primarily from the fact that most aluminum alloys exhibit superplasticity only at low strain rates (typically 10^{-4}–10^{-3} s^{-1}). Increasing the deformation rate generally leads to a reduction in superplastic response, thereby limiting process efficiency.

To overcome this limitation, significant research efforts have focused on developing high-strain-rate superplastic (HSRS) aluminum alloys capable of exhibiting substantial elongation at strain rates $\geq 10^{-2}$ s^{-1} [14]. While such alloy design approaches have shown promise, they often require complex thermomechanical processing or costly alloying additions, which can limit their industrial scalability.

An alternative and more practical approach is the development of advanced forming technologies designed to operate at higher strain rates. These include processes such as Quick Plastic Forming (QPF) and Hybrid Superplastic Forming (HSF), which aim to reduce cycle time while maintaining acceptable formability [10]. QPF achieves this by operating at intermediate strain rates through mechanisms such as solute drag creep, whereas HSF combines conventional deformation with superplastic forming.

An example of HSF is High-Speed Blow Forming (HSBF), which integrates an initial high strain-rate mechanical forming stage (crash forming) with a subsequent low strain-rate superplastic gas forming stage. This hybrid approach significantly reduces forming time—

by up to an order of magnitude compared to conventional SPF—while retaining the ability to form complex geometries. In addition, HSBF enables the use of commercially available Al–Mg 5xxx alloys with relatively modest superplastic properties, making it highly attractive for industrial applications, particularly in automotive body panel manufacturing [10].

Despite these advantages, HSBF introduces complex deformation conditions involving rapid transitions between high and low strain-rate regimes, coupled with transient thermal cycles. These conditions strongly influence deformation mechanisms, microstructural evolution, and damage processes such as cavitation. However, current understanding of these interactions remains limited, particularly for conventionally processed Al–Mg 5xxx alloys.

Therefore, a systematic investigation of the effects of forming parameters—especially temperature and strain rate—on deformation behavior, microstructure evolution, and superplastic response under HSBF-relevant conditions is essential. Such understanding is critical for optimizing HSBF processing and for the development of alloys specifically tailored to sustain stable deformation under hybrid forming conditions. This limitation highlights the need for integrated studies that link deformation mechanisms, microstructural stability, and damage evolution across the full strain-rate spectrum characteristic of HSBF.

2.7 Recycled aluminum and scrap-based alloy design

Increasing the use of recycled aluminum is important for reducing the environmental impact of automotive aluminum production. Aluminum can be recycled repeatedly with the potential to retain its intrinsic material properties, provided that alloy composition and impurity levels are adequately controlled. The growing use of aluminum sheet in vehicles is expected to generate increasing quantities of end-of-life 5xxx and 6xxx sheet scrap, creating opportunities for closed-loop recycling [61]. However, conventional recycling is constrained

by alloy mixing and the accumulation of residual elements, which can restrict the reuse of scrap in wrought automotive alloys with narrow compositional limits [61,62]. Recent recycling strategies therefore emphasize improved scrap separation together with alloy designs capable of tolerating greater compositional variability [62].

This challenge is particularly important for wrought automotive sheet alloys, where Fe, Si, and Cu are among the major residual elements of concern because excessive concentrations can alter phase formation and adversely affect mechanical properties and formability [63]. In Al–Mg 5xxx alloys, increased Fe promotes the formation of coarse Fe-containing intermetallic particles, while Si can combine with Mg to form Mg_2Si [63]. In Al–Mg–Mn alloys, Mn modifies the composition and morphology of Fe-containing constituent particles and promotes the formation of Al–Mn-based dispersoids during homogenization. Consequently, the Fe/Mn ratio, solidification conditions, and subsequent thermomechanical processing influence the size, morphology, and distribution of primary constituent particles and secondary dispersoids [64,65]. Therefore, controlling the type, size, and distribution of these second-phase particles is particularly important when designing recycled Al–Mg–Mn alloys for elevated-temperature forming.

For automotive applications, compositionally controlled manufacturing scrap is particularly attractive because it reduces cross-contamination compared with mixed post-consumer scrap [61,62]. Nevertheless, increasing recycled content requires alloy and process designs capable of accommodating compositional variability while maintaining the microstructural stability, mechanical properties, and formability required for sheet applications [62,63]. For Al–Mg–Mn alloys intended for elevated-temperature forming, control of coarse intermetallic particles is particularly important because they can promote strain localization and cavity nucleation [41,55–57,66], whereas fine dispersoids and

precipitates can restrict grain-boundary migration and improve microstructural stability [5,23,67,68]. Thus, combining controlled Al–Mg–Mn scrap with appropriate microalloying and thermomechanical processing provides a potential route for developing more sustainable alloys suitable for high-temperature forming.

2.8 Superplastic Al–Mg alloy design strategy

The superplastic response of Al–Mg alloys can be enhanced by increasing the contribution of GBS to the overall deformation process. However, the relatively weak GBS contribution in these alloys has been attributed to the segregation of Mg atoms at grain boundaries (GBs), leading to the formation of Al–Mg clusters. These clusters reduce atomic mobility along grain boundaries, thereby increasing the threshold stress required for GBS and limiting superplastic elongation [22]. Since the kinetics of GBS is strongly influenced by grain boundary structure and chemistry [34], tailoring the grain boundary state through alloy design and processing presents a viable strategy for enhancing superplasticity.

Grain boundary engineering approaches have demonstrated that modifying grain boundary chemistry can significantly improve GBS activity. For instance, studies on ultrafine-grained Al–15Zn (at.%) alloys [33,34] have shown that Zn segregation at grain boundaries can form a lubricating nanolayer, which reduces the energy barrier for GBS and enables enhanced superplasticity even at relatively low homologous temperatures. However, the ultrafine-grained structures required for such behavior were achieved through severe plastic deformation techniques such as high-pressure torsion (HPT), which are costly and not suitable for large-scale industrial sheet production [21].

These limitations highlight the need for alternative alloy-design strategies that are both effective and industrially scalable. A promising approach involves the combined use of thermomechanical processing (TMP) and microalloying with elements such as Zr, Sc, and Er to develop thermally stable fine-grained microstructures. In this approach, homogenization treatments can be designed to promote a favorable distribution of fine Mn-rich dispersoids and coherent $Al_3(Sc,Zr)$- or $Al_3(Sc,Er,Zr)$-based precipitates within the matrix. These second-phase particles can restrict grain-boundary migration through Zener pinning and thereby improve grain-structure stability during subsequent processing and high-temperature deformation.

Kishchik et al. [69] demonstrated that a two-step homogenization treatment (400 °C/5 h + 470 °C/3 h) produced a significantly higher number density of $Al_3(Sc,Zr)$ precipitates compared with a single-step treatment (400 °C/8 h) in Al–Mg–Fe–Zr–Sc alloys. The increased precipitate density resulted in enhanced superplastic performance, with elongation reaching ~650 % at a strain rate of 0.01 s^{-1} and 540 °C. Similarly, Algendy et al. [38] employed a three-step homogenization process (275 °C/12 h + 375 °C/48 h + 425 °C/12 h) to achieve a high density of Mn-rich dispersoids in combination with coherent $Al_3(Sc,Zr)$ precipitates in Al–Mg–Mn–Sc–Zr alloys. Although the superplastic response was not directly evaluated, the resulting particle distribution promoted grain refinement and improved microstructural stability, both of which are favorable for GBS. These findings demonstrate that controlled thermomechanical processing can be used to tailor the size, distribution, and number density of dispersoids and precipitates to develop microstructures favorable for superplastic deformation.

Despite these advances, most existing alloy-design strategies rely on relatively high additions of Sc, which significantly increase material cost. Furthermore, these approaches

have primarily been developed for conventional SPF conditions and do not explicitly account for the complex hybrid deformation behavior associated with HSBF. Consequently, there remains a need for cost-effective Al–Mg–Mn alloys with tailored microstructures capable of sustaining stable deformation across a wide strain-rate regime. This may potentially be achieved through the synergistic integration of microalloying with Sc, Zr, and Er, optimized thermomechanical processing, and sustainable material sources such as controlled industrial scrap.

2.9 Summary and research gaps

The literature reviewed in this chapter demonstrates that the superplastic behavior of aluminum alloys is strongly governed by the interplay between microstructural characteristics, deformation mechanisms, and thermomechanical processing conditions. In particular, the development of a fine and thermally stable grain structure, supported by appropriate precipitation and dispersoid distributions, is important for facilitating GBS and achieving high superplastic elongation.

Significant progress has been made in understanding the roles of grain size, grain-boundary character, precipitation behavior, and deformation temperature in controlling superplastic response. Advanced thermomechanical processing routes and microalloying strategies, particularly involving Sc and Zr, have been shown to improve microstructural stability by restricting grain-boundary migration and controlling recrystallization and grain growth during processing and elevated-temperature deformation. In addition, the development of advanced forming processes such as QPF and HSBF has addressed some of the limitations of conventional SPF, particularly its low production rate.

Despite these advances, several critical gaps remain. First, most existing studies on Al–Mg–Mn 5xxx alloys have focused on deformation under low strain-rate superplastic conditions ($\leq 10^{-2}$ s^{-1}), where GBS makes a significant contribution to deformation. In contrast, tensile deformation behavior at high strain rates (≥ 1 s^{-1}), which is directly relevant to the rapid initial deformation stage of HSBF, remains insufficiently explored. Moreover, many high-strain-rate studies are conducted under compressive loading, which does not represent the tensile stress state experienced during sheet forming and cannot directly capture tensile damage mechanisms such as cavitation.

Second, while the influence of annealing temperature on microstructural evolution has been widely investigated, the effect of short-duration annealing, representative of rapid HSBF processing, on recrystallization and grain-structure stability has received comparatively limited attention. Many studies employ longer annealing durations that do not adequately represent the rapid thermal cycles associated with HSBF.

Third, although the individual deformation mechanisms governing elevated-temperature deformation, including GBS, SDC, and dislocation-controlled deformation, are well established, their relative contributions and transitions across a wide strain-rate regime remain incompletely understood. This is particularly important under HSBF-relevant conditions, where the material may experience deformation paths involving transitions between high and lower strain-rate regimes.

Fourth, cavitation behavior in Al–Mg 5xxx alloys has predominantly been studied under conventional low strain-rate superplastic conditions. A systematic understanding of the combined effects of strain rate and accumulated strain on cavity nucleation, growth, and coalescence, particularly at the higher strain rates relevant to HSBF, remains limited. This

restricts the ability to understand damage evolution and establish processing conditions that minimize cavitation.

Finally, existing alloy-design strategies have largely been developed for conventional SPF applications and do not explicitly account for the complex deformation conditions associated with HSBF. There has been limited systematic effort to develop Al–Mg–Mn 5xxx alloys specifically tailored for HSBF, where microstructural stability, deformation compatibility across a wide strain-rate range, and resistance to cavitation are required. Furthermore, despite increasing interest in closed-loop recycling of automotive aluminum, the integration of controlled scrap feedstock, microalloying with Sc, Zr, and Er, and thermomechanical processing for the development of HSBF-compatible Al–Mg–Mn alloys remains largely unexplored.

Therefore, there is a need for a systematic investigation of the relationships among microstructural evolution, deformation mechanisms, and cavitation behavior across the strain-rate regime relevant to HSBF. Addressing these gaps can provide the scientific basis for developing cost-effective and sustainable Al–Mg–Mn 5xxx alloys with improved microstructural stability and deformation capability under HSBF-relevant conditions, thereby supporting more efficient high-speed forming technologies for automotive applications.

References

1. Chokshi AH. Grain boundary processes in strengthening, weakening, and superplasticity. *Adv Eng Mater*. 2020;22:1900748. https://doi.org/10.1002/adem.201900748.

2. Smolej A, Skaza B, Slaček E. Superplasticity of the 5083 aluminium alloy with the addition of scandium. *Mater Technol*. 2009;43(6):299–302.

3. Luo Y, Luckey SG, Friedman PA, Peng Y. Development of an advanced superplastic forming process utilizing a mechanical pre-forming operation. *Int J Mach Tools Manuf*. 2008;48:1509–1518. https://doi.org/10.1016/j.ijmachtools.2007.12.010.

4. Liu J, Tan MJ, Aue-U-Lan Y, Jarfors AEW, Fong KS, Castagne S. Superplastic-like forming of non-superplastic AA5083 combined with mechanical pre-forming. *Int J Adv Manuf Technol*. 2011;52:123–129. https://doi.org/10.1007/s00170-010-2729-9.

5. Kishchik AA, Mikhaylovskaya AV, Kotov AD, Rofman OV, Portnoy VK. Al-Mg-Fe-Ni based alloy for high strain rate superplastic forming. *Mater Sci Eng A*. 2018;718:190–197. https://doi.org/10.1016/j.msea.2018.01.099.

6. Bhatta L, Pesin A, Zhilyaev AP, Tandon P, Kong C, Yu H. Recent development of superplasticity in aluminum alloys: A review. *Metals*. 2020;10:77. https://doi.org/10.3390/met10010077.

7. Grimes R. Superplastic forming of aluminium alloys. In: *Superplastic Forming of Advanced Metallic Materials*. Cambridge, UK: Woodhead Publishing; 2011. p. 247–271. https://doi.org/10.1533/9780857092779.3.247.

8. Barnes AJ. Superplastic aluminum forming—expanding its techno-economic niche. *Mater Sci Forum*. 1999;304–306:785–796. https://doi.org/10.4028/www.scientific.net/MSF.304-306.785.

9. Kawasaki M, Langdon TG. Superplasticity in ultrafine-grained materials. *Rev Adv Mater Sci*. 2018;54(1):46–55. https://doi.org/10.1515/rams-2018-0019.

10. Majidi O, Jahazi M, Bombardier N. Finite element simulation of high-speed blow forming of an automotive component. *Metals*. 2018;8:901. https://doi.org/10.3390/met8110901.

11. Jeon J, Lee S, Kyeong J, Shin S, Kang H. Effect of geometrical parameters of microscale particles on particle-stimulated nucleation and recrystallization texture of Al-Si-Mg-Cu-based alloy sheets. *Materials*. 2022;15:7924. https://doi.org/10.3390/ma15227924.

12. Giuliano G. *Superplastic Forming of Advanced Metallic Materials*. Woodhead Publishing Limited; 2011. https://doi.org/10.1533/9780857092779.

13. Ebenberger P, Uggowitzer PJ, Gerold B, Pogatscher S. Effect of compositional and processing variations in new 5182-type AlMgMn alloys on mechanical properties and deformation surface quality. *Materials*. 2019;12:1645. https://doi.org/10.3390/ma12101645.

14. Yakovtseva OA, Kishchik AA, Cheverikin VV, Kotov AD, Mikhaylovskaya AV. The mechanisms of the high-strain-rate superplastic deformation of Al-Mg-based alloy. *Mater Lett*. 2022;325:132883. https://doi.org/10.1016/j.matlet.2022.132883.

15. Venkataraman A, Sangid MD. *Deformation Mechanisms at Grain Boundaries in Polycrystals*. Final Report to the U.S. Department of Energy, Office of Basic Energy Sciences, Division of Materials Sciences and Engineering; 2019.

16. Jeong HT, Park HK, Kang HS, Kim WJ. Operation of solute-drag creep in an AlCoCrFeMnNi high-entropy alloy and enhanced hot workability. *J Alloys Compd*. 2020;824:153829. https://doi.org/10.1016/j.jallcom.2020.153829.

17. McNelley TR, Oh-Ishi K, Zhilyaev AP, Swaminathan S, Krajewski PE, Taleff EM. Characteristics of the transition from grain-boundary sliding to solute drag creep in superplastic AA5083. *Metall Mater Trans A*. 2008;39:50–64. https://doi.org/10.1007/s11661-007-9401-5.

18. Hsiao IC, Huang JC. Deformation mechanisms during low- and high-temperature superplasticity in 5083 Al-Mg alloy. *Metall Mater Trans A*. 2002;33:1373–1384. https://doi.org/10.1007/s11661-002-0062-0.

19. Li H, Liu X, Sun Q, Ye L, Zhang X. Superplastic deformation mechanisms in fine-grained 2050 Al-Cu-Li alloys. *Materials*. 2020;13:2705. https://doi.org/10.3390/ma13122705.

20. Yakovtseva OA, Mikhaylovskaya AV, Mochugovskiy AG, Cheverikin VV, Portnoy VK. Superplastic deformation mechanisms in high magnesium contenting aluminum alloy. *Mater Sci Forum*. 2016;838–839:66–71. https://doi.org/10.4028/www.scientific.net/MSF.838-839.66.

21. Duan Y, Xu G, Zhou L, Xiao D, Deng Y, Yin Z, et al. Achieving high superplasticity of a traditional thermal-mechanical processed non-superplastic Al-Zn-Mg alloy sheet by low Sc additions. *J Alloys Compd*. 2015;638:364–373. https://doi.org/10.1016/j.jallcom.2015.03.090.

22. Mikhaylovskaya AV, Yakovtseva OA, Irzhak AV. The role of grain boundary sliding and intragranular deformation mechanisms for a steady stage of superplastic flow for Al–Mg-based alloys. *Mater Sci Eng A*. 2022;833:142524. https://doi.org/10.1016/j.msea.2021.142524.

23. Sotoudeh K, Bate PS. Diffusion creep and superplasticity in aluminium alloys. *Acta Mater*. 2010;58:1909–1920. https://doi.org/10.1016/j.actamat.2009.11.034.

24. Pérez-Prado MT, González-Doncel G, Ruano OA, McNelley TR. Texture analysis of the transition from slip to grain boundary sliding in a discontinuously recrystallized superplastic aluminum alloy. *Acta Mater*. 2001;49:2259–2268. https://doi.org/10.1016/S1359-6454(01)00128-8.

25. Kishchik AA, Mikhaylovskaya AV, Levchenko VS, Portnoy VK. Formation of microstructure and the superplasticity of Al–Mg-based alloys. *Phys Met Metallogr*. 2017;118:96–103. https://doi.org/10.1134/S0031918X16120085.

26. Kotov AD, Mikhaylovskaya AV, Kishchik MS, Tsarkov AA, Aksenov SA, Portnoy VK. Superplasticity of high-strength Al-based alloys produced by thermomechanical treatment. *J Alloys Compd*. 2016;688:336–344. https://doi.org/10.1016/j.jallcom.2016.07.045.

27. Wang XG, Li QS, Wu RR, Zhang XY, Ma L. A review on superplastic formation behavior of Al alloys. *Adv Mater Sci Eng*. 2018;2018:7606140. https://doi.org/10.1155/2018/7606140.

28. Zou GT, Chen SJ, Xu YQ, Shen BK, Zhang YJ, Ye LY. Microstructural evolution and deformation mechanisms of superplastic aluminium alloys: A review. *Trans Nonferrous Met Soc China*. 2024;34:3069–3092. https://doi.org/10.1016/S1003-6326(24)66596-9.

29. Figueiredo RB, Langdon TG. Effect of grain size on strength and strain rate sensitivity in metals. *J Mater Sci*. 2022;57:5210–5229. https://doi.org/10.1007/s10853-022-06919-0.

30. Rust MA, Todd RI. Surface studies of Region II superplasticity of AA5083 in shear: Confirmation of diffusion creep, grain neighbour switching and absence of dislocation activity. *Acta Mater*. 2011;59:5159–5170. https://doi.org/10.1016/j.actamat.2011.04.051.

31. Mikhaylovskaya AV, Yakovtseva OA, Golovin IS, Pozdniakov AV, Portnoy VK. Superplastic deformation mechanisms in fine-grained Al-Mg based alloys. *Mater Sci Eng A*. 2015;627:31–41. https://doi.org/10.1016/j.msea.2014.12.099.

32. Koju RK, Mishin Y. Atomistic study of grain-boundary segregation and grain-boundary diffusion in Al-Mg alloys. *Acta Mater*. 2020;201:596–603. https://doi.org/10.1016/j.actamat.2020.10.029.

33. Chinh NQ, Murashkin MY, Bobruk EV, Lábár JL, Gubicza J, Kovács Z, et al. Ultralow-temperature superplasticity and its novel mechanism in ultrafine-grained Al alloys. *Mater Res Lett*. 2021;9:475–482. https://doi.org/10.1080/21663831.2021.1976293.

34. Song Z, Niu R, Cui X, Bobruk EV, Murashkin MY, Enikeev NA, et al. Mechanism of room-temperature superplasticity in ultrafine-grained Al–Zn alloys. *Acta Mater*. 2023;246:118671. https://doi.org/10.1016/j.actamat.2023.118671.

35. Liu FC, Ma ZY. Contribution of grain boundary sliding in low-temperature superplasticity of ultrafine-grained aluminum alloys. *Scr Mater*. 2010;62:125–128. https://doi.org/10.1016/j.scriptamat.2009.10.010.

36. Mikhaylovskaya AV, Yakovtseva OA, Cheverikin VV, Kotov AD, Portnoy VK. Superplastic behaviour of Al-Mg-Zn-Zr-Sc-based alloys at high strain rates. *Mater Sci Eng A*. 2016;659:225–233. https://doi.org/10.1016/j.msea.2016.02.061.

37. Totten GE, Mackenzie DS. *Handbook of Aluminum: Physical Metallurgy and Processes*. New York: Marcel Dekker, Inc.; 2003.

38. Algendy AY, Liu K, Rometsch P, Parson N, Chen XG. Effects of AlMn dispersoids and Al_3(Sc,Zr) precipitates on the microstructure and ambient/elevated-temperature mechanical properties of hot-rolled AA5083 alloys. *Mater Sci Eng A*. 2022;855:143950. https://doi.org/10.1016/j.msea.2022.143950.

39. Sun YB, Chen XP, Xie J, Wang C, An YF, Liu Q. High strain rate superplasticity and secondary strain hardening of Al-Mg-Sc-Zr alloy produced by friction stir processing. *Mater Today Commun*. 2022;33:104217. https://doi.org/10.1016/j.mtcomm.2022.104217.

40. Mikhaylovskaya AV, Esmaeili Ghayoumabadi M, Mochugovskiy AG. Superplasticity and mechanical properties of Al–Mg–Si alloy doped with eutectic-forming Ni and Fe, and dispersoid-forming Sc and Zr elements. *Mater Sci Eng A*. 2021;817:141319. https://doi.org/10.1016/j.msea.2021.141319.

41. Li M, Pan Q, Shi Y, Sun X, Xiang H. High strain rate superplasticity in an Al–Mg–Sc–Zr alloy processed via simple rolling. *Mater Sci Eng A*. 2017;687:298–305. https://doi.org/10.1016/j.msea.2017.01.091.

42. Fan T, Lin L, Liang H, Ma Y, Tang Y, Hu T, et al. First-principles study of the structural, mechanical and thermodynamic properties of $Al_{11}RE_3$ in aluminum alloys. *Crystals*. 2023;13(2):347. https://doi.org/10.3390/cryst13020347.

43. Kang W, Li HY, Zhao SX, Han Y, Yang CL, Ma G. Effects of homogenization treatments on the microstructure evolution, microhardness and electrical conductivity of dilute Al-Sc-Zr-Er alloys. *J Alloys Compd*. 2017;704:683–692. https://doi.org/10.1016/j.jallcom.2017.02.043.

44. Booth-Morrison C, Dunand DC, Seidman DN. Coarsening resistance at 400 °C of precipitation-strengthened Al–Zr–Sc–Er alloys. *Acta Mater*. 2011;59:7029–7042. https://doi.org/10.1016/j.actamat.2011.07.057.

45. Liu L, Jiang J, Cui X, Zhang B, Zhen L, Ringer SP. Correlation between precipitates evolution and mechanical properties of Al-Sc-Zr alloy with Er additions. *J Mater Sci Technol*. 2022;99:61–72. https://doi.org/10.1016/j.jmst.2021.05.031.

46. Van Dalen ME, Karnesky RA, Cabotaje JR, Dunand DC, Seidman DN. Erbium and ytterbium solubilities and diffusivities in aluminum as determined by nanoscale characterization of precipitates. *Acta Mater*. 2009;57:4081–4089. https://doi.org/10.1016/j.actamat.2009.05.007.

47. De Luca A, Dunand DC, Seidman DN. Mechanical properties and optimization of the aging of a dilute Al-Sc-Er-Zr-Si alloy with a high Zr/Sc ratio. *Acta Mater*. 2016;119:35–42. https://doi.org/10.1016/j.actamat.2016.08.018.

48. Gao Z, Li H, Lai Y, Ou Y, Li D. Effects of minor Zr and Er on microstructure and mechanical properties of pure aluminum. *Mater Sci Eng A*. 2013;580:92–98. https://doi.org/10.1016/j.msea.2013.05.035.

49. Kotov AD, Mochugovskiy AG, Mosleh AO, Kishchik AA, Rofman OV, Mikhaylovskaya AV. Microstructure, superplasticity, and mechanical properties of Al–Mg–Er–Zr alloys. *Mater Charact*. 2022;186:111825. https://doi.org/10.1016/j.matchar.2022.111825.

50. Mikhaylovskaya AV, Ryazantseva MA, Portnoy VK. Effect of eutectic particles on the grain size control and the superplasticity of aluminium alloys. *Mater Sci Eng A*. 2011;528:7306–7309. https://doi.org/10.1016/j.msea.2011.06.042.

51. Mikhaylovskaya AV, Kishchik AA, Kotov AD, Rofman OV, Tabachkova NY. Precipitation behavior and high strain rate superplasticity in a novel fine-grained aluminum based alloy. *Mater Sci Eng A*. 2019;760:37–46. https://doi.org/10.1016/j.msea.2019.05.099.

52. Shi C, Chen XG. Hot workability and processing maps of 7150 aluminum alloys with Zr and V additions. *J Mater Eng Perform*. 2015;24:2126–2139. https://doi.org/10.1007/s11665-015-1478-1.

53. Bae DH, Ghosh AK. Cavity growth during superplastic flow in an Al-Mg alloy: I. Experimental study. *Acta Mater*. 2002;50:993–1009. https://doi.org/10.1016/S1359-6454(01)00399-8.

54. Yi L, Gu Z, Yu G, Li X, Tang Z, Zhao Y. Damage behavior and performance analysis of Al5083 alloy in superplastic bulging. *Eng Fail Anal*. 2024;164:108732. https://doi.org/10.1016/j.engfailanal.2024.108732.

55. Jin H, Gerlich AP. Effects of intermetallic particles on cavitation during superplastic forming of aluminium alloy. *Mater Sci Technol*. 2019;35:1428–1435. https://doi.org/10.1080/02670836.2019.1627498.

56. Toda H, Shamsudin ZAB, Shimizu K, Uesugi K, Takeuchi A, Suzuki Y, et al. Cavitation during high-temperature deformation in Al-Mg alloys. *Acta Mater*. 2013;61:2403–2413. https://doi.org/10.1016/j.actamat.2013.01.012.

57. Campbell J. Cavitation during superplastic forming. *Materials*. 2011;4:1271–1286. https://doi.org/10.3390/ma4071271.

58. Liu FC, Ma ZY. Achieving high strain rate superplasticity in cast 7075Al alloy via friction stir processing. *J Mater Sci*. 2009;44:2647–2655. https://doi.org/10.1007/s10853-009-3346-6.

59. Hosseini ME, Hosseinipour SJ, Jooybari MB. Analysis of void growth during superplastic deformation of commercial AL5083 alloy. *Iran J Sci Technol Trans Mech Eng*. 2018;42:41–49. https://doi.org/10.1007/s40997-017-0075-3.

60. Alabort E, Kontis P, Barba D, Dragnevski K, Reed RC. On the mechanisms of superplasticity in Ti–6Al–4V. *Acta Mater*. 2016;105:449–463. https://doi.org/10.1016/j.actamat.2015.12.003.

61. Zhu Y, Chappuis LB, De Kleine R, Kim HC, Wallington TJ, Luckey G, et al. The coming wave of aluminum sheet scrap from vehicle recycling in the United States. *Resour Conserv Recycl*. 2021;164:105208. https://doi.org/10.1016/j.resconrec.2020.105208.

62. Krall P, Weißensteiner I, Pogatscher S. Recycling aluminum alloys for the automotive industry: Breaking the source–sink paradigm. *Resour Conserv Recycl*. 2024;202:107370. https://doi.org/10.1016/j.resconrec.2023.107370.

63. Raabe D, Ponge D, Uggowitzer PJ, Roscher M, Paolantonio M, Liu C, et al. Making sustainable aluminum by recycling scrap: The science of "dirty" alloys. *Prog Mater Sci*. 2022;128:100947. https://doi.org/10.1016/j.pmatsci.2022.100947.

64. Grasserbauer J, Weißensteiner I, Falkinger G, Uggowitzer PJ, Pogatscher S. Influence of Fe and Mn on the microstructure formation in 5xxx alloys—Part II: Evolution of grain size and texture. *Materials*. 2021;14(12):3312. https://doi.org/10.3390/ma14123312.

65. Grasserbauer J, Weißensteiner I, Falkinger G, Kremmer TM, Uggowitzer PJ, Pogatscher S. Influence of Fe and Mn on the microstructure formation in 5xxx alloys—Part I: Evolution of primary and secondary phases. *Materials*. 2021;14(12):3204. https://doi.org/10.3390/ma14123204.

66. Carunchio AF, Pereira DA, Fernandes Batalha MH, Resende HB, da Silva Antunes A. The effectiveness of back pressure in superplastic blow forming of aluminum alloy AA 5083 performed at very favorable conditions for cavitation growth. *Mater Res*. 2018;21. https://doi.org/10.1590/1980-5373-MR-2018-0261.

67. Liu K, Chen XG. Development of Al-Mn-Mg 3004 alloy for applications at elevated temperature via dispersoid strengthening. *Mater Des*. 2015;84:340–350. https://doi.org/10.1016/j.matdes.2015.06.140.

68. Algendy AY, Liu K, Chen XG. Effect of Mn-bearing dispersoids on tensile properties and recrystallization resistance of Al-3Mg-0.8Mn rolled alloy. *Adv Eng Mater*. 2023;25:2300667. https://doi.org/10.1002/adem.202300667.

69. Kishchik A, Mikhaylovskaya AV, Kotov AD, Portnoy VK. Effect of homogenization treatment on superplastic properties of aluminum based alloy with minor Zr and Sc additions. *Defect Diffus Forum*. 2018;385:84–90. https://doi.org/10.4028/www.scientific.net/DDF.385.84.

Chapter 3

Effect of Annealing Time on Grain Structure Evolution and Superplastic Response of Al–Mg 5xxx Alloys

(This article has been published in: Materials (MDPI), 17(22) (2024), 5492)

Abstract

The impact of annealing on the recrystallized grain structure and superplastic behavior of two Al–Mg 5xxx alloys used for high-speed blow forming (HSBF) was studied. The results revealed that both alloys demonstrated rapid static recrystallization after only a few minutes of annealing at 520 °C, forming fine and equiaxed grain structures. After four min of annealing, Alloy 2 (Al–4.0Mg–1.18Mn) exhibited a higher fraction of small grains (<10 μm) compared to Alloy 1 (Al–4.5Mg–0.74Mn). Moreover, Alloy 2 displayed enhanced resistance to grain coarsening with increasing annealing times, which was attributed to a higher number density of Mn dispersoids. Optimizing the annealing time can effectively develop a fine and stable grain structure in Al–Mg 5xxx alloys. During tensile deformation, Alloy 2 consistently showed higher ductility compared to Alloy 1 at low strain rates (170 % vs. 138 % at 0.001 s^{-1} and 163 % vs. 134 % at 0.01 s^{-1}), whereas at a high strain rate of 1 s^{-1}, both alloys displayed comparable tensile elongation. The high superplastic response of Alloy 2 at low strain rates renders it a superior superplastic alloy for HSBF applications

Keywords: Al–Mg 5xxx alloys; superplastic response; high-temperature annealing; recrystallized grain structure; high-speed blow forming (HSBF)

3.1 Introduction

Aluminum alloys are emerging as preferred materials in the automotive industry owing to their lightweight characteristics for reducing energy consumption [1,2]. Among Al alloys, Al–Mg 5xxx alloys have garnered special interest from automakers because of their excellent combination of high specific strength, toughness, weldability, corrosion resistance [3,4], and low cost [5]. Alloys of the 5xxx variety exhibit superplastic behavior at specific temperatures and strain rates, resulting in a remarkable increase in ductility, often exceeding 300% [6]. This excellent ductility has been commercially exploited through superplastic forming (SPF) to produce large and intricate autobody components that are unattainable through conventional forming methods [7,8]. Despite its cost-effectiveness [3,4,9–11], SPF is characterized by slow cycle times, often exceeding 30 min per part [7,12–14]. This is because Al–Mg alloys generally exhibit superplasticity at low strain rates (10^{-4} to 10^{-3} s^{-1}) [15].

To widely apply SPF in manufacturing auto body components, it is necessary to develop Al–Mg 5xxx alloys that exhibit optimal superplasticity at higher strain rates ($\geq 10^{-2}$ s^{-1}) [15]. Although some promising progress has been made in developing high-strain-rate superplastic (HSRS) Al–Mg 5xxx alloys [16,4], these alloys contain expensive elements such as Sc, which significantly increases the manufacturing cost. Thus, developing cost-effective HSRS Al–Mg 5xxx alloys remains challenging, prompting the need to explore alternative SPF methods.

High-speed blow forming (HSBF) offers a promising alternative to SPF, enabling a forming rate approximately 30 times faster than that of conventional SPF [12]. HSBF shapes preheated Al–Mg 5xxx alloy blanks into complex auto parts by combining crash forming and SPF. Most of the forming occurs during the crash forming stage, with the final intricate

details of the parts formed at low strain rates using SPF. Because of the small amount of SPF required, commercial Al–Mg 5xxx alloys that exhibit relatively low superplasticity can be used in the HSBF process [7,17].

A fine-grained structure with an average grain size of <10 μm is generally required for superplasticity [16,18–22]. For HSBF, the grain structure necessary to support the formation process is formed during preheating and annealing. Unlike SPF, annealing in HSBF is rapid and involves high heating rates and short holding times of less than five minutes. The grain structure that develops during fast annealing is crucial for alloy formability during HSBF. However, there are no extensive studies on the effect of this fast-annealed grain structure on the superplastic response of Al–Mg 5xxx alloys. Most studies on the superplasticity of 5xxx alloys have been conducted under slow-annealing conditions that do not simulate the HSBF. In these studies [20,23,24], the alloys were annealed for more than 20 min before hot deformation. Therefore, the grain structure evolution and deformation behavior of Al–Mg 5xxx alloys under HSBF-relevant conditions remain mostly unknown.

Given that the process time is a key parameter in HSBF, understanding how the microstructure of the alloy evolves with time at the desired forming temperature will provide valuable insights into both the optimal annealing conditions required to achieve the ideal grain structure and the deformation behavior of Al–Mg 5xxx alloys for HSBF. This study investigated the influence of annealing time on the grain structure evolution of two commercial Al–Mg 5xxx alloys used in HSBF. The study subsequently examined the superplastic performance of these alloys under conditions that closely simulated HSBF. Specifically, the alloys were subjected to rapid annealing and deformed at strain rates similar to those used in crash forming (1 s^{-1}) and superplastic forming (0.001 and 0.01 s^{-1}). A better understanding of the microstructural evolution and deformation behavior of Al–Mg 5xxx

alloys under such conditions can be leveraged to fully exploit the potential of HSBF in the automobile industry.

3.2 Material and methods

Two commercial Al–Mg 5xxx alloys utilized for the HSBF process in the form of cold-rolled thin sheets (H18-temper) were supplied by Verbom Inc. (Valcourt, QC, Canada). The chemical compositions of the two alloys were analyzed using an Agilent 7800 inductively coupled plasma mass spectrometer (ICP-MS) from Canada. A total of 200 mg of the alloy samples was digested in a 2% HNO3 and 1% HCl acid solution using a microwave (CEM mars 6). The prepared solution was introduced into the ICP-MS for elemental analysis. The concentration of the minor elements was previously calibrated using an internal calibration curve, and the accuracy was verified at the beginning and end of the sequence using a standard prepared from a certified reference solution.

Samples of the cold-rolled sheets of the two alloys were cut along the rolling direction to examine the as-received microstructure. To observe the grain structure, the samples were mechanically polished and electro-etched in Barker's reagent (3 vol.% HBF4 solution) at 17 V for 90 s. Subsequently, the grain structure was examined using optical microscopy under polarized light. The intermetallic phases (IMCs) in the rolled sheets were analyzed using a scanning electron microscope (SEM, JSM-6480LV, Tokyo, Japan) equipped with an energy-dispersive X-ray spectrometer (EDS). The area fraction of the IMCs was quantified by evaluating 50 optical light micrographs using ImageJ software V1.53t.

Additionally, a transmission electron microscope (TEM, JEM-2100, Japan) operating at 200 kV was used to observe the distribution of the dispersoids. The TEM images along the

[001]Al zone axis and the dispersoid attributes were quantified using ImageJ software. The number density (N_d) of the dispersoids was evaluated using Equation (1) [25].

$$N_d = \frac{N}{A(D+t)} \quad (1)$$

Here, N is the number of dispersoids, A is the total area, D is the equivalent diameter of the dispersoids, and t is the thickness of the TEM foil [26]. More than 200 particles were analyzed, and the average was reported.

To study the effect of the annealing time, sheet samples measuring 20 mm × 10 mm with a thickness of 2 mm were isothermally heated in an electric-resistant furnace for 2, 4, 10, 15, and 30 min, following a procedure similar to that used by McNelley et al. [27]. The furnace was maintained at 520 °C, and the samples were directly placed in the preheated furnace with a thermocouple attached to them. The annealing time was measured from the moment when the temperature of the samples reached 520 °C. Owing to their small dimensions, the samples' preheating time for reaching 520 °C was approximately 3 min. After annealing, the samples were removed from the furnace and cooled in air. The grain structure of the annealed samples was examined by optical microscopy under polarized light after electro-etching and electron backscattered diffraction (EBSD). The EBSD analysis was conducted with a step size of 1 μm in a sample area of 300 μm × 250 μm. The average grain size was determined from the polarized light micrographs using the linear intercept method in accordance with ASTM E112-12 [28].

To investigate the superplastic behavior of the alloys, high-temperature tensile testing was conducted using a Gleeble 3800, Dynamic Systems Inc. (DSI), New York, USA,

thermomechanical simulation system, following the test procedure outlined in Figure 3.1a. Tensile samples were cut and machined along the rolling direction (Figure 3.1b). During the testing, the samples were first heated rapidly with a heating rate of 2.77 °C/s to 520 °C and annealed for 4 min before undergoing tensile deformation. Tensile tests were performed at three strain rates of 0.001, 0.01, and 1 s^{-1}. Unlike the conventional isothermal furnace system typically used for hot tensile tests, the Gleeble 3800 unit employs electroresistance heating that allows the rapid heating of samples to reach the target deformation temperature [29,30], similar to the HSBF operation. The ASTM E21 standard [31] for superplastic tests requires a sample holding time of more than 20 min to establish thermal equilibrium in a conventional isothermal furnace [32,33]. The slow heating rate and prolonged holding time render the conventional isothermal heating approach unsuitable for simulating the HSBF process, which involves rapid microstructural changes during high-temperature annealing.

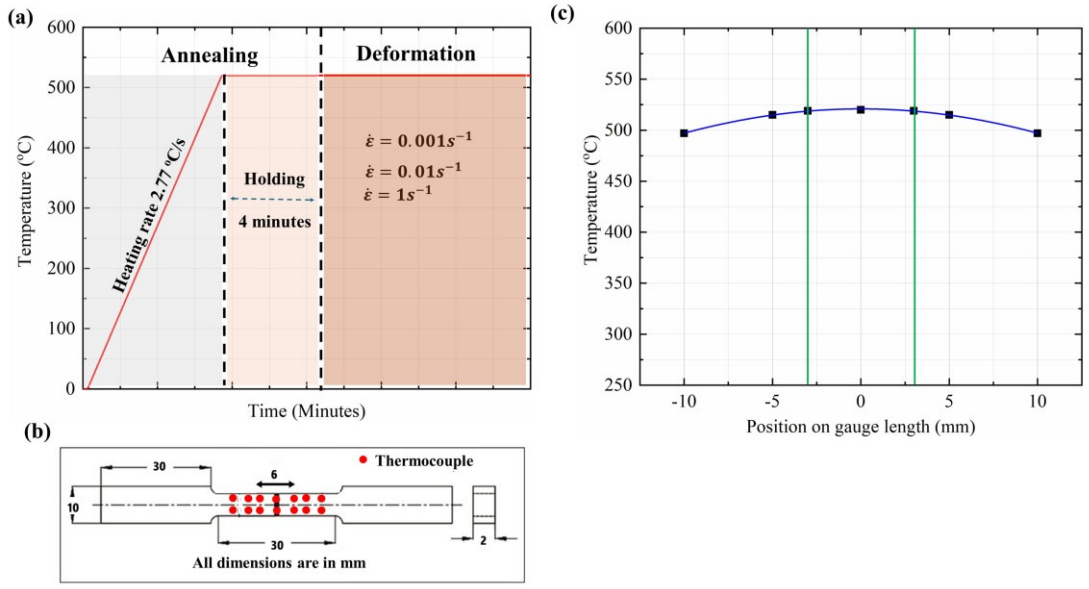


Figure 3.1 Experimental procedure and condition for high-temperature tensile testing. (a) Gleeble tensile test procedure showing the annealing stage and deformation at three different

strain rates ($\dot{\varepsilon}$). (b) Dimensions of tensile samples with red dots indicating the surface attached thermocouples during the temperature distribution study. (c) Temperature distribution profile along the gauge length. The green lines show the 6 mm uniform temperature zone in the center region of the sample.

Temperature distribution and control are critical during Gleeble high-temperature tensile testing, because a parabolic temperature distribution is produced along the sample length. During the primary annealing tests, several K-type thermocouples were spot-welded on the sample surface at different positions (0, ± 3 mm, ± 5 mm, ± 10 mm) (see red dots in Figure 3.1b). This was performed to determine the uniform temperature zone (UTZ) along the gauge length [29,34]. Figure 3.1c shows the temperature distribution profiles at various positions on the sample. The temperature at the center of the sample was 520 °C, while the readings at the ± 3 mm, ± 5 mm, and ± 10 mm positions were 519 °C, 514 °C, and 497 °C, respectively. The temperature varied only 1 °C at the ± 3 mm position; as a result, the uniform temperature zone was identified as the 6 mm center region of the sample, which was chosen as the gauge zone for tensile elongation measurements. During tensile testing, only one thermocouple was spot-welded to the sample center to monitor and control the test temperature. The tensile tests were repeated three times for each condition to ensure reproducibility and consistency.

3.3 Results

3.3.1 Chemical composition and as-received microstructure

Table 3.1 shows the chemical compositions of the two alloys. The main point of differentiation between the two alloys was the Mn content, in which Alloy 1 (Al–4.5Mg–

0.74Mn) contained 0.74 wt.% Mn, whereas Alloy 2 (Al–4.0Mg–1.18Mn) contained 1.18 wt.% Mn.

Table 3.1. Chemical composition of Al-Mg 5xxx alloys studied (wt.%).

Alloys	Mg	Mn	Si	Fe	Cu	Cr	Ti	Zn	Al
Alloy 1 (Al–4.5Mg–0.74Mn)	4.52	0.74	0.4	0.12	0.1	0.01	0.02	0.01	Bal.
Alloy 2 (Al–4.0Mg–1.18Mn)	4.00	1.18	0.4	0.12	0.1	0.01	0.02	0.01	Bal.

Figure 3.2 shows the grain structures of the alloys in the as-received state. It was evident that both alloys exhibited similar deformed grain structures. All the grains were heavily deformed and elongated in the rolling direction, similar to the fibrous grain structure typically observed in cold-rolled AA5038 superplastic sheets [27]. Cold rolling increases the strain energy and number of nucleation sites for the formation of fine and equiaxed grain structures during static recrystallization [35,36].

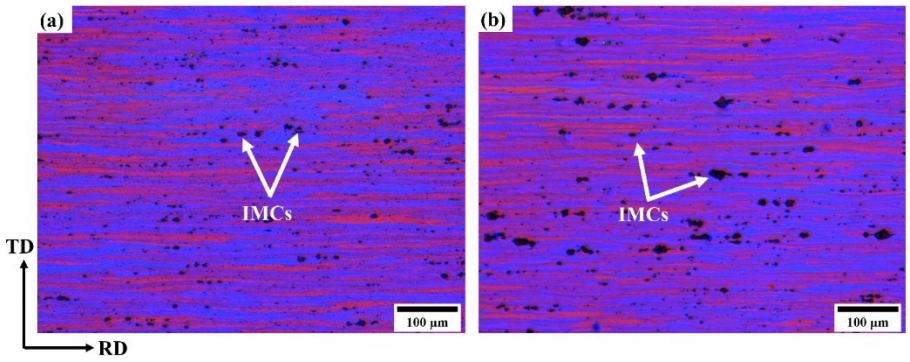


Figure 3.2 Polarized light optical micrographs showing the deformed grain structure; (a) Alloy 1 and (b) Alloy 2 in the as-received state; the black dots indicated by the white arrows show intermetallic phases (IMCs) in the microstructure.

Figure 3.3 shows the intermetallic phases (IMCs) observed in the microstructure. In both alloys (Figure 3.3a,c), the IMCs were broken during the rolling process and randomly distributed in the rolling direction. Two types of IMCs were observed: gray-like large particles and dark small particles. An SEM-EDS analysis identified the gray-like particles as $Al_6(Fe,Mn)$ (Figure 3.3b) and the small dark particles as Mg_2Si (Figure 3.3d). These two IMCs observed in the alloys were consistent with those commonly reported for Al–Mg 5xxx alloys [25,37–39]. As shown in Figure 3.3e, larger quantities of $Al_6(Mn,Fe)$ and Mg_2Si particles were found in Alloy 2 (2.33 % and 0.3 %, respectively) compared to that in Alloy 1 (1.52 % and 0.17 %, respectively).

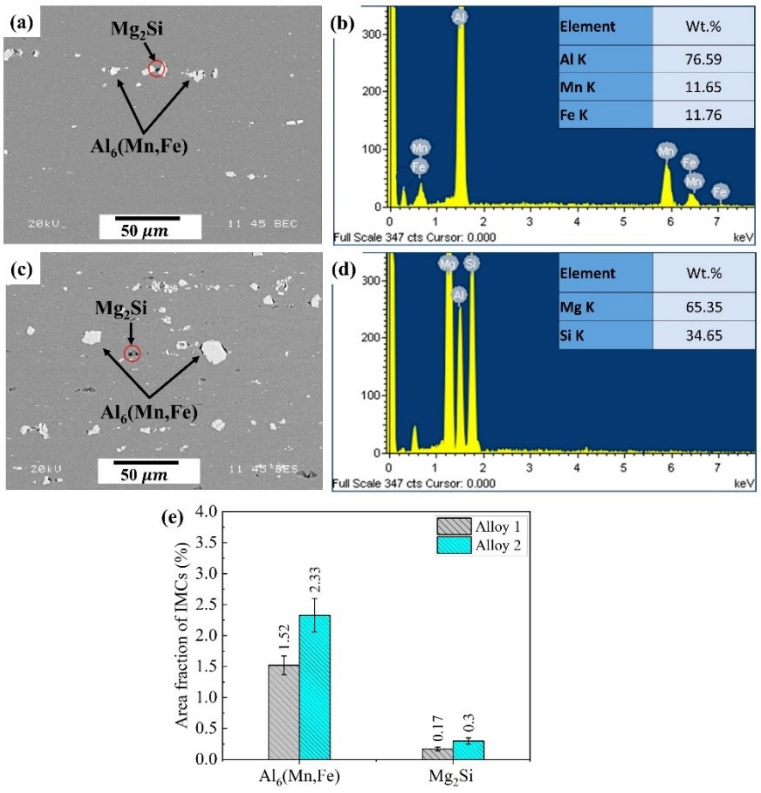


Figure 3.3 SEM images depicting intermetallic phases (IMCs) in (a) Alloy 1 and (c) Alloy 2. SEM-EDS spectra and inserted EDS results showing (b) $Al_6(Mn,Fe)$ and (d) Mg_2Si IMCs in Alloy 1 and Alloy 2. (e) Area fraction diagram of two IMCs.

The large quantity of $Al_6(Mn,Fe)$ IMCs in Alloy 2 was attributed to its high Mn content (1.18 wt.%). Mn has a relatively low solubility in Al; hence, it readily forms $Al_6(Mn,Fe)$ IMCs with Fe during solidification [40]. During cold rolling, heavily deformed zones are usually created around IMC particles (size > 1 μm), which serve as nucleation sites [41] for forming fine recrystallized grain structures during annealing. This phenomenon is known as particle-stimulated nucleation (PSN) [19,25,43] and is widely employed to develop superplastic Al alloys. Although IMCs are crucial to PSN, they may adversely affect superplasticity by promoting cavitation [13,43].

In addition to the relatively large IMCs, submicron-Mn-containing dispersoids were observed in both alloys, as shown in Figure 3.4. These Mn dispersoids exhibited cubic and rod-like morphologies, similar to those reported for Al–Mg 5xxx alloys [44]. The quantitative TEM analysis of the Mn-dispersoid attributes of the two alloys is presented in Table 3.2. It appeared that Alloy 2 had a higher number density (*Nd*) of Mn dispersoids (9.3×10^{-3} μm^{-3}) compared to Alloy 1 (4×10^{-3} μm^{-3}) .The average equivalent diameter (*d*) of the Mn dispersoids was smaller in Alloy 2 (166 nm) than in Alloy 1 (234 nm).

During solidification, Mn readily forms a supersaturated solid solution, which subsequently decomposes to form Mn dispersoids during homogenization [41,45]. Therefore, the relatively large amount of Mn dispersoids in Alloy 2 could be attributed to its high Mn content. Mn dispersoids are known to efficiently suppress grain growth during recrystallization [41,45,46], thereby promoting the formation of fine recrystallized grain structures, which are critical for superplasticity.

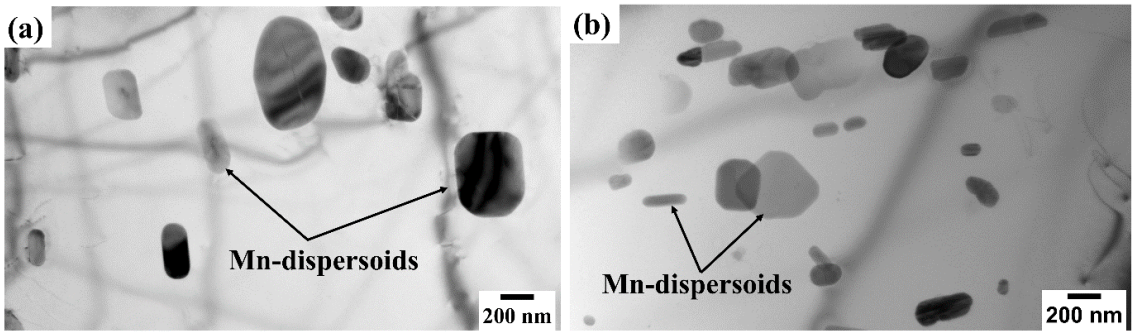


Figure 3.4 Bright-field TEM images showing the distribution of Mn dispersoids in (a) Alloy 1 and (b) Alloy 2. TEM images were taken along the $[001]_{Al}$ zone axis.

Table 3.2 Quantitative TEM analysis of Mn dispersoids in the two alloys.

Alloy	**Mn-Dispersoids**	
	Equivalent diameter, $\bar{d}$ (nm)	*Number density,* $N_d \times 10^{-3}$ (μm^{-3})
Alloy 1	234 ± 36	4 ± 0.3
Alloy 2	166 ± 17	9.3 ± 1.4

3.3.2 Grain structure evolution during annealing

Figures 3.5 and 3.6 show the evolution of the grain structure for the two alloys during annealing at 520 °C for various durations: 2, 4, 10, 15, and 30 min. The fibrous grain structure present in the as-received state (Figure 3.2) was entirely transformed into an equiaxed recrystallized grain structure after annealing.

Notably, complete recrystallization occurred in both the alloys after only 2 min of annealing. This rapid recrystallization could be attributed to the high annealing temperature (520 °C) and significant strain energy imparted by the cold rolling (H18 temper) of the alloys. Temperature and strain energy profoundly affect recrystallization rates [36]. In the HSBF, it is crucial that a fine and equiaxed grain structure is formed quickly prior to deformation

during annealing. The rapid recrystallization behavior suggested that both alloys met the fast-annealing requirements of HSBF.

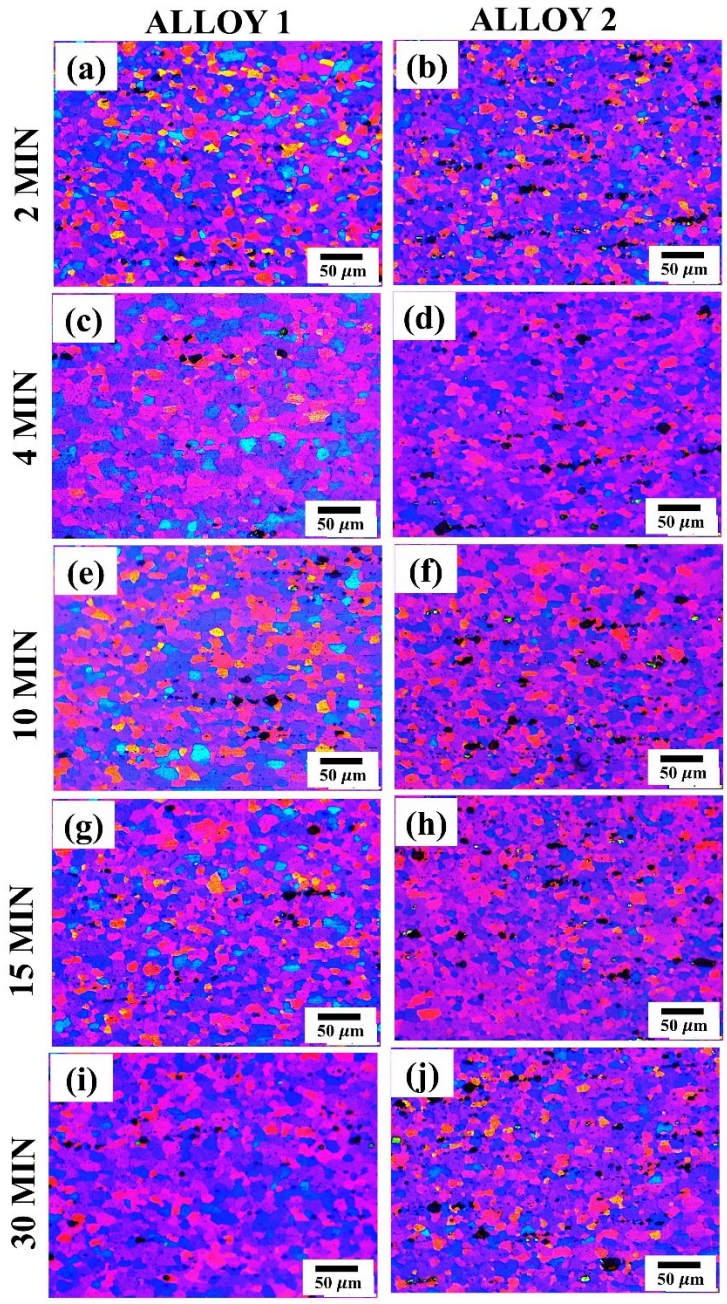


Figure 3.5 Polarized light optical micrographs illustrating the evolution of grain structure in Alloy 1 (a,c,e,g,i) and Alloy 2 (b,d,f,h,j) after annealing at 520 °C for 2, 4, 10, 15, and 30 min, respectively.

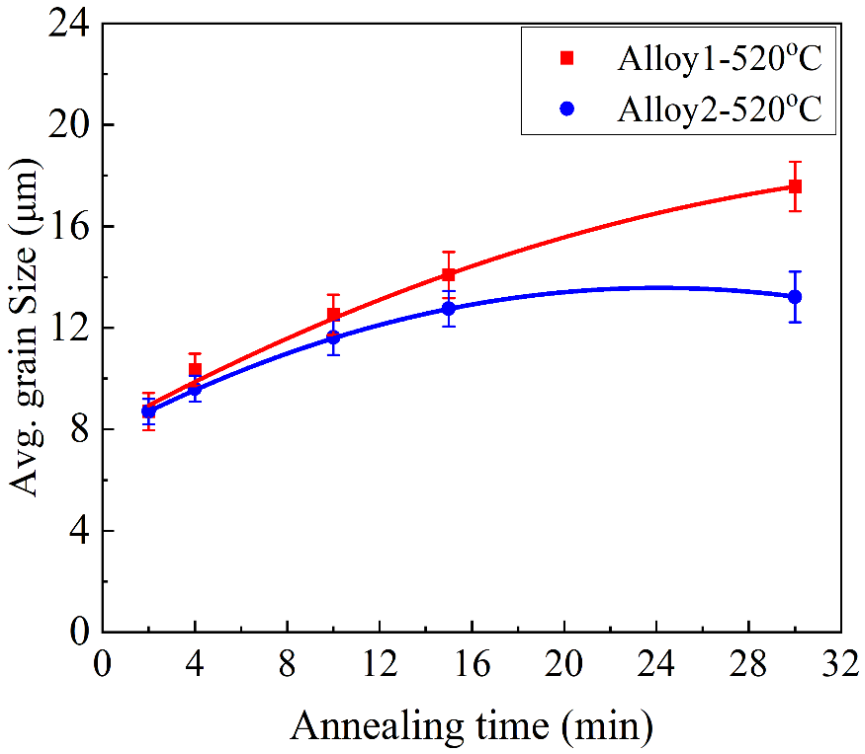


Figure 3.6 Grain size variation with annealing time at 520 °C for Alloy 1 and Alloy 2.

As shown in Figure 3.6, the average grain sizes of both the alloys increased with an increasing annealing time. Both alloys displayed the same grain size of 8.7 ± 0.5 µm after 2 min of annealing. However, over time, the grain size increased significantly to 17.5 ± 1 µm and 13.2 ± 1 µm for Alloy 1 and Alloy 2, respectively, after 30 min of annealing. A clear correlation between grain growth and annealing time is shown in Figure 3.6. However, grain growth was significantly slower in Alloy 2 than in Alloy 1. Thus, Alloy 1 exhibited a higher grain growth tendency than Alloy 2 after prolonged thermal exposure. Grain growth usually occurs after recrystallization to minimize the total grain boundary energy [35] and becomes more rapid at elevated temperatures owing to enhanced diffusion.

For a better understanding of the grain structure evolution during annealing, samples annealed for 4, 10, and 15 min were selected for the EBSD studies. The results are presented

in Figures 3.7 and 3.8. The EBSD studies confirmed the formation of a fine recrystallized microstructure in both alloys after annealing. The inverse pole figures in Figure 3.7 clearly demonstrate that the grains were equiaxed and randomly oriented in both alloys after recrystallization.

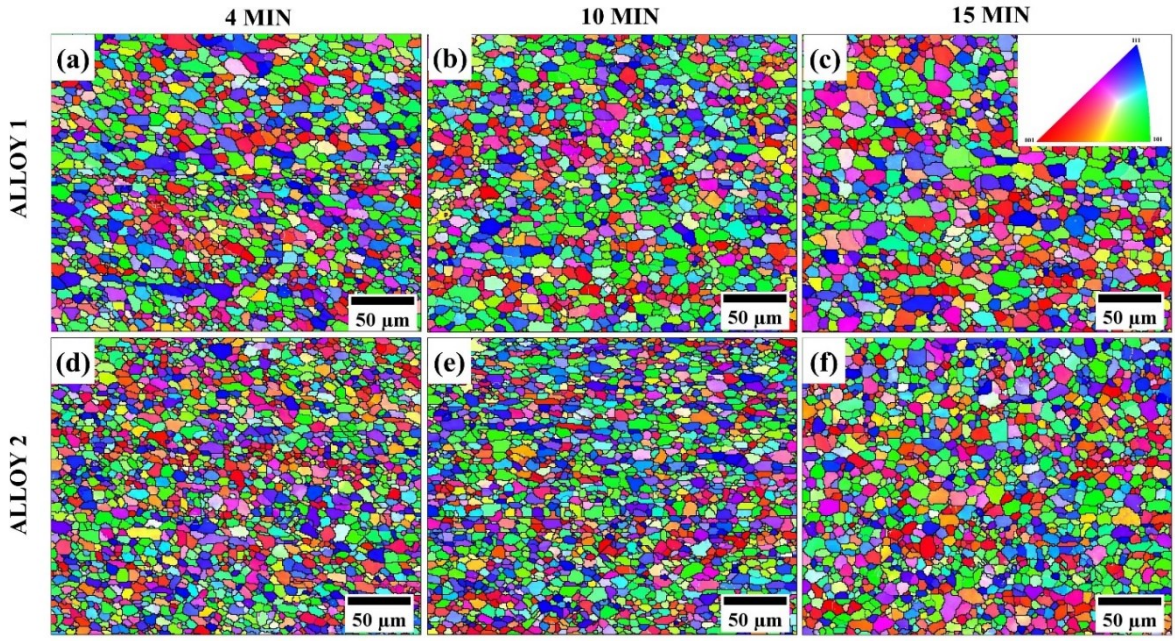


Figure 3.7 Inverse pole figures of EBSD showing grain structure in Alloy 1 (a–c) and Alloy 2 (d–f) after annealing for 4, 10, and 15 min at 520 °C.

Figure 3.8 shows the changes in the grain size distributions of both alloys with increasing annealing times. The data show that the recrystallized grains were finer in Alloy 2 than in Alloy 1. The fraction of grains with a size of less than 10 µm (f_{SG}) was higher in Alloy 2 (87 %) compared to Alloy 1 (80 %) after 4 min of annealing. The fraction of small grains (f_{SG}) decreased with an increasing annealing time. It was confirmed that Alloy 1 exhibited fast grain growth, with f_{SG} decreasing by 10 % compared to a 7 % decrease in Alloy 2 after 15 min of annealing.

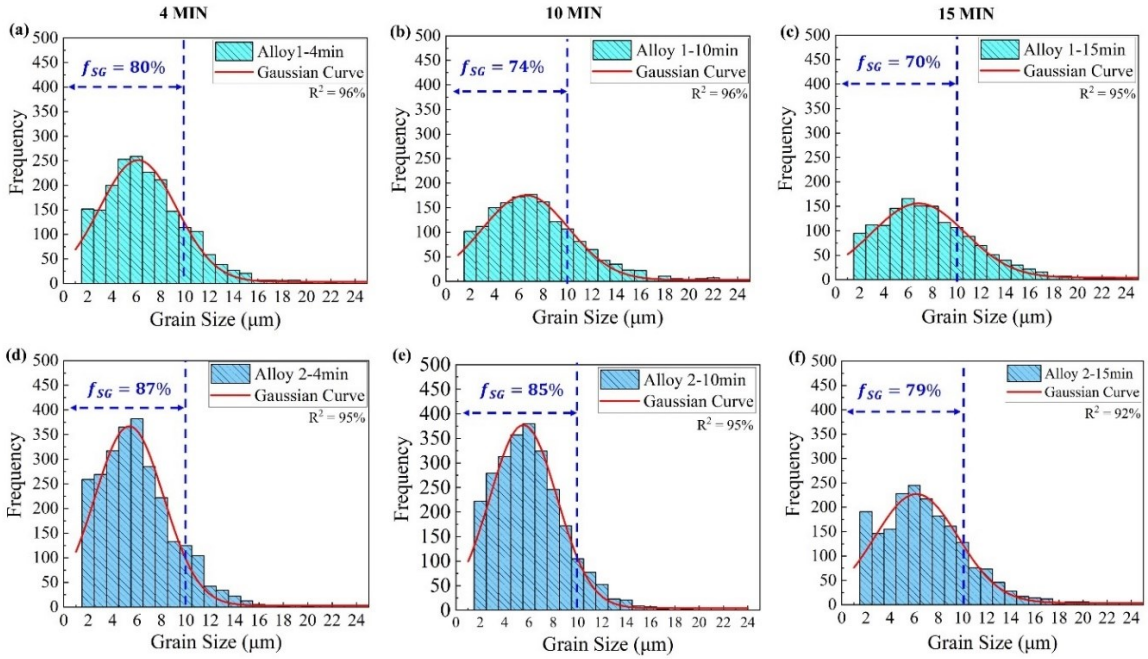


Figure 3.8 Grain size distribution in Alloy 1 (a–c) and Alloy 2 (d–f) after annealing for 4,10, and 15 min at 520 °C obtained by EBSD analysis. The blue dash line indicates the fractions of grains with a size less than 10 μm f_{SG} in the annealed samples.

Notably, Alloy 2 displayed high resistance to grain growth within 15 min of annealing. The EBSD studies confirmed the optical microscopy findings shown in Figure 3.5 Both observations indicated that Alloy 2 contained a finer and more thermally stable grain structure than Alloy 1. It is well known that a fine and stable grain structure is a key indicator of superplasticity [4,20,24,42], suggesting that Alloy 2 should exhibit a better superplastic response than Alloy 1. The results in Figures 3.7 and 3.8 show that both alloys developed a large number of small grains after four minutes of annealing, suggesting that the optimal annealing time for achieving the desirable grain structure for superplasticity in both alloys was within four minutes. Subsequently, the superplastic response of the alloys was investigated after a four-minute annealing period.

3.3.3 Tensile properties

The engineering stress–strain curves obtained from the tensile tests at different strain rates (0.001, 0.01, and 1 s^{-1}) and a temperature of 520 °C are presented in Figure 3.9. The samples deformed at 0.001 s^{-1} exhibited a steady-state flow region (Figure 3.9a), with Alloy 1 and Alloy 2 displaying yield strengths (YS) of 12.6 MPa and 10.7 MPa, respectively. Similarly, Figure 9b shows that at a strain rate of 0.01 s^{-1}, both alloys initially experienced hardening, and the YS increased to 27.0 MPa for Alloy 1 and 23.4 MPa for Alloy 2. Figure 3.9c shows that the YS reached 70.2 MPa and 67.5 MPa for Alloy 1 and Alloy 2, respectively, at a strain rate of 1 s^{-1}. Deformation at a strain rate of 1 s^{-1} was characterized with significant hardening and followed by softening. In general, the YS increased with increasing strain rates, which can be attributed to the strain-hardening effect at the onset of deformation [47,48].

Figure 3.10a presents the tensile elongation of both alloys at different strain rates (0.001, 0.01, and 1 s^{-1}) and a temperature of 520 °C. The highest elongation was observed at the lowest strain rate (0.001 s^{-1}), with Alloy 1 displaying a 138 % elongation compared to 170 % for Alloy 2. At a strain rate of 0.01 s^{-1}, the tensile elongation declined to 135 % and 164 % in Alloy 1 and Alloy 2, respectively. When further increasing the strain rate to 1 s^{-1}, both alloys exhibited comparable elongations of 132 % and 135 % in Alloy 1 and Alloy 2, respectively. Thus, the tensile elongation decreased in both alloys with increasing strain rates. However, Alloy 2 exhibited a larger elongation than Alloy 1 at slower strain rates.

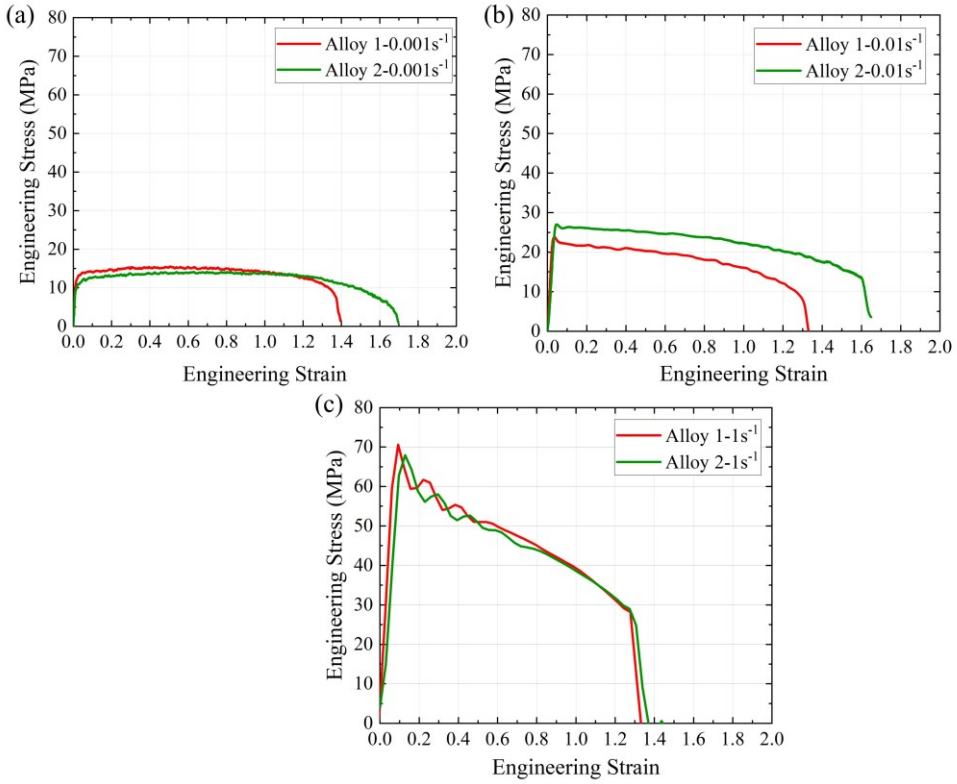


Figure 3.9 Engineering stress–strain curves of the alloys at different strain rates: (a) 0.001 s^{-1}, (b) 0.01 s^{-1}, and (c) 1 s^{-1}.

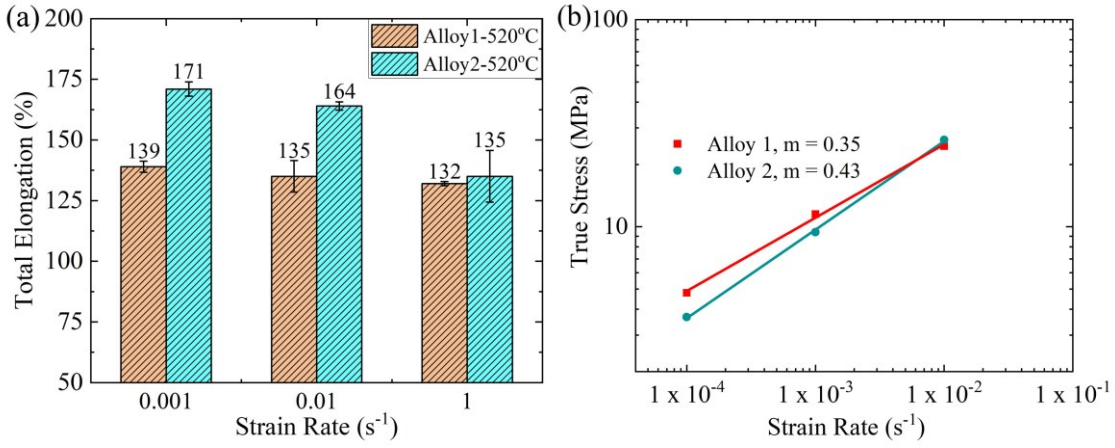


Figure 3.10 (a) Tensile elongation of the alloys at different strain rates and (b) flow stress as a function of the strain rate in the logarithmic scale, from which the strain rate sensitivity (m-value) is evaluated.

Figure 10b shows the dependence of the flow stress on the strain rate for both alloys. It is evident that the flow stress increased with the strain rate. It should be mentioned that some tests were carried out at a very low strain rate of 0.0001 s^{-1} to measure the strain rate sensitivity. The slopes of the lines represent the strain rate sensitivity index (m-value), defined by the following equation [4]:

$$m - value = \frac{\partial ln\sigma}{\partial ln\dot{\varepsilon}} \qquad (2)$$

where σ is the flow stress and $\dot{\varepsilon}$ is the strain rate.

Notably, Alloy 2 displayed a higher m value (0.43) than Alloy 1 (0.35), which could be attributed to its fine-grained structure (Figures 3.6 and 3.7). In fact, both alloys had m values >0.3, which signified the superplastic nature of deformation [4]. The m-value measures the anti-necking response during superplastic deformation [49] and increases with a finer grain structure [50]. The activation of grain boundary sliding depends on fine grain structure (<10 μm) and high strain rate sensitivity (m-value > 0.3) [16,51]. In brief, Alloy 2 exhibited superior superplastic performance in comparison to Alloy 1 at low strain rates (0.001 and 0.01 s^{-1}), which could be attributed to its fine, stable grain structure and high strain rate sensitivity.

3.4 Discussion

3.4.1 Effect annealing time on grain structure evolution

As shown in Figure 3.2, the as-received alloys exhibited fibrous and deformed microstructures that rapidly recrystallized upon annealing for 2 min (Figure 3.5). This rapid

recrystallization was mainly due to the (i) high strain energy from cold working, (ii) high annealing temperature, and (iii) intermetallic phases and dispersoids within the microstructure, which provided favorable nucleation sites for the formation of new grains during recrystallization. Cold working increases the strain energy and creates heavily deformed zones around the intermetallic phases and dispersoids [35,36], both of which accelerate recrystallization. Additionally, a high annealing temperature (520 °C) reduces the solute drag effect, which often slows down recrystallization in Al–Mg alloys [52], thereby enhancing the recovery process for rapid recrystallization. The rapid recrystallization ability of both alloys resulted in the formation of fine and equiaxed grains during the fast annealing of HSBF.

As shown in Figure 3.6, both alloys exhibited grain growth with increasing annealing time. This change in the grain structure with increasing annealing time was further confirmed by an EBSD analysis, as shown in Figures 3.7 and 3.8. Grain growth is a phenomenon that naturally follows recrystallization and can be modeled using the Sellars–Whiteman equation (Equation (3)) [53]:

$$D^b = {D_o}^b + At_q \, exp^{(\frac{-Q}{RT})} \quad (3)$$

where D is the final grain size; D_o is the initial grain size (or fully recrystallized grain size); t_q is the holding time (or time after complete recrystallization); Q is the activation energy for grain growth; T is the temperature; R is the gas constant; and b and A are constants that depend on the chemical composition of the alloy.

From Equation (3), the grain growth depends on the holding time, annealing temperature, and alloy composition. Therefore, for an alloy undergoing isothermal annealing,

the holding time significantly influences the final grain size. As observed in this study, the grain sizes of both alloys increased with increasing annealing times, which was consistent with the Sellars–Whiteman grain growth model. Grain growth occurs during recrystallization to minimize the total grain boundary energy [35,36,48]. In this process, large grains increase in size, whereas smaller and thermodynamically less stable grains are eliminated. This phenomenon further explains the observed changes in the grain size distribution and fraction of fine grains (<10 μm) as the annealing time increased (Figure 3.8)

The two alloys exhibited different degrees of grain growth resistance owing to their different Mn contents. Alloy 2, with a higher Mn content, possessed a higher amount of Al_6(Mn,Fe) intermetallic particles (Figure 3.3) and a higher number density of Mn dispersoids (Figure 3.4 and Table 3.2), which resulted in a finer and more thermally stable grain structure than Alloy 1, resulting in a superior resistance to grain coarsening compared to Alloy 1 (Figures 3.7 and 3.8). After cold rolling, small Al_6(Mn,Fe) intermetallic particles and submicron-sized Mn dispersoids are known to efficiently impede grain growth by pinning high-angle grain boundaries via Zener pinning mechanisms [4,36,42,45,46,54]. However, the pinning effectiveness can be partially reduced because the Mn dispersoids can coarsen at high annealing temperatures [36,48], which could explain the excessive grain growth observed in the alloys after 30 min of annealing.

These results demonstrated that maintaining a short annealing time (<10 min) is effective for producing a fine and stable grain structure suitable for superplasticity in the studied alloys. In contrast, reducing the size and increasing the number density of both the Al_6(Mn,Fe) intermetallic particles and Mn dispersoids can further improve the grain growth resistance of the recrystallized grain structure

3.4.2 Superplastic behavior

Both alloys exhibited distinct superplastic performances at low strain rates (0.001 and 0.01 s^{-1}). Notably, Alloy 2 displayed a superior superplastic response compared to Alloy 1, showing higher tensile elongation values relative to Alloy 1 (170 % vs. 138 % at 0.001 s^{-1} and 164 % vs. 134 % at 0.01 s^{-1}). This enhanced superplastic performance can be attributed to fine and thermally stable grain structures. In general, a fine and stable grain structure (<10 μm) is required for superplasticity [16,18–22]. Figure 3.8 reveals that after 4 min of annealing, Alloy 2 possessed a higher fraction of small grains <10 μm in contrast to Alloy 1 (86 % vs. 80 %). This suggests that Alloy 2 potentially developed finer grains during the fast-annealing stage before tensile deformation. Moreover, the analysis of the grain structure evolution (Figures 3.7 and 3.8) indicated that Alloy 2 exhibited greater resistance to grain growth, which stabilized its fine grain structure more effectively. Conversely, Alloy 1 showed a weaker resistance to grain growth despite its fine initial grain structure, resulting in a weaker superplastic response. Grain growth is a key factor constraining the superplastic performance of Al–Mg 5xxx alloys [6,42,55]. Thus, although an initial fine grain structure is necessary before deformation, the thermal stability of the grains is equally crucial for enhancing the superplastic response, particularly during deformation at low strain rates, which involves prolonged thermal exposure. This observation aligns with the previous findings reported by Nieh et al. [6], in which an Al–Mg alloy exhibited a low superplastic response despite its initial nanocrystalline structure with a grain size of ~200 nm.

It can be observed in Figure 3.10 that both alloys exhibited comparable tensile elongation at a high strain rate (1 s^{-1}): 132 % for Alloy 1 and 135 % for Alloy 2. The deformation at a high strain rate was rapid, limiting the time for dislocation motion, which

resulted in a high YS (strain hardening), and hence, a weak tensile elongation. Additionally, the short exposure time at high deformation temperatures (520 °C) could limit the potential for grain growth in both alloys. Therefore, the tensile elongation of the alloys at high strain rates depends primarily on the initial grain structure.

HSBF is a hybrid superplastic forming process that combines crash and gas blow forming [12]. Most of the deformation of large aluminum sheets occurs during crash forming at high strain rates, whereas the final intricate details of the forming component are formed at relatively low strain rates [17] by gas blow forming. Owing to the similar tensile elongations at a high strain rate, Alloys 1 and 2 may display comparable forming performances during the crash forming of the HSBF. However, during the subsequent blow forming at low strain rates, Alloy 2 is expected to exhibit superior forming performance with less defect susceptibility.

3.5 Conclusions

1. The as-received Al-Mg 5xxx cold-rolled alloys exhibited a fibrous grain structure that quickly recrystallized after two minutes of annealing at 520 °C. This rapid recrystallization behavior of the alloys was attributed to the high annealing temperature and significant strain energy of cold working. Notably, the small sample size enabled uniform temperature distribution, allowing for the quick attainment of recrystallization conditions.
2. The microstructural analysis revealed that the recrystallized grains during high-temperature annealing were finer in Alloy 2 (Al–4.0Mg–1.18Mn) than in Alloy 1 (Al–4.5Mg–0.74Mn). After 4 min of annealing, Alloy 2 possessed a higher fraction of small grains (<10 μm) of 87 % compared to 80 % of Alloy 1. While both alloys

experienced grain growth with increasing annealing time, Alloy 2 demonstrated better resistance to grain growth owing to the presence of a higher amount of $Al_6(Mn,Fe)$ intermetallic particles and a higher number density of Mn dispersoids, which provided effective Zener pinning.

3. Both alloys exhibited distinct superplastic performances during deformation, which were largely influenced by their respective recrystallized grain structures. Alloy 2, with its fine and stable grain structure, demonstrated superior tensile elongation compared to Alloy 1 at low strain rates of 0.001 s^{-1} and 0 01 s^{-1}. However, both alloys displayed comparable tensile elongation at a strain rate of 1 s^{-1}.
4. These findings suggest that optimizing the annealing time could effectively develop a fine and equiaxed grain structure in Al–Mg 5xxx alloys, making them suitable for HSBF applications. However, reducing the size and increasing the number density of both intermetallic particles and Mn dispersoids are crucial for improving the grain growth resistance of recrystallized grains to further enhance the forming performance during HSBF.

References

1. Miller, W.S.; Zhuang, L.; Bottema, J.; Wittebrood, A.J.; De Smet, P.; Haszler, A.; Vieregge, A. Recent development in aluminium alloys for the automotive industry. *Mater. Sci. Eng. A* 2000, *280*, 37–49. https://doi.org/10.1016/S0921-5093(99)00653-X.

2. Jeon, J.; Lee, S.; Kyeong, J.; Shin, S.; Kang, H. Effect of geometrical parameters of microscale particles on particle-stimulated nucleation and recrystallization texture of Al-Si-Mg-Cu-based alloy sheets. *Materials* 2022, *15*, 7924. https://doi.org/10.3390/ma15227924.

3. Grimes, R. Superplastic forming of aluminium alloys. In *Superplastic Forming of Advanced Metallic Materials*; Woodhead Publishing Limited: Cambridge, UK, 2011; pp. 247–271. https://doi.org/10.1533/9780857092779.3.247.

4. Kishchik, A.A.; Mikhaylovskaya, A.V.; Kotov, A.D.; Rofman, O.V.; Portnoy, V.K. Al-Mg-Fe-Ni based alloy for high strain rate superplastic forming. *Mater. Sci. Eng. A* 2018, *718*, 190–197. https://doi.org/10.1016/j.msea.2018.01.099.

5. Ebenberger, P.; Uggowitzer, P.J.; Gerold, B.; Pogatscher, S. Effect of compositional and processing variations in new 5182-type AlMgMn alloys on mechanical properties and deformation surface quality. *Materials* 2019, *12*, 1645. https://doi.org/10.3390/ma12101645.

6. Nieh, T.G.; Hsiung, L.M.; Wadsworth, J.; Kaibyshev, R. High strain rate superplasticity in a continuously recrystallized Al–6%Mg–0.3%Sc alloy. *Acta Mater.* 1998, *46*, 2789–2800. https://doi.org/10.1016/S1359-6454(97)00452-7.

7. Luo, Y.; Luckey, S.G.; Friedman, P.A.; Peng, Y. Development of an advanced superplastic forming process utilizing a mechanical pre-forming operation. *Int. J. Mach. Tools Manuf.* 2008, *48*, 1509–1518. https://doi.org/10.1016/j.ijmachtools.2007.12.010.

8. Liu, J.; Tan, M.J.; Aue-U-Lan, Y.; Jarfors, A.E.W.; Fong, K.S.; Castagne, S. Superplastic-like forming of non-superplastic AA5083 combined with mechanical pre-forming. *Int. J. Adv. Manuf. Technol.* 2011, *52*, 123–129. https://doi.org/10.1007/s00170-010-2729-9.

9. Bhatta, L.; Pesin, A.; Zhilyaev, A.P.; Tandon, P.; Kong, C.; Yu, H. Recent development of superplasticity in aluminum alloys: A review. *Metals* 2020, *10*, 77. https://doi.org/10.3390/met10010077.

10. Barnes, A.J. Superplastic aluminum forming—Expanding its techno-economic niche. *Mater. Sci. Forum* 1999, *304–306*, 785–796. https://doi.org/10.4028/www.scientific.net/MSF.304-306.785.

11. Kawasaki, M.; Langdon, T.G. Superplasticity in ultrafine-grained materials. *Rev. Adv. Mater. Sci.* 2018, *54*, 46–55. https://doi.org/10.1515/rams-2018-0019.

12. Majidi, O.; Jahazi, M.; Bombardier, N. Finite element simulation of high-speed blow forming of an automotive component. *Metals* 2018, *8*, 901. https://doi.org/10.3390/met8110901.

13. Liu, F.C.; Ma, Z.Y. Achieving high strain rate superplasticity in cast 7075Al alloy via friction stir processing. *J. Mater. Sci.* 2009, *44*, 2647–2655. https://doi.org/10.1007/s10853-009-3346-6.

14. Giuliano, G. *Superplastic Forming of Advanced Metallic Materials*; Woodhead Publishing Limited: Cambridge, UK, 2011. https://doi.org/10.1533/9780857092779.

15. Duan, Y.; Xu, G.; Zhou, L.; Xiao, D.; Deng, Y.; Yin, Z.; Peng, B.; Pan, Q.; Wang, Y.; Lu, L. Achieving high superplasticity of a traditional thermal-mechanical processed non-superplastic Al-Zn-Mg alloy sheet by low Sc additions. *J. Alloys Compd.* 2015, *638*, 364–373. https://doi.org/10.1016/j.jallcom.2015.03.090.

16. Yakovtseva, O.A.; Kishchik, A.A.; Cheverikin, V.V.; Kotov, A.D.; Mikhaylovskaya, A.V. The mechanisms of the high-strain-rate superplastic deformation of Al-Mg-based alloy. *Mater. Lett.* 2022, *325*, 132883. https://doi.org/10.1016/j.matlet.2022.132883.

17. Prasannavenkatesan, R.; Parker, M.; Laplante, Y.; Bombardier, N.; Rush, B.; Li, S. High speed blow forming processes. U.S. Patent US20170087617A1, 30 March 2017.

18. Kishchik, A.A.; Mikhaylovskaya, A.V.; Levchenko, V.S.; Portnoy, V.K. Formation of microstructure and the superplasticity of Al–Mg-based alloys. *Phys. Met. Metallogr.* 2017, *118*, 96–103. https://doi.org/10.1134/S0031918X16120085.

19. Yakovtseva, O.A.; Mikhaylovskaya, A.V.; Mochugovskiy, A.G.; Cheverikin, V.V.; Portnoy, V.K. Superplastic deformation mechanisms in high magnesium-containing aluminum alloy. *Mater. Sci. Forum* 2016, *838–839*, 66–71. https://doi.org/10.4028/www.scientific.net/MSF.838-839.66.

20. Mikhaylovskaya, A.V.; Yakovtseva, O.A.; Golovin, I.S.; Pozdniakov, A.V.; Portnoy, V.K. Superplastic deformation mechanisms in fine-grained Al-Mg based alloys. *Mater. Sci. Eng. A* 2015, *627*, 31–41. https://doi.org/10.1016/j.msea.2014.12.099.

21. Kotov, A.D.; Mikhaylovskaya, A.V.; Kishchik, M.S.; Tsarkov, A.A.; Aksenov, S.A.; Portnoy, V.K. Superplasticity of high-strength Al-based alloys produced by thermomechanical treatment. *J. Alloys Compd.* 2016, *688*, 336–344. https://doi.org/10.1016/j.jallcom.2016.07.045.

22. Kweitsu, E.K.; Sarkar, D.K.; Chen, X.G. A short review on superplasticity of aluminum alloys. *Eng. Proc.* 2023, *43*, 43. https://doi.org/10.3390/engproc2023043043.

23. Portnoy, V.K.; Rylov, D.S.; Levchenko, V.S.; Mikhaylovskaya, A.V. The influence of chromium on the structure and superplasticity of Al–Mg–Mn alloys. *J. Alloys Compd.* 2013, *581*, 313–317. https://doi.org/10.1016/j.jallcom.2013.07.075.

24. Pérez-Prado, M.T.; González-Doncel, G.; Ruano, O.A.; McNelley, T.R. Texture analysis of the transition from slip to grain boundary sliding in a discontinuously recrystallized superplastic aluminum alloy. *Acta Mater.* 2001, *49*, 2259–2268. https://doi.org/10.1016/S1359-6454(01)00128-8.

25. Algendy, A.Y.; Liu, K.; Rometsch, P.; Parson, N.; Chen, X.G. Effects of AlMn dispersoids and Al_3(Sc,Zr) precipitates on the microstructure and ambient/elevated-

temperature mechanical properties of hot-rolled AA5083 alloys. *Mater. Sci. Eng. A* 2022, *855*, 143950. https://doi.org/10.1016/j.msea.2022.143950.

26. Allen, S.M. Foil thickness measurements from convergent-beam diffraction patterns. *Philos. Mag. A* 1981, *43*, 325–335. https://doi.org/10.1080/01418618108239412.

27. McNelley, T.R.; Oh-Ishi, K.; Zhilyaev, A.P.; Swaminathan, S.; Krajewski, P.E.; Taleff, E.M. Characteristics of the transition from grain-boundary sliding to solute drag creep in superplastic AA5083. *Metall. Mater. Trans. A* 2008, *39*, 50–64. https://doi.org/10.1007/s11661-007-9401-5.

28. ASTM E112-12. *Standard Test Methods for Determining Average Grain Size*; ASTM International: West Conshohocken, PA, USA, 2012.

29. Rakhmonov, J.; Qassem, M.; Larouche, D.; Liu, K.; Javidani, M.; Colbert, J.; Chen, X.G. A new approach to determine tensile stress-strain evolution in semi-solid state at near-solidus temperature of aluminum alloys. *Metals* 2021, *11*, 396. https://doi.org/10.3390/met11030396.

30. Zhao, Y.; Li, L.; Lu, Z.; Teng, G.; Liu, S.; Hu, Z.; He, A. The effect of annealing temperature on the recrystallization and mechanical properties of severe plastic deformed commercial pure aluminium during ultra-fast annealing. *Mater. Res. Express* 2021, *8*, 046515. https://doi.org/10.1088/2053-1591/abf3e3.

31. ASTM E21. *Standard Test Methods for Elevated Temperature Tension Tests of Metallic Materials*; ASTM International: West Conshohocken, PA, USA.

32. Abu-Farha, F.; Curtis, R. On the standard test methods for evaluating the tensile properties of superplastic sheets. In *Proceedings of the 6th EUROSPF Conference*; Carcassonne, France, 2008.

33. Erie, P.S.; Curtis, R.; London, C. Standards for superplastic forming of metals. In *Superplastic Forming of Advanced Metallic Materials*; Woodhead Publishing Limited: Cambridge, UK, 2011; pp. 34–48. https://doi.org/10.1533/9780857092779.1.34.

34. Li, Y.; Li, S.; Chen, Y.; Han, G. Constitutive parameters identification based on DIC-assisted thermo-mechanical tensile test for hot stamping of boron steel. *J. Mater. Process. Technol.* 2019, *271*, 429–443. https://doi.org/10.1016/j.jmatprotec.2019.04.020.

35. Callister, W.D., Jr.; Rethwisch, D.G. *Materials Science and Engineering: An Introduction*, 10th ed.; John Wiley & Sons, Inc.: New York, NY, USA, 2018; ISBN 9781119405436.

36. Humphreys, F.J.; Rohrer, G.S.; Rollett, A. *Recrystallization and Related Annealing Phenomena*, 3rd ed.; Elsevier Ltd.: Amsterdam, The Netherlands, 2017; ISBN 9780080982694.

37. Algendy, A.Y.; Rometsch, P.; Chen, X.G. Impact of hot rolling temperature on the mechanical properties and microstructural evolution of hot/cold-rolled AA5083 with Sc and Zr microalloying. *Mater. Sci. Eng. A* 2024, *896*, 146275. https://doi.org/10.1016/j.msea.2024.146275.

38. Engler, O.; Miller-Jupp, S. Control of second-phase particles in the Al-Mg-Mn alloy AA5083. *J. Alloys Compd.* 2016, *689*, 998–1010. https://doi.org/10.1016/j.jallcom.2016.08.070.

39. Engler, O.; Kuhnke, K.; Hasenclever, J. Development of intermetallic particles during solidification and homogenization of two AA 5xxx series Al-Mg alloys with different Mg contents. *J. Alloys Compd.* 2017, *728*, 669–681. https://doi.org/10.1016/j.jallcom.2017.09.060.

40. Davis, J.R. *Alloying: Understanding the Basics*; ASM International: Materials Park, OH, USA, 2001; ISBN 0-87170-744-6.

41. Grasserbauer, J.; Weißensteiner, I.; Falkinger, G.; Kremmer, T.M.; Uggowitzer, P.J.; Pogatscher, S. Influence of Fe and Mn on the microstructure formation in 5xxx alloys—Part I: Evolution of primary and secondary phases. *Materials* 2021, *14*, 3204. https://doi.org/10.3390/ma14123204.

42. Sotoudeh, K.; Bate, P.S. Diffusion creep and superplasticity in aluminium alloys. *Acta Mater.* 2010, *58*, 1909–1920. https://doi.org/10.1016/j.actamat.2009.11.034.

43. Jin, H.; Gerlich, A.P. Effects of intermetallic particles on cavitation during superplastic forming of aluminium alloy. *Mater. Sci. Technol.* 2019, *35*, 1428–1435. https://doi.org/10.1080/02670836.2019.1627498.

44. Algendy, A.Y.; Liu, K.; Chen, X.G. Evolution of dispersoids during multistep heat treatments and their effect on rolling performance in an Al-5%Mg-0.8%Mn alloy. *Mater. Charact.* 2021, *181*, 111487. https://doi.org/10.1016/j.matchar.2021.111487.

45. Liu, K.; Chen, X.G. Development of Al-Mn-Mg 3004 alloy for applications at elevated temperature via dispersoid strengthening. *Mater. Des.* 2015, *84*, 340–350. https://doi.org/10.1016/j.matdes.2015.06.140.

46. Kenyon, M.; Robson, J.; Fellowes, J.; Liang, Z. Effect of dispersoids on the microstructure evolution in Al–Mg–Si alloys. *Adv. Eng. Mater.* 2019, *21*, 1800494. https://doi.org/10.1002/adem.201800494.

47. Jiang, W.; Zhou, J.; Zhou, K.; Mao, Q.; Zhao, Y.; Meng, A.; Li, Z.; Li, J. Coupling effect of temperature and strain rate on mechanical properties and deformation mechanisms of Cr26Mn20Fe20Co20Ni14 high-entropy alloy. *Mater. Sci. Eng. A* 2024, *901*, 146525. https://doi.org/10.1016/j.msea.2024.146525.

48. Verlinden, B.; Driver, J.; Samajdar, I.; Doherty, R.D. *Thermo-Mechanical Processing of Metallic Materials*; Elsevier: Cambridge, UK, 2007; ISBN 9780080544489.

49. Chokshi, A.H. Grain boundary processes in strengthening, weakening, and superplasticity. *Adv. Eng. Mater.* 2020, *22*, 1900748. https://doi.org/10.1002/adem.201900748.

50. Figueiredo, R.B.; Langdon, T.G. Effect of grain size on strength and strain rate sensitivity in metals. *J. Mater. Sci.* 2022, *57*, 5210–5229. https://doi.org/10.1007/s10853-022-06919-0.

51. Jeong, H.T.; Park, H.K.; Kang, H.S.; Kim, W.J. Operation of solute-drag creep in an AlCoCrFeMnNi high-entropy alloy and enhanced hot workability. *J. Alloys Compd.* 2020, *824*, 153829. https://doi.org/10.1016/j.jallcom.2020.153829.

52. Buken, H.; Kozeschnik, E. Modeling static recrystallization in Al-Mg alloys. *Metall. Mater. Trans. A* 2021, *52*, 544–552. https://doi.org/10.1007/s11661-020-06100-9.

53. Du, S.; Li, Y.; Zheng, Y. Kinetics of austenite grain growth during heating and its influence on hot deformation of LZ50 steel. *J. Mater. Eng. Perform.* 2016, *25*, 2661–2669. https://doi.org/10.1007/s11665-016-2162-9.

54. Mikhaylovskaya, A.V.; Yakovtseva, O.A.; Cheverikin, V.V.; Kotov, A.D.; Portnoy, V.K. Superplastic behaviour of Al-Mg-Zn-Zr-Sc-based alloys at high strain rates. *Mater. Sci. Eng. A* 2016, *659*, 225–233. https://doi.org/10.1016/j.msea.2016.02.061.

55. Li, H.; Liu, X.; Sun, Q.; Ye, L.; Zhang, X. Superplastic deformation mechanisms in fine-grained 2050 Al-Cu-Li alloys. *Materials* 2020, *13*, 2705. https://doi.org/10.3390/ma13122705.

Chapter 4

Superplastic Deformation and Microstructural Evolution of an Al–Mg–Mn 5xxx Alloy for High-Speed Blow Forming Applications

(This article has been published in: Journal of Materials Science, 61 (2026), 16033–16053)

Abstract

This study investigates the deformation behavior and microstructural evolution of an Al–Mg–Mn 5xxx alloy under conditions relevant to high-speed blow forming (HSBF). The alloy was tested between 450 and 520 °C at strain rates ranging from 0.001 to 1 s^{-1}, following a short-time annealing treatment that produced a fine, fully recrystallized grain structure (4.5-5.6 μm). Mechanical testing revealed a pronounced dependence of elongation and flow stress on both temperature and strain rate, with maximum ductility observed at 500 °C. At this temperature, grain-boundary sliding (GBS) dominated deformation at low strain rates, whereas solute-drag creep (SDC) constrained ductility at 450 °C and diffusion-controlled grain growth reduced formability at 520 °C. Notably, significant grain refinement was observed after deformation at 1 s^{-1}, indicating active continuous dynamic recrystallization (CDRX). Furthermore, Mn-containing dispersoids enhanced grain-boundary pinning and promoted CDRX, thereby maintaining microstructural stability during high-strain-rate deformation. Overall, these findings provide a practical and cost-effective pathway for tailoring microstructure to enable stable high-strain-rate formability in Al–Mg–Mn alloys, supporting the development of materials suitable for future HSBF applications.

Keywords: Al–Mg–Mn 5xxx alloy; high temperature deformation; microstructural evolution; grain-boundary sliding; continuous dynamic recrystallization; high-strain-rate formability.

4.1 Introduction

The growing demand for lightweight transportation structures drives the development of aluminum alloys with improved formability. Superplasticity (SP), defined as tensile elongation exceeding 200 % at elevated temperatures, enables single-step fabrication of complex geometries with reduced part count and manufacturing cost [1,2]. SP was historically associated with aluminum, magnesium, and titanium alloys. However, recent studies on lean Fe-Mn-Al steels [3] and high-entropy alloys (HEAs) [4–6] show that SP can occur across diverse metallic systems when a fine and thermally stable grain structure is maintained.

Among aluminum alloys, Al–Mg–Mn 5xxx alloys, particularly AA5083, are widely used for superplastic forming (SPF) due to their favorable combination of strength, corrosion resistance, weldability, and cost-effectiveness [7–10]. Superplastic flow in fine-grained aluminum alloys is governed primarily by grain-boundary sliding (GBS), accommodated by dislocation creep and diffusion at low strain rates (~0.0001-0.001 s^{-1}) [11–13]. However, these low strain-rate conditions lead to long forming cycles (>30 min), thereby constraining productivity and limiting the large-scale industrial application of SPF [14,15]. Consequently, achieving superplasticity at strain rates ≥ 0.01 s^{-1}—high strain rate superplasticity (HSRS)—has become a key research objective to improve forming efficiency and reduce manufacturing costs.

Ultrafine-grained (UFG) microstructures are essential for achieving HSRS, as grain refinement shifts the strain-rate window for GBS toward higher values [16–18]. Recent studies have demonstrated that Al-Mg alloys processed by severe plastic deformation (SPD) and micro-alloyed with Sc and Zr exhibit remarkable HSRS. The addition of Sc and Zr promotes the formation of coherent $Al_3(Sc,Zr)$ precipitates, which effectively stabilize the UFG structure produced by SPD. This stabilization enables GBS-controlled superplastic flow at strain rates of 0.01-0.1 s^{-1} [11,19,20] and facilitates low-temperature superplasticity [21,22]. For instance, Sun *et al.* [23] reported an elongation of 343 % at a strain rate of 0.1 s^{-1} in a friction-stir-processed Al-Mg-Sc-Zr alloy.

Similarly, thermomechanically processed (TMP) Al-Mg alloys with Sc and Zr additions also exhibit HSRS. In such alloys, Sc and Zr effectively control dynamic recrystallization (DRX) and grain growth, producing stable fine-grained structures that sustain HSRS [24–28]. Kishchik *et al*. [29], for example, reported elongations up to 535 % at 0.1 s^{-1} in an Sc-modified Al-Mg-based alloy, attributed to dynamically formed grains measuring 2-4 μm. These results underscore the critical role of Sc microalloying in achieving HSRS in Al–Mg alloys. However, SPD techniques are complex and energy-intensive [30], and the use of Sc to stabilize SPD- and TMP-processed alloys substantially increases cost, limiting large-scale industrial adoption.

Conventional processing of Al–Mg rolled sheets typically yields grain sizes of 8-10 μm [31–33] and therefore does not exhibit pronounced HSRS. Nevertheless, under Quick Plastic Forming (QPF) and High-Speed Blow Forming (HSBF) conditions, these alloys can enable rapid forming of complex automotive components, offering a more cost-effective alternative to TMP- or SPD-processed Sc/Zr-containing alloys. In QPF, cycle times are

shortened to 1–5 min [14] by activating solute-drag creep (SDC), a dislocation-controlled deformation mechanism in which diffusing Mg solute atoms interact with and retard dislocation motion. This solute–dislocation interaction stabilizes plastic flow at intermediate strain rates (~0.001–0.01 s^{-1}) [34]. In contrast, HSBF employs a two-stage strategy: an initial crash-forming step at high strain rates (≥1 s^{-1}), followed by low-strain-rate superplastic gas-blow finishing, enabling forming rates up to 30 times faster than conventional SPF. The alloy must accommodate this hybrid deformation regime—high-strain-rate deformation followed by superplastic forming—without failure. However, HSBF is often associated with cavitation, non-uniform thinning, and dimensional inaccuracies [35,36].

Recent studies highlight the critical role of tribological conditions in HSBF, as lubrication and temperature strongly influence friction, strain localization, and overall forming quality [37]. Furthermore, constitutive models for AA5083, developed using phenomenological [38] and data-driven approaches [35,36,39], have significantly improved predictive accuracy and process optimization in advanced forming technologies. Despite these advances, several challenges remain. Achieving an optimal balance between high strain-rate capability and cavitation resistance while maintaining dimensional precision in HSBF remains difficult. This requires a deeper mechanistic understanding of deformation and microstructural evolution under hybrid forming conditions.

Most superplasticity studies [32,40,41] on Al–Mg–Mn 5xxx alloys have focused on low strain-rate regimes (≤ 0.01 s^{-1}). Tensile deformation at or above 1 s^{-1}—relevant to the crash-forming stage of HSBF—has received comparatively limited attention. Although hot deformation studies in aluminum alloys provide insight into high-rate flow behavior (0.01–10 s^{-1}), they are typically conducted under compressive loading [42–44]. Compression does

not replicate the tensile stress state in sheet forming and cannot fully capture cavitation or strain localization that critically affect forming performance. Furthermore, while HSRS has been demonstrated in SPD- and Sc/Zr-modified Al–Mg alloys, most reported tensile strain rates remain within 0.01–0.1 s^{-1} [24–29]. Detailed microstructural characterization of tensile behavior at ≥1 s^{-1} remains limited, particularly in conventionally processed 5xxx alloys. This gap restricts mechanistic understanding of deformation under HSBF-relevant conditions.

The present study addresses this gap by systematically examining the deformation behavior and microstructural evolution of a conventionally processed Al–Mg–Mn 5xxx alloy at 450-520 ºC and strain rates from 0.001 to 1 s^{-1}. The alloy was rapidly annealed and tensile-tested at strain rates representative of crash forming (1 s^{-1}) and superplastic forming (0.001–0.01 s^{-1}), replicating the sequential stages of HSBF. Particular attention is given to the interplay among GBS, SDC, and strain-induced continuous dynamic recrystallization (CDRX) across this strain-rate range. The role of annealing and Mn-containing dispersoids in stabilizing grain structures capable of sustaining deformation over a broad strain-rate spectrum is also evaluated.

By establishing quantitative relationships among strain-rate sensitivity, activation energy, and post-deformation microstructure, this work advances the fundamental understanding of high-strain-rate deformation mechanisms as well as the optimization of HSBF for lightweight structural applications. The results demonstrate that substantial high-strain-rate formability can be achieved in a conventionally processed Al–Mg–Mn 5xxx alloy without reliance on SPD or costly Sc/Zr microalloying. These findings clarify how short-time annealing combined with Mn-dispersoid stabilization enables thermally stable grain structures capable of sustaining deformation under HSBF-relevant conditions

4.2 Material and methods

4. 2.1 Material

A commercial Al–Mg–Mn 5xxx alloy used for HSBF, supplied as cold-rolled sheets with H18 temper, was provided by Verbom Inc. (Valcourt, QC, Canada). The chemical composition, analyzed by inductively coupled plasma mass spectrometry (Agilent 7800, Santa Clara, CA, USA), is listed in Table 4.1. Tensile specimens with a gauge length of 30 mm were machined along the rolling direction of the 2-mm-thick sheet, following the geometry described in our previous work [45].

Table 4.1 Chemical composition of Al–Mg–Mn 5xxx alloy (wt.%)

Alloy	Mg	Mn	Si	Fe	Cu	Cr	Ti	Zn	Al
Al–4.0Mg–1.18Mn	4.00	1.18	0.40	0.12	0.10	0.01	0.02	0.01	Bal.

4.2.2 Tensile test

Uniaxial hot tensile tests were performed at four temperatures (450, 480, 500, and 520 °C) and three initial strain rates (0.001, 0.01, and 1 s^{-1}) using a Gleeble 3800 thermomechanical simulator (Dynamic Systems Inc., New York, USA). The Gleeble 3800 allows rapid heating to the target deformation temperature, simulating the high heating rates of HSBF that cannot be achieved in conventional isothermal furnaces. The selected temperatures and strain rates were chosen to simulate HSBF-relevant conditions, with 1 s^{-1} representing the high-strain-rate crash-forming stage and 0.01–0.001 s^{-1} corresponding to the low-strain-rate superplastic stage used for final shaping. Additional tests at 0.0001 s^{-1} were conducted to evaluate the overall strain-rate sensitivity of the alloy. During testing, the specimens were rapidly heated to the target temperature within 3 min, held isothermally for

4 min, and then strained to failure. Each testing condition was repeated three times to ensure data reproducibility and reliability.

Further details regarding the tensile testing procedure and temperature uniformity are provided in our previous study [45]. Briefly, in the Gleeble 3800 setup, the temperature distribution across the 30 mm gauge section was assessed, confirming that uniform heating was maintained within the central 6 mm of the specimen. Accordingly, all microstructural observations and deformation measurements reported in this study were obtained from this 6 mm central region to ensure representative and reliable results. To characterize the alloy microstructure in the annealed condition, additional specimens were subjected to the same thermal cycles (450, 480, 500 and 520 °C for 4 min) in the Gleeble system without deformation.

4.2.3 Microstructure analysis

The as-received microstructure was examined on samples sectioned along the rolling direction of the cold-rolled aluminum sheet. These samples were mechanically polished and then electroetched in Barker's reagent (3 vol.% HBF_4 solution) at 17 V for 90 s, followed by polarized-light observation using optical microscopy (Nikon Eclipse ME600 microscope, Tokyo Japan). The composition of intermetallic phases in the cold-rolled sheet was analyzed by scanning electron microscopy (SEM; JSM-6480LV, JEOL Inc., Tokyo, Japan) equipped with an Oxford Instruments X-Max 80 energy-dispersive X-ray spectroscopy (EDS) detector. SEM imaging was conducted at an accelerating voltage of 20 kV and a working distance of 15 mm.

Electron backscatter diffraction (EBSD) was performed using an Oxford Symmetry detector attached to the SEM at an accelerating voltage of 20 kV. Data were collected over a

scan area of 300 × 250 μm. For the annealed condition (average grain size of 4.5–5.6 μm), a step size of 1.5 μm was used to obtain representative grain size measurements over a large sampling area. For the deformed microstructures that contained finer grains (3-4 μm), a step size of 0.5 μm was employed to ensure adequate spatial resolution for reliable grain boundary characterization. Grain boundaries were classified based on misorientation angle (θ) : low-angle boundaries (LAB) were defined as $\theta < 5^{o}$, medium-angle boundaries (MAB) as $5^{o} \leq \theta < 15^{o}$, and high-angle boundaries (HAB) as $\theta > 15^{o}$. Indexing was performed using the aluminum CIF standard, and EBSD data were processed with HKL Channel 5 software to quantify grain size, boundary distribution, and texture evolution.

Post-deformation microstructural analysis was performed on the central region of the fractured half of the gauge section. This region provides a representative view of the deformation-induced microstructural features, while minimizing artifacts associated with localized necking and non-uniform strain near the fracture tip. Transmission electron microscopy (TEM; JEM-2100, JEOL Inc., Tokyo Japan) was used to examine dispersoid characteristics and dislocation structures. Specimens were mechanically ground to ~70 μm thickness and twin-jet electropolished in 30 % nitric acid in methanol at −20 °C and 20 V. TEM observations were conducted at an accelerating voltage of 200 kV. Multiple regions of each sample were examined to ensure representative observations. Based on this experimental approach, Section 4.3 presents the results obtained from microstructural characterization and hot tensile testing under different processing conditions.

4.3 Results

4.3.1 As-received and annealed microstructures

Figure 4.1 presents the microstructure of the as-received (cold rolled) Al–Mg–Mn alloy. The grains were elongated along the rolling direction with pronounced shear bands (Figure 4.1a), indicating the degree of plastic deformation during cold rolling. The enlarged SEM micrograph (Figure 4.1b) reveals two distinct intermetallic phases in the matrix, identified by SEM–EDS analysis as $Al_6(Mn,Fe)$ (Figure 4.1c) and Mg_2Si (Figure 4.1d) intermetallic particles. Due to heavy cold rolling, both intermetallic particles were fragmented and aligned in the rolling direction.

Figure.4.2 presents the EBSD inverse pole figure (IPF) maps of the alloy annealed at 450, 480, 500 and 520 °C for 4 min prior to hot tensile testing. The heavily deformed grains in the cold-rolled condition experienced rapid static recrystallization, resulting in a fine, equiaxed grain structure exhibiting random crystallographic texture (Figures. 4.2a–d). This behavior is consistent with the high stored energy of the cold-rolled state and the presence of intermetallic particles that can act as nucleation sites.

Figure. 4.2e presents the grain size analysis of the annealed samples at various temperatures. The sample annealed at 450 °C exhibited an average grain size of 4.5 ± 0.10 μm, which gradually increased to 5.6 ± 0.10 μm at 520 °C. The fraction of fine grains smaller than 5 μm ($f_{G<5\ \mu m}$) decreased from 49 % to 33 % with increasing temperature. Despite slight coarsening, the grain structure remained fine, confirming that short-time annealing yields a microstructure suitable for superplastic deformation.

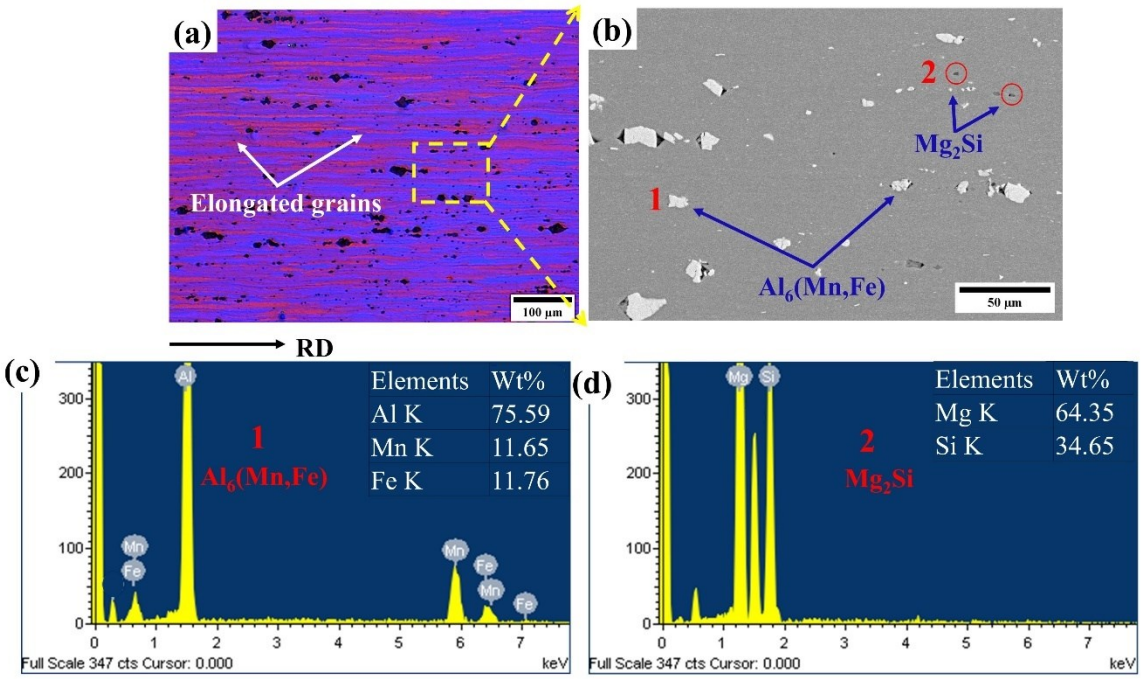


Figure 4.1 Optical and SEM microstructures of the as-received (cold-rolled) alloy: (a) polarized optical image showing elongated grains along the rolling direction (RD); (b) SEM image revealing $Al_6(Mn,Fe)$ and Mg_2Si intermetallic particles within the Al matrix; (c) EDS spectrum of $Al_6(Mn,Fe)$; (d) EDS spectrum of Mg_2Si.

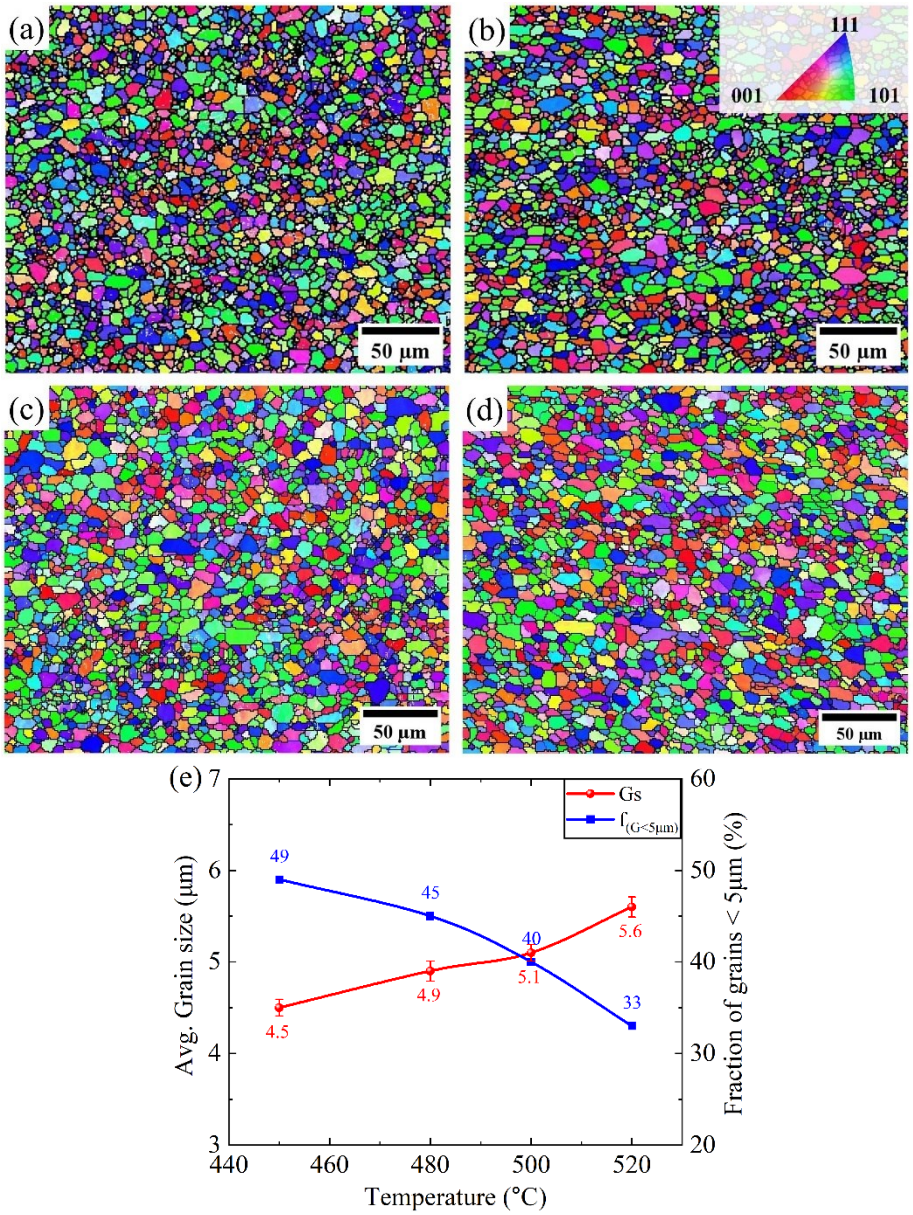


Figure 4.2 EBSD IPF maps showing grain structures after 4 min annealing at (a) 450 °C, (b) 480 °C, (c) 500 °C, and (d) 520 °C; (e) average grain size and the fraction of recrystallized grains smaller than 5 μm at various annealing temperatures. The grains remain fine and equiaxed at all annealing temperatures, with slight coarsening observed as temperature increased.

4.3.2 Hot tensile deformation and superplastic behavior

Uniaxial hot tensile tests were performed at strain rates of 0.001, 0.01, and 1 s^{-1} and deformation temperatures of 450, 480, 500, and 520 °C. Representative tensile stress–strain curves obtained under these conditions are shown in Figure 4.3. The flow curves exhibited a characteristic response, consisting of rapid strain hardening to a peak stress followed by flow stabilization or softening prior to necking. The extent of hardening and subsequent softening varied systematically with strain rate and deformation temperature. At the lowest strain rate of 0.001 s^{-1} (Figure 4.3a), the alloy exhibited nearly stable flow following yielding, with minimal strain hardening. The flow stress decreased progressively with increasing temperature. At the intermediate strain rate of 0.01 s^{-1} (Figure. 4.3b), modest strain hardening was observed prior to the establishment of a relatively stable flow regime. Similar to the behavior at 0.001 s^{-1}, increasing temperature led to a pronounced reduction in flow stress.

In contrast, deformation at 1 s^{-1} (Figure 4.3c) showed a markedly different response, characterized by rapid work hardening to a higher peak stress followed by significant flow softening. Both the peak stress and the overall flow stress were highest at 450 ^{o}C and decreased progressively with increasing temperature. Overall, across the temperature range of 450–520 ^{o}C, the flow stress decreased systematically with increasing temperature and decreasing strain rate. The shape of the stress–strain curves was primarily governed by strain rate, whereas temperature acted as the dominant softening variable, reducing the alloy's resistance to plastic flow under all test conditions.

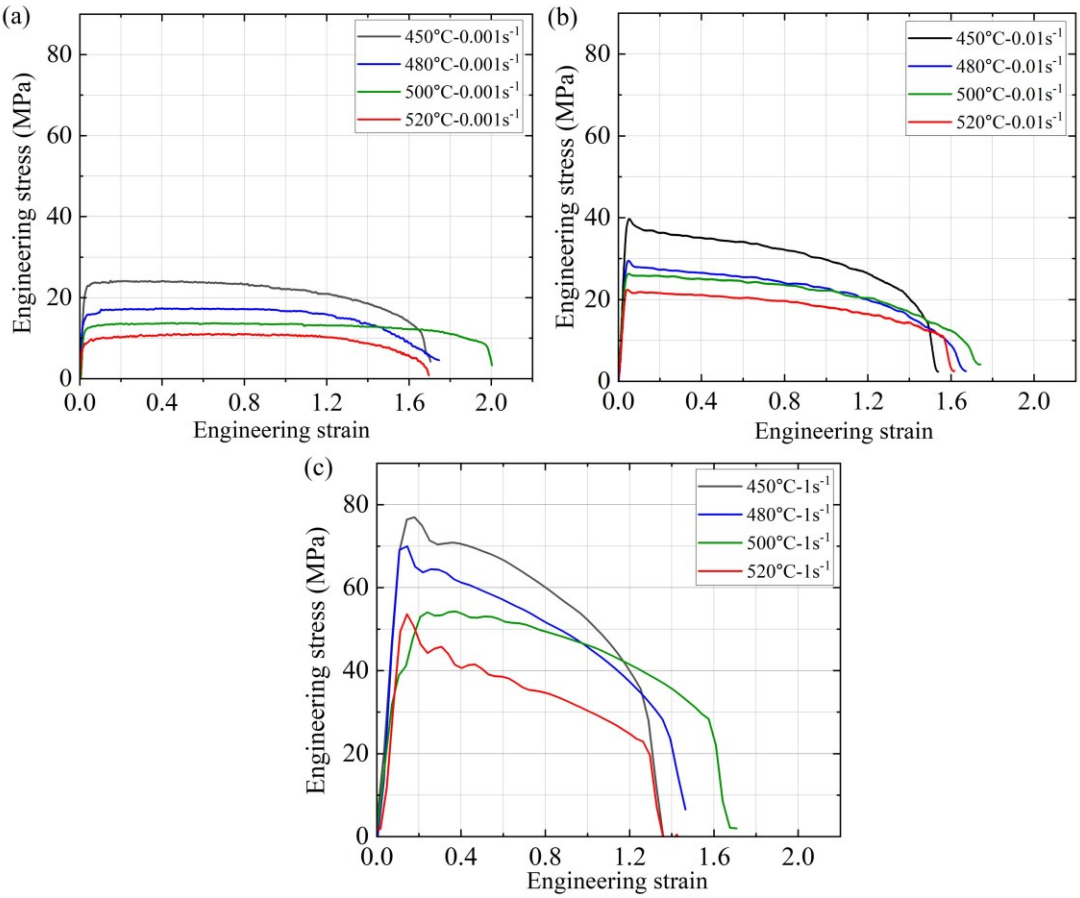


Figure 4.3 Stress-strain curves of the Al–Mg–Mn alloy deformed at strain rates of (a) 0.001 s^{-1}, (b) 0.01 s^{-1}, and (c) 1 s^{-1} over 450-520 ºC. Flow stress decreased with increasing temperature at all strain rates, indicating thermal softening.

Figure 4.4 presents the tensile elongation of the alloy under different testing conditions. At 450 ºC, the alloy exhibited an elongation of 170 ± 2 % at 0.001 s^{-1}, decreasing to 152 ± 11 % and 141 ± 7 % at 0.01 s^{-1} and 1 s^{-1}, respectively. A similar trend was observed at 480 ºC, with elongations of 175 ± 19 % at 0.001 s^{-1}, 167 ± 16 % at 0.01 s^{-1}, and 147 ± 5 % at 1 s^{-1}. The highest ductility was obtained at 500 °C, where the alloy reached 211 ± 12 % at 0.001 s^{-1}, corresponding to an increase of approximately 24 % relative to 450 °C. At this temperature, elongation remained comparatively high at increased strain rates, reaching 174

± 10 % at 0.01 s^{-1} and 168 ± 5 % at 1 s^{-1}. At 520 °C, elongation decreased across all strain rates to 171 ± 3 %, 164 ± 2 %, and 135 ± 10 % at 0.001, 0.01, and 1 s^{-1}, respectively.

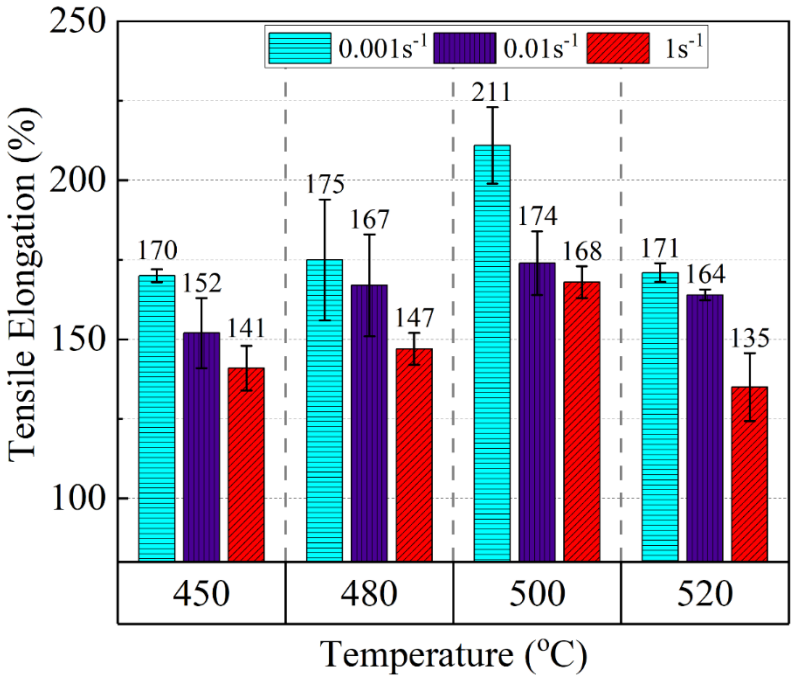


Figure 4.4 Tensile elongation of the Al–Mg–Mn alloy as a function of deformation temperature and strain rate. Elongation increased with temperature up to 500 °C due to enhanced strain-rate sensitivity (m) and activation of GBS, then decreased at 520 °C due to grain coarsening.

To elucidate the deformation behavior and underlying mechanisms, the strain rate sensitivity (m) and the activation energy for hot deformation (Q) were determined using Equation (1) [29,46] and Equation (2) [47,48], respectively.

$$m = \left(\frac{\partial ln\sigma}{\partial ln\dot{\varepsilon}}\right) \quad (1)$$

$$Q = \left(\frac{R}{m}\frac{\partial \ln\sigma}{\partial(1/T)}\right)_{\dot{\varepsilon}} \quad (2)$$

where σ is the flow stress, $\dot{\varepsilon}$ is the strain rate, R is the gas constant, and T is the absolute temperature. The m reflects the ability of the alloy to accommodate plastic deformation under

varying strain rates whereas Q represents the apparent thermal activation energy associated with the dominant deformation mechanism. For the determination of m and Q, engineering stress–strain data were converted to true stress–true strain. The flow stress at a true strain of 0.10 at each temperature was used for the calculation of m consistent with methodologies reported in the literature [12].

Figure 4.5a presents the variation of the m with temperature. The m value increased steadily with temperature, from 0.30 at 450 ºC to 0.37 at 480 ºC, reaching 0.42 and 0.43 at 500 and 520 °C, respectively. Values of $m \geq 0.3$ are commonly associated with superplastic-like deformation behavior and improved resistance to strain localization [4]. The observed increase in m with temperature is consistent with previous reports on Al-Mg alloys [48,49]. Figure 5b shows the corresponding Q values obtained from Arrhenius plots of ln(σ) versus 1/T. The apparent activation energy decreased from 145 kJ mol^{-1} at 0.001 s^{-1} to 96 kJ mol^{-1} at 0.01 s^{-1} and further to 87 kJ mol^{-1} at 1 s^{-1}, indicating a systematic dependence of Q on strain rate.

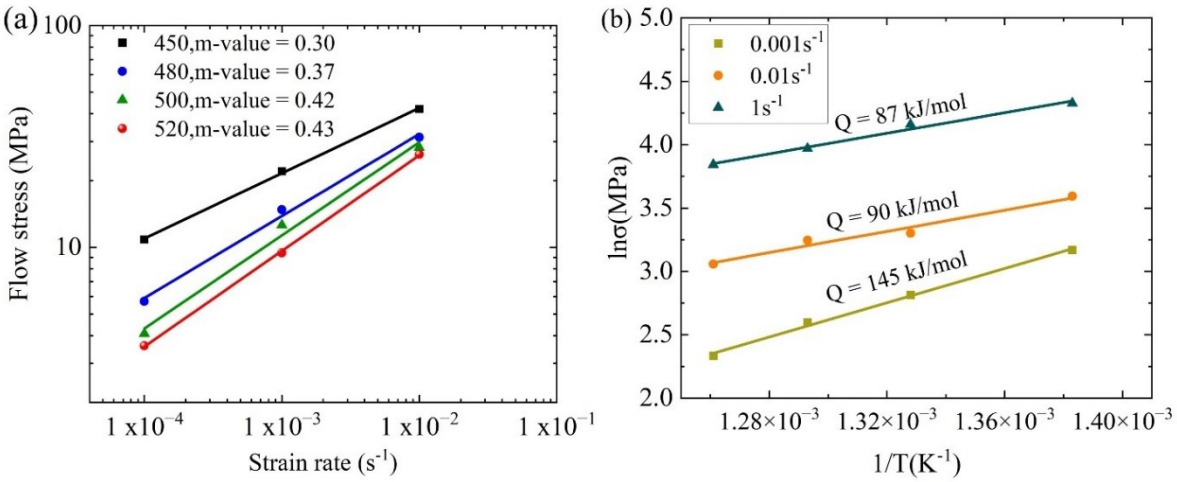


Figure 4.5 (a) Log–log plot of flow stress (σ) versus strain rate (ε̇) used to determine the strain-rate sensitivity (m), and (b) Arrhenius plot of ln(σ) versus 1/T (K-1) used to calculate

Q for deformation. The m increases with temperature (0.30–0.43), indicating favorable conditions for superplasticity at high temperatures. The Q decreases with increasing strain rate, suggesting a transition from lattice diffusion to grain boundary or dislocation-based mechanisms.

4.3.3 Grain structure after deformation

The grain structure was examined after deformation to failure at 450, 500, and 520 ºC under low (0.001 s^{-1}) and high (1 s^{-1}) strain-rate conditions. The EBSD-IPF maps in Figure 4.6 show the deformed grain structures, while quantitative analyses of the average grain size, grain aspect ratio, and the fraction of grains smaller than 5 μm ($f_{G<5\ \mu m}$) are presented in Figure 4.7. At 0.001 s^{-1}, deformation resulted in relatively coarse and elongated grains (Figs. 4.6a–c). The average grain size increased from 5.4 ± 0.2 μm at 450 ºC to 7.3 ± 0.4 μm at 500 ºC and further to 8.9 ± 0.5 μm at 520 ºC (Figure 4.7a). Concurrently, the grain aspect ratio decreased from 2.7 at 450 ºC to 1.7 at 520 ºC, indicating reduced grain elongation with increasing temperature.

In contrast, deformation at 1 s^{-1} produced a predominantly fine and equiaxed grain structure (Figs. 4.6d–f). At 450 ºC, a limited fraction of elongated grains was observed, resulting in a mixed morphology. The average grain size increased slightly with temperature, from 2.8 ± 0.1 μm at 450 ºC to 3.4 ± 0.2 μm at 500 ºC and 4.0 ± 0.1 μm at 520 ºC. Despite this increase, the grain aspect ratio remained close to unity across all temperatures, confirming a largely equiaxed structure. As shown in Figure 4.7b, $f_{G<5\ \mu m}$ remained high (75–91 %) at 1 s^{-1}, compared with 36–43 % at 0.001 s^{-1}. These results indicate a pronounced influence of strain rate on the final grain size and morphology.

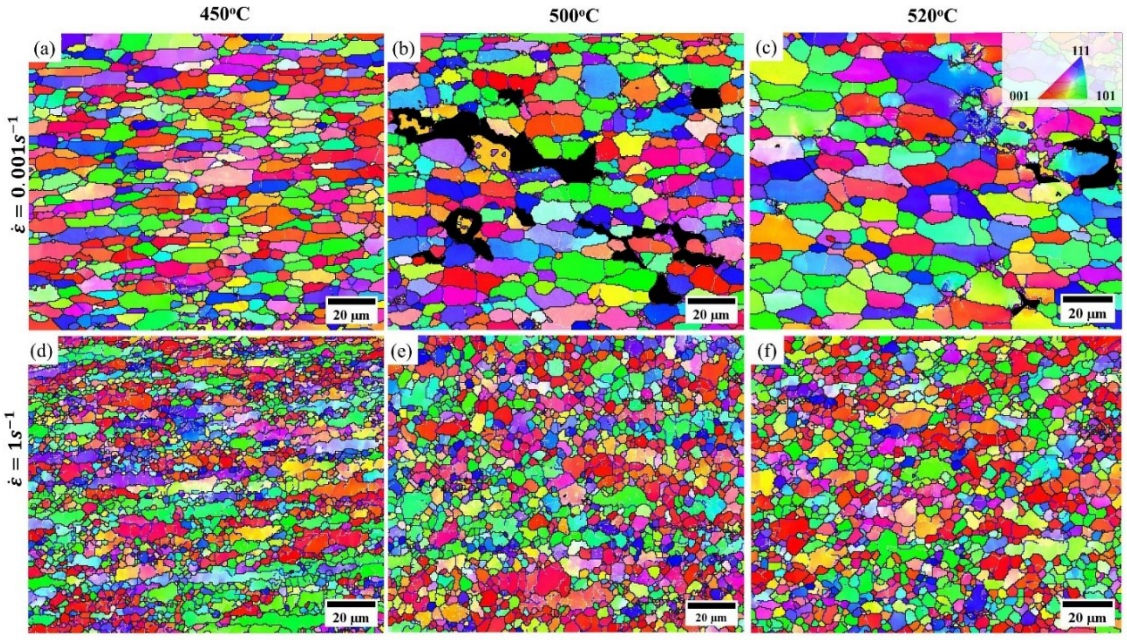


Figure 4.6 EBSD IPF maps showing the grain structure after deformation at (a) and (d) 450 °C, (b) and (e) 500 °C, and (c) and (f) 520 °C; (a)–(c) correspond to strain rates of 0.001 s^{-1} and (d) – (f) 1 s^{-1}. All EBSD maps were obtained from the central region of the fractured half of the gauge section, where deformation was most representative of the specimen. Black regions in (b) and (c) are cavities after deformation.

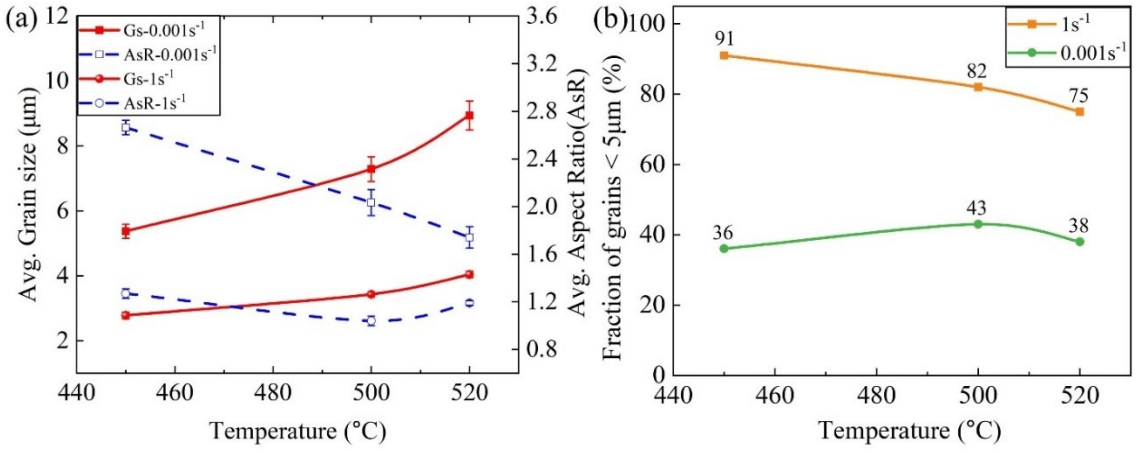


Figure 4.7 Influence of deformation temperature on (a) average grain size and aspect ratio, and (b) fraction of fine grains (< 5 μm) after deformation at strain rates of 0.001 and 1 s^{-1}.

At 0.001 s^{-1}, grain size increases with temperature, while at 1 s^{-1}, grains remain fine and equiaxed.

To further evaluate the influence of strain rate at the optimal temperature, samples deformed at 0.001, 0.01, and 1 s^{-1} at 500 ºC were compared with the annealed condition. The corresponding EBSD Euler maps are shown in Figure 4.8, and quantitative analyses of grain size, aspect ratio, and grain-boundary character distribution are presented in Figure 4.9 As shown in Figure 4.8a, the annealed alloy exhibited a fine, equiaxed grain structure with an average grain size of 5.1 ± 0.1 μm. After deformation, the grain size increased to 7.3 ± 0.4 μm at 0.001 s^{-1} and 5.8 ± 0.4 μm at 0.01 s^{-1} (Figure 4.9a). The grain aspect ratio increased from 1.4 in the annealed condition to 2.1 at 0.001 s^{-1} and 1.6 at 0.01 s^{-1}. In contrast, deformation at 1 s^{-1} resulted in a finer grain structure (3.4 ± 0.2 μm) than that of the annealed condition, together with a nearly equiaxed morphology (aspect ratio ≈ 1.1). The yellow circles in Figure 4.8c highlight localized grain refinement at 0.01 s^{-1}, where elongated and equiaxed grains coexist. At 1 s^{-1}(Figure 4.8d), the microstructure became predominantly fine and equiaxed.

Deformation at 1 s^{-1} was accompanied by pronounced substructure development. As shown in Figure 4.8d–e, an increased population of LABs was observed, together with progressive increases in boundary misorientation toward MABs and, locally, HABs. Correspondingly, Figure 4.9b indicates that the relative fractions of LABs and MABs increased to 12 % and 19 %, respectively, at 1 s^{-1}, whereas only minor changes were observed at lower strain rates. The relative HAB fraction decreased from 88 % in the annealed condition to 69 % at 1 s^{-1}. This change reflects redistribution of boundary character resulting from the formation of additional LABs and MABs during deformation rather than an absolute

reduction of HABs. The progressive increase in misorientation is illustrated in Figure 4.8e and is consistent with boundary subdivision behavior reported during CDRX in Al alloys [50].

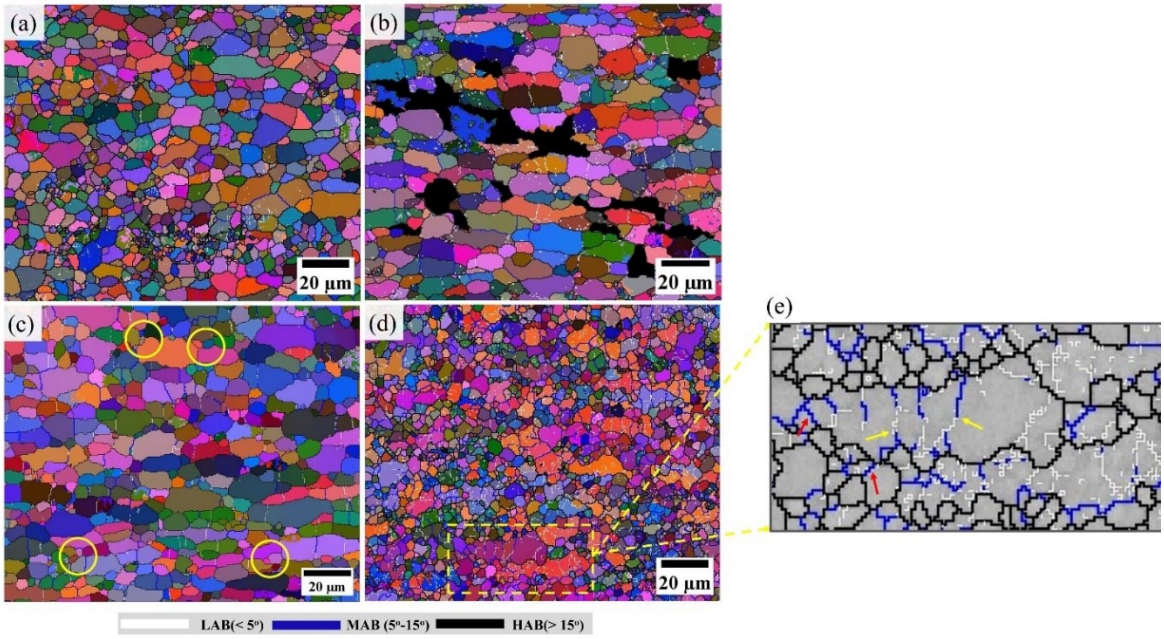


Figure 4.8. EBSD Euler maps of the alloy in (a) the annealed condition and after deformation at 500 °C at strain rates of (b) 0.001 s^{-1}, (c) 0.01 s^{-1}, and (d) 1 s^{-1}. (e) Fragmentation of large grains into finer ones in (d), where LABs (white) evolved into MABs (blue) and subsequently into HABs. The yellow circles in (c) show small grains, indicating the onset of continuous dynamic recrystallization at 0.01 s^{-1}.

Furthermore, Figure 4.10 compares the misorientation distributions between the annealed and deformed conditions. At 0.001 s^{-1} and 0.01 s^{-1}, the distributions closely resemble that of the annealed state. In contrast, at 1 s^{-1}, the misorientation profile shifts toward lower and intermediate angles, consistent with the increased relative fractions of LABs and MABs shown in Figure 4.9b. These results indicate a clear modification of grain-boundary character with increasing strain rate. The combined evolution of grain structure and

boundary character forms the basis for the mechanistic interpretation of deformation behavior presented in the following section.

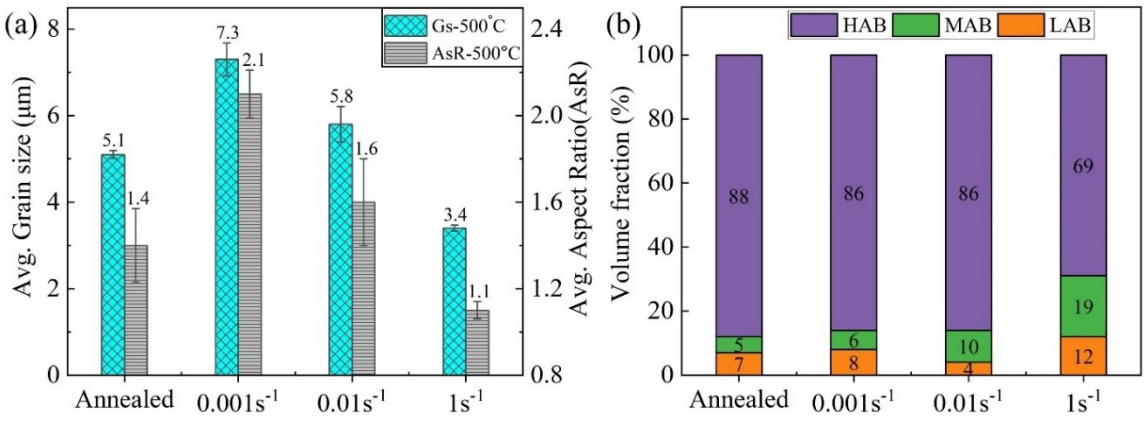


Figure 4.9 Comparison of (a) average grain size and aspect ratio of the alloy in the annealed and deformed conditions at 500 °C, and (b) relative volume fractions of LABs, MABs, and HABs under the same conditions

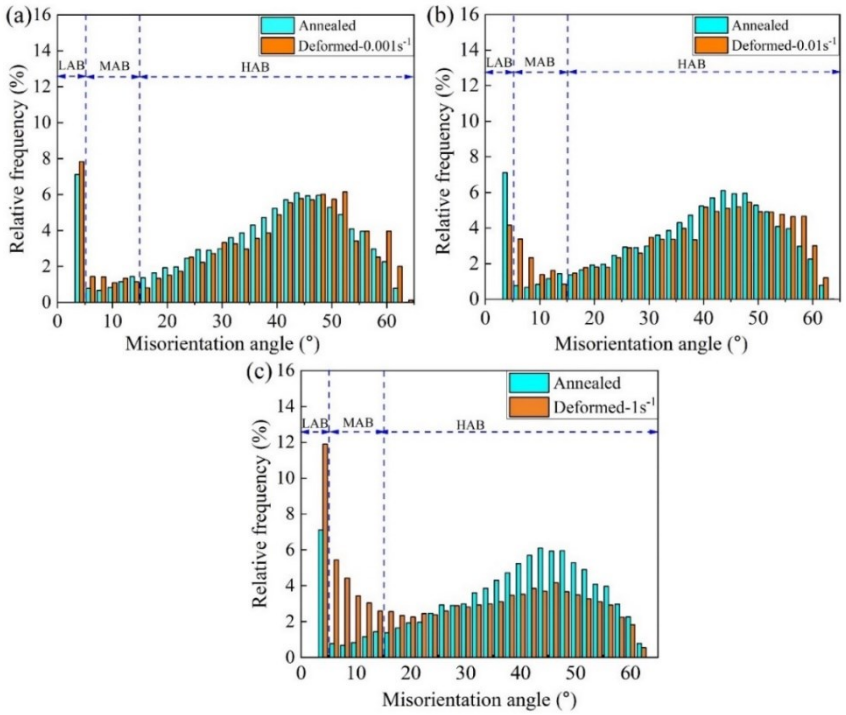


Figure 4.10 Misorientation angle distributions after deformation at 500 °C and strain rates of (a) 0.001 s^{-1}, (b) 0.01 s^{-1}, and (c) 1 s^{-1}. The distributions at lower strain rates remain

similar to that of the annealed condition, whereas at 1 s^{-1} the profile changes markedly, showing increased relative fractions of LABs and MABs.

4.4. Discussion

4.4.1 Effect of temperature on grain structure and superplastic deformation behavior

As shown in Figure 4.2, the alloy exhibited a fully recrystallized and fine-grained structure after annealing at 450-520 °C for 4 min. The rapid recrystallization is attributed to the high stored strain energy introduced during cold rolling [51,52], which was retained during rapid heating to the annealing temperature [53]. In addition, intermetallic particles (Figure 4.1d) promoted particle-stimulated nucleation (PSN), enhancing recrystallization through heterogeneous nucleation sites [31,32,54].

The average grain size increased modestly from 4.5 ± 0.10 μm at 450 ºC to 5.6 ± 0.10 μm at 520 °C. Grain growth remained limited due to the short annealing duration and the presence of Mn-containing dispersoids. In our previous study on the same alloy and thermomechanical condition [45], TEM analysis revealed Mn-rich dispersoids with an average equivalent diameter of 166 ± 17 nm and a number density of (9.3 ± 1.4) × 10^{15} m^{-3}. This relatively high dispersoid density provides effective Zener pinning pressure on migrating grain boundaries [29,31,55,56], thereby stabilizing the fine recrystallized microstructure. Consequently, a substantial fraction of fine grains (($f_{G<5\ \mu m}$= 33–49 %) was retained across the annealing temperatures. Fine-grained microstructures facilitate GBS [29,31,32,41], which is essential for superplastic deformation and shifts the strain-rate window toward higher values [16,17,57]. Although the present grain sizes do not fall within

the UFG regime, they are comparable to those achieved via friction stir processing (~5 μm) [33], which support enhanced ductility at elevated strain rates. Thus, short-time annealing provides a stable fine-grained structure suitable for high-strain-rate forming.

Despite the similar recrystallized grain structures obtained after annealing, the alloy exhibited a clear temperature dependence during deformation, particularly at the lower strain rates (0.001 and 0.01 s^{-1}). As shown in Figure 4.3, the flow stress decreased systematically with increasing temperature, reflecting enhanced thermal activation of dynamic recovery and reduced resistance to plastic deformation [2,42]. This thermal softening was accompanied by an increase in m-value from 0.30-0.37 at 450-480 °C to 0.42-0.43 at 500-520 °C (Figure 4.5a). The higher m-values indicate an increased contribution of GBS and improved strain accommodation at elevated temperatures [49].

At 450 °C, where the m-value was lowest (0.30) and ductility was limited (Figure 4.4), deformation was likely dominated by SDC. In Al–Mg alloys, SDC involves dislocation glide through a Mg solute atmosphere, which impedes dislocation motion and reduces strain-rate sensitivity [34,58,59]. This mechanism results in lower m-values and limited ductility compared with GBS-controlled deformation. Similar behavior was reported for AA5083 by Hsiao *et al.* [49], where SDC dominated at lower temperatures when m fell below approximately 0.33. The pronounced grain elongation observed at 450 °C (Figure 4.6 and 4.7) further supports a dislocation-controlled deformation mode accompanied by early strain localization.

At 500 ºC, both strain-rate sensitivity and ductility improved, particularly at 0.001 s^{-1}. This behavior indicates a transition to GBS-dominated deformation and the onset of superplastic response at the lowest strain rate [15,60]. Enhanced diffusion at this temperature

likely reduced the influence of SDC, enabling more effective GBS accommodation. GBS occurs along grain interfaces and is accommodated by dislocation activity within narrow mantle regions adjacent to grain boundaries [32,61,62]. Although the maximum elongation (211 %) was achieved at 500 ºC and 0.001 s^{-1}, the grains remained nearly equiaxed during deformation (Figure 4.11). The aspect ratio increased only modestly from 1.4 in the annealed state to 2.1 at fracture, indicating limited intragranular distortion despite large macroscopic strain. Such behavior is characteristic of GBS-controlled deformation.

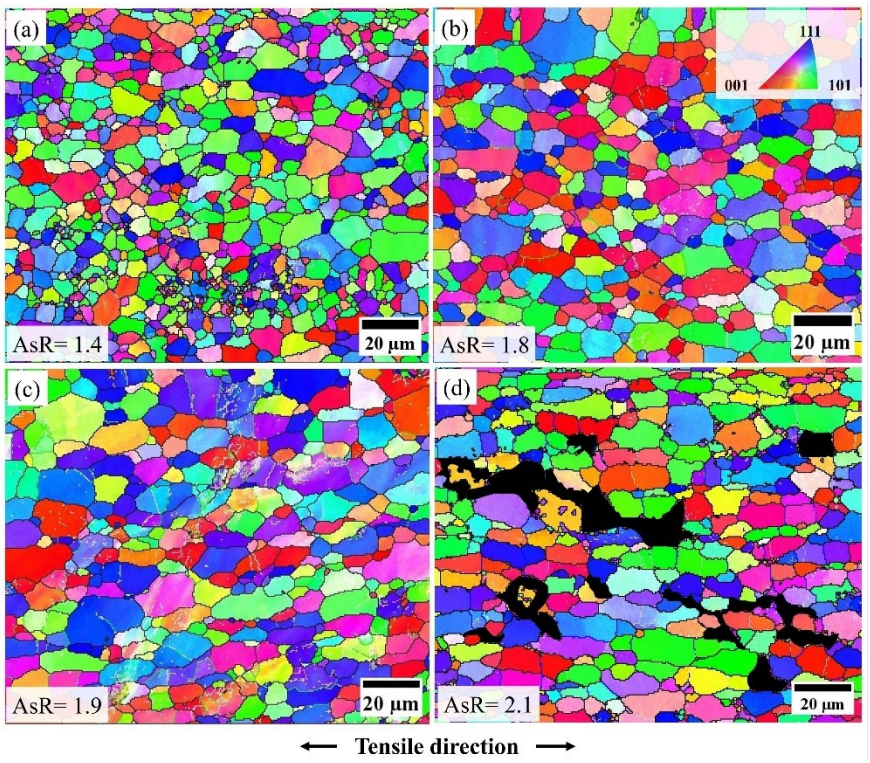


Figure 4.11 EBSD–IPF maps showing the grain structure evolution of the alloy deformed at 500 °C and a strain rate of 0.001 s^{-1}, corresponding to strain levels of (a) ε = 0, (b) ε = 0.2, (c) ε = 1.0, and (d) post–fracture. Black regions in (d) indicate cavities formed in the microstructure during fracture. The grains remained nearly equiaxed with a modest aspect ratio increase from 1.4 to 2.1, indicating limited grain elongation.

At 520 °C, ductility decreased (Figure 4.4) despite a relatively high m-value (0.43), indicating a departure from optimal superplastic conditions. Microstructural analysis (Figure 4.6) revealed pronounced dynamic grain growth at 0.001 s^{-1}, which reduced the grain-boundary area available for GBS [31,63]. Prolonged deformation at this temperature may also have promoted grain-boundary cavitation and excessive grain coarsening, leading to localized failure [12]. Under these conditions, deformation likely shifted toward diffusion creep (DC) [64], a mechanism controlled by atomic diffusion through the lattice or along grain boundaries and generally less effective than GBS in sustaining high tensile elongation [9,62,65].

In summary, at low strain rates the dominant deformation mechanism transitioned from SDC at lower temperatures to GBS at intermediate temperatures, and increasingly toward diffusion-controlled processes at the highest temperature. In contrast, at 1 s^{-1}, tensile elongation decreased across all temperatures, reflecting limited time for diffusion-controlled accommodation and an increased contribution from dislocation-driven processes. These strain-rate-dependent effects are examined in greater detail in the following section.

4.4.2 Effect of strain rate on grain structure and superplastic deformation behavior

The alloy exhibited distinctly different deformation behavior at low (0.001 and 0.01 s^{-1}) and high (1 s^{-1}) strain rates. At lower strain rates, the stress–strain curves (Figure 4.3) displayed stable flow following yielding, indicating a dynamic balance between work hardening and recovery [43]. The longer deformation time allowed recovery processes to partially offset dislocation accumulation, resulting in steady-state flow prior to necking. In

contrast, deformation at 1 s^{-1} exhibited pronounced post-peak softening, suggesting a shift in the governing deformation processes.

This mechanistic transition is quantitatively supported by the variation of Q with strain rate (Figure 5b). The Q value of ~145 $kJ \cdot mol^{-1}$ obtained at 0.001 s^{-1} falls within the range reported for lattice-diffusion-controlled superplastic flow in Al-Mg systems (135–205 $kJ \cdot mol^{-1}$) [16,41,44,64,66] and closely matches the lattice self-diffusion energy of aluminum (~142 $kJ \cdot mol^{-1}$)[46]. This indicates that deformation at low strain rates is dominated by lattice-diffusion-assisted process, consistent with GBS accommodated by diffusion and dynamic recovery. As the strain rate increases to 0.01 and 1 s^{-1}, Q decreases to 97 and 87 $kJ \cdot mol^{-1}$, respectively. These values approach the grain-boundary diffusion energy of aluminum (~84 $kJ \cdot mol^{-1}$) [48] and fall below the activation energies typically reported for SDC in Al-Mg alloys (109-135 $kJ \cdot mol^{-1}$) [66]. The reduced Q suggests diminished lattice diffusion control and an increasing contribution from boundary-mediated and dislocation-assisted processes. The limited time available for long-range diffusion at high strain rates promotes dislocation accumulation [67] and subgrain formation, facilitating strain-induced CDRX. Thus, the progressive decrease in Q supports a transition from diffusion-assisted GBS at low strain rates to increased dislocation activity and strain-induced CDRX at high strain rates.

Consistent with this mechanistic transition, tensile ductility decreased progressively with increasing strain rate (Figure 4.4). At 500 °C, elongation declined from 211 % at 0.001 s^{-1} to 174 % at 0.01 s^{-1} and further to 168 % at 1 s^{-1}. This reduction reflects a gradual shift from GBS-dominated deformation toward increased dislocation activity at higher strain rates. The relatively modest decrease in ductility between 0.01 s^{-1} and 1 s^{-1} suggests progressive

activation of CDRX, as evidenced by the coexistence of elongated and fine equiaxed grains at 0.01 s^{-1} (Figure 4.8c) and the pronounced grain refinement observed at 1 s^{-1} (Figure 4.6c). CDRX-induced refinement increases grain-boundary density and promotes more uniform strain accommodation. This likely contributes to sustaining substantial tensile ductility at high strain rates, despite the reduced contribution of diffusion-controlled GBS.

Post-deformation grain structure analysis provides further evidence for this strain-rate-dependent transition. At low strain rates, the initially fine recrystallized microstructure underwent grain coarsening, consistent with deformation dominated by GBS and diffusion-controlled processes. In contrast, at 1 s^{-1}, the grains were finer than in the initial state (Figure 8), indicating strain-induced CDRX. Grain refinement at 1 s^{-1} was accompanied by pronounced subgrain formation and boundary subdivision (Figure 8e). The relative fractions of LABs and MABs increased to 12 % and 19 %, respectively (Figure 9b), whereas only minor changes were observed at lower strain rates. The apparent reduction in the relative HAB fraction—from 88 % in the annealed condition to 69 % at 1 s^{-1}—reflects redistribution of boundary character due to increased LAB and MAB formation during deformation, rather than an absolute loss of HABs.

The misorientation distributions (Figure 4.10) further corroborate this evolution. At 0.001 and 0.01 s^{-1}, the distributions resemble that of the annealed condition, indicating limited boundary reconfiguration. In contrast, at 1 s^{-1}, the distribution shifts toward lower and intermediate misorientation angles, consistent with progressive lattice rotation and subgrain subdivision. Such gradual boundary evolution is characteristic of CDRX [50,67–69], where misorientation increases through dislocation rearrangement rather than abrupt nucleation of strain-free grains [51].

TEM observations provide direct evidence for dispersoid-assisted CDRX during deformation at 1 s^{-1}. Samples deformed under these conditions (Figure 4.12c–e) exhibit dense dislocation forests and well-developed subgrain structures, which are absent in the annealed (Figure 4.12a) and low-strain-rate (Figure 4.12b) conditions. Dislocation accumulation at Mn-rich dispersoids (Figure 4.12c–d) indicates strong particle–dislocation interactions, whereby dispersoids act as effective pinning sites that impede dislocation glide and promote dislocation storage [51,52].

Subgrain boundaries are frequently observed to be anchored by dispersoids (Figure 12e), demonstrating that particle pinning restricts boundary migration and suppresses dynamic recovery. This stabilization promotes the gradual conversion of LABs and MABs into HABs, consistent with a CDRX mechanism. In addition, dispersoids located along grain boundaries (Figure 12c,e) exert a Zener drag effect that limits grain boundary mobility and suppresses dynamic grain growth. By constraining boundary migration, Mn-rich dispersoids enable the retention of a refined grain structure during deformation, thereby stabilizing plastic flow.

Collectively, these mechanisms highlight the critical role of Mn-rich dispersoids in governing microstructural stability and promoting strain-induced CDRX at high strain rates. This behavior is consistent with the refined grain structures and increased LAB/MAB relative fractions observed by EBSD. Similar dispersoid-assisted CDRX behavior has been reported in Al–Mg alloys [24,41]. Although coarse Al_6(Mn,Fe) intermetallic particles (Figure 4.1b) can promote CDRX in partially recrystallized alloys [29], their contribution in the present study is limited due to the fully recrystallized microstructure prior to deformation.

Grain boundaries serve as active sites for subgrain formation via dislocation accumulation and interaction (Figure 4.12e). Accordingly, the high grain-boundary density of the fine annealed microstructure (Figure 4.2) facilitates boundary subdivision and lattice rotation, promoting CDRX at 1 s^{-1}. At 450 °C, despite the high fraction of fine grains ($f_{G<5\,\mu m} \approx 91$ %), the persistence of elongated grains (Figure 4.6d) indicates sluggish and heterogeneous CDRX. Reduced atomic mobility at this temperature limits dynamic recovery and boundary migration. Consequently, dislocation accumulation outpaces recovery, delaying progressive lattice rotation and complete boundary subdivision [44,50]. At higher temperatures (500-520 °C), recovery and boundary migration became more effective, producing uniform equiaxed grains (Figure 4.6).

The reduction in elongation from 168 % at 500 °C to 135 % at 520 °C at 1 s^{-1} may be primarily attributed to grain growth (Figure 4.7) and reduced grain-boundary stability at the highest temperature. Localized adiabatic heating at high strain rates, as reported in previous studies [12,50], may further contribute to boundary weakening and the associated loss of ductility. Although CDRX refines the microstructure at high strain rates, rapid dislocation accumulation combined with limited recovery time constrains tensile elongation. Nevertheless, at 1 s^{-1} the alloy retains substantial high-strain-rate ductility, reflecting effective strain accommodation through boundary subdivision and grain refinement. While below the classical superplastic threshold, this level of ductility is relevant to deformation under HSBF-representative conditions.

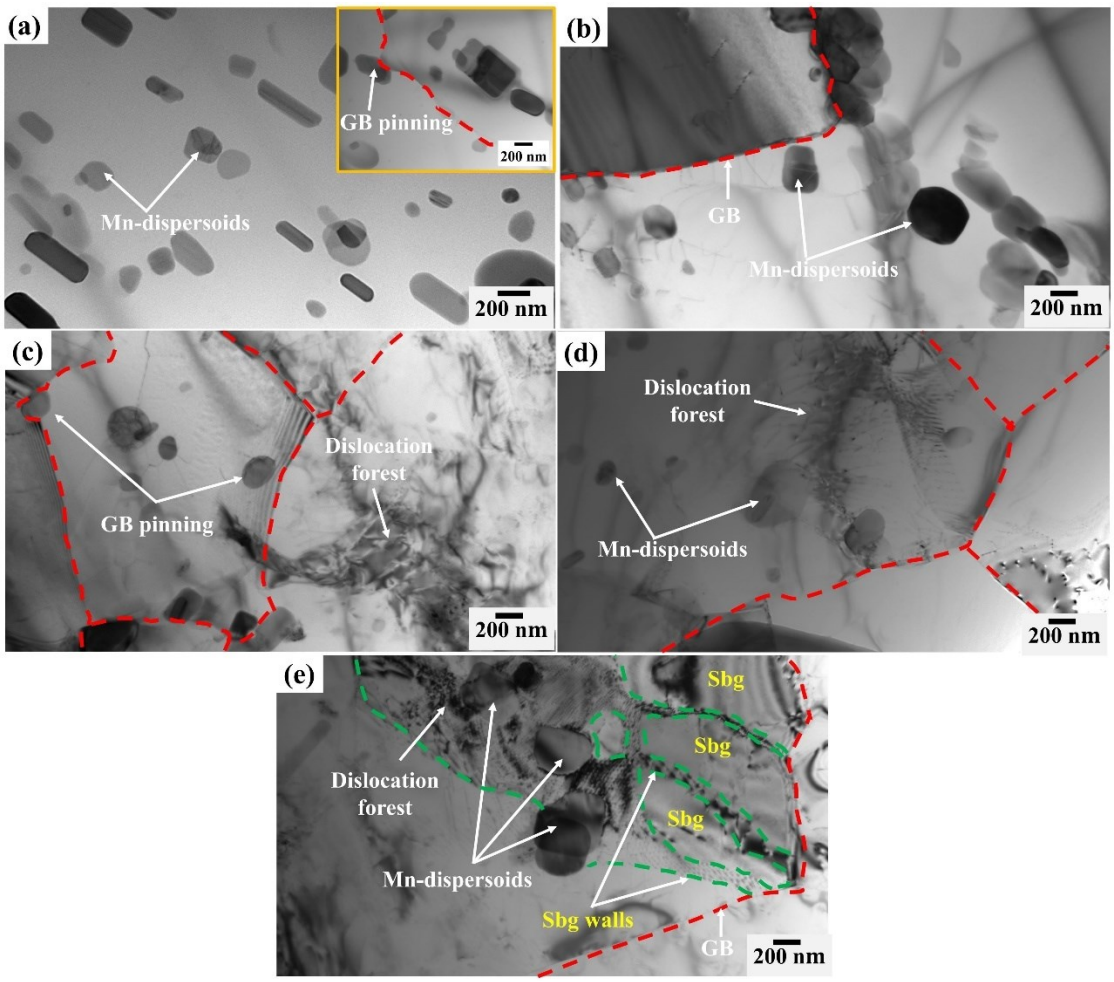


Figure 4.12. Bright-field TEM images showing Mn-rich dispersoids at 500 °C: (a) annealed condition (4 min); (b) deformation at 0.001 s^{-1}; and (c) deformation at 1 s^{-1}, revealing increased dislocation density and substructure formation. (d) Dispersoid–dislocation interaction at 1 s^{-1}. (e) Dislocation structures and subgrains (Sbg) formed during high-strain-rate deformation.

4.4.3 Implications of deformation behavior on HSBF

As discussed above, the Al–Mg–Mn 5xxx alloy exhibited pronounced strain-rate-dependent deformation behavior, with significant variations in flow stress, ductility, and microstructural evolution. These results have important implications for HSBF, where the

alloy must accommodate rapid preforming followed by a lower-strain-rate superplastic gas-blow stage. The high-strain-rate preforming step (≈1 s^{-1}) is particularly critical, as it influences both microstructural state and strain distribution prior to the final forming stage.

Deformation at 1 s^{-1} promoted grain refinement (Figure 4.6d–f), which may facilitate subsequent strain accommodation during the lower-strain-rate forming stage. This effect is especially relevant in geometrically complex regions—such as sharp radii or transition zones—where material may experience sequential high- and low-strain-rate deformation. However, the reduced ductility at 1 s^{-1} (Figure 4.4) highlights the importance of carefully controlling forming temperature and strain-rate transitions to avoid premature localization.

Among the conditions investigated, 500 °C produced the highest ductility at both high and low strain rates (Figure 4.4). At this temperature, the alloy exhibited an m-value of approximately 0.42, exceeding the commonly cited threshold ($m \geq 0.3$) associated with enhanced resistance to strain localization [4]. Under HSBF-relevant conditions, such strain-rate sensitivity is advantageous for maintaining stable flow during rapid preforming and for promoting uniform strain distribution prior to gas-blow forming. The concurrent activation of CDRX at high strain rates and GBS at lower strain rates supports stable deformation across a broad strain-rate range. Within the temperature window examined, 500 °C therefore represents an effective balance between thermal activation and microstructural stability for HSBF-relevant deformation.

From a processing perspective, factors such as sheet thickness, component geometry, and thermal uniformity during rapid forming are expected to influence strain distribution and microstructural evolution. In large and complex components, localized temperature gradients and strain-rate variations may promote non-uniform thinning or cavitation [35,36].

Accordingly, careful control of heating conditions, strain-rate paths, and die design will be important for translating laboratory-scale results to industrial forming practice.

A dual-temperature strategy may offer additional flexibility. Short annealing at 450 °C (4 min) produced the finest recrystallized grain structure (Figure 4. 2), increasing grain-boundary density and promoting strain-induced boundary subdivision. However, deformation at 450 °C resulted in limited ductility due to lower thermal activation and reduced strain-rate sensitivity ($m \approx 0.3$). Increasing the forming temperature to 500 °C provided improved strain-rate sensitivity ($m \approx 0.4$) and enhanced ductility. This suggests that decoupling annealing and forming temperatures may provide additional control over HSBF performance.

Finally, further alloy optimization may focus on tailoring thermally stable dispersoid populations, particularly Mn-containing dispersoids. As demonstrated (Figure 4.12), these particles contribute to grain-boundary stabilization and promote boundary subdivision under high-strain-rate deformation. Refinement of dispersoid size, morphology, and number density through alloy design and homogenization control may further enhance high-strain-rate formability in conventionally processed Al–Mg–Mn alloys.

4.5. Conclusion

This study systematically investigated the effects of temperature and strain rate on the deformation behavior and microstructural evolution of an Al–Mg–Mn 5xxx alloy under conditions simulating HSBF. The key findings are summarized as follows:

1. Short-time annealing (450-520 ºC, 4 min), coupled with Mn-dispersoid stabilization, produced fine, fully recrystallized grains capable of sustaining high-strain-rate formability without costly alloying additions.
2. Maximum ductility was observed at 500 ºC and 0.001 s^{-1}, owing to an enhanced m-value and stable fine grains that facilitate GBS. Ductility decreased at 450 ºC due to solute-drag–controlled creep, and at 520 °C due to dynamic grain growth.
3. High-strain-rate deformation (1 s^{-1}) promoted further grain refinement via CDRX at all studied temperatures (450–520 °C), while Mn-dispersoids enhanced boundary pinning and CDRX activity, ensuring microstructural stability during deformation.
4. At 500 °C, the alloy exhibits 168 % elongation at 1 s^{-1} and 211 % elongation at 0.001 s^{-1}, corresponding to the high-strain-rate and superplastic regimes, respectively. These results suggest that the alloy may accommodate the strain-rate spectrum relevant to HSBF without premature failure.
5. The findings highlight a viable processing window at 500 °C for integrating Al–Mg–Mn 5xxx alloys into industrial HSBF applications. The combination of fine-grain stability, high-strain-rate formability, and thermal efficiency provides a cost-effective route for the rapid production of complex lightweight automotive components.

Reference

1. Bhatta, L.; Pesin, A.; Zhilyaev, A.P.; Tandon, P.; Kong, C.; Yu, H. Recent development of superplasticity in aluminum alloys: A review. *Metals* 2020, *10*, 77. https://doi.org/10.3390/met10010077.

2. Giuliano, G. *Superplastic Forming of Advanced Metallic Materials*; Woodhead Publishing: Cambridge, UK, 2011. https://doi.org/10.1533/9780857092779.

3. Han, J.; Kang, S.H.; Lee, S.J.; Kawasaki, M.; Lee, H.J.; Ponge, D.; et al. Superplasticity in a lean Fe–Mn–Al steel. *Nat. Commun.* 2017, *8*, 1611. https://doi.org/10.1038/s41467-017-00814-y.

4. Nguyen, N.T.C.; Asghari-Rad, P.; Sathiyamoorthi, P.; Zargaran, A.; Lee, C.S.; Kim, H.S. Ultrahigh high-strain-rate superplasticity in a nanostructured high-entropy alloy. *Nat. Commun.* 2020, *11*, 16601. https://doi.org/10.1038/s41467-020-16601-1.

5. Myshlyaev, M.; Mironov, S.; Korznikova, G.; Konkova, T.; Korznikova, E.; Aletdinov, A.; et al. EBSD study of superplasticity: New insight into a well-known phenomenon. *J. Alloys Compd.* 2022, *898*, 162949. https://doi.org/10.1016/j.jallcom.2021.162949.

6. Motallebi, R.; Savaedi, Z.; Mirzadeh, H. Superplasticity of high-entropy alloys: A review. *Arch. Civ. Mech. Eng.* 2022, *22*, 1–14. https://doi.org/10.1007/s43452-021-00344-x.

7. Mochugovskiy, A.G.; Mikhaylovskaya, A.V.; Zadorognyy, M.Y.; Golovin, I.S. Effect of heat treatment on grain size control, superplasticity, internal friction, and mechanical properties of zirconium-bearing aluminum-based alloy. *J. Alloys Compd.* 2021, *856*, 157455. https://doi.org/10.1016/j.jallcom.2020.157455.

8. Zhang, H.M.; Jiang, P.; Pan, H.J.; Peng, J.; Wang, Z.Z.; Yan, K.T.; et al. Dynamic recrystallization-dependent high-temperature tensile properties and deformation mechanisms in Al–Mg–Sc–Zr alloys. *Mater. Sci. Eng. A* 2023, *880*, 145304. https://doi.org/10.1016/j.msea.2023.145304.

9. Kweitsu, E.K.; Sarkar, D.K.; Chen, X.G. A short review on superplasticity of aluminum alloys. *Eng. Proc.* 2023, *43*, 43. https://doi.org/10.3390/engproc2023043043.

10. Song, C.R.; Dong, B.X.; Zhang, S.Y.; Yang, H.Y.; Liu, L.; Kang, J.; et al. Recent progress of Al–Mg alloys: Forming and preparation process, microstructure manipulation and application. *J. Mater. Res. Technol.* 2024, *31*, 3255–3286. https://doi.org/10.1016/j.jmrt.2024.07.051.

11. Chuvil'deev, V.N.; Gryaznov, M.Y.; Shotin, S.V.; Nokhrin, A.V.; Likhnitskii, C.V.; Nagicheva, G.S.; et al. Effect of Sc/Zr ratio on superplastic behavior of ultrafine-grained Al–6%Mg alloys. *Mater. Sci. Eng. A* 2024, *898*, 146409. https://doi.org/10.1016/j.msea.2024.146409.

12. Nieh, T.G.; Wadsworth, J.; Sherby, O.D. *Superplasticity in Metals and Ceramics*, 1st ed.; Cambridge University Press: New York, NY, USA, 1997.

13. Mikhaylovskaya, A.V.; Yakovtseva, O.A.; Irzhak, A.V. The role of grain boundary sliding and intragranular deformation mechanisms for a steady stage of superplastic flow in Al–Mg-based alloys. *Mater. Sci. Eng. A* 2022, *833*, 142524. https://doi.org/10.1016/j.msea.2021.142524.

14. Liu, C.W.; Lee, S.; Chou, D.; Hsu, S.H.; Chu, C.L. Dimensional accuracy in quick plastic forming of aluminum alloy using demolding mechanism. *Adv. Mech. Eng.* 2021, *13*, 1–11. https://doi.org/10.1177/16878140211021731.

15. Yakovtseva, O.A.; Kishchik, A.A.; Cheverikin, V.V.; Kotov, A.D.; Mikhaylovskaya, A.V. The mechanisms of high-strain-rate superplastic deformation of Al–Mg-based alloy. *Mater. Lett.* 2022, *325*, 132883. https://doi.org/10.1016/j.matlet.2022.132883.

16. Nieh, T.G.; Hsiung, L.M.; Wadsworth, J.; Kaibyshev, R. High strain rate superplasticity in a continuously recrystallized Al–6%Mg–0.3%Sc alloy. *Acta Mater.* 1998, *46*, 2789–2800. https://doi.org/10.1016/S1359-6454(97)00452-7.

17. McNelley, T.R.; Swisher, D.L.; Pérez-Prado, M.T. Deformation bands and the formation of grain boundaries in a superplastic aluminum alloy. *Metall. Mater. Trans. A* 2002, *33*, 279–290. https://doi.org/10.1007/s11661-002-0089-2.

18. Perevezentsev, V.N.; Rybin, V.V.; Chuvil'deev, V.N. The theory of structural superplasticity—I. The physical nature of the superplasticity phenomenon. *Acta Metall. Mater.* 1992, *40*, 887–894. https://doi.org/10.1016/0956-7151(92)90065-M.

19. Astanin, V.V.; Bobruk, E.V.; Ramazanov, I.A.; Abramova, M.M.; Zaripov, N.G.; Enikeev, N.A. High strain-rate superplasticity of ultrafine-grained Al–Mg–Mn–Zn–Zr alloy. *Lett. Mater.* 2023, *13*, 408–413. https://doi.org/10.22226/2410-3535-2023-4-408-413.

20. Myshlyaev, M.; Mironov, S.; Korznikova, G.; Konkova, T.; Korznikova, E.; Aletdinov, A.; et al. EBSD study of superplastically strained Al–Mg–Li alloy. *Mater. Lett.* 2020, *275*, 128063. https://doi.org/10.1016/j.matlet.2020.128063.

21. Chinh, N.Q.; Murashkin, M.Y.; Bobruk, E.V.; Lábár, J.L.; Gubicza, J.; Kovács, Z.; et al. Ultralow-temperature superplasticity and its novel mechanism in ultrafine-grained Al alloys. *Mater. Res. Lett.* 2021, *9*, 475–482. https://doi.org/10.1080/21663831.2021.1976293.

22. Bobruk, E.V.; Zaripov, N.G.; Ramazanov, I.A.; Chinh, N.Q.; Valiev, R.Z. Low-temperature superplasticity of ultrafine-grained aluminum alloys: Recent discoveries and innovative potential. *Materials* 2024, *17*, 3311. https://doi.org/10.3390/ma17133311.

23. Sun, Y.B.; Chen, X.P.; Xie, J.; Wang, C.; An, Y.F.; Liu, Q. High strain rate superplasticity and secondary strain hardening of Al–Mg–Sc–Zr alloy produced by friction stir processing. *Mater. Today Commun.* 2022, *33*, 104217. https://doi.org/10.1016/j.mtcomm.2022.104217.

24. Mikhaylovskaya, A.V.; Kishchik, A.A.; Kotov, A.D.; Rofman, O.V.; Tabachkova, N.Y. Precipitation behavior and high strain rate superplasticity in a novel fine-grained aluminum-based alloy. *Mater. Sci. Eng. A* 2019, *760*, 37–46. https://doi.org/10.1016/j.msea.2019.05.099.

25. Algendy, A.Y.; Liu, K.; Rometsch, P.; Parson, N.; Chen, X.G. Effects of AlMn dispersoids and $Al_3(Sc,Zr)$ precipitates on the microstructure and ambient/elevated-temperature mechanical properties of hot-rolled AA5083 alloys. *Mater. Sci. Eng. A* 2022, *855*, 143950. https://doi.org/10.1016/j.msea.2022.143950.

26. Yakovtseva, O.; Sitkina, M.; Mosleh, A.O.; Mikhaylovskaya, A. High strain rate superplasticity in Al–Zn–Mg-based alloy: Microstructural design, deformation behavior, and modeling. *Materials* 2020, *13*, 2098. https://doi.org/10.3390/ma13092098.

27. Li, M.; Pan, Q.; Shi, Y.; Sun, X.; Xiang, H. High strain rate superplasticity in an Al–Mg–Sc–Zr alloy processed via simple rolling. *Mater. Sci. Eng. A* 2017, *687*, 298–305. https://doi.org/10.1016/j.msea.2017.01.091.

28. Mikhaylovskaya, A.V.; Esmaeili Ghayoumabadi, M.; Mochugovskiy, A.G. Superplasticity and mechanical properties of Al–Mg–Si alloy doped with eutectic-forming Ni and Fe, and dispersoid-forming Sc and Zr elements. *Mater. Sci. Eng. A* 2021, *817*, 141319. https://doi.org/10.1016/j.msea.2021.141319.

29. Kishchik, A.A.; Mikhaylovskaya, A.V.; Kotov, A.D.; Rofman, O.V.; Portnoy, V.K. Al–Mg–Fe–Ni-based alloy for high strain rate superplastic forming. *Mater. Sci. Eng. A* 2018, *718*, 190–197. https://doi.org/10.1016/j.msea.2018.01.099.

30. Bagherpour, E.; Pardis, N.; Reihanian, M.; Ebrahimi, R. An overview on severe plastic deformation: Research status, techniques classification, microstructure evolution, and applications. *Int. J. Adv. Manuf. Technol.* 2019, *100*, 1647–1694. https://doi.org/10.1007/s00170-018-2652-z.

31. Sotoudeh, K.; Bate, P.S. Diffusion creep and superplasticity in aluminium alloys. *Acta Mater.* 2010, *58*, 1909–1920. https://doi.org/10.1016/j.actamat.2009.11.034.

32. Pérez-Prado, M.T.; González-Doncel, G.; Ruano, O.A.; McNelley, T.R. Texture analysis of the transition from slip to grain boundary sliding in a discontinuously recrystallized superplastic aluminum alloy. *Acta Mater.* 2001, *49*, 2259–2268. https://doi.org/10.1016/S1359-6454(01)00128-8.

33. McNelley, T.R. Friction stir processing (FSP) and superplasticity. *Lett. Mater.* 2015, *5*, 246–252. https://doi.org/10.22226/2410-3535-2015-3-246-252.

34. Samberger, S.; Weißensteiner, I.; Stemper, L.; Kainz, C.; Uggowitzer, P.J.; Pogatscher, S. Fine-grained aluminium crossover alloy for high-temperature sheet forming. *Acta Mater.* 2023, *253*, 118952. https://doi.org/10.1016/j.actamat.2023.118952.

35. Aleyari, A.; Majidi, O.; Bombardier, N.; Pham, X.T.; Jahazi, M. Finite element and experimental analysis of the preheating stage of high-speed blow forming (HSBF) process. *J. Manuf. Process.* 2020, *49*, 10–17. https://doi.org/10.1016/j.jmapro.2019.10.009.

36. Majidi, O.; Jahazi, M.; Bombardier, N. Finite element simulation of high-speed blow forming of an automotive component. *Metals* 2018, *8*, 901. https://doi.org/10.3390/met8110901.

37. Gobber, F.S.; Tancau, A.; Scintilla, L.D.; Fontana, M.; Actis Grande, M. Design of a test rig for the characterization of friction and wear in hot-metal gas-forming of AA5083 aluminium sheets. *Int. J. Light. Mater. Manuf.* 2025, *8*, 241–251. https://doi.org/10.1016/j.ijlmm.2024.09.002.

38. Fuerth, Z.; Green, D.E.; Altenhof, W.J. A novel phenomenological material model and calibration for high-temperature material behaviour of AA5083. *Proc. Inst. Mech. Eng. Part L J. Mater. Des. Appl.* 2025. https://doi.org/10.1177/14644207251340061.

39. Yi, L.; Gu, Z.; Yu, G.; Li, X.; Tang, Z.; Zhao, Y. Damage behavior and performance analysis of Al5083 alloy in superplastic bulging. *Eng. Fail. Anal.* 2024, *164*, 108732. https://doi.org/10.1016/j.engfailanal.2024.108732.

40. Portnoy, V.K.; Rylov, D.S.; Levchenko, V.S.; Mikhaylovskaya, A.V. The influence of chromium on the structure and superplasticity of Al–Mg–Mn alloys. *J. Alloys Compd.* 2013, *581*, 313–317. https://doi.org/10.1016/j.jallcom.2013.07.075.

41. Mikhaylovskaya, A.V.; Yakovtseva, O.A.; Golovin, I.S.; Pozdniakov, A.V.; Portnoy, V.K. Superplastic deformation mechanisms in fine-grained Al–Mg-based alloys. *Mater. Sci. Eng. A* 2015, *627*, 31–41. https://doi.org/10.1016/j.msea.2014.12.099.

42. Shi, C.; Chen, X.G. Hot workability and processing maps of 7150 aluminum alloys with Zr and V additions. *J. Mater. Eng. Perform.* 2015, *24*, 2126–2139. https://doi.org/10.1007/s11665-015-1478-1.

43. Shakiba, M.; Parson, N.; Chen, X.G. Hot deformation behavior and rate-controlling mechanism in dilute Al–Fe–Si alloys with minor additions of Mn and Cu. *Mater. Sci. Eng. A* 2015, *636*, 572–581. https://doi.org/10.1016/j.msea.2015.04.029.

44. McQueen, H.J.; Ryan, N.D. Constitutive analysis in hot working. *Mater. Sci. Eng. A* 2002, *322*, 43–63. https://doi.org/10.1016/S0921-5093(01)01117-0.

45. Kweitsu, E.K.; Sarkar, D.K.; Algendy, A.Y.; Chen, X.G.; Veilleux, J.; Bombardier, N. Effect of annealing time on grain structure evolution and superplastic response of Al–Mg 5xxx alloys. *Materials* 2024, *17*, 5492. https://doi.org/10.3390/ma17225492.

46. Kotov, A.D.; Mikhaylovskaya, A.V.; Kishchik, M.S.; Tsarkov, A.A.; Aksenov, S.A.; Portnoy, V.K. Superplasticity of high-strength Al-based alloys produced by thermomechanical treatment. *J. Alloys Compd.* 2016, *688*, 336–344. https://doi.org/10.1016/j.jallcom.2016.07.045.

47. Zou, G.; Zhang, R.; Wang, W.; Li, J.; Ye, L. Understanding effects of deformation parameters on dynamic recrystallization-dependent superplasticity in an Al–Cu–Li alloy. *Mater. Des.* 2025, *252*, 113734. https://doi.org/10.1016/j.matdes.2025.113734.

48. Duan, Y.; Xu, G.; Zhou, L.; Xiao, D.; Deng, Y.; Yin, Z.; et al. Achieving high superplasticity of a traditional thermomechanically processed non-superplastic Al–Zn–Mg alloy sheet by low Sc additions. *J. Alloys Compd.* 2015, *638*, 364–373. https://doi.org/10.1016/j.jallcom.2015.03.090.

49. Hsiao, I.C.; Huang, J.C. Deformation mechanisms during low- and high-temperature superplasticity in 5083 Al–Mg alloy. *Metall. Mater. Trans. A* 2002, *33*, 1373–1384. https://doi.org/10.1007/s11661-002-0062-0.

50. Gourdet, S.; Montheillet, F. A model of continuous dynamic recrystallization. *Acta Mater.* 2003, *51*, 2685–2699. https://doi.org/10.1016/S1359-6454(03)00078-8.

51. Humphreys, F.J.; Rohrer, G.S.; Rollett, A.D. *Recrystallization and Related Annealing Phenomena*, 3rd ed.; Elsevier: Amsterdam, The Netherlands, 2017.

52. Callister, W.D.; Rethwisch, D.G. *Materials Science and Engineering: An Introduction*, 10th ed.; Wiley: New York, NY, USA, 2020.

53. Attallah, M.M.; Strangwood, M.; Davis, C.L. Influence of the heating rate on the initiation of primary recrystallization in a deformed Al–Mg alloy. *Scr. Mater.* 2010, *63*, 371–374. https://doi.org/10.1016/j.scriptamat.2010.04.016.

54. Kishchik, A.A.; Mikhaylovskaya, A.V.; Levchenko, V.S.; Portnoy, V.K. Formation of microstructure and superplasticity of Al–Mg-based alloys. *Phys. Met. Metallogr.* 2017, *118*, 96–103. https://doi.org/10.1134/S0031918X16120085.

55. Liu, K.; Chen, X.G. Development of Al–Mn–Mg 3004 alloy for applications at elevated temperature via dispersoid strengthening. *Mater. Des.* 2015, *84*, 340–350. https://doi.org/10.1016/j.matdes.2015.06.140.

56. Algendy, A.Y.; Liu, K.; Chen, X.G. Effect of Mn-bearing dispersoids on tensile properties and recrystallization resistance of Al–3Mg–0.8Mn rolled alloy. *Adv. Eng. Mater.* 2023, *25*, 2300667. https://doi.org/10.1002/adem.202300667.

57. Kral, P.; Dvorak, J.; Kvapilova, M.; Horita, Z.; Sklenicka, V. Microstructure changes in superplastically deformed ultrafine-grained Al–3Mg–0.2Sc alloy. *Lett. Mater.* 2015, *5*, 306–312. https://doi.org/10.22226/2410-3535-2015-3-306-312.

58. Taleff, E.M.; Henshall, G.A.; Nieh, T.G.; Lesuer, D.R.; Wadsworth, J. Warm-temperature tensile ductility in Al–Mg alloys. *Metall. Mater. Trans. A* 1998, *29*, 1081–1091. https://doi.org/10.1007/s11661-998-1017-x.

59. Koju, R.K.; Mishin, Y. Atomistic study of grain-boundary segregation and grain-boundary diffusion in Al–Mg alloys. *Acta Mater.* 2020, *201*, 596–603. https://doi.org/10.1016/j.actamat.2020.10.029.

60. Jeong, H.T.; Park, H.K.; Kang, H.S.; Kim, W.J. Operation of solute-drag creep in an AlCoCrFeMnNi high-entropy alloy and enhanced hot workability. *J. Alloys Compd.* 2020, *824*, 153829. https://doi.org/10.1016/j.jallcom.2020.153829.

61. McNelley, T.R.; Oh-Ishi, K.; Zhilyaev, A.P.; Swaminathan, S.; Krajewski, P.E.; Taleff, E.M. Characteristics of the transition from grain-boundary sliding to solute drag creep in superplastic AA5083. *Metall. Mater. Trans. A* 2008, *39*, 50–64. https://doi.org/10.1007/s11661-007-9401-5.

62. Chokshi, A.H. Grain boundary processes in strengthening, weakening, and superplasticity. *Adv. Eng. Mater.* 2020, *22*, 1900748. https://doi.org/10.1002/adem.201900748.

63. Li, H.; Liu, X.; Sun, Q.; Ye, L.; Zhang, X. Superplastic deformation mechanisms in fine-grained 2050 Al–Cu–Li alloys. *Materials* 2020, *13*, 2705. https://doi.org/10.3390/ma13122705.

64. Yakovtseva, O.A.; Mikhaylovskaya, A.V.; Mochugovskiy, A.G.; Cheverikin, V.V.; Portnoy, V.K. Superplastic deformation mechanisms in high-magnesium-containing aluminum alloy. *Mater. Sci. Forum* 2016, *838–839*, 66–71. https://doi.org/10.4028/www.scientific.net/MSF.838-839.66.

65. Mikhaylovskaya, A.V.; Yakovtseva, O.A.; Cheverikin, V.V.; Kotov, A.D.; Portnoy, V.K. Superplastic behaviour of Al–Mg–Zn–Zr–Sc-based alloys at high strain rates. *Mater. Sci. Eng. A* 2016, *659*, 225–233. https://doi.org/10.1016/j.msea.2016.02.061.

66. Kulas, M.A.; Green, W.P.; Taleff, E.M.; Krajewski, P.E.; McNelley, T.R. Deformation mechanisms in superplastic AA5083 materials. *Metall. Mater. Trans. A* 2006, *37*, 645–655. https://doi.org/10.1007/s11661-006-0036-8.

67. Shin, D.H.; Joo, Y.J.; Kim, W.J.; Lee, C.S. Microstructural evolution during superplastic deformation of a 7475 Al alloy. *J. Mater. Sci.* 1998, *33*, 3073–3078. https://doi.org/10.1023/A:1004383420256.

68. Huang, K.; Logé, R.E. A review of dynamic recrystallization phenomena in metallic materials. *Mater. Des.* 2016, *111*, 548–574. https://doi.org/10.1016/j.matdes.2016.09.012.

69. Dehghan-Manshadi, A.; Hodgson, P.D. Dependency of recrystallization mechanism on the initial grain size. *Metall. Mater. Trans. A* 2008, *39*, 2830–2840. https://doi.org/10.1007/s11661-008-9656-5.

Chapter 5

Strain-Rate-Dependent Cavitation in Al–Mg–Mn 5xxx Alloys: Mechanistic Insights for High-Speed Blow Forming

Abstract

Cavitation damage during high-temperature deformation limits the formability and damage tolerance of Al–Mg–Mn 5xxx alloys under the wide strain-rate conditions encountered in high-speed blow forming (HSBF). This study investigates the strain-rate-dependent cavitation behavior of two Al–Mg–Mn alloys containing 0.74 and 1.18 wt.% Mn, deformed at 500 °C and strain rates ranging from 0.001 to 1 s^{-1}. The results reveal a systematic transition in cavitation behavior with increasing strain rate. At 0.001 s^{-1}, diffusion-assisted cavity growth and coalescence are promoted during grain-boundary-sliding-assisted deformation, with cavity area fractions reaching approximately 4.5 % and 7.6 % in AlMg–0.74Mn and AlMg–1.18Mn, respectively. Increasing strain rate progressively suppresses diffusion-assisted cavity growth and coalescence, reducing the cavity area fractions to approximately 0.14–1.0 % at 1 s^{-1}. However, cavitation is not eliminated at high strain rate; rather, cavity nucleation persists, while the limited time available for subsequent growth and coalescence results in a predominantly fine and directionally extended microvoid population. Despite exhibiting a higher cavity nucleation density due to its larger intermetallic compound (IMC) population, AlMg–1.18Mn maintains superior ductility because its finer and more stable grain structure accommodates greater cavity accumulation while delaying cavity linkage and damage localization. This study establishes a strain-rate-dependent cavitation

framework linking deformation mechanisms, microstructural stability, and damage evolution under HSBF-relevant conditions. The findings further highlight that damage-tolerant alloy design should control excessive coarse IMCs while promoting stable fine-grained microstructures.

Keywords: Al–Mg–Mn 5xxx alloys; Cavitation; Strain-rate effects; Grain boundary sliding; High-speed blow forming.

5.1 Introduction

High-speed blow forming (HSBF) has emerged as an advanced route for producing complex-shaped lightweight aluminum components with shorter cycle times than conventional superplastic forming (SPF). Unlike SPF, which relies on deformation at very low strain rates [1,2], HSBF involves a hybrid deformation path. It combines rapid forming with subsequent gas-pressure slow forming to complete part shaping and improve dimensional accuracy [3,4]. This process exposes the sheet to a wide strain-rate range, typically from 1 s^{-1} during rapid forming to 0.001–0.01 s^{-1} during gas-pressure forming. Among candidate materials used for HSBF, Al–Mg–Mn 5xxx alloys are attractive because of their good formability, corrosion resistance, weldability, strength, and cost-effectiveness [5–7]. Their ability to exhibit large elongations above 200% at elevated temperatures also makes them suitable for lightweight automotive structures [5,6,8–11].

Despite these advantages, cavitation remains a major damage mechanism limiting the formability and post-forming integrity of Al–Mg–Mn alloys under HSBF-relevant conditions [3,4]. Cavities formed during high-temperature deformation can reduce load-bearing capacity, accelerate fracture, and compromise component reliability [3,12–18]. This issue is particularly important in HSBF because the material undergoes a broad and non-steady

strain-rate path. Such deformation path can alter the cavity nucleation and growth behavior. At high strain rates, local stress concentrations may promote cavity nucleation at particle–matrix interfaces, while the short deformation time may restrict diffusion-assisted cavity growth. In contrast, at lower strain rates, longer deformation times and enhanced diffusion may promote cavity enlargement and linkage. Therefore, understanding cavitation evolution across HSBF-relevant strain-rate regimes is essential for improving forming reliability and damage tolerance.

Cavitation during high-temperature deformation is controlled by coupled nucleation, growth, and coalescence processes. Cavities commonly nucleate at grain boundaries, triple junctions, and particle–matrix interfaces due to local strain incompatibility, stress concentration, and interfacial decohesion [13,17–21]. Their subsequent growth depends on strain level, grain structure, particle distribution, and the active deformation mechanism [13,18,22,23]. Under low strain-rate superplastic conditions, grain-boundary sliding (GBS) enables high ductility [2,24,25]. However, GBS also generates local incompatibilities at grain boundaries and triple junctions, which require accommodation by diffusion creep and/or dislocation slip [26,27]. When accommodation is insufficient, cavity growth and coalescence are promoted [18,28]. Intermetallic particles (IMCs) can further accelerate cavity nucleation by acting as stress concentration sites [17–20,29]. Grain-structure stability also influences resistance to cavity enlargement and linkage. Thus, high elongation alone is insufficient to ensure defect-free forming; the mechanisms controlling cavitation should be considered.

Most existing studies on cavitation in Al–Mg alloys have focused on conventional SPF conditions, where deformation occurs at steady low strain rates. Under these conditions, cavity growth is often governed by diffusion-assisted processes associated with GBS

[18,22,23,30,31]. However, cavitation behavior under HSBF-relevant conditions, where the material may experience transitions between high- and low-strain-rate deformation regimes, remains insufficiently understood. In particular, it is unclear how cavity nucleation, growth and coalescence evolve across the wide strain-rate range from 0.001 to 1 s^{-1}. Furthermore, the coupled influence of intermetallic particles and grain-structure stability on damage evolution under HSBF-relevant conditions has not been systematically studied. This knowledge gap limits the ability to predict cavitation behavior and optimize alloy design and forming conditions for HSBF applications.

Therefore, this study aims to clarify the strain-rate-dependent transition in cavitation behavior by correlating cavity statistics, grain-structure evolution, and fracture morphology in two Al–Mg–Mn 5xxx alloys with different Mn contents. Tensile deformation was conducted at 500 °C and strain rates ranging from 0.001 to 1 s^{-1}, covering the range relevant to HSBF. Quantitative cavitation analysis, grain-structure characterization by electron backscatter diffraction (EBSD), and fractographic analysis by scanning electron microscopy (SEM) were combined to investigate the roles of intermetallic particles and grain-structure stability in cavity nucleation, damage evolution, and ductility. This approach provides insight into the microstructural factors governing damage tolerance under HSBF-relevant deformation conditions.

5.2 Materials and methods

5.2.1 Materials and hot tensile testing

Two commercial cold-rolled Al–Mg–Mn 5xxx alloy sheets, Al–4.52 wt.% Mg–0.74 wt.% Mn and Al–4.00 wt.% Mg–1.18 wt.% Mn with 0.4 wt.% Si and 0.12 wt.% Fe and trace

Cu, Cr and Ti (≤ 0.1 wt.% each), in the H18 temper were supplied by Verbom Inc. (Valcourt, QC, Canada) [32]. The primary compositional difference between the two alloys is the Mn content. Accordingly, the alloys are designated as AlMg–0.74Mn (low-Mn alloy) and AlMg–1.18Mn (high-Mn alloy).

Dog-bone tensile specimens with a gauge length of 30 mm were machined from the 2 mm-thick sheets along the rolling direction (RD). The specimen geometry was identical to that used in our previous study [32]. Uniaxial tensile tests were conducted at 500 °C using a Gleeble 3800 thermomechanical simulator (Dynamic Systems Inc., New York, USA) at constant strain rates of 0.001, 0.01, and 1 s^{-1}. The selected strain rates correspond to deformation regimes relevant to industrial HSBF, with 1 s^{-1} representing the high strain-rate forming stage and 0.001–0.01 s^{-1} representing the lower strain-rate regime associated with gas-assisted forming.

The deformation temperature of 500 °C was selected because it lies within the typical superplastic forming temperature range for Al–Mg–Mn 5xxx alloys and provides a suitable balance between grain-boundary sliding activity and thermal stability [33–35]. The specimens were rapidly heated to 500 °C within 3 min, held isothermally for 4 min, and subsequently strained to failure under isothermal conditions. Some selected specimens were subjected to the same thermal cycle without deformation to characterize the annealed grain structure prior to tensile testing. Details of the tensile testing procedure, including the measures implemented to ensure temperature uniformity and minimize thermal gradients during testing, are described elsewhere [32]. Each test condition was repeated three times to ensure reproducibility.

5.2.2 Microstructure characterization

The as-received microstructure was examined on samples sectioned parallel to the rolling direction of cold-rolled sheets. The samples were mechanically polished and electroetched in Barker's reagent (3 vol.% HBF_4) at 17 V for 90 s, followed by observation using optical microscopy (OM, Nikon Eclipse ME600, Tokyo, Japan) under polarized light. The area fraction and size distribution of IMCs were quantified from 50 optical micrographs per alloy using ImageJ software.

Cavitation was analyzed on longitudinal thickness sections (RD–ND plane) of fractured specimens, as illustrated in Figure 5. 1. The sections were polished to a mirror-like finish and observed without etching using OM. For each deformation condition, at least 10 fields of view were analyzed at identical magnification to ensure statistical reliability. The cavity area fraction, size, size distribution and number density were determined using image segmentation in ImageJ with consistent threshold parameters across all samples. Cavity size was quantified using the equivalent circular diameter, while D_{90}, defined as the cavity diameter below which 90 % of the measured cavities fall, was calculated to characterize the upper range of the cavity size distribution. Fracture surfaces normal to the tensile direction (Figure 5.1) were examined using SEM (JSM-6480LV, JEOL Inc., Tokyo, Japan) to characterize dimple size, morphology and size distribution. Fractographic analysis was used to complement longitudinal cavitation measurements by revealing microvoid features that may not be fully captured on polished longitudinal sections.

EBSD analysis for the grain structure was performed using an Oxford Symmetry EBSD detector attached to the SEM. EBSD scans were acquired at 20 kV with a step size of 0.5 μm over an area of approximately 300 × 250 μm. Post-deformation EBSD analyses were

conducted on longitudinal thickness sections (RD–ND plane) in the central region of the fractured gauge section (Figure 5.1). This approach enabled direct correlation between grain-structure evolution and damage development. Transmission electron microscopy (TEM; JEM-2100, JEOL, Japan), operated at 200 kV, was used to characterize the size and distribution of Mn-rich dispersoids.

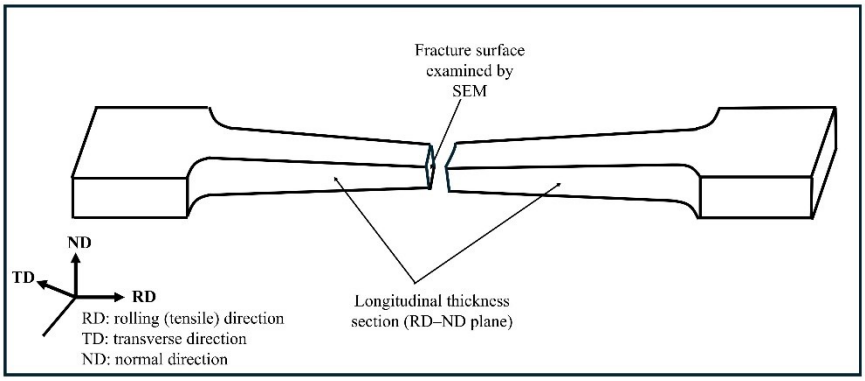


Figure 5.1. Schematic illustration of the fractured tensile specimen showing the longitudinal thickness section (RD–ND plane) used for cavitation and EBSD analyses, and the fracture surface normal to the tensile direction used for SEM fractography

.

5.3 Results

5.3.1 As-received microstructure

Figure 5.2 shows the as-received microstructures of both AlMg–0.74Mn and AlMg–1.18Mn alloys. Polarized-light optical micrographs (Figure5.2a,c) reveal elongated grains along the rolling direction (RD), characteristic of the cold-rolled H18 temper condition. Backscattered electron SEM images (Figure 5.2b,d) show fragmented IMCs, primarily $Al_6(Mn,Fe)$ and few Mg_2Si, distributed and aligned along the RD. Occasional dark gaps are observed around some particle edges, which may be associated with particle pull-out or local

particle–matrix decohesion during sample preparation. However, no clear deformation-induced cavitation is observed before tensile testing.

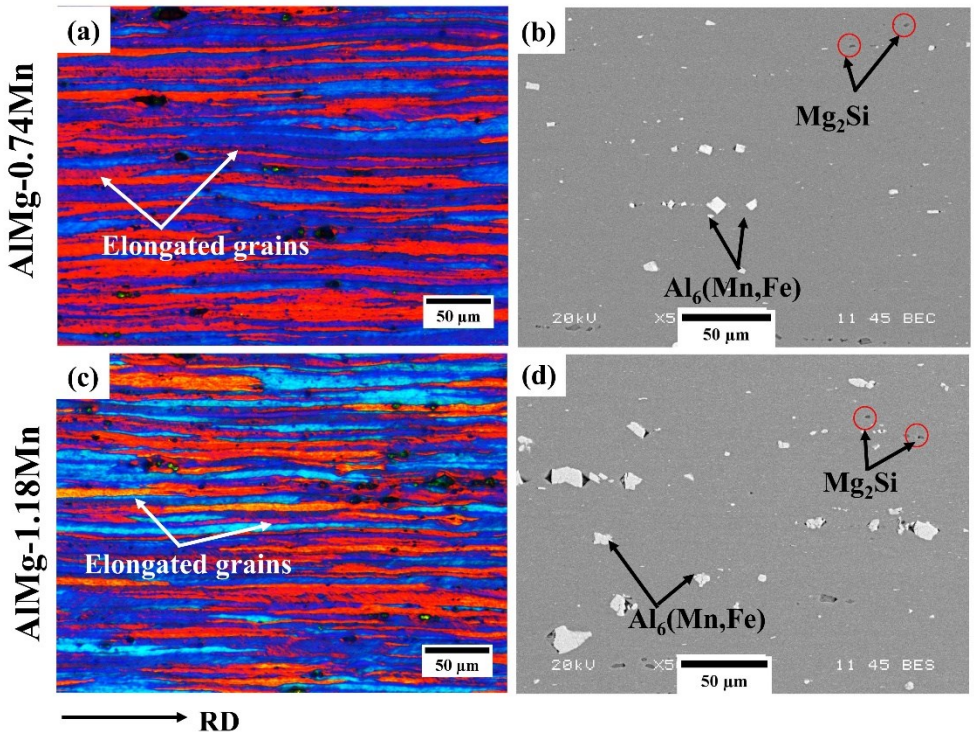


Figure 5.2. As-received microstructures of the AlMg–0.74Mn and AlMg–1.18Mn alloys: (a, c) polarized-light optical micrographs showing elongated grains along the rolling direction, and (b, d) backscattered electron (BSE) micrographs showing fragmented intermetallic particles, mainly $Al_6(Mn,Fe)$ and few Mg_2Si, distributed along the rolling direction.

Figure 5.3 presents the IMC area fraction and size distributions. The total IMC area fraction is higher in AlMg–1.18Mn (2.63 ± 0.32 %) than in AlMg–0.74Mn (1.69 ± 0.18 %), as shown in Figure 5.3a. However, the AlMg–1.18Mn alloy shows a clear shift toward larger particle sizes (Figure 5.3b). The relative fraction of IMCs with equivalent diameters greater

than 20 μm ($f_{\mathrm{IMC}>20\,\mu m}$) is significantly higher in AlMg–1.18Mn (35 %) than in AlMg–0.74Mn (20 %). The combined increase in IMC area fraction and coarse particle population indicates a higher density of particle-related heterogeneities in the high-Mn alloy. These intermetallic particles are expected to act as preferential sites for cavity nucleation during subsequent high-temperature deformation.

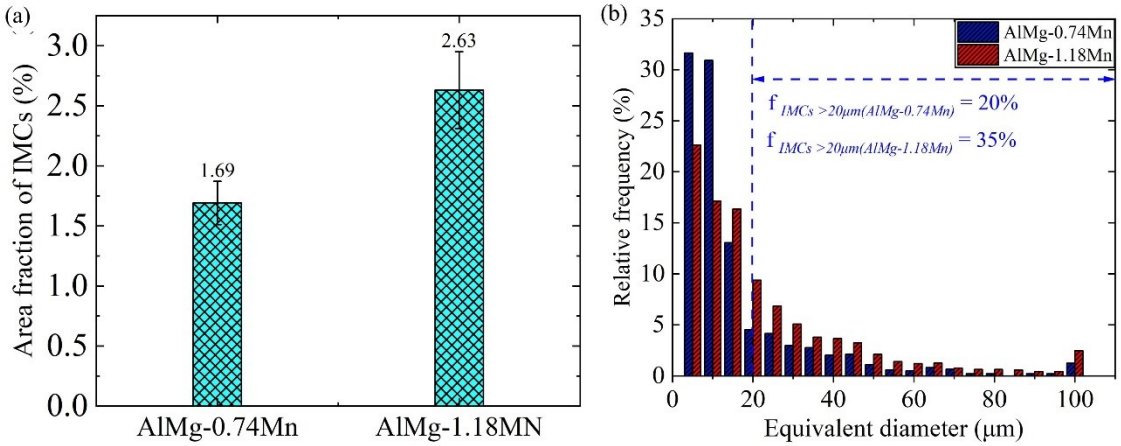


Figure 5.3. Quantitative analysis of intermetallic compounds (IMCs) in AlMg–0.74Mn and Al–1.18Mn alloys. (a) IMC area fraction and (b) equivalent diameter distribution of IMCs. The blue vertical dashed line indicates the 20 μm threshold used to quantify the relative fraction of coarse IMCs.

Figure 5.4 presents TEM micrographs illustrating the presence of Mn-containing dispersoids in the aluminum matrix for both alloys. As previously reported [32], the AlMg–1.18Mn alloy exhibits a higher number density than the AlMg–0.74Mn alloy, with values of 9.3 x 10^{-3} and 4.0 x 10^{-3} μm^{-3}, respectively. In addition, the average dispersoid size is smaller in AlMg–1.18Mn (166 ± 17 nm) than in AlMg–0.74Mn (234 ± 36 nm). This difference is mainly attributed to the higher Mn content in AlMg–1.18Mn alloy, which promotes greater

dispersoid precipitation. The higher density of finer Mn-dispersoids is expected to enhance grain-structure stability through Zener pinning during high-temperature deformation.

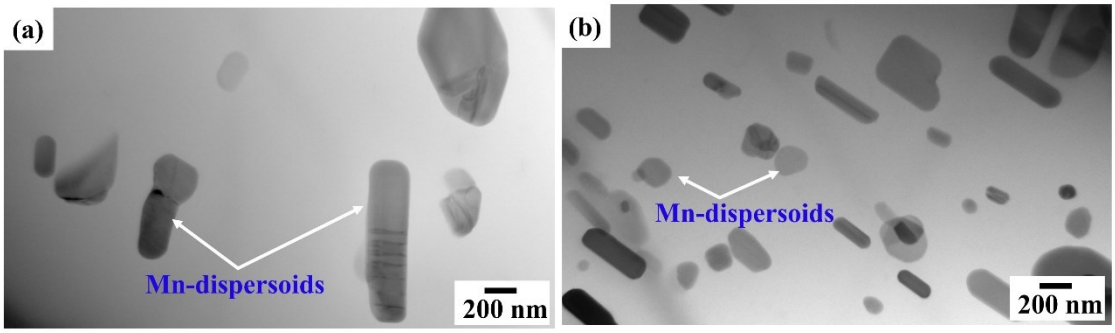


Figure 5.4. Bright-field TEM micrographs revealing Mn-rich dispersoids in (a) AlMg–0.74Mn and (b) AlMg–1.18Mn.

5.3.2 High-temperature deformation behavior

Figure 5.5 summarizes the tensile behavior of the AlMg–0.74Mn and AlMg–1.18Mn alloys at 500 °C over strain rates ranging from 0.001 to 1 s^{-1}. At 0.001 s^{-1}, both alloys exhibit a steady-state flow regime after yielding, with the flow stress of approximately 11 MPa for AlMg–0.74Mn and 10 MPa for AlMg–1.18Mn (Figure 5.5a). This steady-state behavior suggests that strain hardening is effectively balanced by recovery during low strain-rate deformation. Increasing the strain rate to 0.01 s^{-1} increases the flow stress and produces a more pronounced initial strain-hardening stage, with the peak flow stresses increasing to 28 MPa and 25 MPa, respectively (Figure 5.5b). This response indicates that the reduced deformation time at higher strain rate limits time-dependent recovery processes, resulting in a more pronounced initial strain-hardening response.

At the highest strain rate of 1 s^{-1}, the deformation is characterized by pronounced strain hardening followed by flow softening, and the peak flow stress further increases to 53

MPa for AlMg–0.74Mn and 50 MPa for AlMg–1.18Mn (Figure 5.5c). The initial strain hardening reflects rapid dislocation accumulation under high strain-rate deformation, while the subsequent flow softening likely results from the combined effects of dynamic recovery, grain subdivision, and localized deformation accommodation. These features indicate a transition from diffusion-assisted superplastic flow at low strain rates toward a more dislocation-mediated deformation regime at 1 s^{-1}.

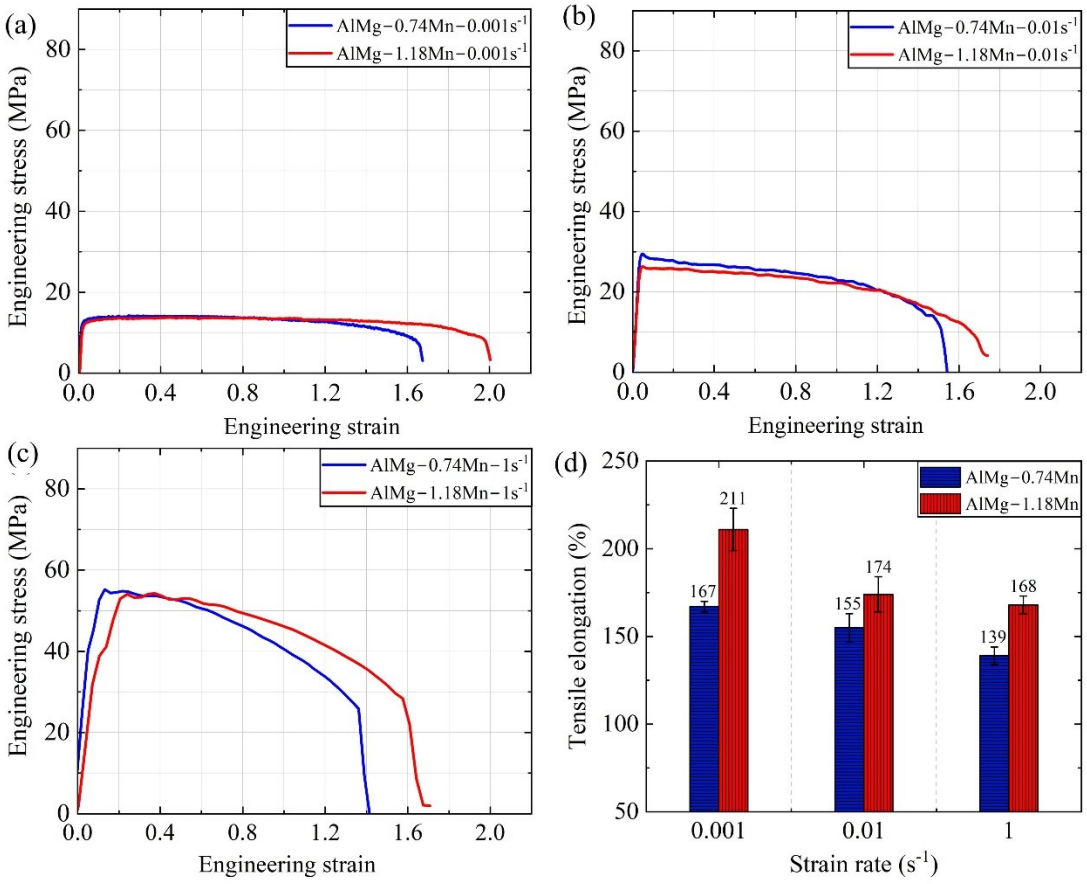


Figure 5.5. Engineering stress–strain curves of the alloys deformed at 500 °C at different strain rates: (a) 0.001 s^{-1}, (b) 0.01 s^{-1}, and (c) 1 s^{-1}.

Figure 5.5d shows the tensile elongations as a function of the strain rate. For both alloys, elongation decreases with increasing strain rate. However, AlMg–1.18Mn consistently exhibits higher ductility across the entire strain-rate range. At 0.001 s^{-1}, elongations reach 211 ± 12% for AlMg–1.18Mn and 167 ± 3% for AlMg–0.74Mn. These values decrease to 168 ± 5% and 139 ± 5%, respectively, at 1 s^{-1}. Notably, both alloys achieve elongations largely exceeding 100% even at 1 s^{-1}, indicating substantial ductility under high strain-rate deformation conditions. The consistently higher elongation of AlMg–1.18Mn suggests improved resistance to premature strain localization, likely associated with its finer and more stable grain structure.

To support interpretation of the strain-rate-dependent cavitation behavior, the strain-rate sensitivity coefficient (m) was evaluated using Eq. (1) [6,36]:

$$m = \left(\frac{\partial ln\sigma}{\partial ln\dot{\varepsilon}}\right)$$

where σ is the flow stress and $\dot{\varepsilon}$ is the strain rate. The flow stress σ was taken at a true strain of 0.10 and used to calculate the m consistent with literature [37,38]. Figure 5.6 shows the flow stress as a function of strain rate and the corresponding local m values. For both alloys, the m-values decrease from approximately 0.48 at low strain rates to about 0.15 at 1 s^{-1}. This decrease is consistent with a reduced contribution of GBS and an increasing role of dislocation-mediated plasticity as the strain rate increases. The m-values of both alloys are almost identical. The strain-rate-dependent deformation behavior shown above is expected to strongly influence grain-structure evolution and cavitation kinetics, which are examined in the following sections.

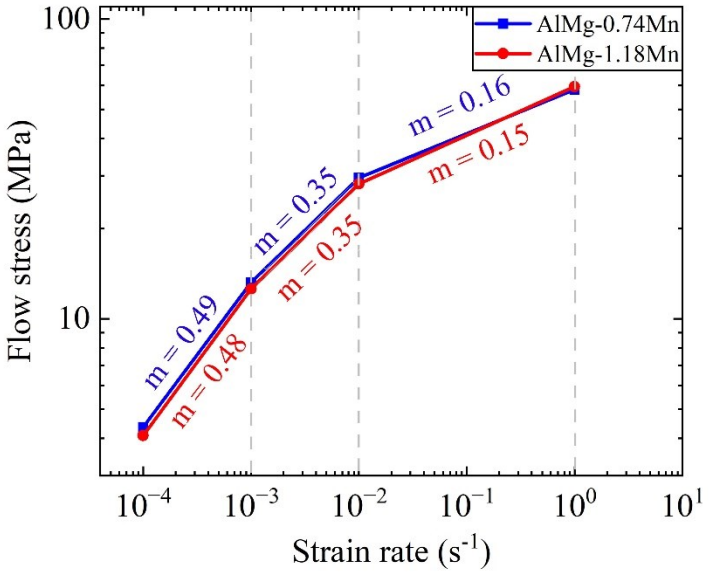


Figure 5.6 Flow stress as a function of strain rate on a logarithmic scale. Local strain-rate sensitivity values (*m*) calculated between adjacent strain-rate intervals are indicated for both alloys.

5.3.3 Grain structure evolution

Figure 5.7 presents the EBSD inverse pole figure (IPF) maps of both alloys following short-term annealing (500 °C, 4 min) and subsequent tensile deformation at 500 °C and strain rates of 0.001 and 1 s^{-1}. The corresponding average grain size and aspect ratio are summarized in Figure 5.8. In the annealed condition (Figure 5.7a,b), both alloys exhibit fully recrystallized microstructures consisting of equiaxed grains with relatively random crystallographic orientations. However, the AlMg–1.18Mn alloy shows a slightly finer grain size of 5.1 ± 0.1 µm compared with 6.7 ± 0.1 µm for AlMg–0.74Mn (Figure 5.8a).

After deformation at 0.001 s^{-1} (Figure 5.7c,d), both alloys exhibit grain coarsening accompanied by grain elongation along the tensile axis. Grain growth is more pronounced in

AlMg–0.74Mn, which reaches an average grain size of 10.2 ± 3.4 μm, compared with 7.3 ± 0.3 μm in AlMg–1.18Mn. Despite this difference in grain size, both alloys show similar grain elongation, with aspect ratios of 2.2 ± 0.6 and 2.1 ± 0.1 for AlMg–0.74Mn and AlMg–1.18Mn, respectively (Figure 5.8b). Notably, AlMg–1.18Mn sustains a higher elongation to failure at 0.001 s^{-1} while retaining a finer grain size and a similar grain aspect ratio, indicating greater grain-structure stability during deformation. The observed coarsening is mainly due to the long deformation time at this low strain rate, which promotes diffusion-assisted grain growth at 500 °C. In addition to these grain-structure changes, non-indexed regions, appearing as black areas in the EBSD maps, are mainly associated with cavities and are evident in both alloys after deformation at 0.001 s^{-1} (Figure 5.7c,d).

Following deformation at 1 s^{-1}, both alloys exhibit a refined and predominantly equiaxed grain structure compared with the annealed condition (Figure 5.7e,f). The average grain size decreases from 6.7 to 4.3 ± 0.7 μm in AlMg–0.74Mn and from 5.1 to 3.4 ± 0.1 μm in AlMg–1.18Mn, while the corresponding grain aspect ratios approach unity, reaching 1.3 and 1.1, respectively (Figure 5.8). The development of a fine, predominantly equiaxed grain structure at 1 s^{-1} suggests that the short deformation time kinetically suppresses diffusion-assisted grain growth, while the high imposed strain rate may promote deformation-induced grain subdivision and/or continuous dynamic recrystallization (CDRX). This interpretation is consistent with the pronounced strain hardening followed by strong softening observed at 1 s^{-1} (Figure 5.5c), reflecting increased dislocation activity followed by dynamic restoration processes associated with the observed grain refinement. The finer and more stable grain structure observed in AlMg–1.18Mn in both the annealed and deformed conditions is consistent with the higher number density of Mn-rich dispersoids in this alloy (Figure 5.4),

which contributes to grain-boundary pinning and restricts grain growth. Overall, the transition from grain coarsening at 0.001 s^{-1} to grain refinement at 1 s^{-1} reflects the combined influence of reduced diffusion time, deformation-induced grain subdivision, and dispersoid-assisted grain-structure stabilization during high-strain-rate deformation [38].

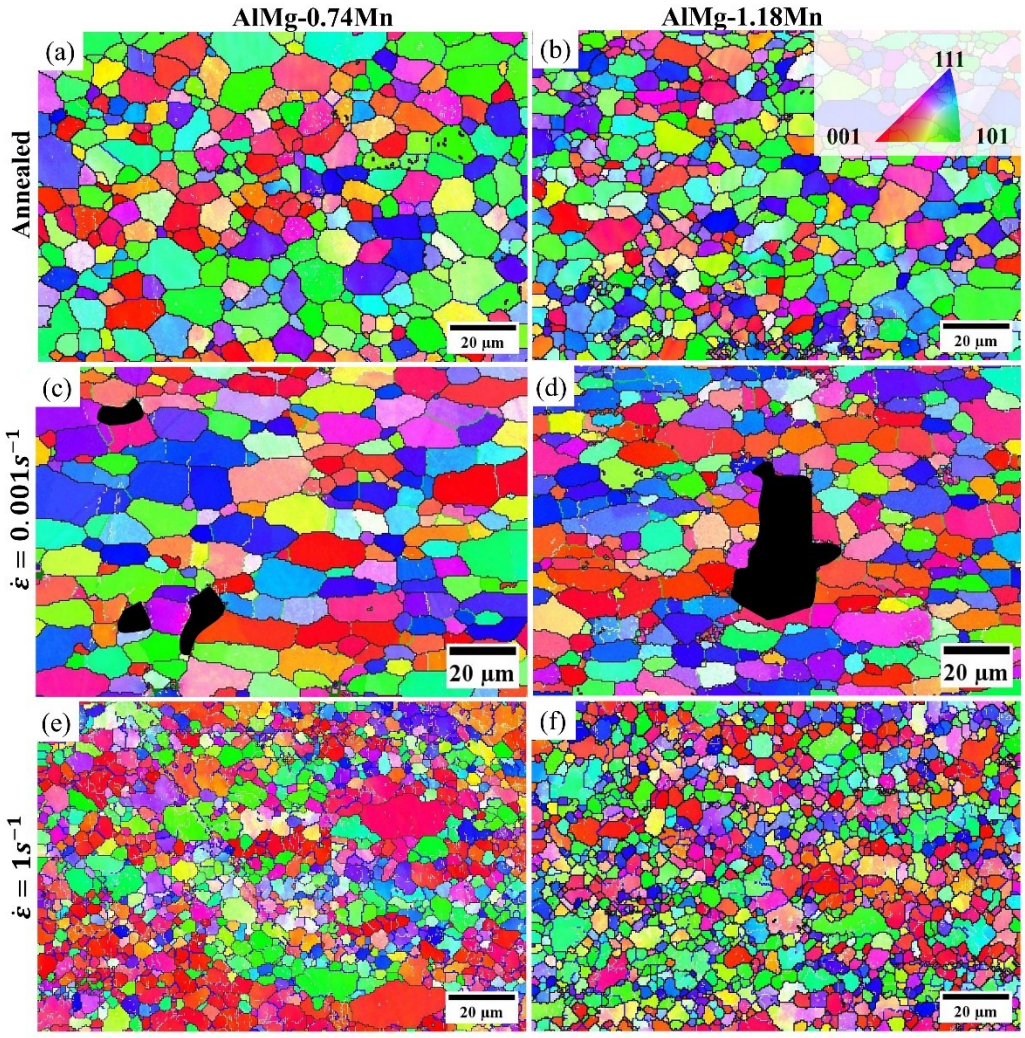


Figure 5.7 EBSD inverse pole figure (IPF) maps comparing the grain structures of the alloys before and after deformation at 500 °C: (a, b) annealed condition, (c, d) after deformation

at 0.001 s^{-1}, and (e, f) after deformation at 1 s^{-1}. Black regions in the IPF maps (c, d) correspond mainly to non-indexed areas associated with cavities.

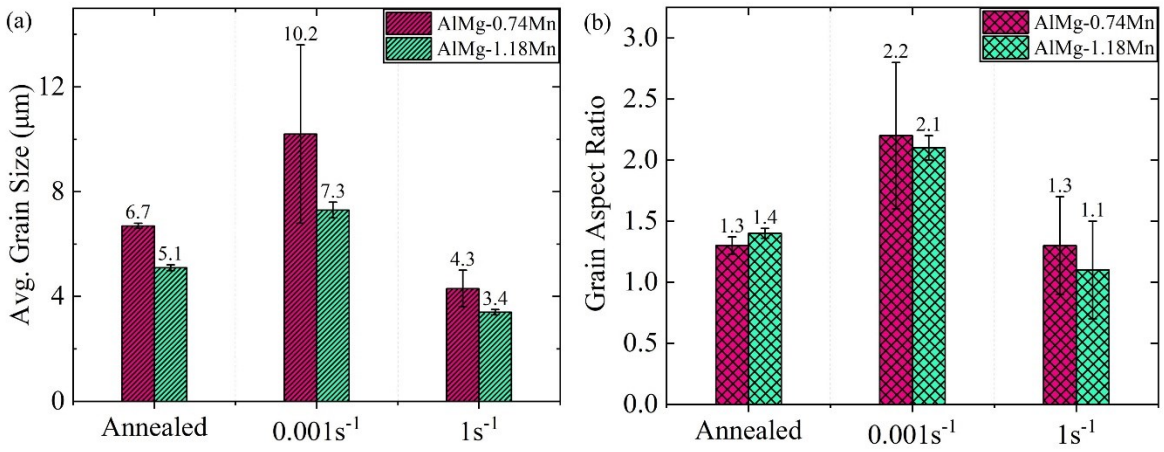


Figure 5.8. Comparison of (a) the average grain size and (b) the grain aspect ratio of AlMg-074Mn and AlMg-1.18Mn alloys in the annealed state and after deformation at 500 °C. Grain coarsening and elongation occurred at 0.001 s^{-1}, while fine, equiaxed grains were retained at 1 s^{-1}.

5.3.4 Strain-rate-dependent cavitation behavior

Cavitation evolution was analyzed using both qualitative microstructural observations and quantitative measurements of cavity area fraction, cavity number density (N_a) and equivalent circular diameter (ECD) distribution. It should be emphasized that the cavitation statistics used for the strain-rate comparison in this section were obtained from fractured specimens and therefore represent the final damage state at fracture rather than cavitation at a common strain level. Thus, the measured cavity area fraction, N_a, and ECD distributions reflect the combined effects of cavity evolution kinetics and the strain accumulated before fracture under each deformation condition. Figure 5.9 presents optical micrographs of cavities observed on longitudinal sections of fractured specimens deformed

at 500 °C and strain rates of 0.001, 0.01, and 1 s^{-1}, while the corresponding cavity area fraction and N_a are summarized in Figure 5.10.

At 0.001 s^{-1}, extensive cavitation is observed in both alloys, characterized by large, irregular cavities distributed throughout the matrix, with some cavities associated with IMCs (Figure 5.9a,d). The prolonged deformation time promotes cavity growth and coalescence, with many cavities linking transverse to the tensile direction, as indicated by the red circles in Figure 5.9a,d. This observation is consistent with the cavity area fraction, which reaches its maximum values of 4.45 ± 2.0 % in AlMg–0.74Mn and 7.57 ± 2.7 % in AlMg–1.18Mn (Figure 5.10a). Similarly, N_a is the highest at this strain rate, reaching approximately 670 cavities mm^{-2} in AlMg–0.74Mn and 1120 cavities mm^{-2} in AlMg–1.18Mn (Figure 5.10b). The higher cavity area fraction and number density in AlMg–1.18Mn are consistent with its higher IMC area fraction and larger population of coarse particles (Figure 5.2), which provide preferential sites for cavity nucleation. However, AlMg–1.18Mn also sustains a higher elongation to failure, indicating that its greater final cavitation level is accompanied by a greater capacity to accommodate cavity accumulation before critical linkage and fracture.

At the intermediate strain rate of 0.01 s^{-1}, both the cavity size and overall extent of cavitation decrease compared with 0.001 s^{-1} (Figure 5.9b,e). Cavities are more frequently associated with particle–matrix interfaces, while cavities within the matrix and along grain boundaries are less prevalent. Cavities elongated along the tensile direction, indicated by blue rectangles, as well as cavities oriented transverse to the tensile axis, indicated by red circles, are observed, revealing a mixed cavity morphology. The cavity area fraction decreases to 3.2 ± 0.8 % in AlMg–0.74Mn and 3.5 ± 1.3 % in AlMg–1.18Mn (Figure 5.10a). The corresponding $N_a$values also decrease to approximately 560 cavities mm^{-2} in AlMg–0.74Mn and 550 cavities mm^{-2} in AlMg–1.18Mn (Figure 5.10b). Despite sustaining a higher

elongation to failure, AlMg–1.18Mn exhibits a final cavity area fraction and N_a comparable to those of AlMg–0.74Mn, indicating a greater capacity to delay critical cavity accumulation and linkage during deformation.

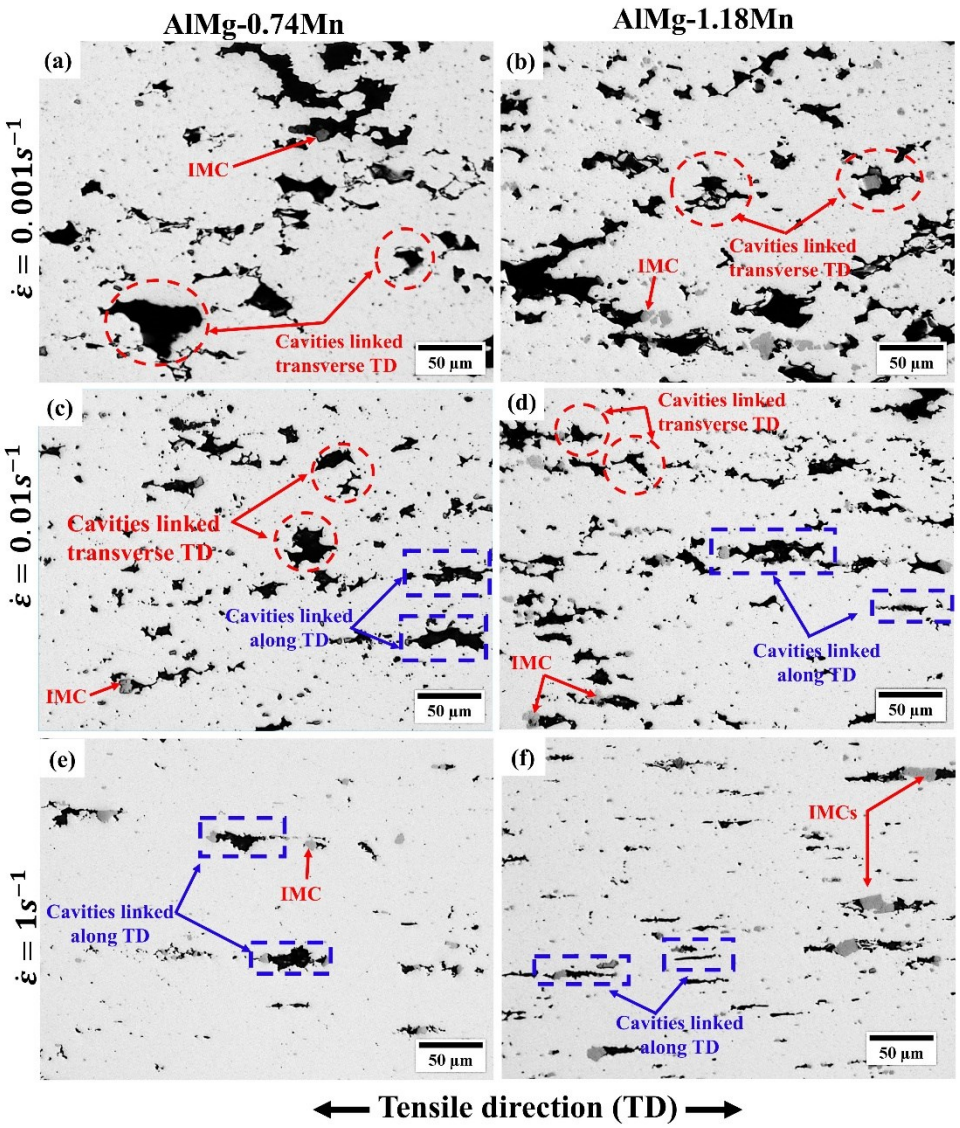


Figure 5.9 Optical micrographs showing cavity formation near the fracture surface of (a,c,e) AlMg–0.74Mn and (b,d,f) AlMg–1.18Mn alloys after tensile deformation at 500 °C under different strain rates (0.001–1 s^{-1}). Red circles indicate cavities linked in the

transverse direction, while blue rectangles indicate those cavities linked along the tensile direction

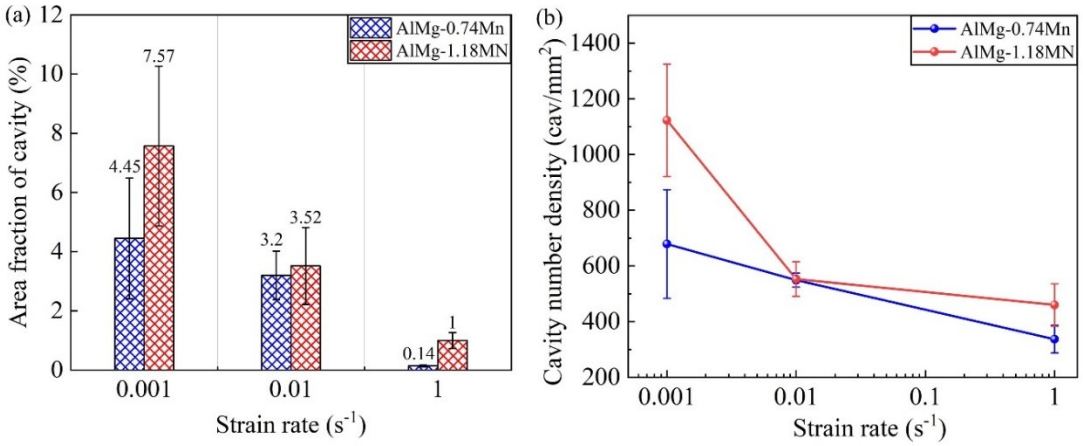


Figure 5.10 (a) Effect of strain rate on (a) cavity area fraction and (b) cavity number density in AlMg–0.74Mn and AlMg–1.18Mn alloys deformed at 500 °C.

At the high strain rate of 1 s^{-1}, cavitation is markedly reduced in both alloys (Figure 5.9c,f). The cavities are predominantly elongated along the tensile axis and are mainly associated with particle–matrix interfaces. Large irregular cavities and transverse cavity linkage are rarely observed, suggesting that extensive isotropic cavity growth and coalescence are suppressed under this condition. The cavity area fraction decreases significantly to 0.14 ± 0.03% in AlMg–0.74Mn and 1.0 ± 0.27 % in AlMg–1.18Mn (Figure 5.10a). The corresponding cavity number density decreases to approximately 310 cavities mm^{-2} in AlMg–0.74Mn and 450 cavities mm^{-2} in AlMg–1.18Mn (Figure 5.10b). Although AlMg–1.18Mn retains a higher N_a and cavity area fraction, it also sustains a higher elongation to failure, indicating that the greater incidence of particle-associated cavity

nucleation does not directly translate into earlier fracture when cavity growth and linkage are strongly suppressed.

The evolution of cavity size was further examined using the cavity-size distributions and cumulative relative frequency curves shown in Figure 5.11, while the corresponding mean ECD and D_{90}values are summarized in Table 5.1. The mean ECD was used to characterize the average cavity size, whereas $D_{90}$was used to characterize the larger-cavity population, representing the cavity diameter below which 90 % of the measured cavities fall. For both alloys, the cavity-size distributions are dominated by small cavities, with the relative frequency decreasing progressively as the cavity diameter increases and only a limited fraction of cavities extending to larger sizes. At each strain rate, the cumulative curve for AlMg–0.74Mn rises more steeply than that for AlMg–1.18Mn, indicating that the low-Mn alloy contains a higher fraction of smaller cavities. This trend is consistent with the mean ECD values in Table 5.1.

At 0.001 s^{-1}, the mean ECD is 4.05 ± 2.75 μm in AlMg–0.74Mn compared with 5.25 ± 3.29 μm in AlMg–1.18Mn. With increasing strain rate to 1 s^{-1}, the mean ECD decreases to 3.43 ± 1.72 μm and 4.22 ± 2.38 μm in AlMg–0.74Mn and AlMg–1.18Mn, respectively. A similar trend is observed for D_{90}, which decreases from 7.7 to 6.0 μm in AlMg–0.74Mn and from 9.7 to 7.4 μm in AlMg–1.18Mn over the same strain-rate range. The consistently higher mean ECD and D_{90} values in AlMg–1.18Mn demonstrate that its final cavity population extends toward larger cavity sizes compared with AlMg–0.74Mn, which may partly reflect the greater deformation sustained by this alloy before fracture.

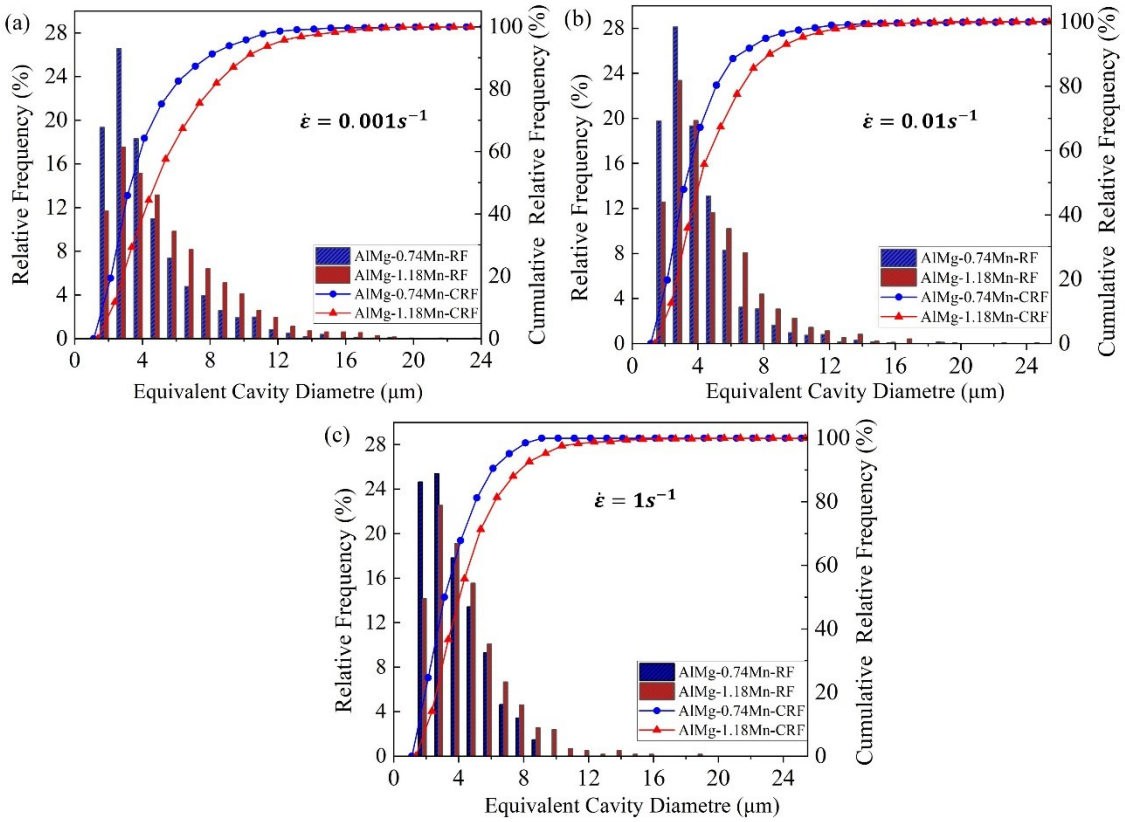


Figure 5.11 Cavity-size distributions and cumulative relative frequency curves for AlMg–0.74Mn and AlMg–1.18Mn alloys deformed at 500 °C at strain rates of (a) 0.001 s^{-1}, (b) 0.01 s^{-1}, and (c) 1 s^{-1}. The cumulative curves were used to determine D_{90}, defined as the cavity diameter below which 90 % of the measured cavities fall.

Table 5.1. Mean cavity ECD and D_{90} values obtained from the cavity-size distributions.

	AlMg–0.74Mn		**AlMg–1.18Mn**	
Strain rate (s^{-1})	Mean ECD (μm)	D_{90} (μm)	Mean ECD (μm)	D_{90} (μm)
0.001	4.05 ± 2.75	7.7	5.25 ± 3.29	9.7
0.01	3.72 ± 2.36	6.4	4.47 ± 2.68	8.0
1	3.43 ± 1.72	6.0	4.22 ± 2.38	7.4

The simultaneous reduction in mean ECD and D_{90} with increasing strain rate indicates that the development of large cavities is progressively suppressed at higher strain rates. This suggests that increasing strain rate limits extensive cavity enlargement and coalescence, even though particle-associated cavity nucleation remains active. The larger cavity-size population in AlMg–1.18Mn is consistent with its higher fraction of coarse IMCs, which promote cavity nucleation, and its higher elongation to failure, which permits greater cavity evolution before fracture. Therefore, the main difference in cavitation evolution between the alloys is that AlMg–1.18Mn promotes more particle-associated cavity nucleation but delays cavity linkage and coalescence, whereas AlMg–0.74Mn develops fewer cavities but is more prone to earlier linkage once cavities form. Overall, the combined analysis of cavity area fraction, N_a, and cavity-size distribution demonstrates that increasing strain rate progressively limits cavity accumulation, growth, and coalescence. Cavitation evolution at intermediate strain levels was subsequently examined at 0.001 s^{-1} to elucidate the progression of cavity damage during deformation prior to fracture.

5.3.5 Cavity evolution with strain during deformation at low strain rate

Figure 5.12 shows cavity development at different strain levels during deformation at 500 °C and 0.001 s^{-1}, the strain rate at which the most pronounced cavitation was observed. At the early deformation stage, $\varepsilon \approx 20$ % (Figure 5.12a,d), both alloys exhibit limited cavitation, with small, isolated cavities distributed mainly in the matrix and often associated with IMCs. The cavity area fraction remains below 1 % in both alloys (Figure 5.12h), while $N_a$is 122 ± 41 mm^{-2} in AlMg–0.74Mn and 179 ± 39 mm^{-2} in AlMg–1.18Mn (Figure 12i).

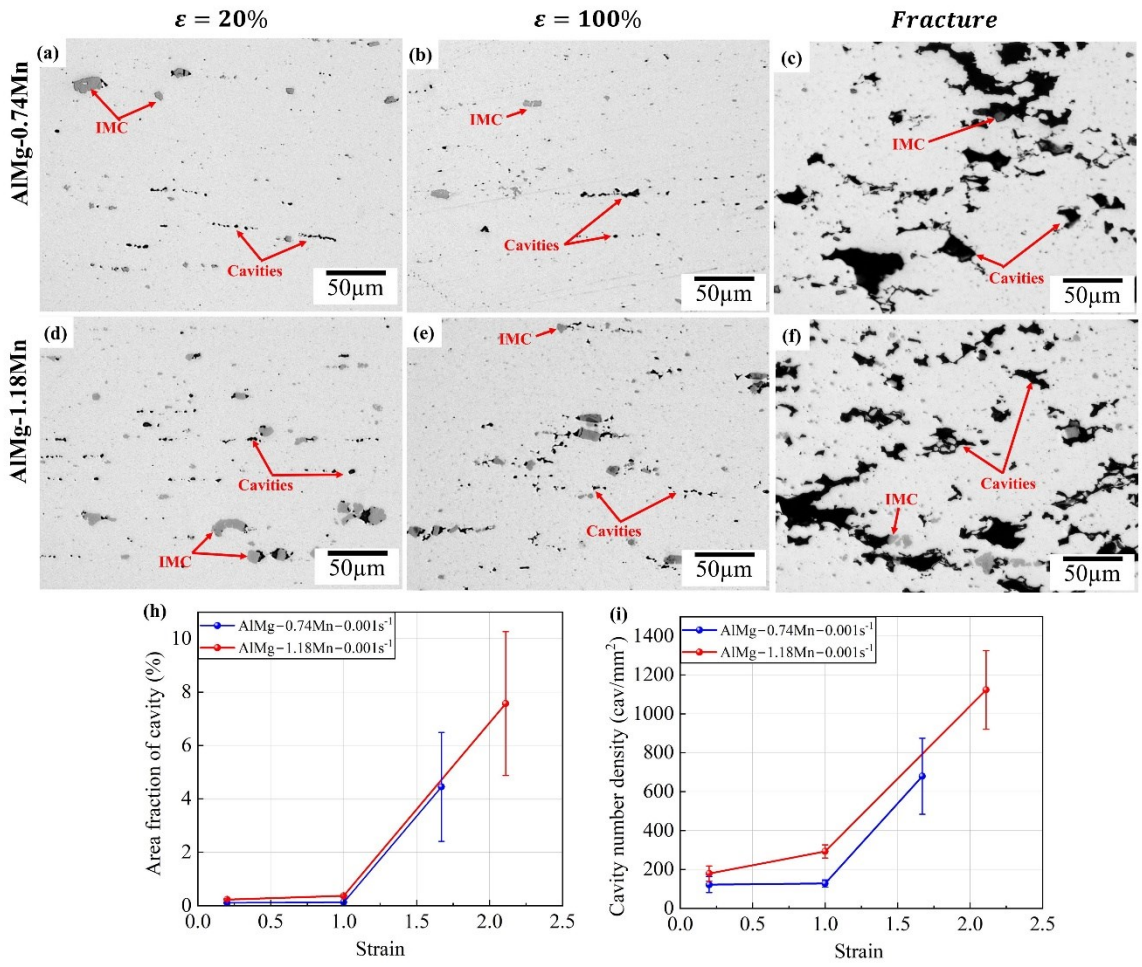


Figure 5.12. Optical micrographs showing cavitation evolution at different strain levels during deformation at 500 °C and 0.001 s^{-1}**:** (a,d) ε ≈ 20 %, (b,e) ε ≈ 100 %**,** and (c,f) after fracture for the two alloys. The corresponding quantitative measurements show (h) the cavity area fraction and (i) the cavity number density, both evolving with strain

As strain increases to ε ≈ 100 % (Figure 5.12b,e), cavity accumulation remains relatively limited, and most cavities are still small and discontinuous. The cavity area fraction remains below 1% in both alloys, indicating that extensive cavity growth and coalescence remain limited at this intermediate deformation stage. In AlMg–0.74Mn, N_a remains nearly unchanged, increasing only slightly to 128 ± 19 mm^{-2}. In contrast, $N_a$in AlMg–1.18Mn

increases to 292 ± 34 mm^{-2}, indicating more active cavity nucleation during deformation. After fracture (Figure 5.12c,f), cavitation becomes much more pronounced, with larger and more connected cavities. The cavity area fraction increases sharply to approximately 4.5 % in AlMg–0.74Mn and 7.6 % in AlMg–1.18Mn, while N_a increases markedly to 679 ± 195 mm^{-2} and 1123 ± 202 mm^{-2}, respectively.

These results show that cavity accumulation is limited during the early and intermediate stages of deformation but increases sharply at higher strain levels in both alloys. AlMg–1.18Mn exhibits higher N_a throughout deformation, indicating more active particle-assisted cavity nucleation, consistent with its higher IMC population. However, AlMg–1.18Mn sustains greater deformation before fracture despite its higher cavity number density and final cavity area fraction. Thus, its greater final cavitation level does not necessarily indicate poorer cavitation resistance, but rather a greater capacity to accommodate cavity accumulation before critical cavity linkage and fracture.

5.3.6 Fracture surface morphology

Figure 5.13 presents the SEM fracture surface morphologies of the AlMg–0.74Mn and AlMg–1.18Mn alloys deformed at different strain rates, together with the corresponding equivalent dimple diameter distributions. The fracture surfaces exhibit typical ductile features associated with microvoid nucleation, growth, and coalescence. At 0.001 s^{-1}, both alloys exhibit rough fracture surfaces containing large, deep, and irregular primary dimples, indicated by red dashed circles, together with fine secondary dimples, indicated by yellow arrows (Figure 5.13a,b). The coalescence of neighboring dimples produces irregular dimple walls, indicating extensive microvoid growth prior to fracture. Consistent with the fracture

surface morphology, the equivalent dimple diameter distribution at 0.001 s^{-1} shows a clear difference between the two alloys (Figure 5.13c). The AlMg–0.74Mn alloy exhibits a broad distribution with a pronounced tail extending toward larger dimple diameters, with an average equivalent dimple diameter of 9.45 ± 8.9 μm. Some dimples extend beyond 20 μm, consistent with extensive microvoid growth and coalescence prior to fracture. In contrast, the AlMg–1.18Mn alloy shows a narrower distribution dominated by smaller dimples, with an average equivalent dimple diameter of 3.00 ± 2.2 μm. This suggests that although AlMg–1.18Mn contains more particle-associated cavities, final fracture occurs through a finer and more uniformly distributed dimple morphology compared with AlMg–0.74Mn.

After deformation at 0.01 s^{-1}, the fracture surfaces are characterized by shallower and more uniformly distributed dimples (Figure 5.13d,e). Compared with 0.001 s^{-1}, large primary dimples are less frequent, while fine secondary dimples become more prevalent. The corresponding dimple diameter distributions shift toward smaller sizes, with a greater concentration of fine dimples (Figure 5.13f). The mean equivalent dimple diameters decrease to 2.80 ± 1.9 μm for AlMg–0.74Mn and 2.70 ± 2.1 μm for AlMg–1.18Mn, with most dimples concentrated within the 2–4 μm range. These similar mean values and comparable dimple-size ranges indicate that the difference in fracture surface morphology between the two alloys becomes less pronounced at 0.01 s^{-1}. Thus, extensive void growth and coalescence are reduced in both alloys relative to the lowest strain-rate condition.

At the highest strain rate of 1 s^{-1}, the fracture surfaces are predominantly composed of fine, shallow, and elongated dimples aligned along the tensile direction, as indicated by blue arrows (Figure 5.13g,h). In addition, a limited number of larger dimples are observed, as indicated by white arrows. The corresponding dimple diameter distributions are mainly

concentrated within the 2–3 μm range (Figure 5.13i), with mean equivalent dimple diameters of 2.92 ± 1.8 μm for AlMg–0.74Mn and 2.96 ± 1.9 μm for AlMg–1.18Mn. The nearly identical mean values indicate that the dominant fine-dimple population is comparable in both alloys at 1 s^{-1}. However, the presence of occasional larger dimples, particularly in AlMg–1.18Mn, is consistent with the longitudinal-section observations showing preferential cavity formation at coarse IMCs (Figure 5.9). This suggests that particle-associated cavity nucleation continues to contribute to the larger-void population even at the highest strain rate. Therefore, deformation at 1 s^{-1} produces a predominantly fine microvoid population together with a limited population of larger voids associated with particle-induced cavitation.

Figure 5.14 presents SEM images highlighting crack-path features on the fracture surfaces of both alloys. At 0.001 s^{-1} (Figure 5.14a,b), features associated with both intragranular cracking (red dashed boxes) and intergranular cracking (yellow dashed boxes) are observed. The intergranular cracks are characterized by separation along interfaces between adjacent grain-like facets, producing relatively smooth and well-defined boundary surfaces. In contrast, the intragranular cracks propagate through the grain interior rather than along these interfaces, producing crack paths that traverse the fractured grains. These crack features occur together with the large dimples and extensive cavity coalescence shown in Figure 5.13. Compared with AlMg–1.18Mn, AlMg–0.74Mn exhibits more pronounced intergranular crack linkage, suggesting a greater tendency for damage localization along grain boundaries at the lowest strain rate. In contrast, AlMg–1.18Mn exhibits a finer fracture morphology with less continuous intergranular crack paths, consistent with delayed cavity linkage and coalescence.

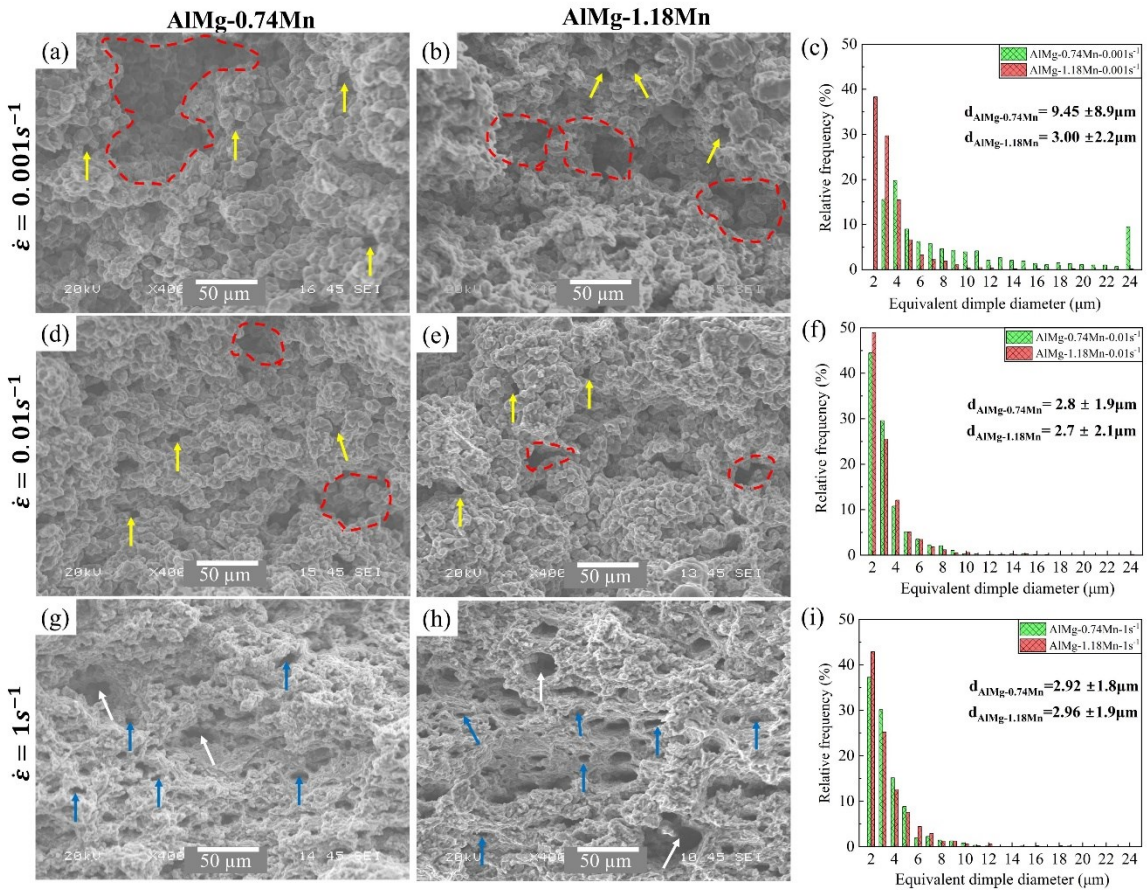


Figure 5.13. SEM fracture surface morphologies of (a, d, g) AlMg–0.74Mn and (b, e, h) AlMg–1.18Mn alloys deformed at 500 °C at strain rates of (a, b) 0.001 s^{-1}, (d, e) 0.01 s^{-1}, and (g, h) 1 s^{-1}; corresponding equivalent dimple diameter distributions at different strain rates of (c) 0.001 s^{-1}, (f) 0.01 s^{-1}, and (i) 1 s^{-1}, illustrating the strain-rate-dependent evolution of cavitation from large, coalesced dimples at the low strain rate to fine microvoid-dominated fracture at the high strain rate

.

With increasing strain rate to 0.01 s^{-1} (Figure 5.14c,d), the fracture morphology shows a greater contribution from intragranular cracking in both alloys, although intergranular crack features remain visible. AlMg–0.74Mn exhibits more pronounced localized crack linkage, consistent with the greater cavity/dimple coalescence observed in Figure 5.13. In contrast,

AlMg–1.18Mn shows a more distributed fracture morphology with less continuous crack linkage. These features suggest that AlMg–1.18Mn accommodates cavity development with less localized linkage than AlMg–0.74Mn under this condition. At 1 s^{-1} (Figure 5.14e,f), the fracture surfaces of both alloys are characterized by tear ridges, indicated by blue dashed boxes. These ridges appear as elongated surface features aligned with the fracture direction and occur together with the fine cellular microvoid structure observed in Figure 5.13. The tear ridges are more clearly defined and continuous in AlMg–1.18Mn than in AlMg–0.74Mn, indicating a more continuous ductile tearing morphology during final fracture. This morphology is consistent with reduced damage localization in AlMg–1.18Mn and its higher tensile elongation.

Overall, the fracture surface observations show that strain rate has the dominant effect on fracture morphology, while the difference between the two alloys is mainly reflected in the extent of crack linkage and damage localization. With increasing strain rate, the fracture morphology evolves from mixed intergranular–intragranular cracking at 0.001 s^{-1}, to a greater contribution from intragranular cracking at 0.01 s^{-1}, and finally to ductile tearing characterized by tear ridges at 1 s^{-1}. AlMg–0.74Mn is more susceptible to intergranular crack linkage and localized damage development, particularly at low strain rate, whereas AlMg–1.18Mn exhibits a finer and more distributed fracture morphology. Together with the cavitation results in Sections 5.3.4 and 5.3.5, these observations indicate that AlMg–1.18Mn exhibits more particle-associated cavity nucleation but delays cavity linkage and coalescence, whereas AlMg–0.74Mn develops fewer cavities but is more prone to earlier damage localization.

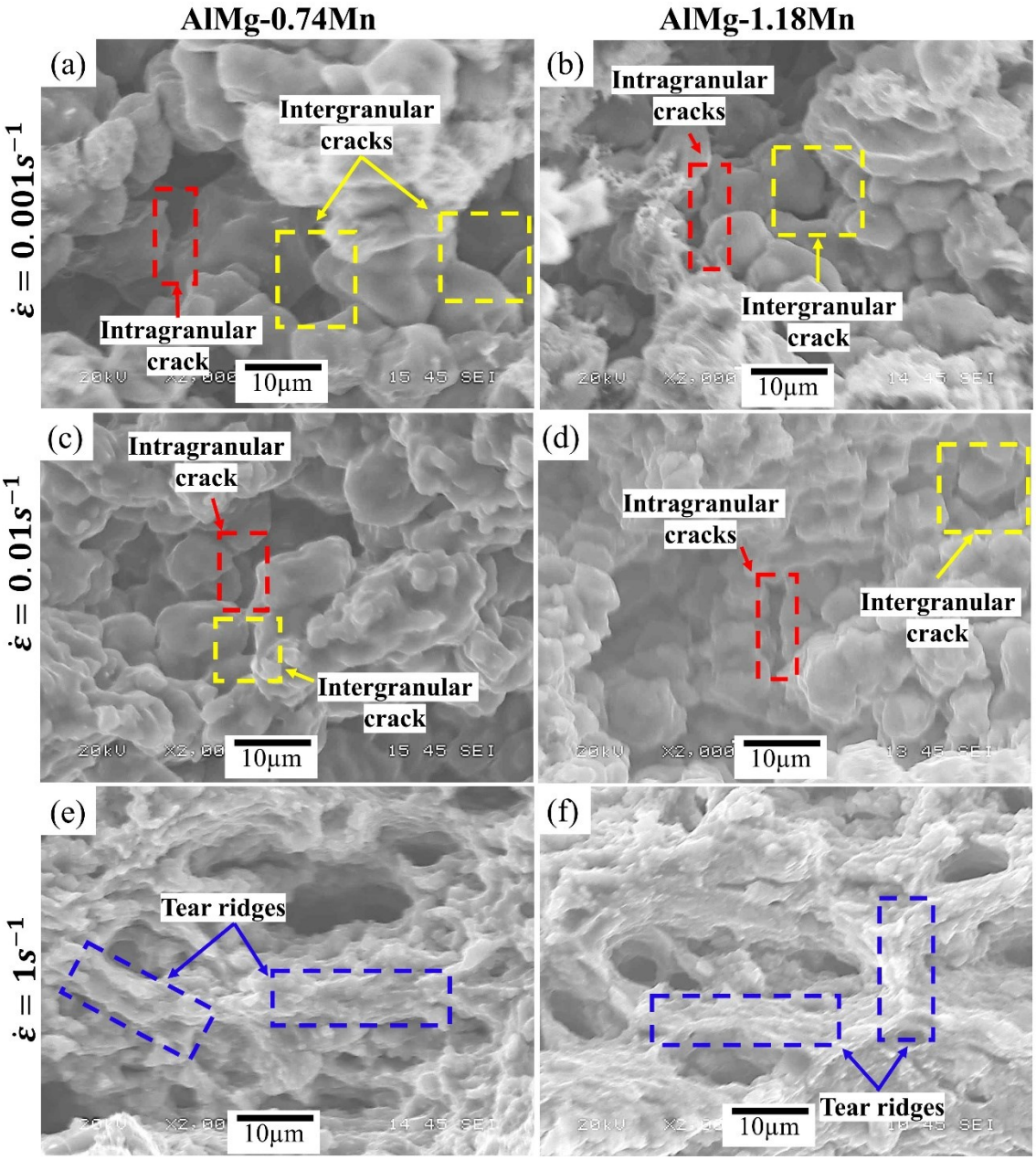


Figure 5.14. SEM images showing crack path features on fracture surfaces of AlMg–0.74Mn and AlMg–1.18Mn alloys deformed at 500 °C under different strain rates: (a,b) 0.001 s^{-1}, (c,d) 0.01 s^{-1}, and (e,f) 1 s^{-1}. Red dashed boxes indicate intragranular cracks, yellow dashed boxes indicate intergranular cracks, and blue dashed boxes highlight tear ridges formed during shear-localized ductile tearing.

5.4. Discussion

5.4.1 Strain-rate-dependent transition in cavitation and fracture behavior

The results demonstrate a clear strain-rate-dependent transition in the cavitation and fracture behavior of Al–Mg–Mn 5xxx alloys deformed at 500 °C. Although both alloys exhibit substantial ductility across the investigated strain-rate range (Figure 5.5), the underlying damage mechanisms evolve significantly with increasing strain rate. At the lowest strain rate of 0.001 s^{-1}, both alloys exhibit the highest cavity area fraction and cavity number density (Figure 5.10), indicating extensive cavitation before fracture. The prolonged deformation time at this strain rate allows GBS, diffusion-assisted accommodation, and local plastic flow to operate over a longer period, promoting cavity nucleation and growth along grain boundaries and at particle–matrix interfaces [13,21,23]. The higher N_a in AlMg–1.18Mn is mainly attributed to its higher IMC area fraction and larger population of coarse particles, which provide additional preferential sites for cavity nucleation. However, despite enhanced cavity nucleation, the final fracture surface of AlMg–1.18Mn shows smaller and more uniformly distributed dimples than AlMg-0.74Mn, suggesting that final-stage void enlargement and coalescence are more limited in the high-Mn alloy. In contrast, AlMg–0.74Mn exhibits more extensive cavity linkage, larger dimples, and more pronounced intergranular fracture features, indicating earlier damage localization. Thus, at the low strain rate, cavitation is governed by the combined effects of particle-assisted nucleation, GBS-assisted cavity growth, diffusion-assisted accommodation, and final-stage void coalescence [18,23,28,29].

As the strain rate increases to 0.01 s^{-1}, the cavitation behavior begins to transition from the classical diffusion-assisted regime observed at 0.001 s^{-1} toward a regime of

increasingly constrained cavity growth and coalescence due to the shorter deformation time. Consequently, both the cavity area fraction and cavity size decrease relative to those at 0.001 s^{-1} (Figures. 5.10a and 5.11). The cavity-size distributions also become narrower, indicating increasingly constrained development of large cavities. This trend is reflected in the fracture surface morphology, where shallower and more uniformly distributed dimples are observed (Figure 5.13d,e). In addition, the fracture morphology at 0.01 s^{-1} shows a greater contribution from intragranular cracking (Figure 5.14c,d), suggesting an increasing role of intragranular plasticity in deformation accommodation alongside GBS. Although the overall cavitation parameters of the two alloys become more comparable at 0.01 s^{-1}, AlMg–0.74Mn exhibits more pronounced cavity/dimple coalescence and crack linkage than AlMg–1.18Mn, indicating greater damage localization in the low-Mn alloy. Overall, this condition represents a transitional cavitation regime in which GBS-assisted cavitation persists, while extensive cavity growth and coalescence become increasingly constrained and intragranular plasticity contributes more strongly to deformation accommodation.

At the highest strain rate of 1 s^{-1}, cavitation behavior undergoes a further transition. The very short deformation time limits diffusion-assisted cavity growth and large-scale coalescence, while deformation is increasingly accommodated by dislocation glide, grain subdivision, and localized plastic flow [38]. As a result, although cavity nucleation continues to occur, the limited time available for subsequent growth restricts the development of large cavities. Consequently, damage is characterized by elongated cavities, some associated with local stress concentrations at particle–matrix interfaces in the longitudinal sections (Figure 5.9c,f), together with numerous fine, elongated dimples on the fracture surfaces, reflecting a fine microvoid population extended along the tensile direction (Figure 5.13g,h). Consistent

with these observations, both alloys exhibit a marked reduction in cavity area fraction and cavity size compared with the lower strain-rate conditions (Figures. 5.10 and 5.11), while tear ridges characteristic of ductile tearing is observed on the fracture surfaces (Figure 5.14e,f). At this high strain rate, the alloy-to-alloy difference becomes less pronounced in terms of cavity and dimple size, although AlMg–1.18Mn exhibits more clearly defined and continuous tear ridges, consistent with delayed damage localization. These observations indicate that increasing strain rate progressively suppresses diffusion-assisted cavity growth and coalescence, resulting in a transition from large-cavity-dominated damage at low strain rate toward fine-microvoid-dominated damage at high strain rate. Importantly, cavitation is not eliminated at 1 s^{-1}; rather, cavity nucleation persists, while the limited time available for subsequent growth and coalescence results in a predominantly fine and directionally extended microvoid population.

The observed strain-rate-dependent cavitation behavior is closely linked to the transition in deformation mechanisms indicated by the strain-rate sensitivity analysis (Figure 5.6) and the accompanying grain-structure evolution (Figure5.7). At 0.001 s^{-1}, the high strain-rate sensitivity, $m > 0.3$, is consistent with a significant contribution from GBS [24,25,39], which facilitates diffusion-assisted cavity growth. In contrast, increasing the strain rate toward 1 s^{-1} reduces the m-value to approximately 0.15, indicating a transition toward increasingly dislocation-mediated plasticity. Combined with the shorter deformation time, this transition limits diffusion-assisted cavity enlargement and large-scale coalescence, resulting in significantly smaller cavities at 1 s^{-1}. The short deformation time also suppresses grain growth, while deformation-induced grain subdivision contributes to the development of the refined grain structure observed at this strain rate. Consequently, final fracture involves

the linkage of numerous fine microvoids, producing the shallow dimple morphology observed at 1 s^{-1}. Together, these observations demonstrate that the strain-rate-dependent transition in deformation mechanisms strongly influences both cavitation evolution and the resulting fracture behavior.

5.4.2 Role of IMCs and grain-structure stability in controlling cavitation damage and ductility

Microstructural features, particularly IMCs, Mn-rich dispersoids, and grain-structure stability, play coupled roles in controlling cavitation damage and ductility during high-temperature deformation. IMCs are especially important because coarse particles act as preferential sites for cavity nucleation due to local strain incompatibility, stress concentration, and particle–matrix decohesion under tensile loading [17–20,29]. As shown in Figure 5.3, AlMg–1.18Mn exhibits a higher IMC area fraction and a larger population of coarse particles than AlMg–0.74Mn. This increases the number of particle–matrix interfaces available for cavity nucleation and is consistent with the higher cavity number density measured in AlMg–1.18Mn across the investigated strain-rate range (Figure 5.10b). Larger particles can also generate higher local triaxial stresses and larger decohesion zones, increasing the probability of void initiation and potentially producing larger initial cavities [17,19,29]. This is consistent with the cavity-size distributions extending toward larger sizes in AlMg–1.18Mn (Figure 5.11). Therefore, the higher cavitation level in AlMg–1.18Mn reflects, at least partly, its greater tendency for particle-assisted cavity nucleation.

The influence of coarse IMCs remains evident at the highest strain rate. At 1 s^{-1}, longitudinal-section observations reveal cavities associated with particle–matrix interfaces

(Figure 5.9c,f), while the fracture surfaces contain a dominant population of fine dimples together with occasional larger dimples (Figure 5.13g,h). The latter are consistent with void formation associated with coarse IMCs, although a direct particle origin cannot be established from the fracture surfaces alone. Under this high-strain-rate condition, cavity nucleation therefore remains active, whereas the short deformation time strongly restricts subsequent diffusion-assisted cavity enlargement and coalescence. Consequently, the damage population remains predominantly fine, with directional cavity/microvoid extension accompanying localized plastic deformation. Similar particle-assisted cavitation has been reported in an Al–Mg–Sc–Zr alloy, where Al_6(Fe,Mn) particles contributed to cavity formation and subsequent fracture [29].

Although AlMg–1.18Mn consistently exhibits higher cavity area fractions and cavity number densities, it maintains superior elongation across the investigated strain-rate range. This demonstrates that ductility is not governed solely by cavity nucleation, but also by the ability of the surrounding microstructure to delay cavity linkage, coalescence, and damage localization. This interpretation is supported by the strain-dependent cavitation results in Figure 5.12, where AlMg–1.18Mn exhibits higher cavity number densities throughout deformation but sustains greater deformation before fracture. Thus, its higher final cavitation level does not indicate poorer damage tolerance; rather, the alloy can accommodate a greater accumulation of cavities before critical linkage and fracture. At 0.001 s^{-1}, this behavior is also reflected in the fracture surfaces, where AlMg–1.18Mn exhibits a finer dimple population and less pronounced crack linkage than AlMg–0.74Mn (Figures. 5.13 and 5.14), consistent with more distributed damage development.

The EBSD results show that the two alloys differ significantly in grain-structure stability during annealing and deformation (Figures. 5.7 and 5.8). AlMg–1.18Mn exhibits a

finer grain size and a lower tendency for grain coarsening, whereas AlMg–0.74Mn shows more pronounced grain growth and grain elongation, particularly after deformation at 0.001 s^{-1}. This difference is attributed primarily to the higher density of Mn-rich dispersoids in AlMg–1.18Mn, which impede grain-boundary migration through Zener pinning [6,27,40,41]. The higher population of μm-scale IMCs in AlMg–1.18Mn may provide an additional contribution to grain-boundary pinning during high-temperature deformation. Thus, the particle population has a dual influence: coarse IMCs provide preferential sites for cavity nucleation, while Mn-rich dispersoids, together with a possible additional pinning contribution from larger IMCs, enhance grain-structure stability.

Grain-structure stability is important for cavitation resistance because cavity evolution at elevated temperature is influenced by GBS, grain-boundary migration, and compatibility stresses at grain-boundary junctions [18,28]. In AlMg–0.74Mn, the lower dispersoid density permits greater grain coarsening and boundary elongation, which can increase strain localization and facilitate cavity interconnection. Conversely, the finer and more stable grain structure in AlMg–1.18Mn provides a more distributed grain-boundary network and may reduce damage localization, thereby delaying critical cavity linkage.

This interpretation is further supported by the grain evolution during deformation at 500 °C and 0.001 s^{-1} (Figure 5.15). The EBSD inverse pole figure maps show progressive grain elongation with increasing strain in both alloys, from initially near-equiaxed grains at $\varepsilon \approx 20$ % to increasingly elongated morphologies at $\varepsilon \approx 100$ % and after fracture. However, grain distortion is consistently lower in AlMg–1.18Mn. The corresponding grain aspect-ratio evolution (Figure 5.15g) confirms that AlMg–1.18Mn maintains lower aspect ratios at comparable strain levels, demonstrating greater grain-structure stability during deformation. When considered together with the cavity evolution in Figure 5.12, these observations

suggest that the more stable grain structure delays strain localization and cavity interconnection despite continued cavity nucleation.

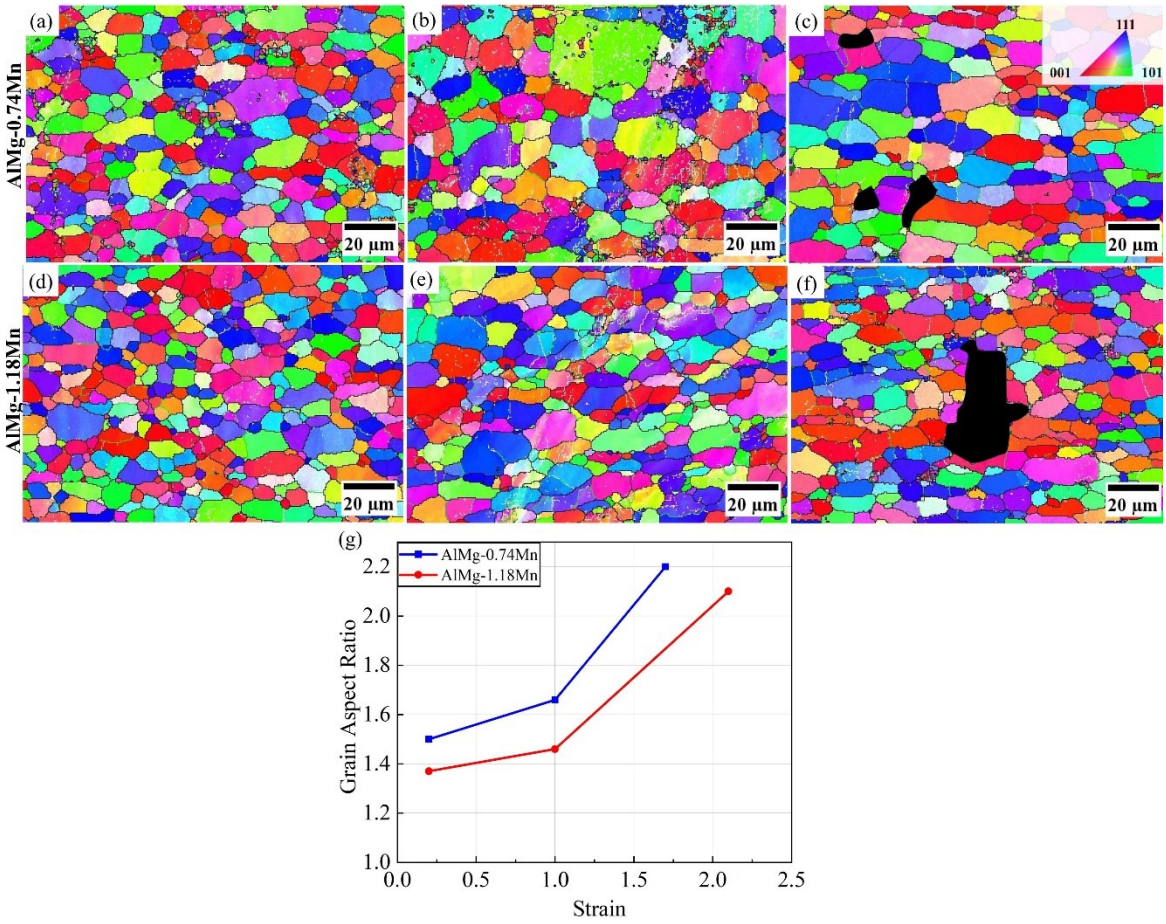


Figure 5.15. SEM–EBSD inverse pole figure (IPF) maps showing the grain structure evolution of the two alloys during progressive deformation at 500 °C and a strain rate of 0.001 s^{-1}. (a and d) correspond to true strains of ε = 20 %, (b and e) ε = 100 %, and (c and f) post-fracture. The black shaded regions in (c and f) indicate cavities formed in the samples after fracture. (g) shows the variation of grain aspect ratio with strain for both alloys

Overall, the consistently higher elongation of AlMg–1.18Mn can be understood as a balance between enhanced cavity nucleation and greater damage tolerance. Its higher population of coarse IMCs provides more preferential sites for cavity nucleation, resulting in higher cavity number density and cavity area fraction. However, this detrimental effect is counterbalanced by greater grain-structure stability, arising primarily from the higher density of Mn-rich dispersoids. At low strain rate, this stability limits grain coarsening and boundary elongation, allowing greater GBS-assisted deformation before critical cavity linkage. At intermediate strain rate, as diffusion-assisted cavity growth becomes increasingly constrained, the stable grain network promotes more distributed damage development and delays continuous crack linkage.

At high strain rate, cavity nucleation persists but the short deformation time restricts subsequent growth and coalescence, resulting in predominantly fine microvoid damage; under this condition, AlMg–1.18Mn continues to exhibit delayed damage localization. Therefore, the superior ductility of AlMg–1.18Mn does not arise from reduced cavity nucleation, but from its greater capacity to accommodate cavity accumulation while delaying critical cavity linkage and damage localization. In contrast, AlMg–0.74Mn contains fewer IMC-related nucleation sites but exhibits greater grain coarsening, boundary elongation, and damage localization. These contrasting responses demonstrate that cavitation resistance and ductility in Al–Mg–Mn alloys are governed not only by the density of cavity nucleation sites, but also by the ability of the grain structure to delay cavity interconnection and damage localization.

5.4.3 Implications for HSBF processing and cavitation modeling

HSBF involves deformation over a broad strain-rate spectrum, typically consisting of an initial high-strain-rate forming stage followed by a lower-strain-rate gas-forming stage [3,4]. The present results demonstrate that cavitation behavior in Al–Mg–Mn 5xxx alloys is strongly strain-rate dependent. This indicates that damage evolution during HSBF cannot be assessed solely from elongation-to-failure or steady-state flow behavior. Instead, the operative cavitation mechanism evolves with deformation conditions.

During the high-strain-rate forming stage, cavity nucleation is expected to remain active, with particle–matrix interfaces providing important preferential nucleation sites because of local stress concentrations. However, the limited deformation time strongly restricts diffusion-assisted cavity growth and coalescence. Consequently, high-strain-rate deformation produces relatively low cavity area fractions and a predominantly fine microvoid population, reflected by the fine, shallow dimples observed on the fracture surfaces. Thus, cavitation is not eliminated at high strain rate; rather, cavity nucleation persists while subsequent growth and coalescence are strongly constrained. In an HSBF deformation path, these microvoids may constitute pre-existing damage that is carried into the subsequent lower-strain-rate gas-forming stage. The final cavitation state may therefore depend not only on cavities generated during the lower-strain-rate stage, but also on the cavity population inherited from the preceding high-strain-rate deformation.

During the subsequent lower-strain-rate gas-forming stage, the longer deformation time provides greater opportunity for diffusion-assisted cavity growth, interconnection, and coalescence. Cavities nucleated during either stage may therefore contribute to localized damage accumulation as deformation proceeds. Under these conditions, grain-structure

stability becomes particularly important because a refined and stable grain-boundary network can promote more distributed deformation and delay critical cavity linkage and damage localization. This distinction between pre-existing damage and its subsequent evolution may be important for predicting failure under the non-steady deformation paths characteristic of HSBF.

The present results therefore identify two important microstructural parameters governing damage tolerance under HSBF-relevant conditions: (i) the IMC population, which strongly influences the density of preferential cavity nucleation sites, and (ii) grain-structure stability, governed primarily by dispersoid-assisted grain-boundary pinning, which influences the subsequent development, linkage, and localization of cavity damage. An excessive population of coarse IMCs increases the number of potential cavity nucleation sites, whereas insufficient grain-boundary stabilization promotes grain coarsening and may facilitate damage localization and cavity interconnection. Achieving an appropriate balance between these competing effects is therefore important for maintaining formability during complex, non-steady deformation paths.

These findings also have implications for cavitation modeling of HSBF processes. Most existing cavitation models for Al–Mg alloys have been developed under conventional superplastic-forming conditions, where deformation occurs at relatively low strain rates and cavitation is commonly described in terms of diffusion- and GBS-assisted cavity growth. The present results indicate that cavitation behavior changes substantially with strain rate and microstructural condition. At high strain rate, cavity nucleation persists, including preferential nucleation associated with coarse particles, while the short deformation time strongly restricts subsequent diffusion-assisted growth and coalescence. At lower strain rates,

cavities have substantially more time to enlarge, interconnect, and coalesce. Cavitation models intended for HSBF should therefore account for the evolving balance between cavity nucleation, growth, and coalescence along non-steady deformation paths, together with the effects of particle population and grain-structure stability. Incorporating the evolution of pre-existing cavity populations between successive deformation stages may further improve the prediction of damage accumulation during high-speed forming compared with models based solely on steady, low-strain-rate superplastic deformation.

Taken together, the results demonstrate that damage evolution in Al–Mg–Mn 5xxx alloys is governed by the coupled effects of IMC population, grain-structure stability, strain rate, and deformation time. Under an HSBF deformation path, microvoids generated during the initial high-strain-rate stage may persist as pre-existing damage during the subsequent lower-strain-rate gas-forming stage, where the longer deformation time provides greater opportunity for their growth, linkage, and coalescence. The extent to which this damage progresses toward fracture will then depend partly on the stability of the surrounding grain structure and its ability to delay damage localization and critical cavity interconnection. This coupled nucleation–growth–coalescence perspective highlights the need to control coarse IMCs while promoting a dispersoid-stabilized grain structure when designing Al–Mg–Mn alloys for HSBF applications.

5.5 Conclusions

This study investigated strain-rate-dependent cavitation in Al–Mg–Mn 5xxx alloys under HSBF-relevant deformation conditions. Cavitation was controlled by the combined

effects of IMC population, grain-structure stability, and deformation strain rate. The main conclusions are as follows:

1. The AlMg–1.18Mn alloy contained a higher IMC area fraction and a larger population of coarse particles than AlMg–0.74Mn**.** These particles provided preferential sites for cavity nucleation, resulting in a higher cavity number density across the investigated strain-rate range. At 0.001 s^{-1}, the cavity density reached approximately 1120 cavities mm^{-2} in AlMg–1.18Mn, compared with ~670 cavities mm^{-2} in AlMg–0.74Mn.
2. Cavitation decreased strongly with increasing strain rate. At 0.001 s^{-1}, diffusion-assisted cavity growth and coalescence produced the highest final cavity area fractions of 7.57 ± 2.7 % in AlMg–1.18Mn and 4.45 ± 2.0 % in AlMg–0.74Mn. At 1 s^{-1}, extensive cavity growth and coalescence were strongly suppressed, but cavity nucleation persisted. The resulting damage was characterized by a predominantly fine microvoid population with directional extension along the tensile direction.
3. AlMg–1.18Mn maintained superior elongation across all investigated strain rates despite its higher cavity density. It exhibited elongations of 211 ± 12 % and 168 ± 5 % at 0.001 and 1 s^{-1}, respectively, compared with 167 ± 3 % and 139 ± 5 % for AlMg–0.74Mn. This demonstrates that cavity density alone does not determine ductility; the subsequent evolution and localization of cavity damage are also critical.

4. Grain-structure stability played an important role in delaying cavity interconnection and damage localization. After deformation at 0.001 s^{-1}, AlMg–0.74Mn exhibited greater grain coarsening, reaching 10.2 ± 3.4 μm, compared with 7.3 ± 0.3 μm for AlMg–1.18Mn. The finer and more stable grain structure of AlMg–1.18Mn, associated with its higher Mn-rich dispersoid density, reduced grain coarsening and deformation-induced grain elongation and delayed critical cavity linkage, contributing to its superior ductility.
5. Damage tolerance under HSBF-relevant conditions depends on the balance between particle-assisted cavity nucleation and grain-structure stability. A high population of coarse IMCs increases the number of preferential cavity nucleation sites, whereas a stable, dispersoid-pinned grain structure delays cavity interconnection and damage localization. Therefore, damage-tolerant Al–Mg–Mn alloys for HSBF should combine control of excessive coarse IMCs with effective dispersoid-assisted grain-structure stabilization.

Overall, this work establishes a strain-rate-dependent cavitation framework linking particle-assisted cavity nucleation, grain-structure stability, and damage evolution in Al–Mg–Mn alloys under HSBF-relevant deformation conditions.

References

1. C. W. Liu, S. Lee, D. Chou, S. H. Hsu, C. L. Chu, “Dimensional Accuracy in Quick Plastic Forming of Aluminum Alloy Using Demolding Mechanism,” Advances in Mechanical Engineering 2021, 13, 1–11. https://doi.org/10.1177/16878140211021731

2. O. A. Yakovtseva, A. A. Kishchik, V. V. Cheverikin, A. D. Kotov, A. V. Mikhaylovskaya, “The Mechanisms of the High-Strain-Rate Superplastic Deformation of Al-Mg-Based Alloy,” Materials Letters 2022, 325, 132883. https://doi.org/10.1016/j.matlet.2022.132883

3. O. Majidi, M. Jahazi, N. Bombardier, “Finite Element Simulation of High-Speed Blow Forming of an Automotive Component,” Metals 2018, 8, 901. https://doi.org/10.3390/met8110901

4. A. Aleyari, O. Majidi, N. Bombardier, X. T. Pham, M. Jahazi, “Finite Element and Experimental Analysis of the Preheating Stage of High Speed Blow Forming (HSBF) Process,” Journal of Manufacturing Processes 2020, 49, 10–17. https://doi.org/10.1016/j.jmapro.2019.10.009

5. R. Grimes, “Superplastic Forming of Aluminium Alloys,” in Superplastic Forming of Advanced Metallic Materials (Ed: G. Giuliano), Woodhead Publishing, Cambridge, UK 2011, pp. 247–271. https://doi.org/10.1533/9780857092779.3.247

6. A. A. Kishchik, A. V. Mikhaylovskaya, A. D. Kotov, O. V. Rofman, V. K. Portnoy, “Al-Mg-Fe-Ni Based Alloy for High Strain Rate Superplastic Forming,” Materials Science and Engineering: A 2018, 718, 190–197. https://doi.org/10.1016/j.msea.2018.01.099

7. P. Ebenberger, P. J. Uggowitzer, B. Gerold, S. Pogatscher, “Effect of Compositional and Processing Variations in New 5182-Type AlMgMn Alloys on Mechanical Properties and Deformation Surface Quality,” Materials 2019, 12, 1645. https://doi.org/10.3390/ma12101645

8. L. Bhatta, A. Pesin, A. P. Zhilyaev, P. Tandon, C. Kong, H. Yu, “Recent Development of Superplasticity in Aluminum Alloys: A Review,” Metals 2020, 10, 77. https://doi.org/10.3390/met10010077

9. A. J. Barnes, “Superplastic Aluminum Forming—Expanding Its Techno-Economic Niche,” Materials Science Forum 1999, 304–306, 785–796. https://doi.org/10.4028/www.scientific.net/MSF.304-306.785

10. M. Kawasaki, T. G. Langdon, “Superplasticity in Ultrafine-Grained Materials,” Reviews on Advanced Materials Science 2018, 54, 46–55. https://doi.org/10.1515/rams-2018-0019

11. J. Jeon, S. Lee, J. Kyeong, S. Shin, H. Kang, “Effect of Geometrical Parameters of Microscale Particles on Particle-Stimulated Nucleation and Recrystallization Texture of Al-Si-Mg-Cu-Based Alloy Sheets,” Materials 2022, 15, 7924. https://doi.org/10.3390/ma15227924

12. Y. Luo, S. G. Luckey, P. A. Friedman, Y. Peng, “Development of an Advanced Superplastic Forming Process Utilizing a Mechanical Pre-Forming Operation,” International Journal of Machine Tools and Manufacture 2008, 48, 1509–1518. https://doi.org/10.1016/j.ijmachtools.2007.12.010

13. F. C. Liu, Z. Y. Ma, “Achieving High Strain Rate Superplasticity in Cast 7075Al Alloy via Friction Stir Processing,” Journal of Materials Science 2009, 44, 2647–2655. https://doi.org/10.1007/s10853-009-3346-6

14. G. Giuliano, Ed., Superplastic Forming of Advanced Metallic Materials, Woodhead Publishing, Cambridge, UK 2011. https://doi.org/10.1533/9780857092779

15. D. H. Bae, A. K. Ghosh, “Cavity Growth during Superplastic Flow in an Al-Mg Alloy: I. Experimental Study,” Acta Materialia 2002, 50, 993–1009. https://doi.org/10.1016/S1359-6454(01)00399-8

16. L. Yi, Z. Gu, G. Yu, X. Li, Z. Tang, Y. Zhao, “Damage Behavior and Performance Analysis of Al5083 Alloy in Superplastic Bulging,” Engineering Failure Analysis 2024, 164, 108732. https://doi.org/10.1016/j.engfailanal.2024.108732

17. H. Jin, A. P. Gerlich, “Effects of Intermetallic Particles on Cavitation during Superplastic Forming of Aluminium Alloy,” Materials Science and Technology 2019, 35, 1428–1435. https://doi.org/10.1080/02670836.2019.1627498

18. H. Toda, Z. A. Bin Shamsudin, K. Shimizu, K. Uesugi, A. Takeuchi, Y. Suzuki, et al., “Cavitation during High-Temperature Deformation in Al-Mg Alloys,” Acta Materialia 2013, 61, 2403–2413. https://doi.org/10.1016/j.actamat.2013.01.012

19. A. F. Carunchio, D. A. Pereira, M. H. Fernandes Batalha, H. B. Resende, A. da Silva Antunes, “The Effectiveness of Back Pressure in Superplastic Blow Forming of Aluminum Alloy AA 5083 Performed at Very Favorable Conditions for Cavitation Growth,” Materials Research 2018, 21. https://doi.org/10.1590/1980-5373-MR-2018-0261

20. J. Campbell, “Cavitation during Superplastic Forming,” Materials 2011, 4, 1271–1286. https://doi.org/10.3390/ma4071271

21. Y. Duan, G. Xu, L. Zhou, D. Xiao, Y. Deng, Z. Yin, et al., “Achieving High Superplasticity of a Traditional Thermal-Mechanical Processed Non-Superplastic Al-

Zn-Mg Alloy Sheet by Low Sc Additions," Journal of Alloys and Compounds 2015, 638, 364–373. https://doi.org/10.1016/j.jallcom.2015.03.090

22. R. A. Al-Hammadi, R. Zhang, C. Cui, X. Tao, Y. Zhou, "Deformation Mechanism and Fracture Behavior of a Coarse-Grain Ni-Co-Based Superalloy during Superplasticity," Acta Metallurgica Sinica (English Letters) 2025, 38, 2024–2034. https://doi.org/10.1007/s40195-025-01914-1

23. M. E. Hosseini, S. J. Hosseinipour, M. B. Jooybari, "Analysis of Void Growth during Superplastic Deformation of Commercial AL5083 Alloy," Iranian Journal of Science and Technology, Transactions of Mechanical Engineering 2018, 42, 41–49. https://doi.org/10.1007/s40997-017-0075-3

24. H. T. Jeong, H. K. Park, H. S. Kang, W. J. Kim, "Operation of Solute-Drag Creep in an AlCoCrFeMnNi High-Entropy Alloy and Enhanced Hot Workability," Journal of Alloys and Compounds 2020, 824, 153829. https://doi.org/10.1016/j.jallcom.2020.153829

25. A. Venkataraman, M. Linne, S. Daly, M. D. Sangid, "Criteria for the Prevalence of Grain Boundary Sliding as a Deformation Mechanism," Materialia 2019, 8, 100499. https://doi.org/10.1016/j.mtla.2019.100499

26. A. V. Mikhaylovskaya, O. A. Yakovtseva, I. S. Golovin, A. V. Pozdniakov, V. K. Portnoy, "Superplastic Deformation Mechanisms in Fine-Grained Al-Mg Based Alloys," Materials Science and Engineering: A 2015, 627, 31–41. https://doi.org/10.1016/j.msea.2014.12.099

27. K. Sotoudeh, P. S. Bate, "Diffusion Creep and Superplasticity in Aluminium Alloys," Acta Materialia 2010, 58, 1909–1920. https://doi.org/10.1016/j.actamat.2009.11.034

28. E. Alabort, P. Kontis, D. Barba, K. Dragnevski, R. C. Reed, "On the Mechanisms of Superplasticity in Ti–6Al–4V," Acta Materialia 2016, 105, 449–463. https://doi.org/10.1016/j.actamat.2015.12.003

29. M. Li, Q. Pan, Y. Shi, X. Sun, H. Xiang, "High Strain Rate Superplasticity in an Al–Mg–Sc–Zr Alloy Processed via Simple Rolling," Materials Science and Engineering: A 2017, 687, 298–305. https://doi.org/10.1016/j.msea.2017.01.091

30. R. A. Al-Hammadi, R. Zhang, C. Cui, Z. Zhou, Y. Zhou, "Effects of Temperature on Superplastic and Fracture Behaviors of a Ni-Co-Based Superalloy," Journal of Alloys and Compounds 2023, 958, 170524. https://doi.org/10.1016/j.jallcom.2023.170524

31. R. A. Al-Hammadi, R. Zhang, C. Cui, Z. Zhou, Y. Zhou, "Revealing the Void Formation Mechanism during Superplastic Deformation of a Fine-Grained Ni–Co-

Base Superalloy," Acta Metallurgica Sinica (English Letters) 2024, 37, 915–920. https://doi.org/10.1007/s40195-024-01670-8

32. E. K. Kweitsu, D. K. Sarkar, A. Y. Algendy, X.-G. Chen, J. Veilleux, N. Bombardier, "Effect of Annealing Time on Grain Structure Evolution and Superplastic Response of Al-Mg 5xxx Alloys," Materials 2024, 17, 5492. https://doi.org/10.3390/ma17225492

33. A. Smolej, B. Skaza, E. Slaček, "Superplasticity of the 5083 Aluminium Alloy with the Addition of Scandium," Materials and Technology 2009, 43, 299–302.

34. A. H. Chokshi, "Grain Boundary Processes in Strengthening, Weakening, and Superplasticity," Advanced Engineering Materials 2020, 22, 1900748. https://doi.org/10.1002/adem.201900748

35. X. G. Wang, Q. S. Li, R. R. Wu, X. Y. Zhang, L. Ma, "A Review on Superplastic Formation Behavior of Al Alloys," Advances in Materials Science and Engineering 2018, 2018, 7606140. https://doi.org/10.1155/2018/7606140

36. A. D. Kotov, A. V. Mikhaylovskaya, M. S. Kishchik, A. A. Tsarkov, S. A. Aksenov, V. K. Portnoy, "Superplasticity of High-Strength Al-Based Alloys Produced by Thermomechanical Treatment," Journal of Alloys and Compounds 2016, 688, 336–344. https://doi.org/10.1016/j.jallcom.2016.07.045

37. T. G. Nieh, J. Wadsworth, O. D. Sherby, Superplasticity in Metals and Ceramics, Cambridge University Press, Cambridge 1997. https://doi.org/10.1017/CBO9780511525230

38. E. K. Kweitsu, D. K. Sarkar, A. Y. Algendy, X.-G. Chen, J. Veilleux, N. Bombardier, "Superplastic Deformation and Microstructural Evolution of an Al–Mg–Mn 5xxx Alloy for High-Speed Blow Forming Applications," Journal of Materials Science 2026, 61, 16033–16053. https://doi.org/10.1007/s10853-026-12693-0

39. N. T. C. Nguyen, P. Asghari-Rad, P. Sathiyamoorthi, A. Zargaran, C. S. Lee, H. S. Kim, "Ultrahigh High-Strain-Rate Superplasticity in a Nanostructured High-Entropy Alloy," Nature Communications 2020, 11, 2736. https://doi.org/10.1038/s41467-020-16601-1

40. K. Liu, X. G. Chen, "Development of Al-Mn-Mg 3004 Alloy for Applications at Elevated Temperature via Dispersoid Strengthening," Materials & Design 2015, 84, 340–350. https://doi.org/10.1016/j.matdes.2015.06.140

41. A. Y. Algendy, K. Liu, X.-G. Chen, "Effect of Mn-Bearing Dispersoids on Tensile Properties and Recrystallization Resistance of Al-3Mg-0.8Mn Rolled Alloy,"

Advanced Engineering Materials 2023, 25, 2300667.
https://doi.org/10.1002/adem.202300667

Chapter 6

Microstructural Evolution and Strain-Rate-Dependent Deformation of Sc–Zr–Er Microalloyed Al–Mg–Mn 5xxx Alloys Produced from Recycled Automotive Sheet Scrap for High-Speed Blow Forming

Abstract

The effects of Sc–Zr–Er microalloying on the microstructural evolution and deformation behavior of scrap-based Al–Mg–Mn 5xxx alloys were investigated under high-speed blow forming (HSBF)-relevant conditions. Short-time annealing at 500 °C produced a fully recrystallized structure in the base alloy (B), whereas the high-Sc (BSc10Zr) and low-Sc + Er (BSc05ZrEr) alloys retained predominantly banded structures owing to the strong pinning effect of nanoscale $L1_2$-structured Al_3(Sc,Zr) and Al_3(Sc,Zr,Er) precipitates. At 0.01 s^{-1}, BSc05ZrEr exhibited the highest elongation, reaching 256 %, compared with 200 % for BSc10Zr and 175 % for B. At 0.1 s^{-1}, BSc10Zr achieved the highest elongation of 259 %, while BSc05ZrEr maintained a comparable value of 254 %, demonstrating high ductility over a broader strain-rate range. EBSD analysis revealed pronounced grain-boundary evolution in the Sc-containing alloys, including increased high-angle grain-boundary fractions consistent with progressive boundary misorientation and CDRX-assisted boundary evolution, contributing to enhanced strain accommodation. At 1 s^{-1}, elongation decreased in all alloys as intragranular deformation became increasingly dominant, although the Sc-containing alloys exhibited greater deformation stability and lower susceptibility to strain localization.

Under dual-stage high-to-low strain-rate deformation, BSc05ZrEr achieved the highest elongation of 286 %, demonstrating superior strain-rate-transition tolerance relative to B. These findings demonstrate that Sc–Zr–Er microalloying influences strain-rate-dependent boundary evolution and deformation stability, providing a mechanistic basis for developing reduced-Sc, scrap-based Al–Mg–Mn alloys with enhanced strain-rate-transition tolerance for HSBF applications.

Keywords: Al–Mg–Mn 5xxx alloys; Sc–Zr–Er microalloying; High strain-rate deformation; Microstructure; $Al_3(Sc,Zr)/Al_3(Sc,Zr,Er)$ precipitates; High-speed blow forming.

6.1 Introduction

Al–Mg–Mn 5xxx series alloys are widely used in automotive sheet applications because of their excellent formability, corrosion resistance, and weldability [1–3]. Suitably processed, fine-grained Al–Mg–Mn 5xxx alloys can exhibit superplastic deformation, with elongations exceeding 200 % under appropriate temperature and strain-rate conditions. This capability enables the fabrication of complex geometries through superplastic forming (SPF) [1,2,4–6] and, more recently, high-speed blow forming (HSBF) [7,8]. Conventional SPF generally requires very low strain rates, typically below 0.01 s^{-1} [9–12], resulting in long forming cycles. HSBF improves forming efficiency by combining rapid deformation with gas-pressure forming, resulting in substantial variations in strain rate during the forming process [10,13]. However, this rapid forming route can promote strain localization, cavitation, and dimensional variation when the alloy's deformation response, temperature distribution, tooling conditions, and pressure path are not adequately controlled [9,14].

Within this broader processing framework, developing alloys capable of maintaining deformation stability over a wide strain-rate range is essential for reliable forming.

The deformation behavior of Al–Mg–Mn alloys under HSBF-relevant conditions is strongly governed by recrystallization, microstructural stability, and the capacity for strain accommodation at elevated temperatures. Resistance to strain localization during rapid deformation, together with the alloy's ability to accommodate subsequent variations in strain rate, is important for preventing premature failure [15]. Most commercial superplastic Al–Mg–Mn alloys, however, were developed for conventional SPF, which operates under relatively low and nearly constant strain-rate conditions [16–18]. Their microstructures may therefore not be optimized for the large strain-rate variations associated with rapid forming processes such as HSBF.

Microalloying with Sc and Zr improves the microstructural stability and high-temperature deformation response of Al–Mg alloys through the formation of coherent $L1_2$-$Al_3(Sc,Zr)$ precipitates, which inhibit grain-boundary migration and retard recrystallization [19–21]. However, Sc additions commonly approaching or exceeding 0.10 wt.% substantially increase alloy cost and limit large-scale industrial application [22–25]. Er additions have therefore been investigated as a potential means of reducing the required Sc content while retaining effective precipitate pinning and thermal stability through the formation of Al_3Er and $Al_3(Sc,Zr,Er)$-based precipitates [26–29]. Owing to differences in solute diffusivity, $Al_3(Sc,Zr,Er)$-based precipitates may develop a core–double-shell architecture comprising an Er-rich core, a Sc-rich intermediate shell, and a Zr-rich outer shell [28,30]. Such compositional partitioning can enhance coarsening resistance and long-term thermal stability. At Er contents above approximately 0.045 at.%, primary Al_3Er particles may also form during solidification [31,32]. Depending on their size and distribution, these

particles may influence the as-cast grain structure and subsequently promote particle-stimulated nucleation during recrystallization, thereby improving the superplastic response of Al–Mg based alloys [33–35].

In addition to nanoscale precipitates, Mn-containing dispersoids and their spatial distribution strongly influence recrystallization and deformation in Al–Mg–Mn alloys [20,36]. Combined Sc, Zr, and Er additions can alter precipitation behavior, producing heterogeneous dispersoid distributions [27,31,37]. In Mn-containing alloys, this heterogeneity may promote the formation of dispersoid-free zones (DFZs), depending on alloy composition and thermomechanical processing [38]. These regions may influence local recrystallization, boundary evolution, strain partitioning, and deformation stability during high-temperature deformation. Nevertheless, their influence on microstructural evolution, deformation behavior, and strain-rate-transition tolerance under HSBF-relevant conditions remains poorly understood. Although enhanced formability has been reported in Sc- and Zr-modified Al–Mg(–Mn) alloys, most previous studies have focused on relatively low strain rates, typically $\leq 0.1\ s^{-1}$ [2,24,25,35,39]. Consequently, the relationship between particle-distribution heterogeneity, microstructural evolution, and deformation stability across the wider strain-rate range relevant to HSBF has not been systematically investigated.

The use of industrial scrap provides an additional pathway for reducing both alloy cost and environmental impact. The manufacture of automotive body panels and other aluminum-sheet components generates substantial quantities of process scrap, while the increasing availability of automotive sheet scrap from end-of-life vehicles creates opportunities for closed-loop recycling [40]. Research on recycled aluminum has nevertheless focused predominantly on casting alloys and impurity management, with comparatively limited attention given to high-performance sheet alloys for advanced forming processes [41]. The

combined effects of Sc–Zr–Er microalloying, recrystallization, and strain-rate-dependent deformation in scrap-based Al–Mg–Mn sheet alloys therefore remain insufficiently understood. Integrating controlled microalloying with scrap-based alloy development may provide a viable route toward more sustainable alloys for HSBF applications.

Building on recent insights into deformation behavior under HSBF-relevant conditions [15], the present work investigates the microstructural evolution and high-temperature deformation behavior of scrap-based Al–Mg–Mn 5xxx alloys microalloyed with Sc–Zr–Er. Particular emphasis is placed on how precipitate formation, dispersoid heterogeneity, and recrystallization behavior influence microstructural evolution and deformation stability across a wide strain-rate range of 0.01–1 s^{-1}, together with the ability of selected alloys to accommodate a dual-stage high-to-low strain-rate deformation path. The results highlight the importance of designing alloys for deformation stability and strain-rate-transition tolerance under HSBF-relevant conditions, rather than solely maximizing low-strain-rate superplasticity. By establishing mechanistic relationships among microstructural evolution, strain-rate-dependent boundary evolution, and deformation behavior, this work provides guidance for designing reduced-Sc, scrap-based Al–Mg–Mn alloys with enhanced deformation stability and strain-rate-transition tolerance for HSBF applications.

6.2 Materials and methods

6.2.1 Alloy preparation

Three Al–Mg–Mn alloys were produced by remelting industrial Al–Mg–Mn 5xxx sheet scrap consisting of clean, uncoated production offcuts from a single production batch supplied by Verbom (Valcourt, Quebec, Canada). Prior to melting, the scrap was cut into

smaller pieces and cleaned to remove surface contaminants The microalloying was achieved using Al–2Sc, Al–15Zr, and Al–6Er master alloys. The alloys were designated as B (base Al–Mg–Mn alloy), BSc10Zr (B + high-Sc, with a maximum combined Sc + Zr addition of 0.25 wt.%), and BSc05ZrEr (B + low-Sc, containing Zr and Er, with a maximum combined Sc + Zr + Er addition of 0.30 wt.%). In BSc05ZrEr, Er was incorporated as part of a reduced-Sc microalloying strategy aimed at maintaining microstructural stability. The exact compositions of the experimental microalloyed alloys are not disclosed due to industrial confidentiality. Approximately 8 kg of scrap material was used for each alloy. Melting was conducted in a graphite crucible using an induction furnace. After complete melting, the chemical composition was verified by optical emission spectroscopy (OES). The melt was held at 750 °C for 30 min and then subjected to argon degassing for 15 min to reduce dissolved hydrogen and assist the removal of non-metallic inclusions through flotation. An Al–5Ti–1B master alloy was added as a grain refiner. The melt was then poured into a permanent steel mold preheated to 250 °C, producing ingots with rectangular cross-sections and dimensions of 30 × 40 × 115 mm.

The cast ingots were subjected to a two-step homogenization treatment (300 °C/12 h + 425 °C/6 h), followed by water quenching to room temperature. The homogenization treatment was designed to (i) promote the formation of Al_3(Sc,Zr) and Al_3(Sc,Zr,Er) precipitates and Mn-containing dispersoids; (ii) dissolve low-melting eutectic phases, particularly the low-melting β-Al_3Mg_2 phase, which forms along grain boundaries under equilibrium conditions. The homogenized ingots were machined to a thickness of 26.5 mm and hot rolled at 425–450 °C to achieve a 70 % thickness reduction, followed by 75 % cold rolling at room temperature to obtain sheets with a final thickness of 2 mm. The cold-rolled sheets were subsequently subjected to isothermal annealing at 400, 450, 500, and 520 °C for

30 min to investigate the static recrystallization behavior and select appropriate deformation temperature. Figure 6.1 illustrates the schematic processing route used for alloy preparation.

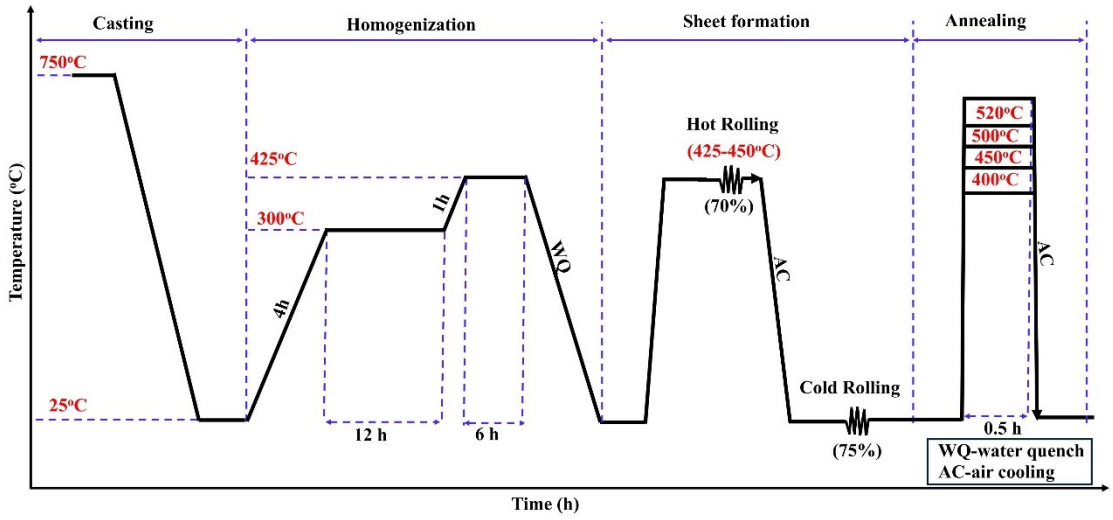


Figure 6.1. Schematic of the alloy processing route, including casting at 750 °C, two-step homogenization (300 °C/12 h + 425 °C/6 h), sheet formation by hot rolling (425–450 °C, 70 % reduction) followed by cold rolling (75 % reduction), and annealing at various temperatures.

6.2.2 Hot tensile testing

Dog-bone tensile specimens with a gauge length of 25 mm were machined from the 2-mm-thick sheets along the rolling direction. Uniaxial hot tensile tests were performed at 500 °C using a ZwickRoell Z100 universal testing machine equipped with a custom-designed sample holder for rapid heating. Tests were conducted under constant crosshead-speed control at nominal initial engineering strain rates of 0.01, 0.1 , and 1 s^{-1}. In addition to the monotonic strain-rate tests, selected specimens were subjected to a dual-stage high-to-low

strain-rate deformation path to assess their tolerance to strain-rate transitions under hybrid-forming conditions. The yield strength (YS) was determined using the conventional 0.2 % offset method from the engineering stress–strain curves.

A schematic illustration of the heating procedure is shown in Figure 6.2. The sample holder was first inserted into the furnace and preheated at 500 °C for 2 h to establish thermally stable conditions (Figure 6.2a,b). Before the tensile-test series, the specimen heating response was calibrated by attaching a thermocouple directly to a representative tensile specimen placed in the preheated holder. The specimen reached the target temperature of 500 °C after approximately two minutes, after which the temperature remained stable. Based on this calibration, a heating period of three minutes was selected for all tensile specimens to ensure that the target temperature was reached before annealing. Each specimen was therefore inserted into the preheated holder, heated for three minutes (Figure 6.2c), and then annealed at 500 °C for 10 min before tensile testing (Figure 6.2d). The 10-min annealing treatment was selected because it promoted appreciable recrystallization in the Sc-containing alloys while limiting additional grain coarsening in the base alloy.

The custom-designed preheated sample holder enabled rapid heating of the specimen to the target temperature, thereby minimizing the prolonged thermal exposure typically associated with conventional furnace-based hot tensile testing. This configuration provided a laboratory approach for investigating deformation following short thermal exposure, a relatively underexplored condition that is relevant to industrial rapid-forming processes such as HSBF. The preheated holder also enabled rapid specimen exchange and consistent thermal conditions between tests.

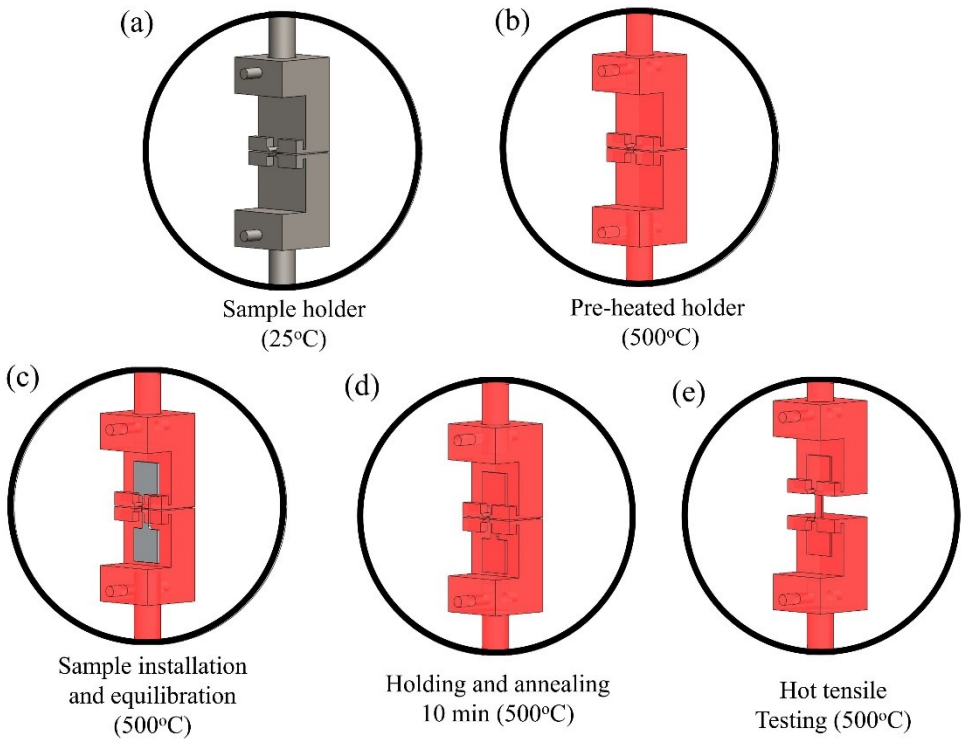


Figure 6.2. Schematic of the heating and tensile-testing procedure: (a) insertion of the tensile-sample holder into the furnace at 25 °C; (b) preheating of the holder at 500 °C for 2 h; (c) installation and thermal equilibration of the specimen for three minutes; (d) annealing at 500 °C for 10 min; and (e) hot tensile testing.

6.2.3 Microstructure characterization

The as-cast microstructure was characterized using samples sectioned from the cast ingots. Grain structure observations were performed by polarized light optical microscopy after mechanical polishing and electroetching in Barker's reagent (3 vol.% HBF_4) at 17 V for 90 s. Intermetallic phases in the as-cast condition were analyzed using scanning electron microscopy (SEM) equipped with an energy-dispersive X-ray spectroscopy (EDS) detector,

operated at 20 kV with a working distance of 15 mm. The homogenized, as-rolled, and annealed microstructures were examined by optical microscopy (OM).

The homogenized and as-rolled samples were mechanically polished and etched in 0.5% HF solution for 30 s to reveal dispersoid zones (DZs) and dispersoid-free zones (DFZs), while the grain structures were characterized by polarized light microscopy after electroetching in Barker's reagent. The DFZ area fraction was quantified from the HF-etched optical micrographs using ImageJ software. Five randomly selected micrographs were analyzed for each alloy at a magnification of 100 x. The bright DFZ regions were segmented using the thresholding tool in ImageJ, and the DFZ area fraction was calculated as the ratio of the segmented DFZ area to the total analyzed image area. The as-rolled samples were sectioned along the rolling direction (RD). In addition, Vickers hardness measurements were performed on the annealed samples using a hardness tester with a load of 25 g and a dwell time of 20 s. For each condition, 20 indentations were measured and the values obtained were averaged.

Selected samples were further characterized using electron backscatter diffraction (EBSD) to quantify grain structure and boundary characteristics. EBSD scans were conducted over an area of 300 μm × 200 μm using a step size of 0.3 μm, and the data were analyzed using HKL Channel 5 software (version 5.0). Grain boundaries were classified according to the misorientation angle (θ) as low-angle boundaries (LAB, $\theta < 5°$), medium-angle boundaries (MAB, $5° \leq \theta < 15°$), and high-angle boundaries (HAB, $\theta \geq 15°$). Indexing was performed using the aluminum CIF standard. Post-deformation OM and EBSD analysis of the microstructure was conducted in the central region of the fractured gauge section to minimize artifacts associated with localized necking near the fracture tip.

Transmission electron microscopy (TEM) was used to examine Mn-containing dispersoids and Al_3(Sc,Zr)- and Al_3(Sc,Zr,Er)-based precipitates. Thin foils for TEM analysis were prepared by twin-jet electropolishing using a solution of 30% nitric acid in methanol at 20 V and −20 °C. TEM observations were conducted at an accelerating voltage of 200 kV. The local TEM foil thickness was determined by convergent-beam electron diffraction (CBED) following the method described by Allen [42]. The number density, N_d, of Mn-containing dispersoids and Sc-, Zr-, and Er-containing precipitates was then calculated as [36]:

$$N_d = \frac{N}{A(D + t)}$$

where $N$is the number of particles counted, $A$is the analyzed area, $D$is the mean equivalent particle diameter, and $t$is the local TEM-foil thickness determined by CBED.

6.3 Results

6.3.1 As-cast microstructures

Figure 6.3 presents the as-cast microstructures of the three alloys. As shown in Figure 6.3(a–c), all alloys exhibit equiaxed grain morphology. The base alloy (B) and the Sc-containing alloy (BSc10Zr) display relatively coarse grains with average grain sizes of 116 ± 13 μm and 115 ± 13 μm, respectively. In contrast, the BSc05ZrEr alloy exhibits a substantially finer grain structure, with an average grain size of 56 ± 3 μm, representing approximately a 50 % reduction compared with the other alloys. SEM–EDS analysis (Figure 6.3d–f) revealed two types of intermetallic compounds (IMCs) in all alloys, with compositions consistent with Al_6(Mn,Fe)-type phases (bright phase) and Mg_2Si (dark phase).

In the BSc05ZrEr alloy, the Al_6(Mn,Fe)-type particles were partially modified through Er enrichment, resulting in the formation of Al_6(Mn,Fe,Er)-type particles (grey phase) in addition to the conventional Al_6(Mn,Fe)-type particles. These particles contribute to pronounced grain refinement in the BSc05ZrEr alloy (inserted Figure 6.3c) [43,44]. Moreover, Figure 6.4 presents SEM–EDS elemental maps of the Mn/Fe-containing IMCs in the BSc05ZrEr alloy, demonstrating localized Er enrichment associated with the Al_6(Mn,Fe,Er)-type particles.

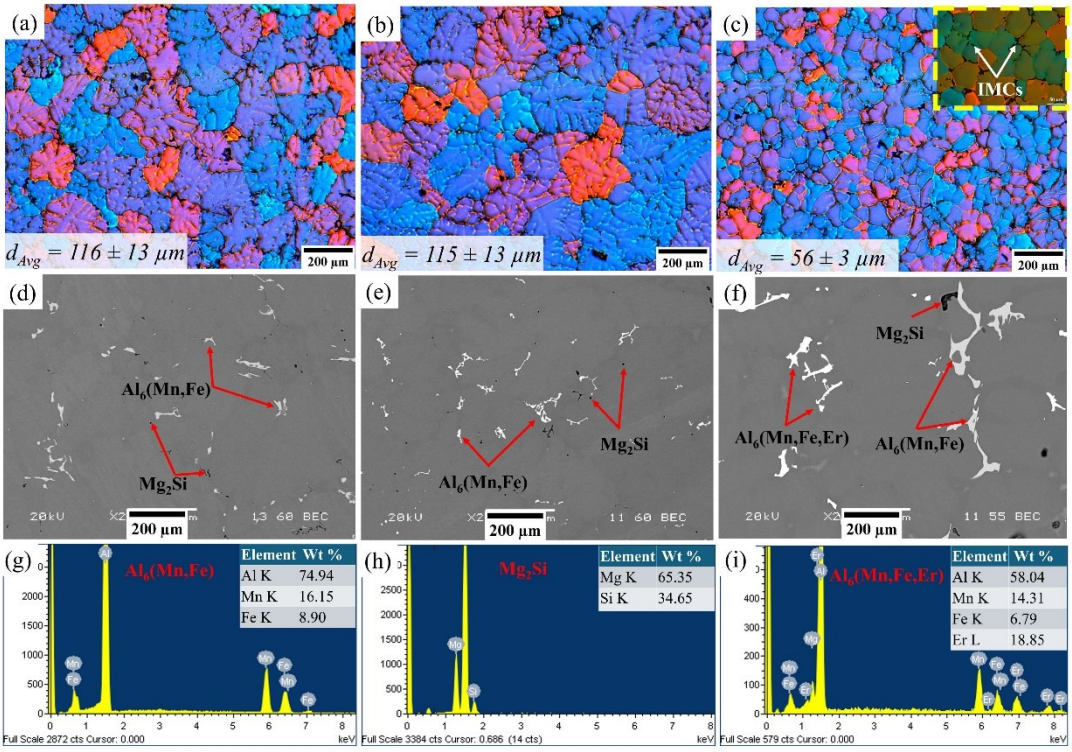


Figure 6.3**.** Optical polarized light images showing the as-cast grain structures of (a) B, (b) BSc10Zr, and (c) BSc05ZrEr. SEM images showing the intermetallic compounds (IMCs) in (d) B, (e) BSc10Zr, and (f) BSc05ZrEr. SEM–EDS spectra of particles with

compositions consistent with (g) $Al_6(Mn,Fe)$-type, (h) Mg_2Si, and (i) $Al_6(Mn,Fe,Er)$-type particles.

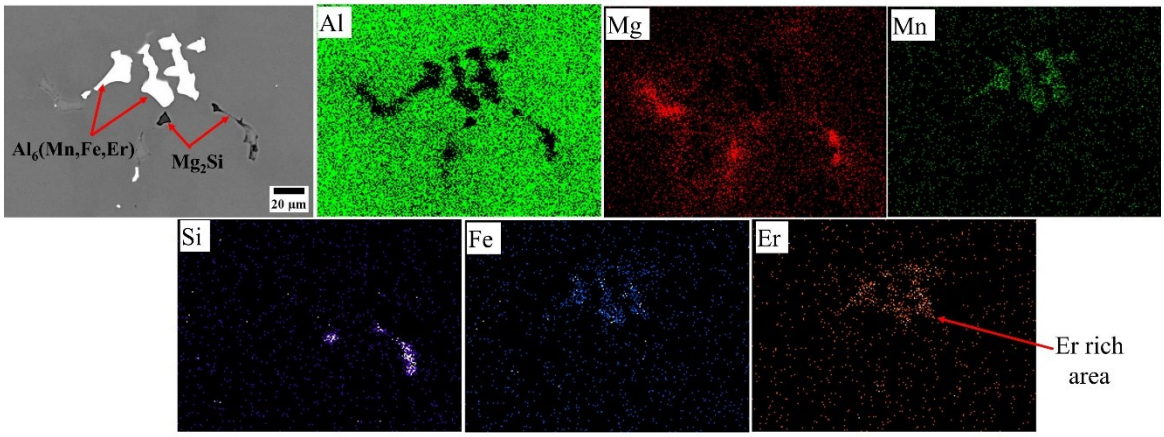


Figure 6.4. SEM–EDS elemental maps showing localized Er enrichment within $Al_6(Mn,Fe,Er)$-type particles in the BSc05ZrEr alloy.

6.3.2 As-homogenized microstructure

Figure 6.5 shows the microstructures of the alloys in the as-homogenized condition. All alloys retained a heterogeneous microstructure consisting of alternating Mn-dispersoid zones (DZ, dark regions) and Mn-dispersoid-free zones (DFZ, bright regions). The DZ regions contained a high density of fine Mn-rich dispersoids, whereas the DFZs appeared as Mn-dispersoid-depleted zones [36,45]. Microalloying increased the DFZ fraction, as shown in Figure 6.5b–d. The base alloy exhibited a DFZ fraction of approximately 20%, which increased slightly to ~25% in BSc10Zr, while the highest DFZ fraction (~35%) was observed in BSc05ZrEr. Because DFZs locally reduce dispersoid pinning, their increased fraction, particularly in BSc05ZrEr, is expected to influence subsequent microstructural evolution and

deformation behavior during high-temperature deformation. These effects are discussed in Sections 6.4.1 and 6.4.2.

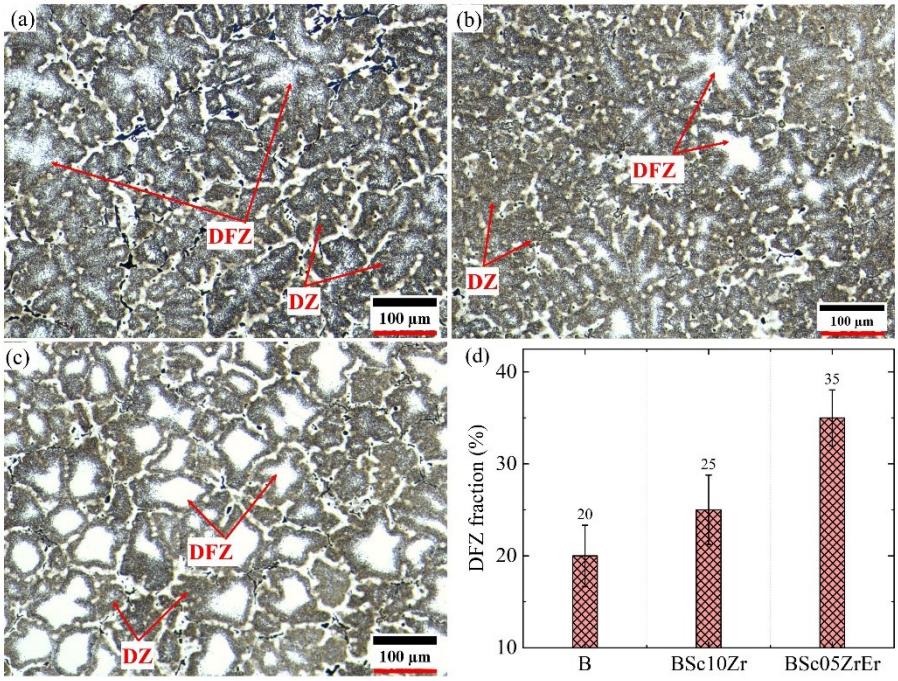


Figure 6.5. Optical images showing as-homogenized microstructures after 0.5% HF etching for 30 s: (a) B, (b) BSc10Zr, and (c) BSc05ZrEr alloys, highlighting Mn dispersoid zones (DZ) and Mn dispersoid-free zones (DFZ). (d) Corresponding DFZ fraction for each alloy.

6.3.3 As-rolled microstructure

Figure 6.6 shows the optical microstructures of alloys B, BSc10Zr, and BSc05ZrEr in the as-rolled condition. As shown in Figure 6.6(a–c), all alloys exhibit elongated grain structures aligned along the rolling direction (RD). Intermetallic particles are also aligned along the RD, consistent with particle fragmentation and redistribution during rolling. All alloys display a banded morphology consisting of alternating Mn-DZs and Mn-DFZs (Figure 6.6a–f), indicating that the DZ–DFZ distribution observed in the as-cast state is retained after

rolling. Differences in band characteristics are evident among the alloys. Alloy B exhibits relatively narrow Mn-DFZ regions with a more uniform dispersoid distribution, whereas BSc10Zr shows broader and more continuous Mn-DFZ bands. BSc05ZrEr exhibits the most pronounced banding, with significantly wider Mn-DFZ regions. The persistence of this DZ–DFZ morphology after rolling establishes the initial microstructural heterogeneity prior to subsequent recrystallization and grain-structure evolution during annealing.

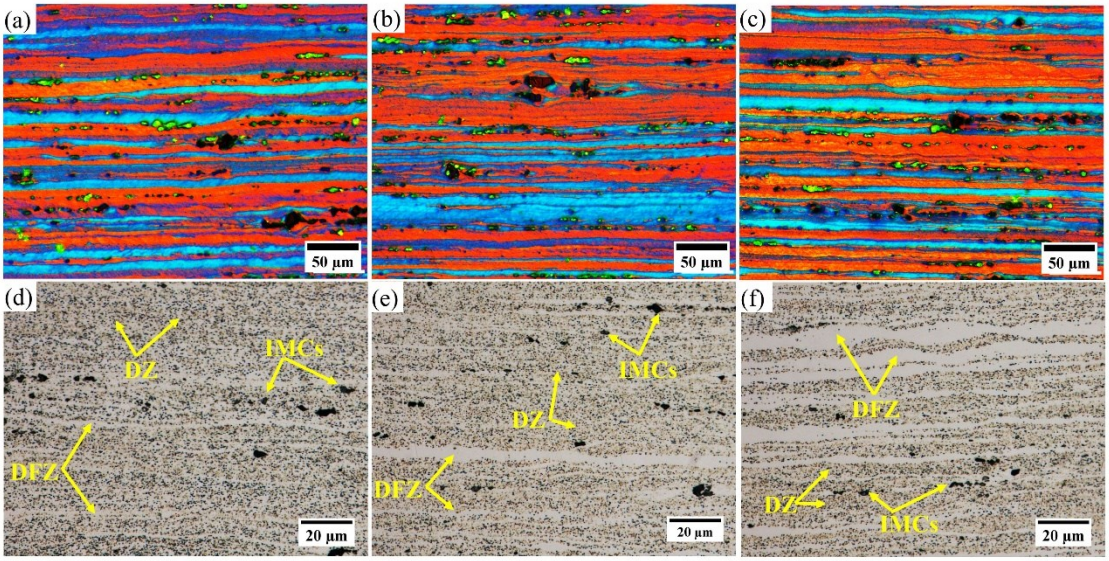


Figure 6.6. Optical micrographs of the as-rolled microstructures. Polarized light OM images showing elongated grain structures in (a) B, (b) BSc10Zr, and (c) BSc05ZrEr alloys. HF-etched OM images (0.5% HF, 30 s) highlighting alternating dispersoid zones (DZ) and dispersoid-free zones (DFZ) in (d) B, (e) BSc10Zr, and (f) BSc05ZrEr.

6.3.4 Static recrystallization behavior during annealing

Figure 6.7 presents the evolution of Vickers hardness during annealing, while Figure 6.8 shows the corresponding grain structure evolution at different annealing temperatures. At

400 °C, the base alloy exhibits a pronounced reduction in hardness relative to the as-rolled condition, corresponding to the development of a fully recrystallized and equiaxed grain structure (Figure 6.8a). As the annealing temperature increases from 450 to 500 °C, the hardness remains low and relatively constant, while progressive grain coarsening is observed (Figure 6.8d,g,j). This indicates that static recrystallization is essentially completed in the base alloy at 400 °C. In contrast, the Sc-containing alloys (BSc10Zr and BSc05ZrEr) retain significantly higher hardness at 400 °C, with deformed and elongated grains (Figure 6.8b,c), indicating a recovery-dominated state. At 450 °C, BSc10Zr still exhibits elongated grains with no clear evidence of recrystallization, whereas BSc05ZrEr shows the emergence of isolated equiaxed grains within the deformed matrix (Figure 6.8e,f), indicating the onset of static recrystallization. These observations indicate that, although both Sc-containing alloys exhibit enhanced recrystallization resistance compared with the base alloy, recrystallization initiates earlier in BSc05ZrEr than in BSc10Zr.

At 500 °C, both Sc-containing alloys exhibit a further reduction in hardness (Figure 6.7), accompanied by more pronounced recrystallization, particularly in BSc05ZrEr. In BSc10Zr, recrystallization remains localized, with large regions of elongated grains still present (Figure 6.8h). In contrast, BSc05ZrEr exhibits a higher density of equiaxed grains distributed throughout the microstructure, although unrecrystallized elongated grains remain present, indicating a more advanced but incomplete recrystallization state (Figure 6.8i). At 520 °C, BSc05ZrEr exhibits a pronounced decrease in hardness, consistent with the more advanced recrystallization observed in the microstructure (Figure 6.8l). By comparison, BSc10Zr retains relatively higher hardness and a larger proportion of elongated grains (Figure 6.8k), indicating stronger resistance to static recrystallization.

Based on these results, 500 °C was selected as an appropriate intermediate temperature at which static recrystallization becomes appreciable in the Sc-containing alloys, while the base alloy remains fully recrystallized without significant additional grain coarsening. This condition therefore provides a suitable microstructural baseline for investigating the influence of Sc–Zr–Er microalloying on subsequent microstructural evolution and high-temperature deformation behavior.

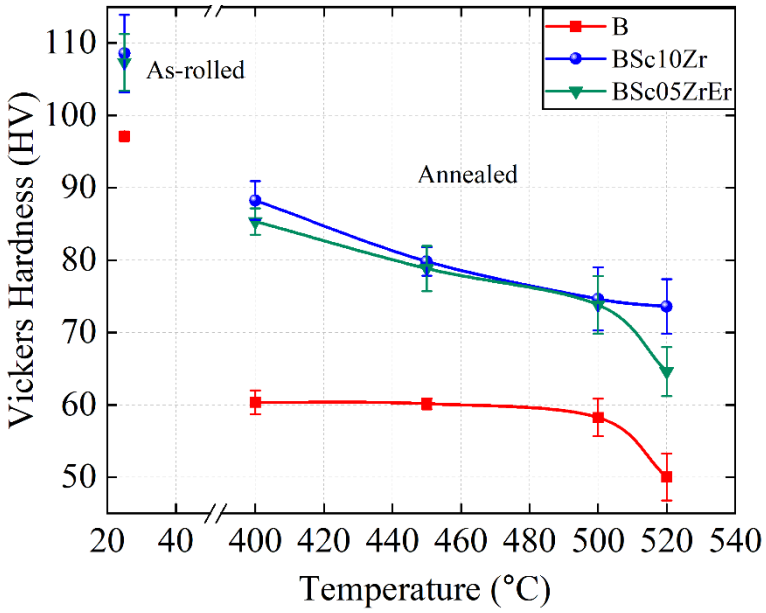


Figure 6.7. Effect of annealing temperature on hardness evolution in the three alloys.

To further examine the recrystallization behavior of the developed alloys under short thermal exposure relevant to rapid forming processes such as HSBF, additional annealing experiments were conducted at 500 °C for 5 and 10 min. Figure 6.9 shows the resulting grain structures, revealing clear differences among the alloys. The base alloy exhibits a fully recrystallized, equiaxed grain structure even after 5 min (Figure 6.9a), with no significant change after extending the holding time to 10 min (Figure 6.9d). In contrast, the Sc-

containing alloys (BSc10Zr and BSc05ZrEr) show a strong dependence on annealing time. After 5 min, BSc05ZrEr already exhibits the onset of recrystallization, whereas BSc10Zr retains a predominantly elongated grain structure (Figure 6.9b,c). Appreciable recrystallization in BSc10Zr becomes evident only after 10 min (Figure 6.9e).

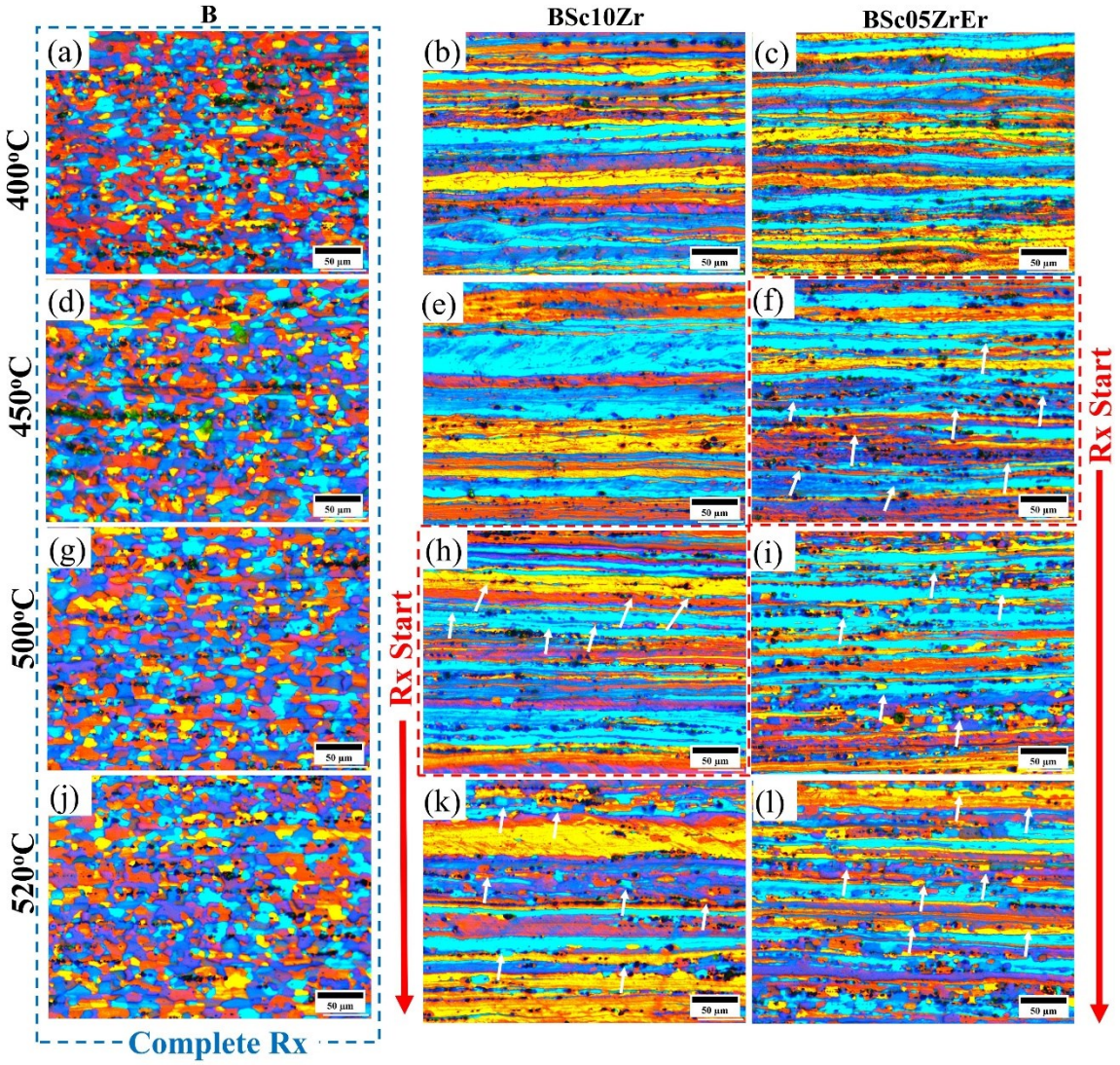


Figure 6.8. Effect of annealing temperature on static recrystallization behaviour of alloys B, BSc10Zr and BSc05ZrEr at (a-c) 400 °C, (d-f) 450 °C, (g-i) 500 °C and (j-l) 520 °C.

These results indicate that 5 min at 500 °C is insufficient to promote appreciable recrystallization in the Sc-containing alloys. Therefore, an annealing condition of 10 min at 500 °C was selected for the subsequent high-temperature tensile experiments. This condition retains a fully recrystallized microstructure with limited additional grain coarsening in the base alloy while promoting appreciable recrystallization in the Sc-containing alloys. It therefore provides an appropriate microstructural baseline for evaluating strain-rate-dependent deformation following relatively short thermal exposure relevant to rapid forming processes.

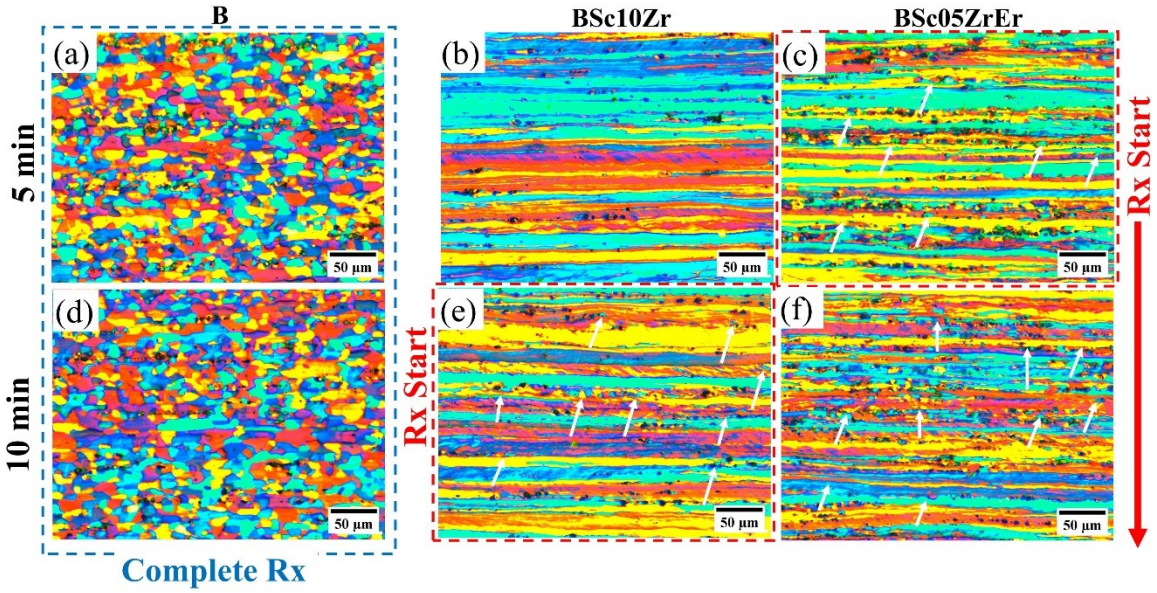


Figure 6.9. Polarized optical OM micrographs showing the grain structure evolution of the three alloys after annealing at 500 °C for two different times: (a–c) 5 min and (d–f) 10 min.

6.3.5 TEM characterization of dispersoids and precipitates after annealing

Figure 6.10 presents the TEM microstructures of the alloys after annealing at 500 °C for 10 min, while the corresponding quantitative analysis of Mn-dispersoids and precipitates is summarized in Table 6.1. Mn-containing dispersoids are observed in all alloys (Figure 6.10a,d,g), which are known to contribute to grain boundary stabilization and recrystallization control in Al–Mg–Mn alloys [8,46,47]. The base alloy exhibits a more uniform spatial distribution of finer Mn-dispersoids, with a mean size of 57.7 ± 29.8 nm, compared with 116.4 ± 71.5 nm in BSc10Zr and 98.2 ± 49.3 nm in BSc05ZrEr. Similarly, the base alloy exhibits a higher number density of Mn-dispersoids ($5.50 \pm 0.9 \times 10^{19}$ m^{-3}) than BSc10Zr ($2.23 \pm 0.7 \times 10^{19}$ m^{-3}) and BSc05ZrEr ($2.40 \pm 0.4 \times 10^{19}$ m^{-3}). The lower dispersoid density in the Sc-containing alloys is consistent with the reduced solubility of Mn in the presence of Sc and Zr, as reported for Al–Mg–Mn alloys [36]. It is also consistent with the presence of DFZs observed in the as-homogenized (Figure 6.5) and as-rolled (Figure 6.6) conditions, suggesting that the heterogeneous dispersoid distribution persists after annealing. TEM–EDS analysis (Figure 6.10b), together with previous reports [36,45,46], indicates that the Mn-containing dispersoids are consistent with Al_6Mn-type phases.

Besides Mn-dispersoids, nanoscale Al_3(Sc,Zr) precipitates are observed in BSc10Zr (Figure 6.10e,f), whereas BSc05ZrEr contains a mixed population of Al_3(Sc,Zr) and Al_3(Sc,Zr,Er) precipitates (Figure 6.10h,i). The precipitates in BSc05ZrEr appear slightly coarser and less numerous than those in BSc10Zr, consistent with differences in microalloying composition and the higher diffusivity of Er [28,30]. Quantitative TEM analysis (Table 6.1) shows that the Al_3(Sc,Zr) precipitates in BSc10Zr have an average size

of 4.03 ± 2.03 nm and a number density of 1.57 ± 0.11 × 10^{22} m^{-3}. In comparison, the precipitates in BSc05ZrEr have a larger average size of 7.78 ± 3.58 nm and a lower number density of 2.08 ± 0.57 × 10^{21} m^{-3}, consistent with its reduced-Sc microalloying strategy and the presence of Er-containing precipitates.

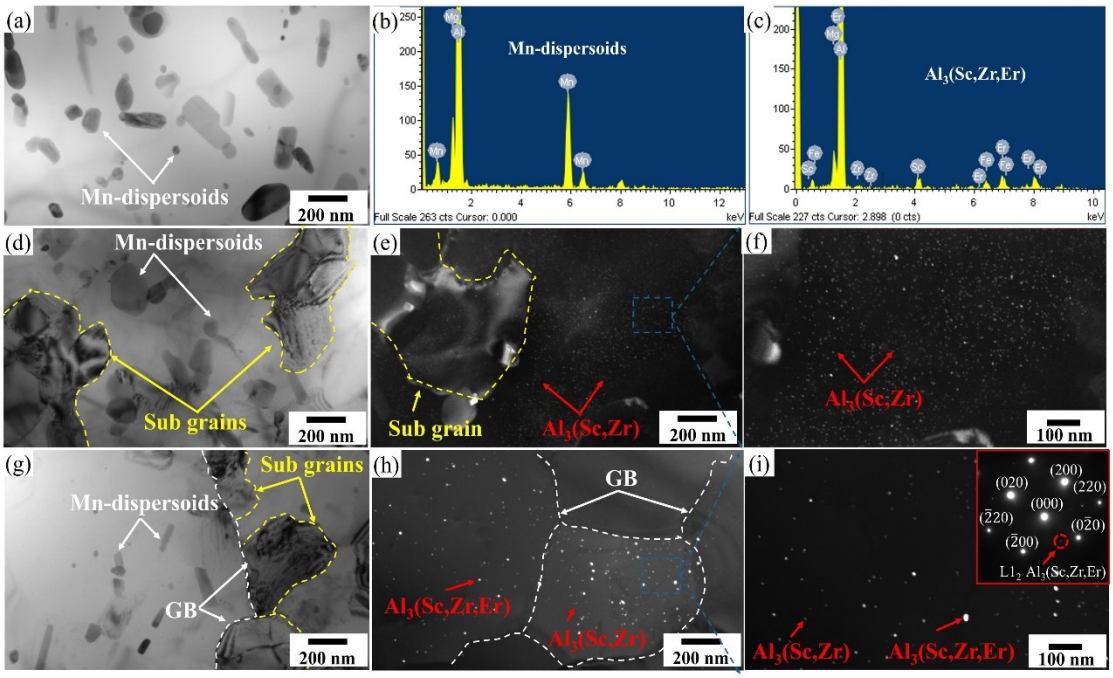


Figure 6.10. TEM bright-field images showing Mn-dispersoids in (a) B, (d) BSc10Zr, and (g) BSc05ZrEr alloys. Dark-field images highlighting nanoscale Sc-containing precipitates in (e–f) BSc10Zr alloy and (h–i) BSc05ZrEr alloy. The corresponding EDS spectra of (b) Mn-dispersoids and (c) Al_3(Sc,Zr,Er) precipitates in the BSc05ZrEr alloy. The inset in (i) shows the corresponding SAED pattern indexed along the [001] zone axis of the Al matrix.

Table 6.1 Characteristics of Mn-dispersoids and precipitates after annealing at 500 °C for 10 min

Alloys	Mn-dispersoids		Precipitates $Al_3(Sc,Zr)/Al_3(Sc,Zr,Er)$	
	Equivalent Diameter ($\overline{D}$) nm	Number Density (N_d) m^{-3}	Equivalent Diameter ($\overline{D}$) nm	Number Density (N_d) m^{-3}
B	57.7 ± 29.8	$5.50 \pm 0.9 \times 10^{19}$	--	--
BSc10Zr	116.4 ± 71.5	$2.23 \pm 0.7 \times 10^{19}$	4.03 ± 2.03	$1.57 \pm 0.11 \times 10^{22}$
BSc05ZrEr	98.2 ± 49.3	$2.40 \pm 0.4 \times 10^{19}$	7.78 ± 3.58	$2.08 \pm 0.573 \times 10^{21}$

The TEM images further reveal pronounced subgrain structures in BSc10Zr (Figure 6.10d), consistent with the delayed recrystallization observed after 10 min of annealing (Figure 6.9e). In contrast, BSc05ZrEr contains fine recrystallized grains (Figure 6.10h), together with retained subgrain features, consistent with the more advanced recrystallization observed in Figure 6.9f. These observations further confirm the distinct recrystallization responses of the two Sc-containing alloys following short-time annealing.

6.3.6 Hot tensile properties.

Figure 6.11 presents the engineering stress–strain curves of the three alloys deformed at 500 °C at different strain rates. At 0.01 s^{-1}, all alloys exhibited relatively low flow stresses, with the engineering stress increasing to a peak followed by a gradual decrease with increasing strain (Figure 6.11a). Increasing the strain rate to 0.1 s^{-1} resulted in higher flow stresses, while relatively stable deformation was maintained over a broad strain range, particularly in the Sc-containing alloys (Figure 6.11b). At 1 s^{-1}, the flow stress increased markedly, followed by a more rapid post-peak decrease in engineering stress (Figure 6.11c). Overall, the flow stress increased with increasing strain rate in all alloys, while the Sc-

containing alloys exhibited more stable deformation over a broader strain range than the base alloy.

The yield strength (YS) showed a clear dependence on both strain rate and alloy composition. At 0.01 s^{-1}, the base alloy exhibited a higher YS (26 MPa) than the Sc-containing alloys (15–16 MPa). A similar trend was observed at 0.1 s^{-1}, where the YS of the base alloy reached 50 MPa, exceeding that of the Sc-containing alloys (33–34 MPa). In contrast, at 1 s^{-1}, the Sc-containing alloys exhibited slightly higher YS values (74–75 MPa) than the base alloy (69 MPa). Thus, the relative YS response of the base and Sc-containing alloys varied with strain rate.

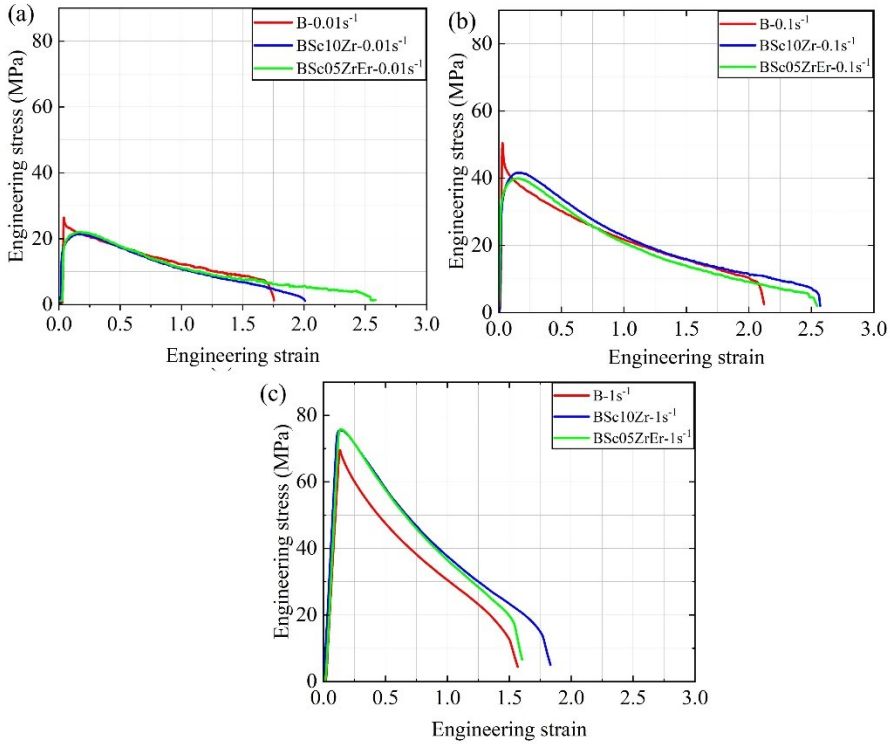


Figure 6.11. Engineering stress–strain curves from tensile tests conducted at 500 °C under different strain rates of (a) 0.01 s^{-1}, (b) 0.1 s^{-1}, and (c) 1 s^{-1}.

Figure 6.12(a) shows the variation in tensile elongation with strain rate for the B, BSc10Zr, and BSc05ZrEr alloys tested at 500 °C. The base alloy and BSc10Zr exhibited a non-monotonic strain-rate dependence, with the highest measured elongations occurring at 0.1 s^{-1}. In contrast, BSc05ZrEr maintained similarly high elongations at both 0.01 and 0.1 s^{-1}, indicating greater ductility retention across this strain-rate range. The base alloy exhibited the lowest elongation across the investigated strain-rate range, increasing from 175 % at 0.01 s^{-1} to a maximum of 217 % at 0.1 s^{-1} before decreasing to 157 % at 1 s^{-1}. BSc10Zr followed a similar trend but exhibited substantially higher ductility, reaching 259 % at 0.1 s^{-1} compared with 200 % and 184 % at 0.01 and 1 s^{-1}, respectively. In contrast, BSc05ZrEr maintained high elongations at both 0.01 s^{-1} (256 %) and 0.1 s^{-1} (254 %) before decreasing to 160% at 1 s^{-1}, demonstrating a broader strain-rate window for high ductility.

Figure 6.12b shows the evolution of the global strain-rate sensitivity index (m) with increasing true strain. The m-values were calculated from the slopes of the $\ln(\sigma_{\text{true}})$versus $\ln(\dot{\varepsilon})$ relationships at true strains of 0.1, 0.3, and 0.5 over the investigated strain-rate range of 0.01–1 s^{-1}. The true stress and true strain values were derived from the engineering stress–strain curves shown in Figure 6.11. The evaluation at different strain levels was used to examine the evolution of strain-rate sensitivity with increasing deformation. The base alloy exhibited consistently lower m-values (0.20–0.22) throughout the investigated strain range, whereas the microalloyed alloys maintained comparatively higher values. BSc10Zr exhibited the highest m-value at low strain (0.28) and subsequently maintained a relatively stable value of approximately 0.26, while BSc05ZrEr increased from 0.24 at a true strain of 0.1 to approximately 0.25–0.26 at higher strains. The slightly higher global m-values of the Sc-

containing alloys are consistent with improved resistance to strain localization relative to the base alloy [8,48,49].

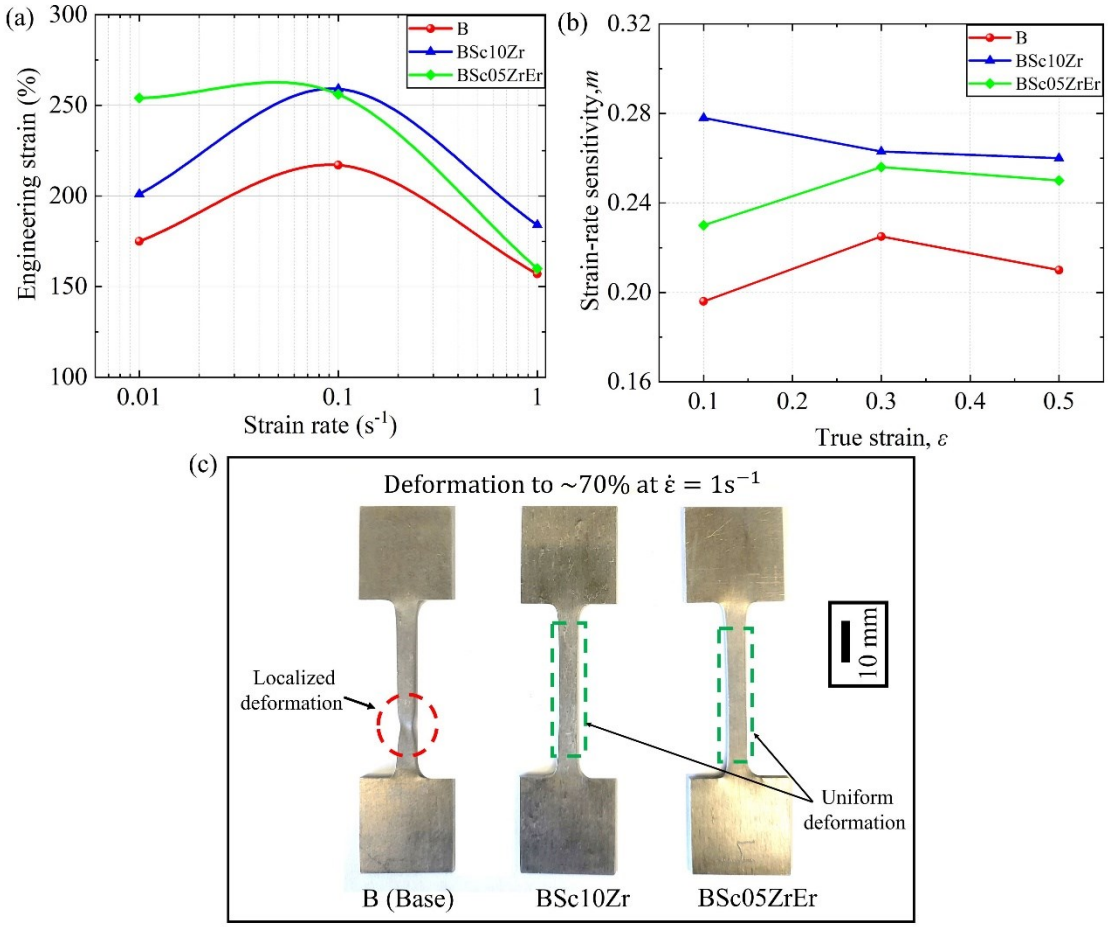


Figure 6.12**.** (a) Engineering elongation as a function of strain rate for alloys B, BSc10Zr, and BSc05ZrEr tested at 500 °C. (b) Evolution of the global strain-rate sensitivity index (m) with true strain, evaluated at 0.1, 0.3, and 0.5 over the investigated strain-rate range of 0.01–1 s^{-1}. (c) Representative tensile specimens after deformation to approximately 70% engineering strain under the high-strain-rate condition (1 s^{-1}), showing pronounced strain localization in the base alloy (B) and more uniform deformation in BSc10Zr and BSc05ZrEr.

To further evaluate deformation stability at high strain rate, interrupted tensile tests were performed at 1 s^{-1} to approximately 70 % engineering strain (true strain ≈ 0.53). This strain level provides a common substantial deformation at high strain rate for evaluating the tendency for strain localization, an important consideration in rapid forming processes. It also enables comparison with the strain-rate sensitivity evolution shown in Figure 6.12b. As shown in Figure 6.12c, the base alloy exhibited pronounced necking, indicating strain localization. In contrast, BSc10Zr and BSc05ZrEr showed more uniform deformation with negligible necking. This behavior is consistent with their higher strain-rate sensitivity and indicates greater resistance to strain localization and improved deformation stability under high-strain-rate conditions.

6.3.7 Dual-stage deformation

To further evaluate the ability of the alloys to accommodate strain-rate transitions, which is critical for rapid forming processes involving large variations in strain rate, such as HSBF [7,8], selected specimens were subjected to high-strain-rate pre-deformation followed by deformation to failure under a lower strain-rate condition. The initial pre-strain was selected to provide substantial high-strain-rate deformation while remaining below the strain range associated with pronounced strain localization observed in Figure 6.12c. This dual-stage loading provides a controlled assessment of strain-rate-transition tolerance. Among the Sc-containing alloys, BSc05ZrEr was selected for comparison with the base alloy because it exhibited high elongation at the low strain rate while containing less Sc than BSc10Zr. This combination makes BSc05ZrEr particularly relevant for evaluating strain-rate-transition tolerance within a reduced-Sc alloy design strategy. The specific pre-strain level and

representative stress–strain curves associated with the dual-stage deformation path are not disclosed due to industrial confidentiality.

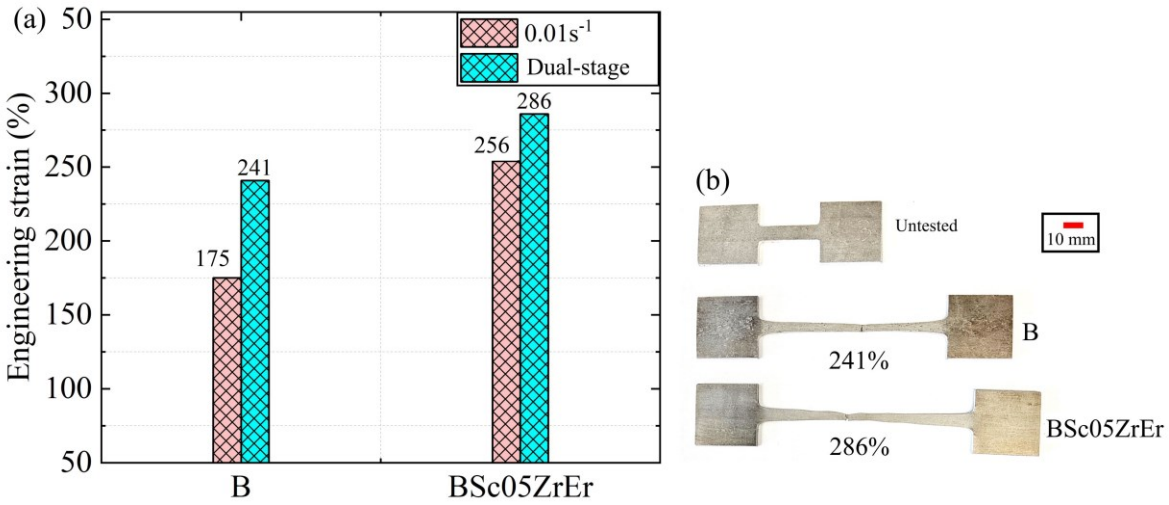


Figure 6.13. (a) Tensile elongation at 500 °C under monotonic deformation at 0.01 s^{-1} and under a dual-stage high-to-low strain-rate deformation path for alloys B and BSc05ZrEr. (b) Representative tensile specimens after dual-stage deformation, showing the retained ductility following the strain-rate transition.

The tensile elongations obtained under monotonic and dual-stage deformation are shown in Figure 6.13a, while representative tensile specimens are presented in Figure 6.13b. Under monotonic deformation at 0.01 s^{-1}, the base alloy exhibited an elongation of 175 %, whereas BSc05ZrEr achieved 256 %. Under dual-stage deformation, both alloys exhibited higher total elongations, reaching 241 % for the base alloy and 286 % for BSc05ZrEr. These results demonstrate that both alloys can accommodate substantial deformation following a high-to-low strain-rate transition. However, the pronounced strain localization observed in the base alloy under the high-strain-rate condition (Figure 6.12c) suggests that its strain-rate-transition tolerance may decrease with increasing high-strain-rate pre-deformation. In

contrast, the greater resistance of BSc05ZrEr to strain localization indicates improved deformation stability, consistent with its superior performance under dual-stage loading. These findings highlight the importance of deformation stability and strain-rate-transition tolerance under HSBF-relevant conditions.

6.3.8 Grain structure evolution during tensile deformation

Figure 6.14 presents polarized-light OM images of the grain structures of the alloys in the annealed condition and after deformation at 0.01, 0.1, and 1 s^{-1}. Prior to deformation, the base alloy exhibits a fully recrystallized and equiaxed grain structure, whereas the Sc-containing alloys retain predominantly deformed and banded grain structures (Figure 6.14a–c). Following deformation at 0.01 s^{-1} (Figure 6.14d–f), the base alloy develops elongated grains aligned along the tensile direction while retaining a relatively heterogeneous grain morphology. In contrast, BSc10Zr largely preserves its continuous banded structure (Figure 6.14e), indicating limited disruption of the initial grain structure during deformation. BSc05ZrEr exhibits a more disrupted banded structure, together with a greater presence of fine grains within the deformation bands (Figure 6.14f), indicating more pronounced grain-structure evolution than in BSc10Zr.

At 0.1 s^{-1} (Figure 6.14g–i), the base alloy develops a heterogeneous microstructure consisting of elongated grains and localized fine-grained regions, highlighted by the white arrows (Figure 6.14g), indicating pronounced grain-structure evolution during deformation. The Sc-containing alloys retain their banded morphology; however, disruption within the bands becomes more pronounced than at 0.01 s^{-1}. In BSc10Zr, localized fine-grained regions are evident within the deformation bands (Figure 6.14h), whereas BSc05ZrEr exhibits a

greater presence of fine grains and more extensive disruption of the banded structure (Figure 6.14i), indicating more pronounced microstructural evolution.

Further increasing the strain rate to 1 s^{-1} (Figure 6.14j–l) results in distinct deformation microstructures. The base alloy continues to exhibit elongated grains with localized fine-grained regions (Figure 6.14j). In contrast, the Sc-containing alloys retain largely continuous banded structures with comparatively limited disruption of the initial grain morphology (Figure 6.14k,l). Compared with the 0.1 s^{-1} condition, less extensive microstructural evolution is evident in the Sc-containing alloys at 1 s^{-1}. Nevertheless, localized fine-grained regions remain visible within the deformation bands, particularly in BSc05ZrEr (Figure 6.14l). Overall, comparison of the annealed and high-strain-rate-deformed microstructures indicates substantially greater grain-structure evolution in the base alloy, whereas the Sc-containing alloys largely retain their initial banded morphology even after deformation at 1 s^{-1}.

To further examine the deformation microstructure under a condition associated with high ductility across the investigated alloys, EBSD analysis was performed on annealed samples and samples deformed at 0.1 s^{-1}, as shown in Figure 6.15. The annealed base alloy (Figure 6.15a) exhibits a fully recrystallized microstructure characterized by equiaxed grains, whereas BSc10Zr (Figure 6.15d) and BSc05ZrEr (Figure 6.15g) retain predominantly elongated and banded structures, indicating incomplete recrystallization. Following deformation at 0.1 s^{-1}, the base alloy (Figure 6.15b) exhibits a heterogeneous microstructure consisting of elongated grains and localized fine-grained regions, indicated by white circles. In contrast, the Sc-containing alloys (Figure 6.15e,h) retain pronounced elongated and banded structures along the tensile direction. BSc10Zr exhibits strong band continuity with embedded fine grains, whereas BSc05ZrEr displays more extensive disruption of the banded

structure, with numerous equiaxed grains distributed within the deformation bands. The fine grains in BSc10Zr appear smaller and more uniformly distributed, whereas those in BSc05ZrEr are comparatively larger.

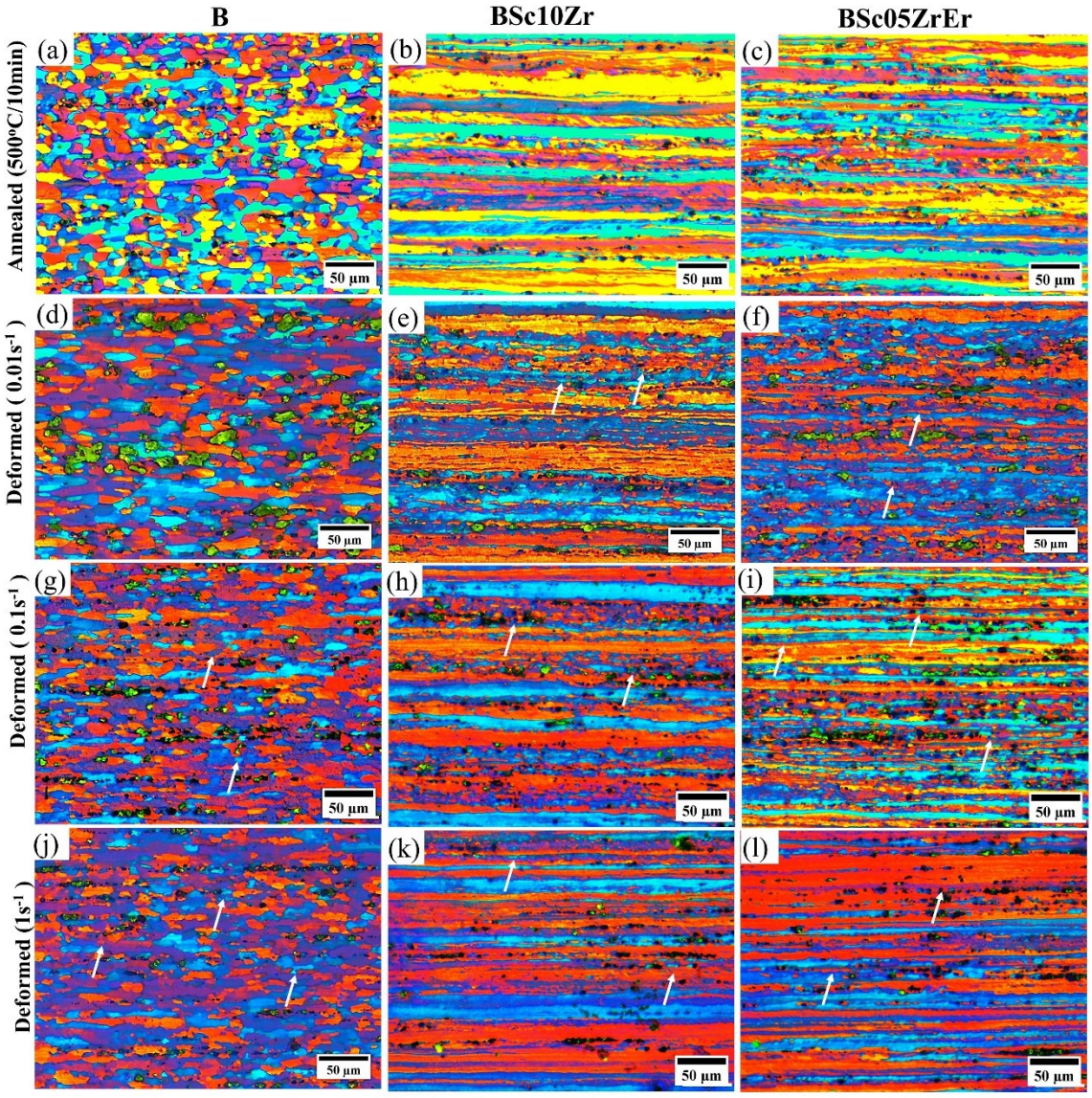


Figure 6.14. Polarized optical OM micrographs showing the microstructural evolution during tensile deformation at 500 °C with increasing strain rates**.** White arrows indicate grain refinement and localized fragmentation.

The corresponding misorientation angle distributions (Figure 6.15c,f,i) and the summarized boundary fractions (Figure 6.16) reveal distinctly different boundary evolution paths. The annealed base alloy initially contains a high relative HAB fraction (~89 %), consistent with its fully recrystallized structure. However, after deformation at 0.1 s^{-1}, the relative HAB fraction decreases to ~53 %, while the relative LAB fraction increases substantially from ~4 % to ~31 %. This indicates that deformation promotes extensive subgrain formation and dislocation accumulation, resulting in the generation of new LABs. Consequently, although the base alloy initially exhibits the highest HAB fraction, deformation-induced boundary subdivision reduces the HAB fraction in the final microstructure.

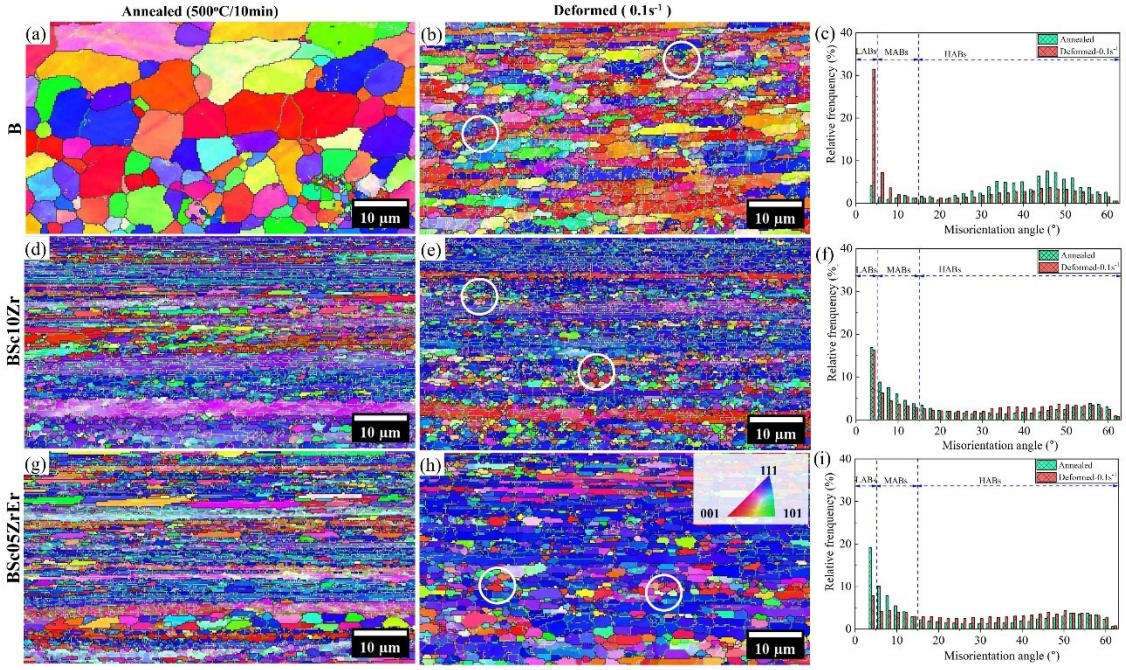


Figure 6.15. EBSD inverse pole figure (IPF) maps at the annealed (500 °C/10 min) and deformed (0.1 s^{-1}) conditions for the (a–b) B, (d-e) BSc10Zr and (g-h) BSc05ZrEr alloys

together with the corresponding misorientation angle distributions (c, f and i). The white circles in (b, e, and h) highlight localized fine grains, consistent with deformation-induced grain subdivision and possible continuous dynamic recrystallization (CDRX)

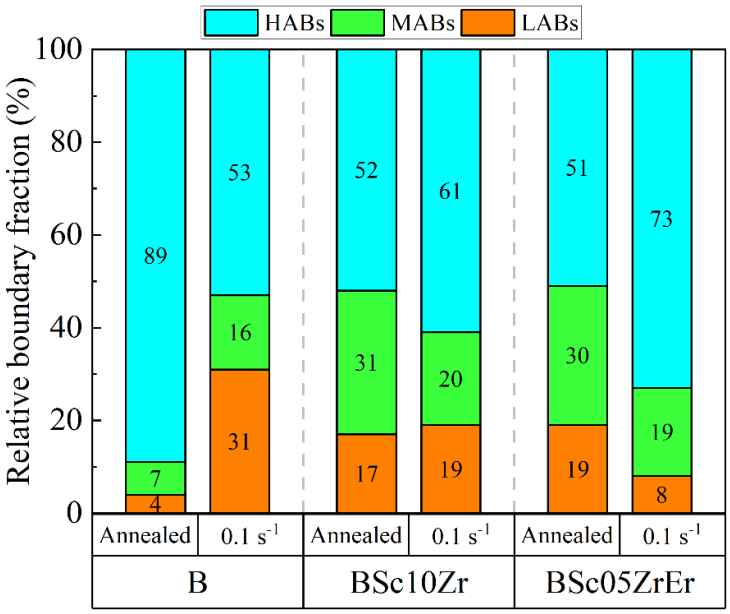


Figure 6.16. Relative fractions of low-angle grain boundaries (LABs), medium-angle grain boundaries (MABs), and high-angle grain boundaries (HABs) in the annealed and deformed (0.1 s^{-1}) conditions for the B, BSc10Zr, and BSc05ZrEr alloys.

In contrast, both Sc-containing alloys exhibit an increase in HAB fraction during deformation. The BSc10Zr alloy shows an increase in HAB fraction from ~52% to ~61%, accompanied by a reduction in MAB fraction. An even more pronounced evolution is observed in BSc05ZrEr, where the HAB fraction increases from ~50% to ~73%, while both LAB and MAB fractions decrease significantly. These changes are consistent with progressive boundary misorientation and transformation of lower-angle boundaries toward HABs during deformation.

Overall, the EBSD results at 0.1 s^{-1} reveal distinctly different boundary evolution paths among the alloys. In the base alloy, the increase in LAB fraction together with the reduction in HAB fraction indicates substantial deformation-induced boundary subdivision. In contrast, the Sc-containing alloys exhibit a progressive increase in HAB fraction accompanied by reductions in LAB and MAB fractions, indicating more pronounced boundary evolution during deformation. The largest increase in HAB fraction is observed in BSc05ZrEr, consistent with the greater disruption of the banded structure and increased presence of equiaxed grains observed in Figure 6.15h.

To further examine grain structure and grain-boundary evolution under high-strain-rate deformation relevant to HSBF, EBSD analysis was performed on samples deformed at 1 s^{-1}, as shown in Figure 6.17. The base alloy exhibits a heterogeneous microstructure comprising elongated grains, subdivided regions, and localized fine grains (Figure 6.17a), consistent with the OM observations in Figure 6.14j. The corresponding boundary fractions are approximately 13% LABs, 17 % MABs, and 70 % HABs. Compared with the annealed condition, deformation at 1 s^{-1} increases the LAB and MAB fractions while reducing the HAB fraction. Relative to deformation at 0.1 s^{-1}, however, the LAB fraction decreases markedly, whereas the MAB and HAB fractions increase. The Sc-containing alloys retain predominantly banded deformation structures with localized fine grains distributed within the bands (Figure 6.17b,c), in agreement with the OM observations in Figure 6.14k,l. BSc10Zr exhibits boundary fractions of approximately 14 % LABs, 28 % MABs, and 58 % HABs, whereas the corresponding fractions for BSc05ZrEr are approximately 10 %, 23 %, and 67 %, respectively. In both alloys, deformation at 1 s^{-1} results in higher HAB fractions than in the annealed condition. Compared with deformation at 0.1 s^{-1}, however, the HAB fractions decrease slightly, accompanied primarily by increases in the MAB fractions.

Among the Sc-containing alloys, BSc05ZrEr exhibits the higher HAB fraction, together with a more visibly disrupted banded structure and localized fine-grained regions.

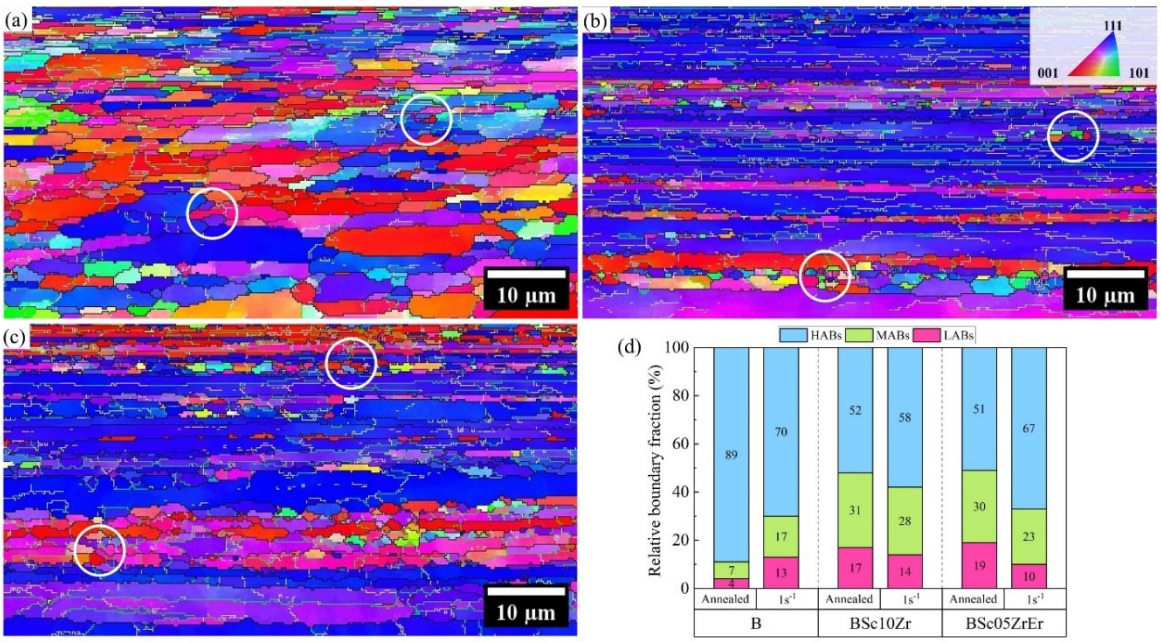


Figure 6.17. EBSD inverse pole figure (IPF) maps of the alloys after tensile deformation at 500 °C and 1 s^{-1}: (a) B, (b) BSc10Zr, (c) BSc05ZrEr, and (d) relative fractions of low-angle grain boundaries (LABs), medium-angle grain boundaries (MABs), and high-angle grain boundaries (HABs) in the annealed and deformed conditions. White circles highlight representative regions of localized grain refinement and boundary evolution.

6.4 Discussion

6.4.1 Effect of microalloying on microstructure evolution and recrystallization behavior

Microalloying with Sc, Zr, and Er strongly influences microstructural evolution throughout solidification, homogenization, and subsequent annealing. As shown in Figure

6.3, the base alloy (B) and BSc10Zr exhibit relatively coarse equiaxed grains in the as-cast condition, whereas BSc05ZrEr develops a much finer equiaxed grain structure. This refinement is likely associated with the low solid solubility of Er in α-Al (~0.008 at.%) [27], which promotes the formation of primary Al_3Er-containing particles during solidification [32,43]. These particles may act as heterogeneous nucleation sites for α-Al, thereby promoting grain refinement [31,43,44,50]. In addition, Er interacts with Mn- and Fe-containing intermetallic phases, resulting in the formation of Al_6(Mn,Fe,Er)-type particles in BSc05ZrEr alongside the conventional Al_6(Mn,Fe)-type particles observed in the other two alloys (Figures 6.3 and 6.4). This observation suggests partial incorporation of Er into the Al_6(Mn,Fe)-type phase and indicates that Er influences both the as-cast grain structure and intermetallic-particle chemistry.

As shown in Figure 6.5, the homogenized Sc-containing alloys exhibit more pronounced Mn-dispersoid-related DFZs than the base alloy. This observation indicates that the spatial heterogeneity inherited from solidification persists more strongly after homogenization in the microalloyed alloys. In the base alloy, homogenization produces a comparatively uniform distribution of Mn-containing dispersoids. In contrast, interactions among Sc, Zr, Er, and Mn may modify Mn redistribution and precipitation behavior, promoting a more spatially heterogeneous dispersoid distribution in the microalloyed alloys. The low diffusivity and tendency of Zr to segregate within dendritic regions may further contribute to this behavior [27]. These effects are most pronounced in BSc05ZrEr, which exhibits the highest DFZ fraction (~35%) (Figure 6.5). The results therefore suggest that solute partitioning and associated precipitation reactions during homogenization contribute to the persistent heterogeneity in Mn-dispersoid distribution.

During annealing of cold-rolled aluminum alloys, microstructural softening occurs primarily through static recovery and recrystallization, followed by grain growth. These processes are governed by annealing temperature, stored deformation energy, and the size, density, and spatial distribution of secondary particles within the Al matrix [36,51]. Because the three alloys underwent comparable cold-rolling reductions, differences in their annealing responses are mainly associated with their secondary-particle populations and initial microstructural heterogeneity. As shown in Figure 6.10, the alloys contain two principal particle populations after annealing: submicron Mn-containing dispersoids and nanoscale Al_3(Sc,Zr) or Al_3(Sc,Zr,Er)-based precipitates. Both populations contribute to microstructural stability by impeding dislocation rearrangement, subgrain-boundary migration, and high-angle grain-boundary motion. However, the much finer nanoscale precipitates in the Sc-containing alloys (Table 6.1) are expected to exert a strong pinning effect, contributing to their greater resistance to recovery and recrystallization despite the lower number density of Mn-containing dispersoids.

The Zener-pinning pressure exerted by a dispersed particle population may be expressed as:

$$P_Z = \frac{3\gamma f}{2r} \qquad (1)$$

where $\gamma$is the grain-boundary energy, $f$is the particle volume fraction, and r is the particle radius. This relationship illustrates that finer particle populations can exert greater resistance to grain-boundary migration for a given particle volume fraction. The nanoscale Al_3(Sc,Zr) and Al_3(Sc,Zr,Er)-based precipitates observed in the Sc-containing alloys are therefore consistent with their greater resistance to recrystallization. Together with the Mn-containing

dispersoids, these precipitates provide additional particle pinning that contributes to the enhanced microstructural stability of the Sc-containing alloys.

According to the microhardness evolution in Figure 6.7 and the grain-structure observations in Figures 6.6 and 6.8, the base alloy undergoes rapid static recrystallization at approximately 400 °C. This is evidenced by the transformation of the cold-rolled fibrous structure into recrystallized equiaxed grains after annealing. The rapid recrystallization response of the base alloy is mainly associated with the absence of nanoscale Al_3(Sc,Zr)-type precipitates. Although the alloy contains the highest number density of fine Mn-dispersoids (Table 6.1), these particles provide less effective resistance to grain-boundary migration than the additional nanoscale Sc-containing precipitates present in the microalloyed alloys. Further increasing the annealing temperature to 500 °C produces no significant additional change in hardness or grain structure, indicating that recrystallization is essentially complete and that the resulting microstructure remains relatively stable over this temperature range. At 520 °C, however, grain coarsening is accompanied by a further decrease in hardness. This behavior may be associated with reduced particle-pinning effectiveness at the highest annealing temperature, potentially resulting from Mn-dispersoid coarsening [36,46].

In contrast, the Sc-containing alloys retain much of their fibrous structure over the investigated annealing-temperature range. The onset of recrystallization is shifted to approximately 450 °C in BSc05ZrEr and 500 °C in BSc10Zr. This behavior is consistent with the effectiveness of nanoscale Al_3(Sc,Zr) and Al_3(Sc,Zr,Er)-based precipitates in retarding dislocation rearrangement, subgrain-boundary migration, and recrystallization-front propagation [44,46]. BSc10Zr contains finer and more numerous nanoscale precipitates than BSc05ZrEr (Figure 10 and Table 6.1), primarily owing to its higher Sc content. These particle characteristics are consistent with stronger precipitate pinning and the greater

recrystallization resistance observed in BSc10Zr [36,46,52]. Conversely, the earlier onset of recrystallization in BSc05ZrEr is attributed to its lower overall precipitate-pinning effectiveness and the presence of more extensive Mn-dispersoid-related DFZ bands (Figure 6.5f), which likely facilitate localized grain-boundary migration and recrystallization.

Despite its higher DFZ fraction and lower Sc content, BSc05ZrEr exhibits microhardness and recrystallization resistance comparable to those of BSc10Zr up to 500 °C (Figure 6.7). Although the larger DFZ fraction reduces the contribution of Mn-containing dispersoids to particle pinning, this effect appears to be partially compensated by the presence of thermally stable nanoscale Al_3(Sc,Zr,Er)- and Al_3(Sc,Zr)-based precipitates throughout the matrix (Figure 6.10h,i). These precipitates contribute to microstructural stability during annealing. Nevertheless, the coexistence of Mn-DZs and Mn-DFZs introduces spatial variations in Mn-dispersoid density, resulting in microstructural heterogeneity that may influence subsequent strain accommodation and boundary evolution, as discussed in Section 6.4.2. Overall, these results indicate that partial substitution of Sc with Er can retain substantial recrystallization resistance while reducing the required Sc addition, providing a promising microalloying strategy for developing more sustainable scrap-based Al–Mg–Mn alloys.

6.4.2 Effect of microalloying on strain-rate-dependent deformation behavior

The differences in microstructural stability induced by Sc, Zr, and Er microalloying strongly influence the elevated-temperature deformation behavior of the developed Al–Mg–Mn alloys across the investigated strain-rate range. As shown in Figure 6.12a, the Sc-

containing alloys exhibit improved ductility, particularly at the intermediate strain rate of 0.1 s^{-1}. The substantial ductility achieved at this increased strain rate is of particular interest for rapid forming applications, where higher deformation rates are desirable for reducing forming time. This behavior is closely linked to differences in the initial recrystallization state, grain-structure stability, and microstructural evolution during high-temperature deformation.

At the low strain rate of 0.01 s^{-1}, deformation is expected to involve grain-boundary-mediated mechanisms, including grain-boundary sliding (GBS) accommodated by intragranular dislocation activity and diffusion-controlled processes [23,53,54]. Under these conditions, the base alloy exhibits limited elongation (~175%) and consistently lower strain-rate sensitivity than the microalloyed alloys, indicating less effective grain-boundary-mediated strain accommodation. This interpretation is supported by the deformed microstructure in Figure 6.14d, in which the base alloy predominantly develops elongated grains aligned with the tensile direction. The persistence of this morphology suggests that a substantial fraction of the imposed strain is accommodated by intragranular deformation rather than extensive grain-boundary-mediated mechanisms. In contrast, the Sc-containing alloys exhibit higher elongations and maintain comparatively higher strain-rate sensitivities with increasing strain, consistent with greater deformation stability and more effective strain accommodation. The nanoscale Al_3(Sc,Zr) and Al_3(Sc,Zr,Er)-based precipitates, together with Mn-rich dispersoids, contribute to greater microstructural stability during deformation. This is reflected in the greater retention of the banded deformation structures at 0.01 s^{-1} compared with the pronounced grain elongation observed in the base alloy (Figure 6.14d–f). Although the base alloy is fully recrystallized before deformation, its microstructural stability

relies primarily on Mn-rich dispersoids and therefore lacks the additional stabilization provided by the nanoscale precipitates in the Sc-containing alloys. Such particle-induced microstructural stability is beneficial for limiting grain growth at elevated temperature, which is important for maintaining the fine-grained structures required for effective superplastic deformation [2,55,56]**.** Consequently, the Sc-containing alloys exhibit greater deformation stability and superior ductility at 0.01 s^{-1}.

Notably, BSc05ZrEr achieves the highest elongation at 0.01 s^{-1} (~254%), compared with ~200% for BSc10Zr. This difference is primarily associated with the more advanced recrystallization of BSc05ZrEr in the annealed condition prior to deformation. The resulting greater availability of high-angle grain boundaries provides more favorable interfaces for GBS. This interpretation is further supported by the deformation microstructures in Figure 6.14e,f. Following deformation at 0.01 s^{-1}, BSc05ZrEr exhibits a more disrupted banded structure and a greater presence of fine grains within the deformation bands, consistent with more effective grain-boundary-mediated strain accommodation. In contrast, BSc10Zr largely retains a continuous banded structure, suggesting more limited boundary-mediated strain accommodation. Its less advanced recrystallization and retained subgrain structure (Figures 6.9e and 6.10d) indicate incomplete boundary transformation following annealing. These lower-angle subgrain boundaries are less favorable for GBS than high-angle grain boundaries [57,58], thereby contributing to the lower ductility of BSc10Zr at 0.01 s^{-1}. Importantly, this difference occurs despite the comparatively high strain-rate sensitivity of BSc10Zr, indicating that strain-rate sensitivity alone does not determine the attainable elongation; the initial boundary structure and its capacity to accommodate deformation are also critical.

At the intermediate strain rate of 0.1 s^{-1}, ductility increases significantly in the base alloy and BSc10Zr, reaching ~217% and ~259%, respectively, while BSc05ZrEr maintains a high elongation of ~254%. EBSD analysis of the deformed microstructures (Figures 6.15 and 6.16) reveals pronounced boundary evolution at this strain rate. In the base alloy, the substantial increase in LAB fraction indicates extensive subgrain formation, whereas the increase in HAB fraction in the Sc-containing alloys is consistent with progressive boundary misorientation and transformation during deformation. These microstructural changes suggest a mixed deformation regime in which grain-boundary-mediated deformation is increasingly accompanied by intragranular dislocation activity, dynamic recovery, and CDRX-related boundary evolution. The interaction among these mechanisms provides additional pathways for strain accommodation, contributing to the improved ductility observed at 0.1 s^{-1}.

The enhanced elongation of the base alloy at 0.1 s^{-1} relative to 0.01 s^{-1} is associated with a more favorable balance between dislocation accumulation and dynamic recovery. The heterogeneous deformation structure (Figure 6.14g), together with the substantial increase in LAB fraction from approximately 4% in the annealed condition to approximately 31% after deformation, indicates extensive deformation-induced subgrain formation and localized grain-structure refinement (Figures 6.15 and 6.16). Concurrently, the decrease in HAB fraction from approximately 89% to approximately 53% suggests that the formation of low-angle deformation substructures predominates over their progressive transformation toward high-angle boundaries. This boundary evolution is consistent with pronounced dynamic recovery accompanied by the early stages of CDRX. The coexistence of deformation substructures and localized fine-grained regions provides complementary pathways for strain

accommodation, thereby delaying strain localization and contributing to the enhanced ductility [15].

At 0.1 s^{-1}, the Sc-containing alloys exhibit superior ductility to the base alloy, which may be attributed to more stable microstructural evolution promoted by nanoscale Al_3(Sc,Zr) and Al_3(Sc,Zr,Er)-based precipitates. By stabilizing the deformation substructure and limiting excessive recovery, these precipitates may facilitate continued subgrain rotation and boundary transformation during deformation. In BSc10Zr, the HAB fraction increases from approximately 52% in the annealed condition to approximately 61% after deformation, accompanied primarily by a decrease in the MAB fraction from approximately 31% to 20%. This redistribution is consistent with progressive development of intermediate-angle boundaries toward higher-misorientation configurations, while the slight increase in LAB fraction reflects continued formation of deformation-induced substructures. BSc05ZrEr exhibits more pronounced boundary evolution, with the HAB fraction increasing from approximately 51% to approximately 73%, while the LAB and MAB fractions decrease from approximately 19% and 30% to 8% and 19%, respectively. These changes are consistent with more advanced CDRX-assisted boundary transformation in BSc05ZrEr. Compared with the base alloy, the Sc-containing alloys therefore exhibit more pronounced evolution toward HAB-rich microstructures, reflecting sustained CDRX-assisted boundary evolution promoted by the nanoscale Al_3(Sc,Zr) and Al_3(Sc,Zr,Er)-based precipitates. The resulting HAB-rich microstructures provide favorable interfaces for grain-boundary-mediated strain accommodation, thereby contributing to the superior ductility of the Sc-containing alloys at 0.1 s^{-1} [24,25,35,39].

The two Sc-containing alloys exhibit distinct strain-rate-dependent microstructural evolution and ductility responses from 0.01 to 0.1 s^{-1}. In BSc10Zr, ductility increases as the

strain rate increases from 0.01 to 0.1 s^{-1}. Optical micrographs reveal that the alloy retains a predominantly continuous banded structure after deformation at 0.01 s^{-1} (Figure 6.14e), whereas localized fine-grained regions become more evident at 0.1 s^{-1} (Figure 6.14h). Correspondingly, the HAB fraction increases from approximately 52% in the annealed condition to approximately 61% after deformation at 0.1 s^{-1} (Figures 6.15 and 6.16), indicating progressive boundary evolution. Together, these observations suggest that the increased strain rate promotes greater dislocation activity, subgrain rotation, and progressive boundary misorientation associated with CDRX. Consequently, the initially banded deformation structure evolves toward a finer, more HAB-rich microstructure capable of more effective strain accommodation [2,59], contributing to the substantially improved ductility of BSc10Zr at 0.1 s^{-1}.

In contrast, BSc05ZrEr exhibits comparable elongations at 0.01 s^{-1} (~256%) and 0.1 s^{-1} (~254%), indicating a broader strain-rate window for high ductility. At 0.01 s^{-1}, optical micrographs reveal a more disrupted banded structure and a greater presence of fine grains in BSc05ZrEr than in BSc10Zr (Figure 6.14f), indicating that substantial grain-structure evolution already occurs at the lower strain rate. At 0.1 s^{-1}, the deformation structure becomes more extensively disrupted (Figure 6.14i), accompanied by an increase in HAB fraction from approximately 50% to approximately 73%, consistent with extensive CDRX-assisted boundary evolution. Despite this pronounced boundary evolution, the elongation remains essentially unchanged. This response may be influenced by the more extensive Mn-related DFZs in BSc05ZrEr, which introduce spatial variations in dispersoid density and local microstructural stability. Such heterogeneity may promote strain partitioning between Mn-DZ and Mn-DFZ regions during deformation, partially offsetting the beneficial effects of

boundary evolution on strain accommodation. Consequently, BSc05ZrEr maintains similarly high ductility at both strain rates rather than exhibiting the pronounced increase observed in BSc10Zr.

At the high strain rate of 1 s^{-1}, the ductility of all alloys decreases relative to 0.1 s^{-1}, although the Sc-containing alloys retain higher elongations than the base alloy. This reduction is consistent with a further shift in deformation behavior, in which grain-boundary-mediated strain accommodation becomes increasingly limited by the rapidly imposed strain. Consequently, intragranular dislocation activity is expected to contribute more strongly to deformation [15], consistent with the increased flow stresses measured at 1 s^{-1} (Figure 6.11). EBSD analysis (Figure 6.17) reveals localized fine-grained regions and substantial boundary evolution in all alloys. In the base alloy, the lower LAB fraction and higher MAB and HAB fractions compared with those at 0.1 s^{-1} are consistent with progressive development of deformation-induced substructures toward higher-misorientation boundaries and localized CDRX-related grain refinement. However, because this microstructural evolution remains spatially heterogeneous, it may not provide sufficiently uniform strain accommodation, thereby contributing to the reduced ductility. The Sc-containing alloys, in contrast, retain predominantly banded microstructures after deformation at 1 s^{-1}, together with localized fine-grained regions within the bands (Figures 6.14k,l and 6.17b,c). Their higher elongations relative to the base alloy are consistent with greater microstructural and deformation stability under high-strain-rate conditions.

Both Sc-containing alloys exhibit higher HAB fractions than in their annealed conditions, indicating substantial boundary evolution during deformation. However, compared with deformation at 0.1 s^{-1}, both alloys exhibit a slight decrease in HAB fraction

accompanied primarily by an increase in MAB fraction. This trend suggests that, at the higher strain rate, the accumulation of intermediate-misorientation boundaries becomes more pronounced relative to their further evolution toward HABs. Consequently, boundary-mediated strain accommodation may become less effective, contributing to the lower ductility at 1 s^{-1}. Although BSc05ZrEr retains a higher HAB fraction, BSc10Zr exhibits greater elongation at 1 s^{-1}. The superior ductility of BSc10Zr may be associated with its more stable and comparatively uniform deformation structure. This stability is supported by its more homogeneous Mn-dispersoid distribution and less extensive Mn-related DFZ network. In contrast, the greater dispersoid heterogeneity in BSc05ZrEr may promote strain partitioning under rapidly imposed deformation, leading to localized strain concentration and partially offsetting the potential benefit of its higher HAB fraction.

Overall, the deformation behavior of the developed alloys is governed by the interaction between boundary evolution and microstructural stability, both of which are strongly influenced by microalloying. In the base alloy, deformation is characterized by dynamic recovery and localized boundary evolution, resulting in enhanced ductility within a comparatively narrow strain-rate window. In contrast, the Sc-containing alloys exhibit greater microstructural stability owing to nanoscale Al_3(Sc,Zr) and Al_3(Sc,Zr,Er)-based precipitates, which stabilize the deformation structure and support continued boundary evolution and strain accommodation over a broader strain-rate range. However, the more extensive Mn-related DFZs in BSc05ZrEr introduce local microstructural heterogeneity that may promote strain partitioning and partially offset these beneficial effects, particularly at higher strain rates. These findings indicate that improved deformation performance under rapid forming conditions requires an appropriate balance between nanoprecipitate-induced microstructural stability and a sufficiently homogeneous Mn-dispersoid distribution.

Accordingly, controlling DFZ formation while retaining the beneficial effects of $Al_3(Sc,Zr)$ and $Al_3(Sc,Zr,Er)$-based precipitates represent an important alloy-design strategy for developing reduced-Sc, scrap-based Al–Mg–Mn alloys with enhanced deformation stability across a broad strain-rate range. Table 6.2 summarizes the proposed principal deformation mechanisms across the investigated strain-rate range and highlights the interplay among initial microstructure, boundary evolution, particle distribution, and strain accommodation.

Table 6.2. Proposed principal deformation mechanisms across the investigated strain-rate range, interpreted from the combined mechanical and microstructural evidence.

Alloy	Initial microstructure (after annealing)	Strain rate (s^{-1})	Proposed principal deformation mechanisms	Microstructural evolution during deformation	Ductility response
B (Base)	Fully recrystallized, equiaxed grains	0.01	Grain-boundary-mediated deformation + intragranular dislocation activity	Elongated grains with heterogeneous morphology; limited boundary-mediated strain accommodation	Moderate (~175%)
		0.1	Mixed deformation regime (dynamic recovery + boundary evolution)	Extensive subgrain formation, increased LAB fraction, localized grain refinement	Improved (~217%)
		1	Dislocation glide + work hardening	Transition to HAB-rich refined regions; localized grain refinement and strain localization	Reduced (~157%)
BSc10Zr	Predominantly unrecrystallized, banded; high LAB fraction	0.01	Boundary-mediated deformation + dislocation accommodation	Continuous banded structure largely retained;	Moderate (~200%)

Alloy	Initial microstructure (after annealing)	Strain rate (s^{-1})	Proposed principal deformation mechanisms	Microstructural evolution during deformation	Ductility response
				limited boundary evolution	
		0.1	CDRX-assisted deformation + boundary-mediated accommodation	Subgrain rotation and LAB→HAB transformation; fine grains within bands	High (~259 %)
		1	Dislocation-dominated deformation with limited boundary evolution	Stable banded structure; slight reduction in HAB fraction and increase in MAB fraction	Reduced (~180 %)
BSc05ZrEr	Partially recrystallized + banded; DFZ present	0.01	Boundary-mediated deformation (GBS-assisted) + dislocation accommodation	Fragmented banded structure with higher fraction of fine grains; effective strain accommodation	High (~256 %)
		0.1	CDRX-assisted deformation + boundary-mediated accommodation	Extensive grain fragmentation and highest HAB fraction	High (~254 %)
		1	Dislocation-dominated deformation + strain partitioning	Stable HAB-rich deformation structure; localized strain partitioning associated with DFZs	Reduced (~160 %)

6.4.3 Implications for high-speed blow forming

The deformation behavior of the developed alloys has important implications for HSBF, where materials must accommodate rapid deformation and variations in strain rate

while maintaining deformation stability [8,9,14]. Resistance to premature strain localization is therefore an important material requirement. The pronounced necking observed in the base alloy under the high-strain-rate condition (Figure 6.12c) indicates limited deformation stability. In contrast, the Sc-containing alloys deform more uniformly, demonstrating greater resistance to strain localization. This response is consistent with their comparatively higher strain-rate sensitivity (Figure 6.12b) and the stabilizing effect of nanoscale Al_3(Sc,Zr) and Al_3(Sc,Zr,Er) precipitates on the deformation microstructure [57,60,61].

The microstructural response developed during high-strain-rate deformation may also influence subsequent deformation following a change in strain rate. Under dual-stage high-to-low strain-rate deformation, the base alloy and BSc05ZrEr reached elongations of approximately 241 % and 286 %, respectively (Figure 13). These results demonstrate that both alloys can sustain substantial additional deformation following a strain-rate transition, which may be influenced by the microstructure inherited from the prior high-strain-rate pre-deformation. However, the microstructure immediately after pre-deformation was not directly characterized. The structures observed after deformation to failure under the high-strain-rate condition (Figures 6.14 and 6.17) therefore provide qualitative insight into the possible microstructural evolution associated with high-strain-rate pre-deformation.

Post-deformation characterization indicates more pronounced microstructural evolution in the base alloy than in the Sc-containing alloys under high-strain-rate deformation. The initially equiaxed grains of the annealed base alloy evolve into a heterogeneous deformation structure containing elongated grains and localized fine-grained regions (Figure 6.14j), while EBSD reveals a HAB fraction of approximately 70 % (Figure 6.17a). These features are consistent with substantial deformation-induced boundary evolution. The localized fine-grained regions may provide additional interfaces for grain-

boundary-mediated strain accommodation following the transition to a lower strain rate, potentially contributing to the improved elongation of the base alloy under dual-stage loading. However, the pronounced strain localization observed under the high-strain-rate condition (Figure 6.12c) suggests that its ability to accommodate subsequent strain may become increasingly limited with increasing high-strain-rate pre-deformation.

In contrast, BSc05ZrEr retains a predominantly banded deformation structure even after deformation to failure at 1 s^{-1} (Figure 6.14l), remaining broadly comparable in overall morphology to the annealed condition despite the grain-boundary evolution revealed by EBSD. This limited change in overall grain morphology suggests that the microstructure at the earlier intermediate pre-strain used during dual-stage loading may also have remained relatively stable, although this state was not directly characterized. EBSD further reveals localized fine-grained regions within the banded structure (Figure 6.17c), together with a relatively high HAB fraction (Figure 6.17d). The HAB-rich regions may provide favorable interfaces for grain-boundary-mediated strain accommodation following the transition to the lower strain rate [58,62,63]. Moreover, although its monotonic ductility at 1 s^{-1} is lower than that of BSc10Zr, the reduced tendency of BSc05ZrEr for macroscopic strain localization (Figure 6.12c) indicates greater deformation stability than the base alloy. Consequently, the superior dual-stage performance of BSc05ZrEr may arise from its ability to maintain a comparatively stable microstructure and deformation uniformity during the preceding high-strain-rate stage. The favorable boundary characteristics may subsequently facilitate strain accommodation following the transition to the lower strain rate. Together, these characteristics contribute to its elongation approaching 300% under dual-stage loading.

These results demonstrate that performance under HSBF-relevant conditions depends not only on ductility at individual strain rates but also on the ability of an alloy to

accommodate strain-rate transitions without premature strain localization. Accordingly, alloy design for HSBF should prioritize strain-rate-transition tolerance and deformation stability in addition to achieving high ductility under low-strain-rate conditions. The high elongations obtained at intermediate strain rates further suggest that optimization of the deformation path may provide opportunities to reduce forming time while maintaining substantial ductility. Additional dual-stage experiments are required to evaluate this possibility, while biaxial testing would be valuable for assessing material response under stress states more representative of industrial forming. Overall, Sc–Zr–Er microalloying provides an effective strategy for improving microstructural stability, deformation stability, and strain-rate-transition tolerance in scrap-based Al–Mg–Mn alloys under HSBF-relevant deformation conditions.

6.5 Conclusions

The effects of Sc–Zr–Er microalloying on the microstructure evolution and deformation behavior of scrap-based Al–Mg–Mn 5xxx alloys under HSBF-relevant conditions were investigated. The main conclusions are as follows:

1. Sc–Zr–Er microalloying enhanced recrystallization resistance through the formation of nanoscale Al_3(Sc,Zr) and Al_3(Sc,Zr,Er)-based precipitates, resulting in greater retention of banded deformation structures after annealing. Notably, partial replacement of Sc with Er retained substantial recrystallization resistance. The nanoprecipitate-stabilized microstructures also contributed to improved deformation stability during high-temperature tensile testing.

2. Mn-containing dispersoids and their spatial distribution strongly influenced recrystallization and strain accommodation. In particular, Mn-related DFZs introduced local microstructural heterogeneity that affected boundary evolution and may promote strain partitioning during deformation.

3. The deformation mechanisms evolved systematically with strain rate. Grain-boundary-mediated deformation contributed strongly at 0.01 s^{-1}, whereas CDRX-assisted subgrain rotation and boundary evolution became most pronounced at 0.1 s^{-1}. At 1 s^{-1}, intragranular deformation became increasingly dominant, reducing elongation despite continued localized boundary evolution.

4. BSc10Zr exhibited the highest elongation at 0.1 s^{-1} (~259 %), whereas BSc05ZrEr maintained high ductility over a broader strain-rate range, reaching approximately 256 % and 254 % at 0.01 and 0.1 s^{-1}, respectively. Under dual-stage high-to-low strain-rate deformation, BSc05ZrEr achieved an elongation approaching 300 %, demonstrating superior strain-rate-transition tolerance relative to the base alloy.

5. Overall, alloy performance under HSBF-relevant conditions is governed by the interplay among initial microstructure, strain-rate-dependent boundary evolution, microstructural stability, and strain accommodation. Alloy design for HSBF should therefore prioritize deformation stability and strain-rate-transition tolerance through appropriate control of nanoprecipitate stability and dispersoid distribution, rather than solely maximizing ductility under conventional low-strain-rate superplastic conditions.

References

1. Grimes R. Superplastic forming of aluminium alloys. In: Giuliano G, editor. Superplastic forming of advanced metallic materials. Cambridge, UK: Woodhead Publishing; 2011, p. 247–271. https://doi.org/10.1533/9780857092779.3.247.

2. Kishchik AA, Mikhaylovskaya AV, Kotov AD, Rofman OV, Portnoy VK. Al–Mg-Fe-Ni based alloy for high strain rate superplastic forming. Mater Sci Eng A 2018;718:190–197. https://doi.org/10.1016/j.msea.2018.01.099.

3. Ebenberger P, Uggowitzer PJ, Gerold B, Pogatscher S. Effect of compositional and processing variations in new 5182-type AlMgMn alloys on mechanical properties and deformation surface quality. Materials 2019;12:1645. https://doi.org/10.3390/ma12101645.

4. Bhatta L, Pesin A, Zhilyaev AP, Tandon P, Kong C, Yu H. Recent development of superplasticity in aluminum alloys: a review. Metals 2020;10:77. https://doi.org/10.3390/met10010077.

5. Barnes AJ. Superplastic aluminum forming–expanding its techno-economie niche. Mater Sci Forum 1999;304–306:785–796. https://doi.org/10.4028/www.scientific.net/msf.304-306.785.

6. Kawasaki M, Langdon TG. Superplasticity in ultrafine-grained materials. Rev Adv Mater Sci 2018;54:46–55. https://doi.org/10.1515/rams-2018-0019.

7. Kweitsu EK, Sarkar DK, Chen XG. A short review on superplasticity of aluminum alloys. Eng Proc 2023;43:43. https://doi.org/10.3390/engproc2023043043.

8. Kweitsu EK, Sarkar DK, Algendy AY, Chen XG, Veilleux J, Bombardier N. Effect of annealing time on grain structure evolution and superplastic response of Al–Mg 5xxx alloys. Materials 2024;17:5492. https://doi.org/10.3390/ma17225492.

9. Majidi O, Jahazi M, Bombardier N. Finite element simulation of high-speed blow forming of an automotive component. Metals 2018;8:901. https://doi.org/10.3390/met8110901.

10. Luo Y, Luckey SG, Friedman PA, Peng Y. Development of an advanced superplastic forming process utilizing a mechanical pre-forming operation. Int J Mach Tools Manuf 2008;48:1509–1518. https://doi.org/10.1016/j.ijmachtools.2007.12.010.

11. Liu FC, Ma ZY. Achieving high-strain-rate superplasticity in cast 7075Al alloy via friction stir processing. J Mater Sci 2009;44:2647–2655. https://doi.org/10.1007/s10853-009-3346-6.

12. Giuliano G. Superplastic forming of advanced metallic materials. Woodhead Publishing Limited; 2011. https://doi.org/10.1533/9780857092779.

13. Prasannavenkatesan R, Parker M, Laplante Y, Bombardier N, Rush B, Li S. High Speed Blow Forming Processes (Patent No: US 2017 / 0116693 A1). US20170087617, 2017.

14. Aleyari A, Majidi O, Bombardier N, Pham XT, Jahazi M. Finite Element and Experimental Analysis of the preheating stage of High Speed Blow Forming (HSBF) process. J Manuf Process 2020;49:10–17. https://doi.org/10.1016/j.jmapro.2019.10.009.

15. Kweitsu EK, Sarkar DK, Algendy AY, Chen XG, Veilleux J, Bombardier N. Superplastic deformation and microstructural evolution of an Al–Mg–Mn 5xxx alloy for high-speed blow forming applications. J Mater Sci 2026;61:16033–16053. https://doi.org/10.1007/s10853-026-12693-0.

16. Portnoy VK, Rylov DS, Levchenko VS, Mikhaylovskaya A V. The influence of chromium on the structure and superplasticity of Al–Mg–Mn alloys. J Alloys Compd 2013;581:313–317. https://doi.org/10.1016/j.jallcom.2013.07.075.

17. Mikhaylovskaya A V., Yakovtseva OA, Golovin IS, Pozdniakov A V., Portnoy VK. Superplastic deformation mechanisms in fine-grained Al–Mg based alloys. Mater Sci Eng A 2015;627:31–41. https://doi.org/10.1016/j.msea.2014.12.099.

18. Pérez-Prado MT, González-Doncel G, Ruano OA, McNelley TR. Texture analysis of the transition from slip to grain boundary sliding in a discontinuously recrystallized superplastic aluminum alloy. Acta Mater 2001;49:2259–2268. https://doi.org/10.1016/S1359-6454(01)00128-8.

19. Zhang Y, Ding L, Zou Q, Su Y, Jia Z, Zhen F. Effect of Al3(Sc,Zr) dispersoids on the mechanical and corrosion behavior of Al–Mg–Sc–Zr alloys. J Alloys Compd 2025;1032:181166. https://doi.org/10.1016/j.jallcom.2025.181166.

20. Deng Y, Zhang G, Yang Z, Xu G. Microstructure characteristics and mechanical properties of new aerospace Al–Mg–Mn alloys with Al3(Sc1−xZrx) or Al3(Er1−xZrx) nanoparticles. Mater Charact 2019;153:79–91. https://doi.org/10.1016/j.matchar.2019.04.032.

21. Algendy AY, Rometsch P, Chen X. Tailoring microstructure and mechanical properties of an AA5454 extruded aluminum alloy with Sc / Zr microalloying and processing conditions. Mater Sci Eng A 2025;948:149318. https://doi.org/10.1016/j.msea.2025.149318.

22. Sun YB, Chen XP, Xie J, Wang C, An YF, Liu Q. High-strain-rate superplasticity and secondary strain hardening of Al–Mg–Sc–Zr alloy produced by friction stir processing. Mater Today Commun 2022;33:104217. https://doi.org/10.1016/j.mtcomm.2022.104217.

23. Yakovtseva OA, Kishchik AA, Cheverikin V V., Kotov AD, Mikhaylovskaya A V. The mechanisms of the high-strain-rate superplastic deformation of Al–Mg-based alloy. Mater Lett 2022;325:132883. https://doi.org/10.1016/j.matlet.2022.132883.

24. Mikhaylovskaya A V., Esmaeili Ghayoumabadi M, Mochugovskiy AG. Superplasticity and mechanical properties of Al–Mg–Si alloy doped with eutectic-forming Ni and Fe, and dispersoid-forming Sc and Zr elements. Mater Sci Eng A 2021;817:141319. https://doi.org/10.1016/j.msea.2021.141319.

25. Li M, Pan Q, Shi Y, Sun X, Xiang H. High strain rate superplasticity in an Al–Mg–Sc–Zr alloy processed via simple rolling. Mater Sci Eng A 2017;687:298–305. https://doi.org/10.1016/j.msea.2017.01.091.

26. Fan T, Lin L, Liang H, Ma Y, Tang Y, Hu T, Ruan Z, Chen D, Wu Y. First-principles study of the structural, mechanical and thermodynamic properties of Al11RE3 in aluminum alloys. Crystals 2023;13:347. https://doi.org/10.3390/cryst13020347.

27. Kang W, Li HY, Zhao SX, Han Y, Yang CL, Ma G. Effects of homogenization treatments on the microstructure evolution, microhardness and electrical conductivity of dilute Al–Sc–Zr–Er alloys. J Alloys Compd 2017;704:683–692. https://doi.org/10.1016/j.jallcom.2017.02.043.

28. Booth-Morrison C, Dunand DC, Seidman DN. Coarsening resistance at 400 °C of precipitation-strengthened Al–Zr–Sc–Er alloys. Acta Mater 2011;59:7029–7042. https://doi.org/10.1016/j.actamat.2011.07.057.

29. Liu L, Jiang J, Cui X, Zhang B, Zhen L, Ringer SP. Correlation between precipitate evolution and mechanical properties of Al–Sc–Zr alloy with Er additions. J Mater Sci Technol 2022;99:61–72. https://doi.org/10.1016/j.jmst.2021.05.031.

30. De Luca A, Dunand DC, Seidman DN. Mechanical properties and optimization of the aging of a dilute Al–Sc–Er–Zr–Si alloy with a high Zr/Sc ratio. Acta Mater 2016;119:35–42. https://doi.org/10.1016/j.actamat.2016.08.018.

31. Gao Z, Li H, Lai Y, Ou Y, Li D. Effects of minor Zr and Er on microstructure and mechanical properties of pure aluminum. Mater Sci Eng A 2013;580:92–98. https://doi.org/10.1016/j.msea.2013.05.035.

32. Van Dalen ME, Karnesky RA, Cabotaje JR, Dunand DC, Seidman DN. Erbium and ytterbium solubilities and diffusivities in aluminum as determined by nanoscale characterization of precipitates. Acta Mater 2009;57:4081–4089. https://doi.org/10.1016/j.actamat.2009.05.007.

33. Kotov AD, Mochugovskiy AG, Mosleh AO, Kishchik AA, Rofman OV, Mikhaylovskaya AV. Microstructure, superplasticity, and mechanical properties of Al–Mg–Er–Zr alloys. Mater Charact 2022;186:111825. https://doi.org/10.1016/j.matchar.2022.111825.

34. Mikhaylovskaya AV, Ryazantseva MA, Portnoy VK. Effect of eutectic particles on the grain size control and the superplasticity of aluminium alloys. Mater Sci Eng A 2011;528:7306–7309. https://doi.org/10.1016/j.msea.2011.06.042.

35. Mikhaylovskaya A V., Kishchik AA, Kotov AD, Rofman O V., Tabachkova NY. Precipitation behavior and high strain rate superplasticity in a novel fine-grained aluminum based alloy. Mater Sci Eng A 2019;760:37–46. https://doi.org/10.1016/j.msea.2019.05.099.

36. Algendy AY, Liu K, Rometsch P, Parson N, Chen XG. Effects of AlMn dispersoids and Al3(Sc,Zr) precipitates on the microstructure and ambient/elevated-temperature mechanical properties of hot-rolled AA5083 alloys. Mater Sci Eng A 2022;855:143950. https://doi.org/10.1016/j.msea.2022.143950.

37. Wu X, Sun M, Hong L, Wen S, Wei W, Gao K, et al. Er-containing microalloyed aluminum alloys: a review. J Mater Sci 2024;59:9685–9696. https://doi.org/10.1007/s10853-023-09185-w.

38. Qian X, Parson N, Chen X. Effects of Mn content on recrystallization resistance of AA6082 aluminum alloys during post-deformation annealing. J Mater Sci Technol 2020;52:189–197. https://doi.org/10.1016/j.jmst.2020.04.015.

39. Yakovtseva O, Sitkina M, Mosleh AO, Mikhaylovskaya A. High-strain-rate superplasticity in Al–Zn–Mg-based alloy: microstructural design, deformation behavior, and modeling. Materials 2020;13:2098. https://doi.org/10.3390/ma13092098.

40. Zhu Y, Chappuis LB, Kleine R De, Chul H, Wallington TJ, Luckey G, et al. The coming wave of aluminum sheet scrap from vehicle recycling in the United States. Resour Conserv Recycl 2021;164:105208. https://doi.org/10.1016/j.resconrec.2020.105208.

41. Krall P, Wei I, Pogatscher S. Recycling aluminum alloys for the automotive industry: breaking the source–sink paradigm. Resour Conserv Recycl 2024;202:107370. https://doi.org/10.1016/j.resconrec.2023.107370.

42. Allen SM. Foil thickness measurements from convergent-beam diffraction patterns. Philos Mag A 1981;43:325–335. https://doi.org/10.1080/01418618108239412.

43. Wen SP, Xing ZB, Huang H, Li BL, Wang W, Nie ZR. The effect of erbium on the microstructure and mechanical properties of Al–Mg–Mn–Zr alloy. Mater Sci Eng A 2009;516:42–49. https://doi.org/10.1016/j.msea.2009.02.045.

44. Wu M, Wei W, Zuo R, Wen S, Shi W, Zhou X, Wu X, Gao K, Huang H, Nie Z. Effect of Zr and Er addition on the microstructural evolution of a novel Al–Mg–Zn–Er–Zr alloy during hot compression. Materials 2023;16:858. https://doi.org/10.3390/ma16020858.

45. Algendy AY, Liu K, Chen XG. Effect of Mn-bearing dispersoids on tensile properties and recrystallization resistance of Al–3Mg–0.8Mn rolled alloy. Adv Eng Mater 2023;25:2300667. https://doi.org/10.1002/adem.202300667.

46. Algendy AY, Rometsch P, Chen XG. Recrystallization behavior of cold-rolled AA5083 microalloyed with 0.1 wt.% Sc and 0.08 wt.% Zr. Materials 2025;18:1701. https://doi.org/10.3390/ma18081701.

47. Grasserbauer J, Weißensteiner I, Falkinger G, Kremmer TM, Uggowitzer PJ, Pogatscher S. Influence of Fe and Mn on the microstructure formation in 5xxx alloys—Part I: evolution of primary and secondary phases. Materials 2021;14:3204. https://doi.org/10.3390/ma14123204.

48. Langdon TG. Seventy-five years of superplasticity: historic developments and new opportunities. J Mater Sci 2009;44:5998–6010. https://doi.org/10.1007/s10853-009-3780-5.

49. Nieh TG, Wadsworth J, Sherby OD. Superplasticity in metals and ceramics. 1st ed. New York: Cambridge University Press; 1997.

50. Chen B, Wang F, Ren S, Xia P, Wang Z, Hao J, et al. Influence of erbium addition on microstructure and performances of AlSi10Mg alloy prepared by selective laser melting. J Rare Earths 2024;42:1988–1994. https://doi.org/10.1016/j.jre.2023.09.017.

51. Humphreys FJ, Rohrer GS, Rollett AD. Recrystallization and related annealing phenomena. 3rd ed. Oxford: Elsevier; 2017.

52. Algendy AY, Rometsch P, Chen XG. Impact of hot rolling temperature on the mechanical properties and microstructural evolution of hot/cold-rolled AA5083 with Sc and Zr microalloying. Mater Sci Eng A 2024;896:146275. https://doi.org/10.1016/j.msea.2024.146275.

53. Daly S, Linne M, Venkataraman A, Sangid MD. Deformation mechanisms at grain boundaries in polycrystals: final report. Washington, DC: U.S. Department of Energy; 2019. https://doi.org/10.2172/1577947.

54. Mikhaylovskaya AV, Yakovtseva OA, Irzhak AV. The role of grain boundary sliding and intragranular deformation mechanisms for a steady stage of superplastic flow for Al–Mg-based alloys. Mater Sci Eng A 2022;833:142524. https://doi.org/10.1016/j.msea.2021.142524.

55. Sotoudeh K, Bate PS. Diffusion creep and superplasticity in aluminium alloys. Acta Mater 2010;58:1909–1920. https://doi.org/10.1016/j.actamat.2009.11.034.

56. Mikhaylovskaya AV, Yakovtseva OA, Cheverikin VV, Kotov AD, Portnoy VK. Superplastic behaviour of Al–Mg–Zn–Zr–Sc-based alloys at high strain rates. Mater Sci Eng A 2016;659:225–233. https://doi.org/10.1016/j.msea.2016.02.061.

57. Duan Y, Xu G, Zhou L, Xiao D, Deng Y, Yin Z, et al. Achieving high superplasticity of a traditional thermomechanically processed non-superplastic Al–Zn–Mg alloy sheet by low Sc additions. J Alloys Compd 2015;638:364–373. https://doi.org/10.1016/j.jallcom.2015.03.090.

58. Liu FC, Ma ZY. Contribution of grain boundary sliding in low-temperature superplasticity of ultrafine-grained aluminum alloys. Scr Mater 2010;62:125–128. https://doi.org/10.1016/j.scriptamat.2009.10.010.

59. Gourdet S, Montheillet F. A model of continuous dynamic recrystallization. Acta Mater 2003;51:2685–2699. https://doi.org/10.1016/S1359-6454(03)00078-8.

60. Hsiao IC, Huang JC. Deformation mechanisms during low- and high-temperature superplasticity in 5083 Al–Mg alloy. Metall Mater Trans A 2002;33:1373–1384. https://doi.org/10.1007/s11661-002-0062-0.

61. Kotov AD, Mikhaylovskaya AV, Kishchik MS, Tsarkov AA, Aksenov SA, Portnoy VK. Superplasticity of high-strength Al-based alloys produced by thermomechanical treatment. J Alloys Compd 2016;688:336–344. https://doi.org/10.1016/j.jallcom.2016.07.045.

62. Chinh NQ, Murashkin MY, Bobruk EV, Lábár JL, Gubicza J, Kovács Z, et al. Ultralow-temperature superplasticity and its novel mechanism in ultrafine-grained Al alloys. Mater Res Lett 2021;9:475–482. https://doi.org/10.1080/21663831.2021.1976293.

63. Song Z, Niu R, Cui X, Bobruk EV, Murashkin MY, Enikeev NA, et al. Mechanism of room-temperature superplasticity in ultrafine-grained Al–Zn alloys. Acta Mater 2023;246:118671. https://doi.org/10.1016/j.actamat.2023.118671

Chapter 7

Conclusions, limitations, and recommendations

7.1 General conclusions

This thesis established a comprehensive mechanistic understanding of the processing–microstructure–deformation–damage relationships in Al–Mg–Mn 5xxx alloys under conditions relevant to HSBF. The work addressed the critical need for cost-effective aluminum alloys capable of sustaining stable high-temperature deformation across the wide strain-rate spectrum (0.001 to 1 s^{-1}) associated with HSBF. The results demonstrate that optimal HSBF performance requires not only high ductility at individual strain rates, but also stable microstructural evolution and deformation uniformity across strain-rate transitions. This highlights the need to move beyond the conventional strategy of optimizing only low strain-rate superplasticity.

The first phase of this thesis demonstrated that short-duration annealing is an effective strategy for producing fine and stable recrystallized grain structures in commercial Al–Mg–Mn 5xxx alloys. The cold-rolled alloys exhibited rapid static recrystallization within 2 min of annealing at 520 °C. The Mn-rich alloy (Al–4.0Mg–1.18Mn) developed a finer and more thermally stable grain structure than the lower-Mn alloy, exhibiting a higher fraction of fine recrystallized grains and greater resistance to grain coarsening. This behavior was attributed to the increased number density of Mn-containing dispersoids, which provided effective Zener pinning of grain boundaries. Correspondingly, the Mn-rich alloy exhibited superior ductility at low strain rates, confirming the importance of fine and stable grain structures in enabling superplastic deformation. These findings demonstrate that HSBF-relevant

microstructures can be achieved through rapid thermal processing, without the prolonged annealing typically required for conventional superplastic forming.

The deformation behavior of the alloys was strongly dependent on temperature and strain rate. An optimum forming condition was identified at 500 °C, where the best balance between ductility, strain-rate sensitivity, and microstructural stability was achieved. At low strain rates (0.001–0.01 s^{-1}), deformation was dominated by GBS, supported by the fine recrystallized grain structure. At 450 °C, ductility was limited by SDC, whereas at 520 °C, excessive diffusion-driven grain growth reduced formability despite increased strain-rate sensitivity. At the high strain rate of 1 s^{-1}, deformation was governed by dislocation slip and CDRX, leading to significant grain refinement across all temperatures. Mn dispersoids played a key role in stabilizing subgrain boundaries, enhancing boundary pinning, and promoting CDRX-driven microstructural evolution. These results confirm that Al–Mg–Mn alloys can accommodate both stages of HSBF within a single processing window.

Cavitation behavior was found to be strongly strain-rate dependent and closely linked to the governing deformation mechanisms and grain structure stability. At 0.001 s^{-1}, diffusion-assisted GBS produced high tensile elongation but also promoted extensive cavity growth and coalescence. At 0.01 s^{-1}, a transitional regime involving both GBS and intragranular dislocation activity improved deformation uniformity and limited cavity growth. At 1 s^{-1}, continuous dynamic recrystallization produced refined equiaxed grains that suppressed diffusion-controlled cavity growth, with failure governed primarily by localized plastic instability and fine microvoid coalescence. Despite a higher intermetallic particle fraction and increased potential for cavity nucleation, the Mn-rich alloy exhibited superior cavitation resistance due to its thermally stable grain structure, which restricted cavity growth and delayed coalescence. These findings demonstrate that cavitation resistance in HSBF-

relevant alloys depends more on developing microstructures capable of suppressing cavity growth during deformation than minimizing nucleation sites.

The final phase of this thesis demonstrated that scrap-derived Al–Mg–Mn alloys can be transformed into HSBF-capable materials through targeted Sc–Zr–Er microalloying. The formation of coherent $Al_3(Sc,Zr)$ and $Al_3(Sc,Zr,Er)$ precipitates delayed recrystallization and enhanced grain boundary pinning, thereby improving thermal stability and deformation behavior across the strain-rate spectrum. The cost effective Er-containing alloy (BSc05ZrEr) exhibited promising performance, achieving superior ductility at intermediate-to-high strain rates (0.01–0.1 s^{-1}) compared with the higher-Sc alloy (BSc10). This demonstrates that partial substitution of Sc with Er provides a cost-effective alloy design strategy. Furthermore, combined strain-rate testing confirmed that microstructural inheritance plays a critical role in HSBF, as the microstructure generated during high strain-rate deformation significantly influences subsequent low strain-rate formability. The Sc–Er alloy exhibited improved resistance to strain localization and achieved the highest overall elongation, demonstrating the feasibility of producing high-performance HSBF alloys from industrial scrap feedstock.

Collectively, these findings provide both fundamental understanding and practical guidance for the design of cost-effective aluminum alloys capable of stable high-speed forming of complex lightweight automotive components. The principal contributions of this thesis may be summarized as follows:

1. Short-duration annealing was demonstrated to be an effective route for producing fine and stable recrystallized grain structures in Al–Mg–Mn 5xxx alloys under HSBF-relevant thermal conditions.

2. Mn-containing dispersoids were shown to play a central role in grain-boundary pinning, thermal stability, CDRX development, and suppression of cavity growth during high-temperature deformation.
3. The deformation mechanisms were shown to evolve systematically with strain rate, transitioning from GBS-dominated deformation at low strain rates to dislocation-mediated and CDRX-assisted deformation at high strain rates.
4. Cavitation resistance was demonstrated to depend primarily on the ability of the microstructure to suppress cavity growth and coalescence, rather than simply minimizing intermetallic particle-related nucleation sites.
5. Combined strain-rate testing demonstrated that prior high-strain-rate deformation influences subsequent lower-strain-rate formability, highlighting the potential importance of deformation history and microstructural inheritance in HSBF alloy design.
6. Cost-effective Sc–Zr–Er microalloying was shown to enhance microstructural stability and extend useful formability toward HSBF-relevant strain rates, demonstrating the feasibility of developing high-performance HSBF alloys from scrap-derived Al–Mg–Mn feedstock.

7.2 Limitations and clarifications of the present study

While this thesis establishes processing–microstructure–deformation–damage relationships for Al–Mg–Mn 5xxx alloys under conditions relevant to HSBF, several considerations define the scope within which the findings should be interpreted. Detailed methodological clarifications concerning these issues are provided in Appendix A.

Clarification of superplasticity terminology. The term *superplastic response* is used in this thesis within the broader context of elevated-temperature deformation and superplastic forming of Al–Mg–Mn 5xxx alloys across a wide strain-rate range. Its use does not imply that every investigated condition represents classical superplasticity. At lower strain rates, the combination of strain-rate sensitivity, large tensile elongation, fine and stable grain structures, and grain-boundary-sliding-assisted deformation is consistent with a superplastic response. At 1 s^{-1}, however, the mechanical and microstructural evidence indicates increasing contributions from dislocation-mediated deformation and CDRX. This condition is therefore interpreted as high-temperature, high-strain-rate deformation relevant to HSBF rather than classical superplasticity.

Experimental limitations. Most quantitative cavitation measurements in Chapter 5 were obtained at fracture and consequently represent terminal damage states attained at different total elongations. Interrupted experiments at common deformation levels provided additional information on strain-dependent cavity development, but equivalent-strain interruption could not be systematically extended to the high-strain-rate regime. Similarly, although the combined EBSD, TEM, and mechanical evidence supports CDRX-assisted deformation at high strain rates, its progressive evolution with strain was not directly tracked through interrupted high-rate experiments. Detailed discussion of these experimental considerations is provided in Sections A.3 and A.4.

The experimental protocols also evolved during the research program. Chapters 3–5 employed the Gleeble 3800, whereas Chapter 6 employed a furnace-equipped ZwickRoell Z250 configuration to accommodate larger deformation and enable controlled strain-rate transitions. Consequently, differences in thermal history, specimen geometry, and testing

configuration should be considered when comparing absolute mechanical properties across the two experimental campaigns. The rationale for the change in experimental configuration and the procedures adopted to control specimen thermal history are detailed in Section A.1.

Finally, the dual-stage deformation experiments were intended as a proof-of-concept assessment of strain-rate-transition effects rather than a complete simulation of industrial HSBF. The experiments were restricted to selected alloys, one high-strain-rate pre-strain condition, and one strain-rate transition, while the intermediate microstructure between the two deformation stages was not characterized. Accordingly, the results demonstrate the feasibility of the approach but do not establish an optimum deformation path or fully resolve the mechanisms governing deformation-history effects. The experimental methodology and scope of these tests are described further in Section A.5.

Overall, these considerations establish appropriate boundaries for interpretation of the results while identifying specific areas requiring further investigation. They form the basis for the recommendations for future work presented in the following section.

7.3 Recommendations for future work

Based on the findings of this thesis, five key recommendations are proposed to further advance the development and implementation of Al–Mg–Mn 5xxx alloys for HSBF applications.

First, future alloy and processing strategies should focus on the optimization of dispersoids, intermetallic particles, and dispersoid-free zones. The present results demonstrate that Mn-rich dispersoids enhance grain stability, promote continuous dynamic recrystallization (CDRX), and suppress cavity growth, whereas coarse intermetallic particles

act as preferential sites for cavity nucleation. Accordingly, thermomechanical processing routes should be designed to refine coarse particles while increasing the number density and uniformity of fine Mn-rich dispersoids. In addition, the formation of continuous dispersoid-free zones, particularly in Er-containing alloys, should be minimized, as they promote strain partitioning and reduce ductility. Optimization of homogenization, rolling, and annealing schedules is therefore essential to improve microstructural uniformity and enhance formability under HSBF-relevant conditions.

Second, cavitation and microstructural evolution under interrupted and dual-stage strain-rate conditions representative of HSBF should be systematically investigated. While this thesis primarily examined cavitation under constant strain-rate conditions, with additional interrupted deformation used to evaluate cavity evolution at selected common strains, equivalent-strain interruption becomes increasingly difficult at high strain rates using the Gleeble configuration employed in this work. Future studies should therefore employ testing configurations capable of accurately interrupting deformation at predetermined strains under high-strain-rate conditions. Particular attention should be given to tracking cavity nucleation, growth, and coalescence, together with grain-boundary evolution, subgrain development, and CDRX using interrupted EBSD and TEM characterization. For dual-stage deformation, different high-strain-rate pre-strain levels should be investigated to determine how the microstructure and damage inherited from the first stage influence subsequent lower-strain-rate deformation. This would provide a more complete mechanistic basis for defining safe forming windows for HSBF.

Third, the Sc–Zr–Er microalloying strategy should be further optimized to reduce alloy cost while maintaining high-strain-rate formability. Although this thesis demonstrated

that partial substitution of Sc with Er provides promising deformation performance in scrap-derived Al–Mg–Mn alloys, the optimal balance between Sc, Zr, and Er remains to be established. Future investigations should additionally distinguish the intrinsic effects of microalloying chemistry from those associated with the resulting recrystallization state by comparing alloys both under identical thermal-processing conditions and, where appropriate, at matched recrystallization fractions and grain sizes.

Fourth, constitutive modeling, finite element simulation, and pilot-scale validation should be pursued to bridge the gap between laboratory-scale findings and industrial implementation. The mechanical and microstructural data generated in this thesis provide a robust foundation for developing constitutive and damage models tailored to HSBF. These models should capture the transition from grain-boundary sliding at low strain rates to dislocation-mediated deformation and CDRX at high strain rates. Implementation of such models in simulation platforms such as ABAQUS would enable prediction of strain localization, thickness distribution, cavitation evolution, and forming limits during both crash-forming and gas-forming stages. Ultimately, the most promising alloy compositions and processing conditions should be validated through pilot-scale HSBF trials using representative automotive geometries, with evaluation of forming time, dimensional accuracy, surface quality, post-forming properties, and overall industrial feasibility.

Fifth, an integrated HSBF deformation-mechanism and processing-window framework should be developed by combining strain rate, temperature, microstructural state, ductility, cavitation, and dominant deformation mechanisms. Future work should expand the experimental matrix to permit quantitative construction and validation of such maps and their implementation in process simulation.

List of Publications

1. Kweitsu, E.K.; Sarkar, D.K.; Chen, X.-G. A Short Review on Superplasticity of Aluminum Alloys. *Eng. Proc.* **2023**, *43*(1), 43. https://doi.org/10.3390/engproc2023043043.

2. Kweitsu, E.K.; Sarkar, D.K.; Algendy, A.Y.; Chen, X.-G.; Veilleux, J.; Bombardier, N. Effect of Annealing Time on Grain Structure Evolution and Superplastic Response of Al-Mg 5xxx Alloys. *Materials* **2024**, *17*(22), 5492. https://doi.org/10.3390/ma17225492.

3. Kweitsu, E.K.; Sarkar, D.K.; Algendy, A.Y.; Chen, X.-G.; Veilleux, J.; Bombardier, N. Superplastic Deformation and Microstructural Evolution of an Al–Mg–Mn 5xxx Alloy for High-Speed Blow Forming Applications. *J. Mater. Sci.* **2026**, *61*, 16033–16053. https://doi.org/10.1007/s10853-026-12693-0.

4. Kweitsu, E.K.; Sarkar, D.K.; Algendy, A.Y.; Chen, X.-G. Strain-Rate-Dependent Cavitation in Al–Mg–Mn 5xxx Alloys: Mechanistic Insights for High-Speed Blow Forming. *Submitted for publication*.

5. Kweitsu, E.K.; Sarkar, D.K.; Algendy, A.Y.; Chen, X.-G.; Levesque, J. Microstructural Evolution and Strain-Rate-Dependent Deformation of Sc–Zr–Er Microalloyed Al–Mg–Mn 5xxx Alloys Produced from Recycled Automotive Sheet Scrap for High-Speed Blow Forming. *Submitted for publication*.

Conference presentations

1. Kweitsu, E.K.; Sarkar, D.K.; Algendy, A.Y.; Chen, X.-G*, Microstructure Evolution and Superplastic Behavior of Al-Mg 5xxx Alloys under High-Speed Blow Forming Conditions* in Proc. COM & LightMat, Montreal, QC, Canada, Jul. 7–10, 2025.
2. Kweitsu, E.K.; Sarkar, D.K.; Chen, X.-G. *A Short Review on Superplasticity of Aluminum Alloys* in 15th International Aluminum Conference, Québec City, Canada, October 2023

Scientific posters

1. A Short Review on Superplasticity of Aluminum Alloys (REGAL 2023)
2. Grain Structure Evolution and Superplastic Response of Al-Mg 5xxx Alloys under High-Speed Blow Forming Conditions (REGAL 2025).

Appendix A

Supplementary Experimental Methodology and Clarifications

A.1 Comparison and Rationale of Experimental Protocols across Chapters

The primary experimental methodologies employed in this thesis are described in detail within the respective article-based chapters. To avoid unnecessary repetition, this appendix provides supplementary methodological information and clarification of experimental procedures that are relevant to the interpretation and comparison of results across the different studies. In particular, the experimental configuration employed for the commercial Al–Mg–Mn alloys in Chapters 3–5 differed from that used for the developed alloys in Chapter 6. These differences reflect the evolving objectives of the experimental program and the experimental capabilities required at each stage of the study.

Chapters 3–5 employed a Gleeble 3800 thermomechanical simulator using direct electrical resistance heating. This configuration enabled rapid heating of the tensile specimens and short pre-deformation thermal treatments, providing a laboratory approach for investigating microstructural evolution, deformation mechanisms, and cavitation under rapid thermal and strain-rate conditions relevant to high-speed blow forming. Specimens were rapidly heated to the prescribed deformation temperature within approximately 3 min and typically held for 4 min before tensile deformation. Deformation was investigated over a broad strain-rate range extending from 0.001 to 1 s^{-1}. The lower strain rates (0.001–0.01

s^{-1}) enabled characterization of deformation behavior associated with the slower gas-pressure-driven forming stage, whereas the high strain rate of 1 s^{-1} was investigated to represent the rapid deformation associated with the initial crush-forming stage of HSBF. The broad strain-rate range additionally enabled systematic investigation of the transition in deformation behavior and associated mechanisms between the lower- and high-strain-rate regimes.

Despite its advantages for rapid thermal simulation, the Gleeble configuration imposed practical limitations when very large tensile deformation and controlled changes in strain rate were required. These limitations became particularly relevant during the alloy-development phase of the research, where the developed alloys exhibited greater deformation under some test conditions and where dual-stage strain-rate loading was introduced to investigate the effect of deformation history and strain-rate transitions. Chapter 6 therefore employed a furnace-equipped ZwickRoell Z250 universal testing system, which provided greater deformation capacity and flexibility for implementing controlled strain-rate paths.

The use of a furnace-equipped system introduced a separate experimental consideration. In conventional furnace-based high-temperature tensile testing, heating the furnace, grips or fixture, and tensile specimen simultaneously from room temperature can result in prolonged thermal exposure of the specimen before deformation. Such prolonged exposure was undesirable for the present study because the thermal history preceding deformation can significantly modify recrystallization and grain structure and is not representative of the relatively short thermal exposure targeted for HSBF. A dedicated specimen-holding fixture was therefore designed for the ZwickRoell system to minimize

unnecessary specimen exposure during furnace heating and thermal stabilization (Figure A.1).

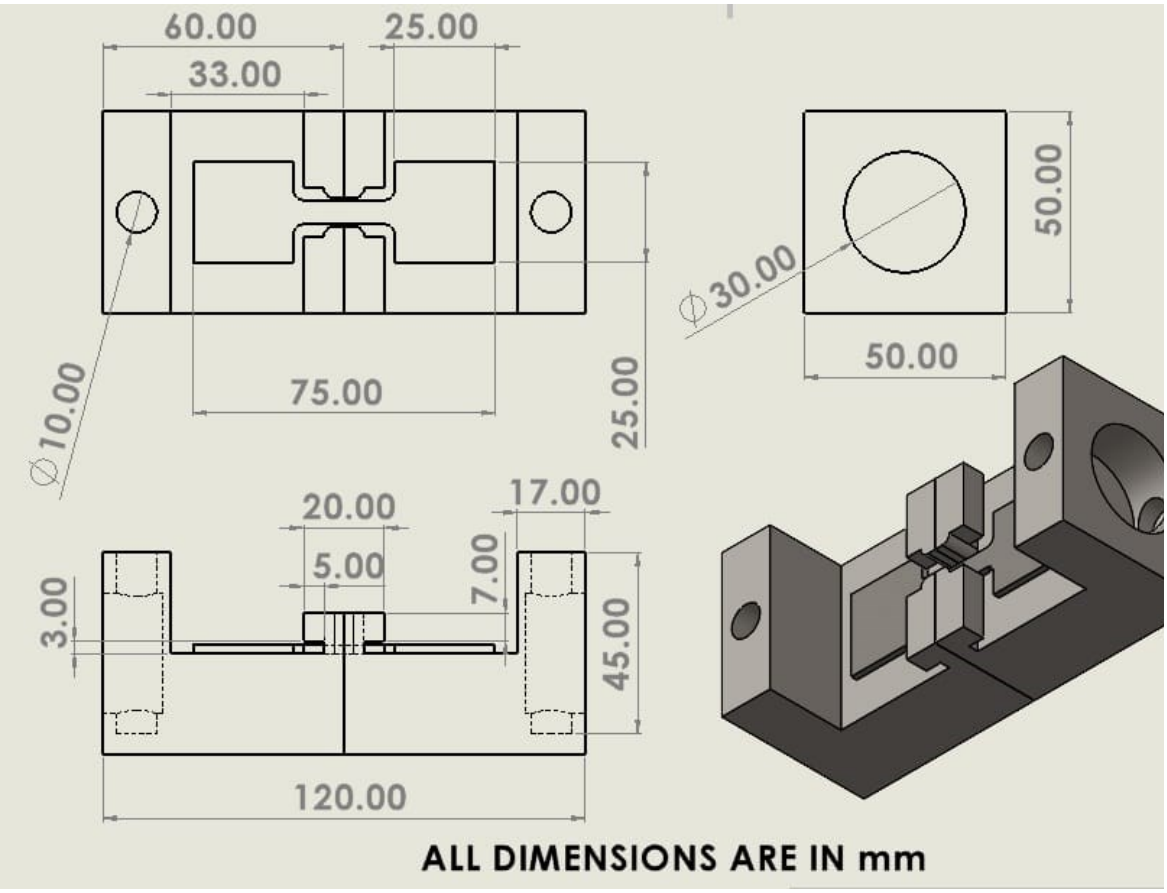


Figure A.1. Schematic and dimensions of the dedicated specimen-holding fixture developed for high-temperature tensile testing using the furnace-equipped ZwickRoell Z250 system. The fixture enabled preheating of the furnace and fixture prior to specimen installation, thereby minimizing unnecessary thermal exposure of the tensile specimen before the prescribed pre-deformation annealing treatment.

The thermal sequence employed with this configuration is illustrated in Figure A.2. The furnace and specimen-holding fixture were first heated to 500 °C without the tensile specimen installed. Heating of the furnace–fixture assembly required approximately 120 min,

after which the fixture was maintained at 500 °C for an additional 30 min to establish thermal stability. The tensile specimen was subsequently installed into the preheated fixture within approximately 10–30 s. Introduction of the room-temperature specimen caused a temporary decrease in temperature, after which the specimen–fixture assembly recovered to the target temperature of 500 °C within approximately 3 min. Importantly, the prescribed pre-deformation annealing period was initiated only after the specimen had reached the target temperature. The specimen was then maintained at 500 °C for 10 min before tensile deformation.

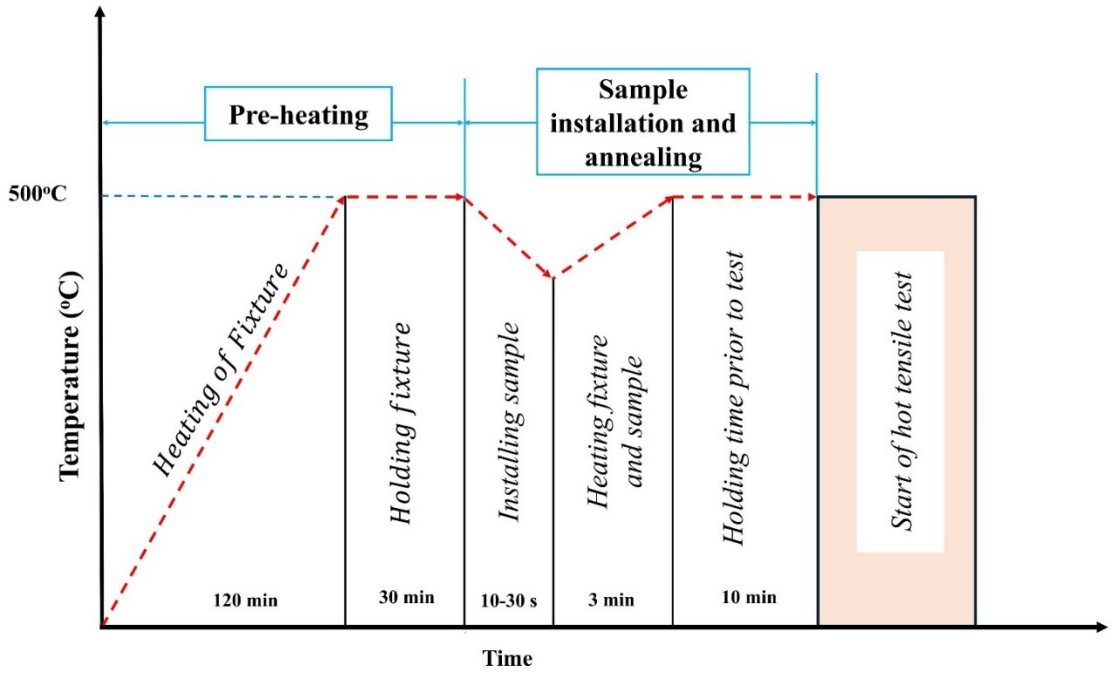


Figure A.2. Schematic thermal sequence employed for high-temperature tensile testing using the furnace-equipped ZwickRoell Z250 system. The furnace and dedicated specimen-holding fixture were preheated to 500 °C for approximately 120 min and thermally stabilized for 30 min before specimen installation. The tensile specimen was installed into the preheated fixture within approximately 10–30 s, after which the

specimen–fixture assembly recovered to 500 °C within approximately 3 min. The specimen was subsequently held at 500 °C for 10 min before initiation of the hot tensile test.

This procedure separated furnace and fixture preheating from specimen heating and therefore limited the specimen heating period to approximately 3 min before the controlled 10-min annealing treatment. Although the Gleeble and ZwickRoell systems employed fundamentally different heating mechanisms, both experimental procedures were consequently designed to achieve short and well-defined specimen heating histories prior to the prescribed pre-deformation holding treatment. The principal thermal difference between the two experimental campaigns was therefore the subsequent pre-deformation holding period—typically 4 min for the Gleeble studies and 10 min for the ZwickRoell experiments—together with differences inherent to resistance and furnace heating.

The strain-rate matrix was deliberately refined during the progression of the experimental program. Chapters 3–5 investigated strain rates of 0.001, 0.01, and 1 s^{-1} to establish the strain-rate-dependent deformation and damage response of the commercial alloys. These studies also showed that increasing strain rate substantially limited cavity growth compared with the low-strain-rate condition. Following the mechanistic understanding developed from these studies, Chapter 6 focused on strain rates of 0.01, 0.1, and 1 s^{-1}. The inclusion of 0.1 s^{-1} enabled assessment of whether substantial deformation could be sustained at a rate higher than the lower-rate forming regime investigated previously, thereby exploring its potential for accelerating the gas-pressure-driven stage of HSBF while limiting cavitation growth. The 1 s^{-1} condition retained the high-strain-rate regime associated with rapid initial deformation, while 0.01 s^{-1} provided continuity with the lower strain-rate

regime investigated in the preceding chapters. The ZwickRoell configuration further enabled controlled transition from high-strain-rate pre-deformation at 1 s^{-1} to subsequent lower-strain-rate deformation during the proof-of-concept dual-stage experiments.

Accordingly, the change from the Gleeble 3800 to the ZwickRoell Z250 and the refinement of the strain-rate matrix should not be interpreted as direct replication of the same experimental protocol using different equipment. Rather, they represent an evolution of the experimental methodology in response to the findings and objectives of successive phases of the research. Chapters 3–5 were designed primarily to establish the effects of thermal treatment and strain rate on microstructural evolution, deformation mechanisms, and cavitation across a broad HSBF-relevant strain-rate range. Chapter 6 subsequently extended this framework toward alloy development, deformation stability at intermediate-to-high strain rates, and the influence of strain-rate transitions. The high ductility subsequently observed at 0.1 s^{-1} supports the potential for shifting the slower HSBF forming stage toward higher strain rates, although further dual-stage forming studies are required to validate this processing strategy.

Nevertheless, differences in heating method, pre-deformation holding time, specimen geometry, and deformation-control configuration can influence the measured mechanical response. Direct quantitative comparison of absolute mechanical properties between the Gleeble and ZwickRoell datasets should therefore account for these experimental differences. Cross-chapter synthesis in this thesis consequently focuses primarily on consistent trends in microstructural evolution, strain-rate-dependent deformation behavior, and underlying deformation mechanisms rather than treating absolute mechanical values obtained from the two experimental systems as directly equivalent. For clarity, the principal

experimental conditions, capabilities, and methodological differences between the Gleeble and ZwickRoell configurations are summarized in Table A.1.

Table A.1. Summary of the principal experimental protocols employed across the thesis

Parameter	**Chapters 3–5**	**Chapter 6**
Testing system	Gleeble 3800	ZwickRoell Z250
Heating method	Direct electrical resistance heating	Preheated furnace with dedicated specimen fixture
Approximate specimen heating time	~3 min	~3 min after specimen installation
Pre-deformation holding time	Typically 4 min	10 min
Selected strain rates	0.001, 0.01, and 1 s^{-1}	0.01, 0.1, and 1 s^{-1}
Loading approach	Constant strain rate	Constant and dual-stage strain-rate loading
Materials	Commercial Al–Mg–Mn 5xxx alloys	Developed recycled Al–Mg–Mn–Sc–Zr–Er alloys
Primary purpose	Thermal treatment, deformation mechanisms, and cavitation	Alloy development, deformation stability, and strain-rate-transition response
Principal advantage	Rapid resistance heating and thermomechanical simulation	Greater deformation capacity and strain-rate-path flexibility
Main experimental consideration	Temperature gradient along specimen length	Furnace heating requiring controlled specimen insertion and heating strategy

A.2 Mechanical Data Analysis and Apparent Activation-Energy Determination

The procedures used to determine stress, strain, strain-rate sensitivity, and apparent activation energy are described in the corresponding article-based chapters. This section provides additional clarification regarding the selection and interpretation of the mechanical parameters used for deformation-mechanism analysis, particularly across the wide strain-rate range investigated.

The strain-rate sensitivity parameter, m , was determined from the dependence of flow stress on strain rate at a given temperature. For consistency across the different deformation conditions, flow stresses were extracted at a common true strain of 0.10. This strain was selected because it provided a common deformation point that could be reliably identified across the investigated temperatures and strain rates, including the high-strain-rate condition of 1 s^{-1}. A well-defined steady-state flow regime was not consistently established across all experimental conditions, particularly at the highest strain rate; therefore, the analysis did not assume the existence of a true steady-state stress.

The apparent activation energy for deformation was similarly determined from the temperature dependence of the flow stresses evaluated at a true strain of 0.10, following the constitutive approach described in the corresponding experimental chapter. The resulting values represent apparent activation energies associated with the overall deformation response and should not be interpreted as unique activation energies of independently isolated elementary deformation mechanisms. This distinction is important because the macroscopic flow response of the investigated alloys can involve simultaneous or evolving

contributions from grain-boundary sliding, solute–dislocation interactions, dislocation-mediated deformation, recovery, and dynamic microstructural evolution depending on temperature and strain rate.

Accordingly, neither the strain-rate sensitivity nor the apparent activation energy was used independently to assign a deformation mechanism. Instead, these parameters were interpreted together with the evolution of flow stress and elongation and with microstructural evidence obtained by EBSD and TEM. The correspondence between the mechanical response and changes in grain morphology, grain-boundary character, dislocation structures, and subgrain formation provided the basis for the strain-rate-dependent mechanistic framework developed in this thesis.

This combined approach was particularly important for interpretation of the deformation response at 1 s^{-1}. Under this condition, the mechanical response and relatively low strain-rate sensitivity, together with EBSD and TEM evidence of grain refinement, dislocation activity, subgrain formation, and boundary evolution, indicated an increasing contribution from dislocation-mediated deformation and CDRX-assisted microstructural evolution. The apparent activation-energy analysis was therefore used as supporting evidence within the overall mechanistic assessment rather than as a standalone criterion for identifying a specific deformation mechanism.

A.3 Interrupted Deformation and Cavitation Assessment

The detailed procedures used for cavitation characterization are provided in Chapter 5. Most quantitative cavitation measurements, including cavity area fraction, number density, and equivalent circular diameter distributions, were obtained from specimens deformed to

fracture. Because the two commercial alloys exhibited different elongations to failure, these measurements represent the respective terminal damage states of the alloys and therefore reflect both the kinetics of cavity development and the different total strains accumulated before fracture. Direct comparison of fracture-state cavity statistics should consequently be interpreted with this distinction in mind.

To provide additional information on cavity development prior to fracture, interrupted tensile tests were performed at 500 °C and an initial strain rate of 0.001 s^{-1}. Specimens were deformed to approximately 20 % and 100 % elongation, after which loading was terminated and the specimens were air cooled. These deformation levels were selected to provide representative observations of cavity development at an early stage and at a substantially more advanced stage of deformation before final fracture. The interrupted specimens were subsequently prepared and characterized using the cavitation-analysis procedure described in Chapter 5.

The interrupted experiments enabled cavity development to be examined at approximately common deformation levels rather than exclusively at the different fracture strains attained by the two alloys. They therefore provided supplementary evidence for distinguishing the evolution of cavitation with increasing deformation from the terminal cavity population observed at fracture. These measurements complement, rather than replace, the fracture-state analysis, since the latter remains important for characterizing the final damage condition associated with failure.

Equivalent-strain interrupted testing was not extended across the higher strain-rate conditions. At high strain rates, particularly at 1 s^{-1}, deformation occurs over a very short

time interval, and precise interruption of the Gleeble tensile test at a predetermined deformation level was not practically feasible with the experimental configuration employed in this study. Consequently, systematic strain-resolved measurements of cavity evolution at equivalent intermediate deformation levels were not obtained for the high-strain-rate regime.

The high-strain-rate cavitation results are therefore interpreted primarily as comparisons of the damage states reached at fracture, together with the corresponding deformation behavior and post-deformation microstructural observations. The interrupted tests at 0.001 s^{-1} provide additional direct evidence of the progressive development of cavitation with deformation, while the absence of equivalent high-strain-rate interrupted measurements remains a limitation of the present experimental study. Future investigations employing high-speed deformation systems capable of precise strain-controlled interruption would enable the proposed strain-rate-dependent cavitation framework to be evaluated at equivalent intermediate strains across the complete HSBF-relevant deformation regime.

A.4 Microstructural Evidence for Identification of Continuous Dynamic Recrystallization

The strain-rate-dependent deformation mechanisms proposed in this thesis were identified through the combined interpretation of mechanical response and post-deformation microstructural characterization. In particular, the identification of continuous dynamic recrystallization (CDRX) at high strain rates was not based on a single microstructural parameter but on the convergence of evidence obtained primarily from EBSD and TEM observations together with the corresponding mechanical behavior.

EBSD characterization of specimens deformed at high strain rates revealed substantial changes in grain morphology and grain-boundary character relative to the pre-deformation condition. These changes included localized grain refinement, the development of fine grains within or adjacent to the deformed grain structure, and changes in the relative fractions of low-angle and high-angle grain boundaries. Such observations are consistent with progressive subdivision of deformed grains and the evolution of subgrain boundaries toward higher misorientations during deformation.

TEM provided complementary evidence at a finer length scale. The deformed microstructures exhibited increased dislocation activity and the formation of dislocation substructures and subgrains. When considered together with the EBSD-observed grain refinement and boundary evolution, these features support a deformation sequence involving dislocation accumulation, rearrangement into subgrain boundaries, and progressive boundary-misorientation development characteristic of CDRX-assisted microstructural evolution. The attribution of CDRX was therefore based on the combined occurrence of dislocation activity, subgrain formation, grain refinement, and grain-boundary evolution, rather than on grain refinement alone. These microstructural observations were further interpreted in conjunction with the corresponding flow behavior and strain-rate sensitivity, which indicated an increasing contribution from dislocation-mediated deformation as the strain rate approached 1 s^{-1}.

Direct strain-resolved tracking of the progressive boundary evolution was not performed. In particular, interrupted EBSD characterization at several intermediate strains and corresponding kernel average misorientation (KAM) analysis were not available for the high-strain-rate conditions. Precise interruption at predetermined intermediate strains was

practically difficult at 1 s^{-1} using the Gleeble configuration employed in this study, as discussed in Section A.3. Consequently, the complete kinetic sequence from dislocation accumulation through subgrain formation and progressive conversion of low-angle boundaries toward high-angle boundaries was not directly followed as a function of strain.

KAM analysis could provide additional information regarding the spatial distribution of local lattice misorientation and stored deformation within the microstructure. However, KAM is not treated in this thesis as an independent or absolute criterion for establishing CDRX. Rather, strain-resolved KAM measurements would provide complementary evidence to the EBSD boundary-character analysis and TEM observations already obtained. Accordingly, the identification of CDRX in this thesis should be interpreted as a mechanistic attribution supported by the convergence of the available mechanical, EBSD, and TEM evidence, while direct strain-resolved characterization of its kinetics remains an opportunity for future investigation.

A.5 Dual-Stage Strain-Rate Deformation Methodology

In addition to the constant-strain-rate tensile experiments described in Chapter 6, dual-stage deformation testing was conducted as a proof-of-concept assessment of the influence of strain-rate transition and deformation history under HSBF-relevant conditions. The experiment was intended to reproduce, in a simplified uniaxial configuration, the transition between a rapid initial deformation stage and a subsequent lower-strain-rate deformation stage characteristic of the conceptual HSBF forming sequence.

The dual-stage experiments were conducted at 500 °C using the furnace-equipped ZwickRoell Z250 testing system and the thermal procedure described in Section A.1.

Following heating and the prescribed 10-min pre-deformation annealing treatment, specimens were initially deformed at 1 s^{-1} to approximately 30% engineering strain (Stage I). Upon reaching the prescribed pre-deformation level, the strain rate was reduced to 0.01 s^{-1}, and deformation was continued to failure (Stage II). The first stage was selected to represent the rapid initial deformation regime associated with the high-strain-rate stage investigated in this thesis, whereas the second stage represented subsequent deformation within the lower strain-rate regime. Unlike the constant-strain-rate experiments, the material entering Stage II had therefore already experienced substantial high-strain-rate deformation. Consequently, the Stage II response represents the deformation behavior of a material conditioned by the preceding high-strain-rate deformation history rather than that of the initial annealed material.

The dual-stage experiments were conducted on the B and BSc05ZrEr alloys rather than all three alloys investigated in Chapter 6 because the experiments were intended as a preliminary proof-of-concept assessment rather than a systematic alloy comparison. The base alloy (B) was selected to provide the reference response, whereas BSc05ZrEr was selected as the representative microalloyed alloy because, among the Sc-containing alloys, it exhibited the higher elongation at 0.01 s^{-1}, corresponding to the strain rate employed during Stage II. Its selection therefore provided a suitable condition for examining whether the enhanced deformation capacity observed under monotonic low-strain-rate loading could be retained following high-strain-rate pre-deformation. The comparison between B and BSc05ZrEr consequently enabled an initial assessment of the effect of the preceding high-rate deformation history on the subsequent deformation response of a baseline and a microalloyed material. BSc10 was not included because the objective of these preliminary

experiments was to establish the feasibility of the dual-stage loading concept rather than to systematically rank the performance of all developed alloys.

Figure A.2 presents the engineering stress–strain responses of the B and BSc05ZrEr alloys during dual-stage loading. Both alloys sustained substantial additional deformation during Stage II following the initial high-strain-rate pre-deformation. The BSc05ZrEr alloy exhibited greater total deformation capacity than the base alloy, demonstrating that substantial subsequent deformation could be retained in the microalloyed material after exposure to the initial high-strain-rate stage. Following fracture, the total elongation was additionally assessed from physical measurements of the specimen gauge section, with the BSc05ZrEr specimen exhibiting an elongation of approximately 283 %, providing an independent assessment of the large deformation sustained during the dual-stage loading sequence.

The dual-stage experiment was designed as a proof-of-concept rather than a complete physical simulation of HSBF. The uniaxial tensile configuration does not reproduce the multiaxial stress state, continuously varying local strain rates, contact conditions, and geometrical evolution associated with industrial HSBF. Nevertheless, the experiment provides a controlled means of examining the response of the material to a transition from high- to lower-strain-rate deformation and demonstrates that substantial subsequent deformation can be sustained following high-strain-rate pre-deformation.

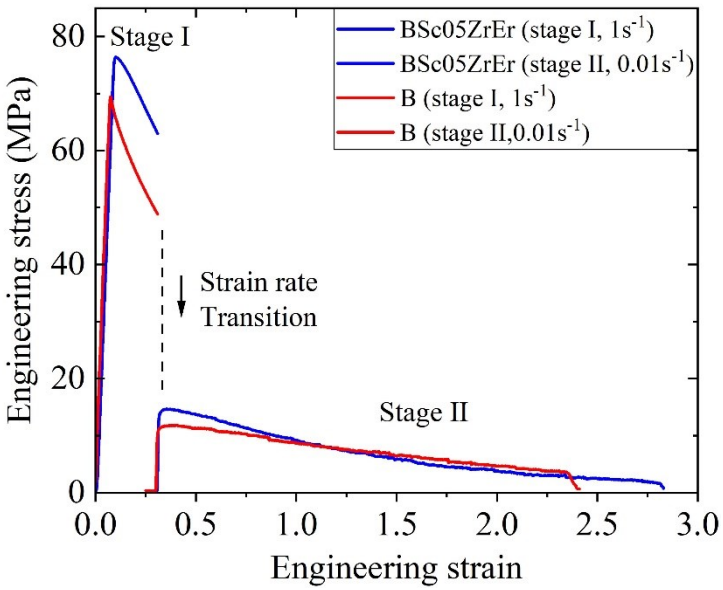


Figure A.2. Engineering stress–strain responses of the B and BSc05ZrEr alloys during dual-stage deformation at 500 °C. Stage I consisted of deformation at 1 s^{-1} to approximately 30% engineering strain, followed by a transition to 0.01 s^{-1} for Stage II deformation to failure. The dashed line indicates the prescribed strain-rate transition.

The intermediate microstructure between Stage I and Stage II was not characterized, and the present experiments were restricted to two alloys, a single high-strain-rate pre-strain condition, and one strain-rate transition. Therefore, although the results demonstrate the feasibility and potential benefit of the dual-stage loading concept, they do not establish an optimum strain-rate path or fully resolve the mechanisms governing the effect of deformation history. In particular, the present results do not independently establish whether the enhanced subsequent deformation originates from CDRX, subgrain development, boundary evolution, or other forms of microstructural inheritance generated during Stage I. Further experiments involving all three developed alloys, different high-rate pre-strain levels, additional strain-rate transitions, and microstructural characterization immediately following Stage I would be

required to validate the underlying mechanisms and optimize the dual-stage deformation strategy for HSBF applications.

Appendix B – Research Ethics Declaration

The research presented in this thesis focuses on the development and characterization of Al–Mg–Mn 5xxx aluminum alloys. The research did not involve human participants or animals. Consequently, no research ethics certification was required for this study.